Subcritical transition to turbulence in shear flows

Yohann Duguet

université PARIS-SACLAY

École doctorale SMEMAG Université Paris–Saclay

Subcritical transition to turbulence in shear flows

HDR

soutenue le 10.12.2021

pour l'obtention d'une

Habilitation de l'Université Paris–Saclay

(mention mécanique)

par

Yohann Duguet

Composition du jury

Rapporteurs :	Laurette S. Tuckerman
	François Charru
	Peter J. Schmid
Examinateurs :	François Daviaud
	Jean-Christophe Robinet

Laboratoire Interdisciplinaire pour les Sciences du Numérique — UMR 9015

Mis en page avec la classe thesul.

Sommaire

This scientific subject represents my largest scientific investment since my PhD thesis and I thus chose to develop it in the rest of the present habilitation thesis. As a short informal introduction to the topic, I would like to mention how I got acquainted with the world of subcritical transition. I simply got entrained by other people who underwent that transition from rotating flows instabilities to shear flow transition, namely Rich Kerswell from Bristol University, who was apparently following the scheme proposed by Fabian Waleffe before him and got interested in the application of dynamical systems theories to these flows. I got seduced initially by the apparent mathematical formalism used in the related studies as well as by the appealing simplicity and importance of the flow configurations under study. After working on pipe flow in Bristol with R.R. Kerswell together with A.P. Willis and C.C.T. Pringle, I continued along (hopefully) the same lines at the Department of Mechanics of KTH Stockholm together with Dan S. Henningson, Philipp Schlatter and Luca Brandt, who were experts of transitional shear flows but somehow new to the nonlinear interpretation schemes. My interest, influenced directly by numerical feasibility, switched from turbulence itself to transition (via the study of "edge states") for which the dynamical systems paradigm semt more relevant... at least to me. At about the same time I got acquainted with Paul Manneville from LadHyx who convinced me that a spatiotemporal look at such flows is not an option, and suggested instead a spatiotemporal if not statistical physics–oriented perspective. Such a view gets challenged periodically by some of my colleagues from the field, including the late Bruno Eckhardt (whose scientific influence I am hardly able to quantify as of now), Predrag Cvitanović, Olivier Dauchot, Yves Pomeau, Björn Hof, John F. Gibson, Marc Avila, Laurette Tuckerman or Dwight Barkley, to name just the most productive of them. My current understanding of transition results from the interplay between these stimulating as well as often conflicting points of views, but more importantly from the scientific optimism of the people mentioned just above.

Preamble

Here are a few words to explain the way I structured my habilitation thesis. First of all I chose to write in English because my priority targets are my own students, those gone as well as those to come. These many students are all different, yet the one thing they have in common is that they understand English. English is not my mother tongue although I use it more than French for Science, nevertheless I apologise in advance for all the pain endured by genuine Anglophones upon reading my manuscript. I chose to tell a story here, or (hopefully) give a course at an advanced scientific level. I hence chose a coherent storyline whose elements were subtle from my past published papers. Choosing to dissert on the transition to turbulence was a natural choice because that is so far the most coherent story line I can offer, and because it covers all the time period since my first post-doctoral position. The story told is almost free from technicalities. In particular, although my own everyday work (and that of my students) has long consisted of implementing numerical schemes and post-processing numerical data, I intended to zoom out and tell a physicist story. There won't be any detail about the numerical codes used, about how "details" were implemented. There are several reasons behind this choice. To start with, this is my second thesis and I wanted it to be as different as possible from the first one which was very numerics-oriented. More importantly perhaps, these details can be found in the published articles. Crucially too, including them would shadow or obscure the thinking underlying all these studies. Instead I would ideally like the potential reader to grasp the subtile connections between the mathematician's approach to the Navier–Stokes equations, the engineer's concern about keeping his pipe flow energetically interesting, and the physicist's wish to understand complexity and summarise it using a few modular concepts. Almost all images included in this document have been published somewhere and the bibliographic reference is always included in the caption or in the related text. A small number of images come from as yet unpublished studies, in which case the collaborator(s) for this image is/are also mentioned. One of the main difficulties in writing a research course, or something close to it, is that each result mentioned, be it from me or someone else, is dated. In the relatively recent field of hydrodynamics, only a very small number of results are universally accepted as being part of a basic knowledge package. This becomes especially relevant when transition to turbulence is concerned, namely a field with almost no established mathematical formulas. As a consequence I had to give in the first chapter an overview of the status of the field as I found it when I began working in it. Obviously, and I am in fact glad to have witnessed so much, during the 15 years in which I have worked on transition the field itself has mutated. The reasons are multiple : huge progress in numerical as well as experimental facilities, understanding of certains concepts evolving with time, newborn scientific analogies, new fashionable directions in this field as in other fields... It was difficult to untangle all the different contributions and to extract mine out of the context of the work of a community (since this was the initially requested homework). This let to a tendency to rewrite history in a different order, rather multiple back and forth in time. And last but not least I hope to convince you that I was among the people responsible for that mutation of the field, although most of the people mentioned in the introductory chapter bring so much more than I could ever dream of. With a certain taste for provocation or intellectual stimulation I took a guilty pleasure in revising some of the well-accepted concepts and to re-define them either more formally, or from a more general or exotic perspective. This is hence a highly subjective report, and I apologise in advance for not citing every single contribution.

1

Transition to turbulence in canonical shear flows

1.1 Introduction and Motivation

Hydrodynamic stability lies at the crossroads between hydrodynamics and applied mathematics. The main reason for this intersection is two-fold : it is due first to the highly mathematical formalism developed in the pioneering studies of G.I. Taylor and co-workers, but also to the historical impact that hydrodynamic stability has had later on other fields of applied mathematics such as pattern formation or chaos theory. The fundamental mathematical property of the governing equations, here the incompressible Navier–Stokes equations, is the multiplicity of their solutions. For the same parameters, some solutions appear stable in time while others happen to be unstable in time. The *dynamics* of the system results from the influence of all these solutions together, and not only from the stable ones. Even stable solutions have, most often, finite-size basins of attraction and do not necessarily act as global attractors, especially in the presence of noise, fluctuations,... or anything that can provoke dynamical transitions. The goal of the present chapter is to introduce the basic concepts necessary for the understanding of the next chapters, together with some historical/bibliographical remarks.

1.2 Governing equations

The fluid system of interest in this thesis is, almost without exception, governed by the incompressible Navier–Stokes equations, in their unsteady form. Before any non-dimensionalisation this system of partial differential equations reads

$$\frac{\partial \boldsymbol{u}}{\partial t} + (\boldsymbol{u}\cdot\nabla)\boldsymbol{u} = -\frac{1}{\rho}\nabla p + \nu\nabla^2\boldsymbol{u} + \boldsymbol{f}(t) \tag{1.1}$$

$$\nabla\cdot\boldsymbol{u} = 0, \tag{1.2}$$

The space is by default assumed three-dimensional. In Eq. 1.1, ρ is the fluid density (usually taken as unity) and ν the kinematic viscosity of the fluid, which we will assume to be known, constant and homogeneous. The scalar field p denotes the pressure. It can in certain cases incorporate additional potential energies from which additional forces derive, for instance gravity or centrifugal forces. The external force $\boldsymbol{f}(t)$ does not need to be specified at this point. Most flows with the same Newtonian rheology obey the set of equations above. What distinguishes one flow case from another one is, rather than the governing equations, the domain of study, called V, and the boundary conditions that are associated with its boundary ∂V. Close to a solid boundary, consistently with the viscous hypothesis, we will usually consider that the fluid obeys no slip. As a consequence, the fluid velocity close to the wall equals the wall velocity :

$$\boldsymbol{u}(\boldsymbol{x}_{wall}) = \boldsymbol{U}_{wall}. \tag{1.3}$$

The other simple boundary conditions that are sometimes considered are free slip (used for mathematical simplicity), stress-free (at free interfaces) or other types. In particular, for "open" flows, in constrast to "closed" flows, ∂V does not consist only of wall-like boundaries where the velocity is prescribed : the problem needs to consist also of entrance and exit conditions. We are left with the impossible task of modelling the state of the flow as it enters V, whereas we assume that the flow is not known outside V. Several strategies can be adopted : the entrance flow can be modelled, for instance by noise, by incoming flow stemming from another problem... the main hypothesis in this thesis consists of choosing to make the flow periodic, i.e. assuming that outflow is recycled into inflow. This hypothesis corresponds to the imposition of a given fundamental wavelength to the solutions of the system. This approach, highly debatable from a physical point of view, ensures in general that the mathematical problem is well-posed.

1.3 Canonical base flows

1.3.1 Planar flows

The most *trivial* solutions to the usual planar wall-bounded flows form a single parametric family of solutions to the incompressible Navier-Stokes equations. For a planar infinite geometry along the variables

x and z, let y stand for the direction normal to the solid plate(s). If a 2D steady solution is sought for, independently of the third variable z, it is written *a priori* $\boldsymbol{U} = (U_x(x,y), U_y(x,y))$. Incompressibility then leads to to $\partial_x U_x + \partial_y U_y = 0$. Searching for an x-independent flow leads to $\partial_y U_y = 0$ i.e. U_y independent of y. If U_y vanishes at the wall it is identically zero everywhere. Yet that does not necessarily need to be the case, for instance when uniform suction of blowing is applied at the wall, then $U_y = v$ at the wall (with v a constant). In all cases the nonlinear term $(\boldsymbol{U}\cdot\nabla)\boldsymbol{U}$ vanishes altogether too, and the streamwise momentum equation reduces to

$$\nu\frac{\partial^2 U_x}{\partial y^2} = \underbrace{v\frac{\partial U_x}{\partial y}}_{vertical\ transport} + \underbrace{\frac{1}{\rho}\frac{\partial P}{\partial x}}_{pressure\ term} . \tag{1.4}$$

Let us label the main terms $A = U_y\partial_y U_x$ and $B = \rho^{-1}\partial_x P$. The classification of the solutions depends on the values (zero or non-zero) of A and B :

— $A = B = 0 \rightarrow$ plane Couette flow (pCf),

— $A = 0$ and $B \neq 0 \rightarrow$ plane Poiseuille flow (pPf) or Couette-Poiseuille flow (CPf),

— $A \neq 0$ and $B = 0 \rightarrow$ Asymptotic Suction boundary layer flow (ASBL),

— $A \neq 0$ and $B \neq 0 \rightarrow$ generic Couette Poiseuille flow with suction.

We list below the usual velocity profiles for the canonical base flows that will be analysed here, together with the usual conventions for dimensional and non-dimensional variables.

plane Couette flow

Plane Couette flow (pCf) is the simplest example of shear flow, forced by the difference in velocity between the two walls. In a frame travelling at the average velocity, the boundary conditions can be expressed as $U_x(y = \pm h) = \pm U_w$, together with $U_i(y = \pm h) = 0$ for $i = y, z$. The resulting laminar profile is hence given by

$$U_x(y) = \frac{U_w y}{h}. \tag{1.5}$$

The shear is U_w/h and is spatially homogeneous. One frequent convention is to non-dimensionalise distances by the half-gap h between the walls and velocities by the wall velocity $U_w > 0$. The resulting velocity profile is simply $U_x = y$. The Reynolds number is hence $Re = U_w h/\nu$.

plane Poiseuille flow

Plane Poiseuille flow is the flow between two parallel plates, forced by a given axial pressure gradient. Meanwhile, in the frame of the walls, the flow at the walls is at rest, hence the boundary conditions reduce to $U_i(y = \pm h) = 0$ for alisl i. For simplicity we denote $G = -\partial_x P$ the pressure gradient imposed in the x direction. The resulting laminar velocity profile is given by

$$U_x(y) = G(1 - (\frac{y}{h})^2). \tag{1.6}$$

Note that $U_x \geq 0$ when $G \geq 0$, i.e. when the pressure P decreases with x. The shear now depends on y, it is maximal in magnitude at the walls and it vanishes at the centerplane. Many different non-dimensionalisations coexist for plane Poiseuille flow, depending on the culture of the author and the exact forcing protocol selected. For distances, as for pCf the half-gap h is the usual reference length. As for velocities, the most classical is perhaps non-dimensionalisation by the centerline velocity of the laminar regime $U_{cl} = G$. It is related to the bulk velocity $U_b = Q/2h$, where Q is the flow rate by unit width.

The relation for a laminar plane channel flow is simply $U_b = 2U_{cl}/3$. At equilibrium the wall shear rate $\tau_w = \mu \partial u_x/\partial y$ evaluated and averaged at the walls is constant and is given by $\tau_w/h = G$. It is common practice in pressure-driven flows to use the Reynolds number Re_τ based on the friction velocity u_τ defined by $\rho u_\tau^2 = \tau_w$. This results in $Re_\tau = u_\tau h/\nu \sim \sqrt{\tau_w}$ so that $Re_\tau^2 = 3Re_b$ in the laminar regime.

Asymptotic Suction boundary layer flow

The less known Asymptotic Suction boundary layer (ASBL) profile occurs in the presence of only one wall, which by convention is located at $y = 0$. The flow occurs only in the half-space $y > 0$ while the other half-space $y \leq 0$ is ideally a dense porous medium. The system assumes Couette-like boundary conditions for $U_x : U_x(y = 0) = 0$, $U_x(y \to \infty) = U_\infty$. Simultaneously there is constant suction at the wall and U_y is subject to $U_y(y = 0) = -V_S$ at the wall. The resulting base flow profile has two non-zero components rather than one, and is given by

$$U_x(y) = U_\infty(1 - exp(-\frac{y}{\delta^*})), \tag{1.7}$$

$$U_y = -V_S. \tag{1.8}$$

The convention is to non-dimensionalise velocities by U_∞ and distances by the boundary layer thickness thickness δ^*, given analytically by $\delta^* = \nu/V_S$. This yields a definition for the Reynolds number $Re = U_\infty \delta^*/\nu = \frac{U_\infty}{V_S}$. The shear is maximal at the wall and the wall-normal velocity is constant and non-zero everywhere. In any regime this flow verifies the property that the mean friction velocity u_τ is fixed by the Reynolds number by $u_\tau^2 = U_\infty^2/Re$ [1]. The Reynolds number Re_τ based on the friction velocity is hence also constant on average when Re is imposed.

1.3.2 Cylindrical flows

The same problem can also be solved inside a cylindrical geometry of radius r_0 when the mean flow direction is aligned with the cylinder axis (called by convention z). When the flow is forced by an axial pressure gradient, the laminar profile is parabolic and corresponds to the **Hagen-Poiseuille solution (HPf)**

$$U_x(r) = U_z(r) = \frac{G}{4\nu}(1 - (r/r_0)^2). \tag{1.9}$$

A common modification of this geometry consists in adding a coaxial cylindrical wall inside the primary pipe at radius $r = r_i$ whereas the outer wall still lies at $r = r_o$. The flow in the gap between the two cylinders resulting from an applied axial pressure gradient G is referred to as annular Poiseuille flow (aPf). Finally, another canonical annular flow can be suggested where the fluid is entrained, not by an axial pressure gradient, but by the axial translation of the inner rod ; it is labelled **annular Couette flow**. If $\eta = r_i/r_o$, $d = r_0 - r_i$, $y = r - r_i$ and $U(r = r_i) = U_w$, it admits the simple analytical logarithmic solution

$$U_x(r) = U_w \frac{ln((y(1-\eta)+\eta)/d)}{ln(\eta)}. \tag{1.10}$$

1.3.3 Notion of forcing protocol

In practice, depending on the type of boundary conditions applied, two main classes emerge from the list of simple parallel shear flows above. In cases like plane Couette flow, the fluid flow is *entrained*, whereas for plane Poiseuille flow or pipe flow it is *pressure-driven*. There are several ways to achieve a given pressure-driven flow in practice, depending on which physical quantity is strictly imposed and which one is left free to adapt. The simplest conceptual way to achieve such a flow is to impose a fixed pressure gradient, this is the case for example when the fluid inside a straight vertical pipe is subject to a constant gravity field. Another less direct way to achieve a similar flow is to impose a given flow rate,

for instance by considering that the fluid is pushed or pulled by a piston or a syringe, whose own velocity is known. Other protocols can be suggested, for instance imposing a fixed energy input. It is not obvious which protocol characterises a priori a given hydrodynamic device, for instance standard pump engines are rather believed to operate in the constant power input protocol [2]. Even entrained flow cases are subject to such a distinction, if one considers that the shear is imposed at the wall, rather than the velocity. This is the case for instance in standard models of gas–liquid interfaces although this has recently been questioned in liquids [3]. In the strictly steady regime laminar regime there is no mathematical distinction between these protocols. This is not true in other circumstances. For instance in the steady turbulent regime, the mean values of the kinetic energy, dissipation, etc... are independent of the protocol, however the fluctuations around these mean values are not.

The standard convention in wall turbulence studies (but not always in transition studies!) is to use different governing parameters depending on the forcing protocol. For flows driven by an imposed flow rate, the Reynolds number (which necessitates a velocity scale) is usually based on the so-called bulk velocity U_b (defined classically by the flow rate divided by the equivalent cross-sectional area). The advantage of using U_b in that case is that U_b stays the same no matter whether the flow is laminar or turbulent, whereas the value of the corresponding mean pressure gradient is strongly dependent on the regime. For flows driven by an imposed pressure gradient G, one can exploit the equivalence between the pressure gradient G and the mean wall shear stress τ_w. Such a relation only involves average values and is hence not valid instantaneously, unlike its fixed flow rate counterpart. A velocity scale u_τ can be defined from the knowledge of τ_w via the relation $\tau_w = \rho u_\tau^2 \sim G$. This allows one to define the friction Reynolds number Re_τ based on the velocity scale u_τ rather than U_b. By construction Re_τ is proportional to $\sqrt{G}$ independently of whether the flow is in a laminar or turbulent regime.

1.4 Wall turbulence at onset

Writing a whole thesis about transition to turbulence without ever documenting the turbulent state itself would look incomplete. This section does not pretend to contain all the knowledge on wall turbulence. However it aims at presenting briefly the minimum knowledge necessary for a decent theory of transition, including a justification of the present parameter range of investigation.

1.4.1 High-Reynolds number wall turbulence

Anyone who has glanced at the beginning of a textbook about turbulence might have faced the same question : although the meaning of the word is not so ambiguous in everyday life, is there a solid, universally accepted definition of what *turbulent* means in hydrodynamics? Although laminar flows are perfectly well defined, turbulent flows are not, although we expect them to have all the worst possible complications : finite unsteadiness, correlations in time and space, multiscale structure, impredictability... Etymology hardly helps here, at the very least it indicates (from "*turbinis*" in Latin) that the flow has to contain... vortices, which does not really come as a surprise. Everyday intuition might be more useful here. We all have a mental image of what a *very turbulent* flow looks like from watching rivers, cascades, weather maps. Hence it sounds wiser to consider first these conditions which make fluid flows *very turbulent* and to test how far they can be pushed when that same Reynolds number is reduced. In that spirit we should look at published works on huge values of the Reynolds number Re. We emphasize that, no matter how large, Re should nevertheless be finite since it is well known that the infinite Reynolds number/zero viscosity limit is singular and might lead to very wrong speculations. This looks preferable to an abstract theory from scratch à la Bourbaki, because it is more likely to reconnect properly with the real engineering world.

Let us have a look at a set of recent well-resolved turbulent channel flow simulations. Such simulations are considered in periodic domains and run over long enough times to gather converged flow statistics. Figure 1.1 displays a rendition of vortex clusters for a high Reynolds number of $Re_\tau \approx 4200$ in a domain of size $2\pi h \times 2h \times \pi h$. It is confirmed that vortices abound in the flow, but also that many scales

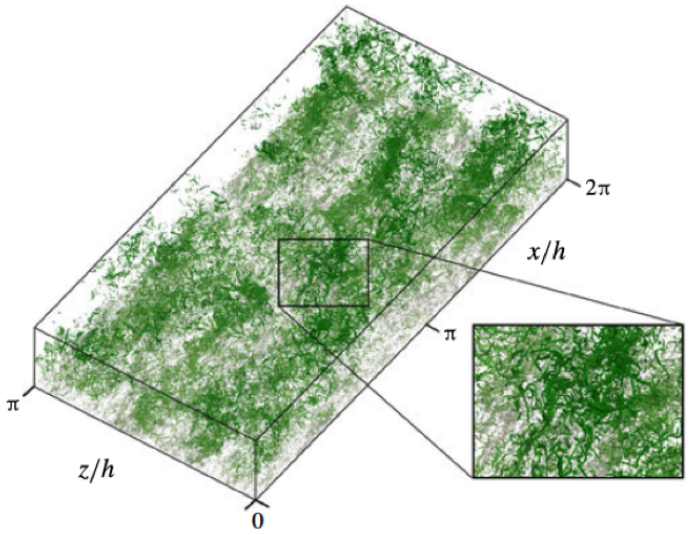

FIGURE 1.1 – Three-dimensional visualisation of vortex clusters in a simulation of channel at $Re_\tau \approx 4200$, from Ref. [4] (only the bottom of the channel is shown).

coexist on a single snapshot, and that clusters of small scales form larger scales. Figure 1.2, based on a simulation of the same flow at a slightly lower value of Re_τ, displays the turbulent kinetic energy of the streamwise velocity component plotted in a (λ_z^+, y^+) diagram. y^+ represents the distance from the lower wall expressed in units of $\delta_\nu = h/Re_\tau$, the classical units of wall turbulence, whereas λ_z^+ represents a wavelength in the spanwise (z) direction, also normalised by δ_ν. Such a figure is less sexy yet more useful than visualisations. It appears clearly that a whole set of scales ranging from $\lambda_z^+ \approx 40$ up to $\lambda_z^+ \approx 10^4$ (and more for higher Re_τ) is present in the flow. Worse : the distribution of scales involved energetically depends strongly on the distance from the wall, with energetic features present from as low as $y^+ \approx 10$. The whole distribution of energy apparently lies around a line $y \sim 0.1\lambda_z$. This echoes the *Attached Eddy Hypothesis* of A. Townsend [5, 6] sketched in figure 1.3. This theory states that the size of each eddy is proportional to its distance from the wall, as opposed to dynamically inert *detached eddies*. In this sketch the wall-parallel space variable can be either x or z. Although the multiscale nature of turbulence is also not surprising, what matters here are the numbers. The smallest eddy in this hierarchy, equivalent to the Kolmogorov scale in isotropic settings, turns out to be slightly less than $100\delta_\nu$ no matter how high Re_τ. This validates the importance of inner units $O(\delta_\nu)$ for scaling laws. The largest eddies in the hierarchy are simply bounded by the channel geometry, which can be estimated as the channel height $2h$. The multiscale nature of wall turbulence can be attributed grossly to the fact that these two orders of magnitude, $100\delta_\nu$ on one hand and $2h$ on the other hand, *do not coincide*. It is precisely in this scale interval that universal features, such as the law of the wall $\bar{U} \approx \frac{1}{\kappa} log(y^+) + B$, are valid [8]. This whole picture holds of course as long as $100\delta_\nu \ll 2h$, which supposes Re_τ large enough.

1.4.2 Estimating the onset of wall turbulence

The previous estimates imply a simple yet powerful reverse idea : multiscale turbulence cannot sustain if $100\delta_\nu > 2h$. Besides, if $100\delta_\nu = 2h$, the resulting turbulent regime is characterised by one lengthscale only. It does feature any log law or $k^{-5/3}$ energy spectrum typical of turbulent cascade, and the turbulent flow is limited to the buffer layer only, together with a viscous sublayer for $y^+ < 5$. Given the definition of $\delta_\nu = h/Re_\tau$, this suggests as a gross estimation that the turbulent state should collapse, should $\delta_\nu = h/Re_\tau < 50$ be verified. Such an estimate is as universal as the scaling laws and is independent of the flow case. It has been advanced or re-discovered several times in the literature [9, 10] and proves correct as a rule of thumb.

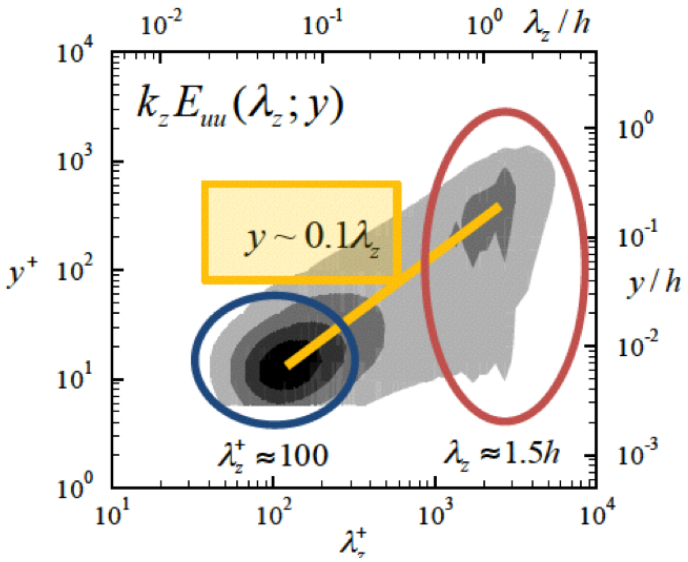

FIGURE 1.2 – Streamwise Energy as a function of (λ_z^+, y^+) for a DNS of channel flow at $Re_\tau = 2003$ (from Ref. [5]).

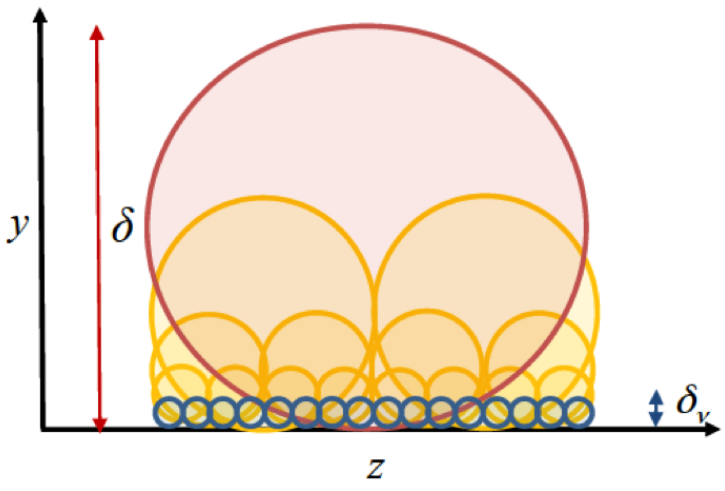

FIGURE 1.3 – Sketch of the Attached Eddy Hypothesis (from Ref. [5]).

What this estimation does not reveal is *what* such a collapse should look like if one starts from a pre-existing turbulent velocity field. There is ample evidence that in almost all wall-contained shear flows, an adiabatic reduction of the Reynolds number yields a spatially and temporally intermittent state of turbulence : where it is turbulent, the flow field looks similar to developed turbulence, but it is not turbulent at every location at the same time.

The way turbulence collapses is illustrated in figure 1.4, taken from Ref. [11] in pipe flow driven by a fixed mass flux. The Reynolds number Re is progressively reduced in small steps starting from a high enough value at which a turbulent flow field is present, no matter how it got generated. The quantity visualised here is the streamwise velocity fluctuation A similar diagram can be found in Ref. [12] for other velocity components and is reproducible, provided the boundary conditions are periodic in the axial direction and the length of the computational domain is large enough. The Reynolds number is here based on the bulk velocity and the pipe diameter. For $Re = 2800$ and above the flow looks unambiguously turbulent, moreover it appears uniformly turbulent, in the mild sense that the large-scale turbulent properties do not depend on the axial coordinate (note that "homogeneous turbulence" is a different, more demanding concept in turbulence theory). For $Re = 2600$ the flow looks similar except for a "hole" located around $x = 150$ where the turbulent activity is less intense, at least at the moment displayed here. More such holes are present at $Re = 2400$. At $Re = 2200$, something has changed qualitatively : rather than laminar-like holes inside a turbulent sea, it is better described by a sequence of localised turbulent-like structures in an otherwise laminar-like environment. These coherent structures look all alike, they are called *puffs* and they form an apparent pattern with defects inside. Whether or not an exact wavelength emerges from a well-defined relation dispersion, like in Turing instabilities, is today still a matter of debate. As Re decreases the number of puffs goes down until extinction. At $Re = 1680$ a last puff survives and it is known from the literature that this puff has a finite lifetime. Once the last puff has died the flow is said to have *relaminarised*. There is a complex dynamics associated with puffs and trains of puffs [13] that cannot be grasped easily from still pictures, but will be explored in Chapter 4.

The collapse of turbulent flows in planar geometries obeys a similar story. It is illustrated in figure 1.5 in the case of plane Poiseuille flow driven by a fixed pressure gradient. The advantage of this kind of forcing over the former fixed mass flow protocol, is precisely that here Re_τ is the control parameter, whereas the traditional Re should be regarded as an (unsteady) output of the simulation. This represents an opportunity to test the above $100\delta_\nu = 2h$ criterion. The quantity visualised in the diagram is the cross-flow energy E_{cf} based on the transverse velocity components only, and the spatial variable is the streamwise coordinate x in a frame moving with the streamwise bulk velocity U, and Re_τ is decreased in steps of 10. As in pipe flow, the flow appears homogeneously turbulent for $Re_\tau = 100$ and above. Large streamwise modulations appear around $Re_\tau = 90$. These modulations travel downstream at a velocity slightly slower than the bulk velocity. They grow in amplitude and turn into increasingly disordered laminar-turbulent patterns present from $Re_\tau = 90$ down to approximately 55. Below $Re_\tau = 50$, a radical change appears : the individual structures forming the already irregular pattern accelerate, they dissociate, and the resulting dynamics resembles ballistic trajectories of uncorrelated localised structures. Lowering further down Re_τ below 40 leads to the individual extinction of each of these structures, eventually leading to a perfectly laminar flow.

The transitional range associated with pressure-driven plane Poiseuille flow occurs grossly, according to the above visualisation, between $Re_\tau = 40$ and 100. This is highly consistent quantitatively with the $100\delta_\nu = 2h$ that suggests a critical value of 50. It remains to understand why there is an extended transitional *range*, rather than a simple critical point with laminar flow below and turbulent flow above.

1.4.3 Relevant interrogations regarding transition to turbulence in shear flows

The Moody diagram illustrates how the friction factor C_f of a given flow evolves as a function of the Reynolds number Re (traditionally understood as the bulk-based Reynolds number Re_b). C_f is often

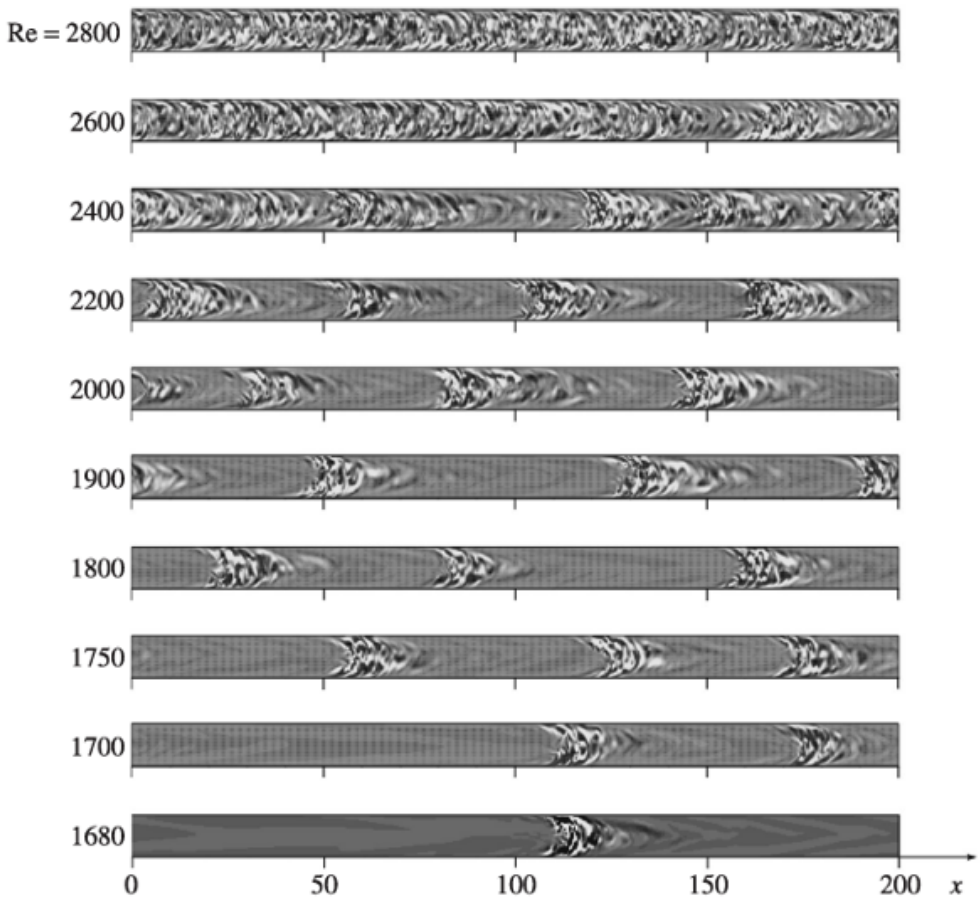

FIGURE 1.4 – Simulations of circular pipe flow for decreasing Re from [11].

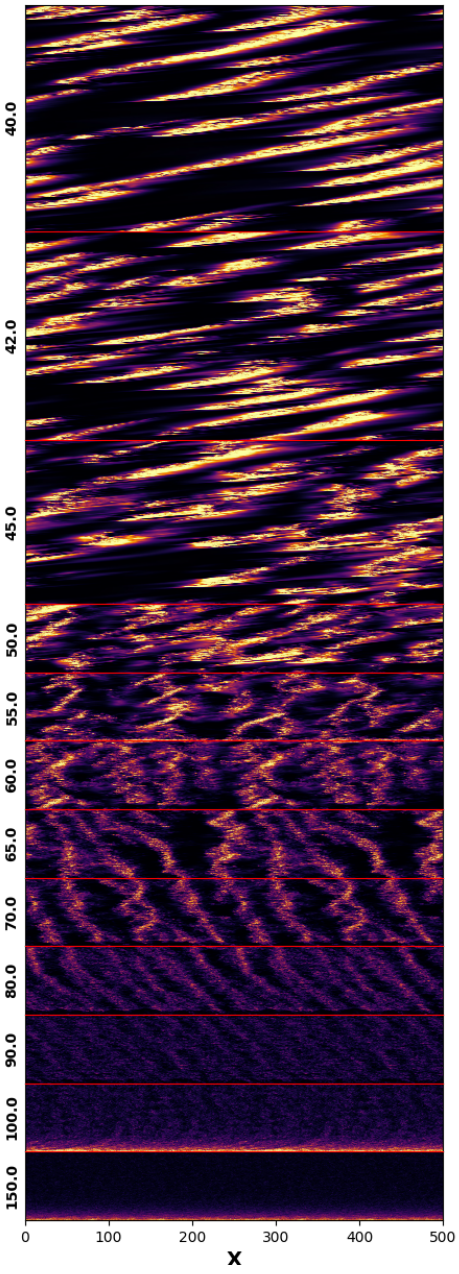

FIGURE 1.5 – Simulations of plane Poiseuille flow for decreasing Re_τ from [14].

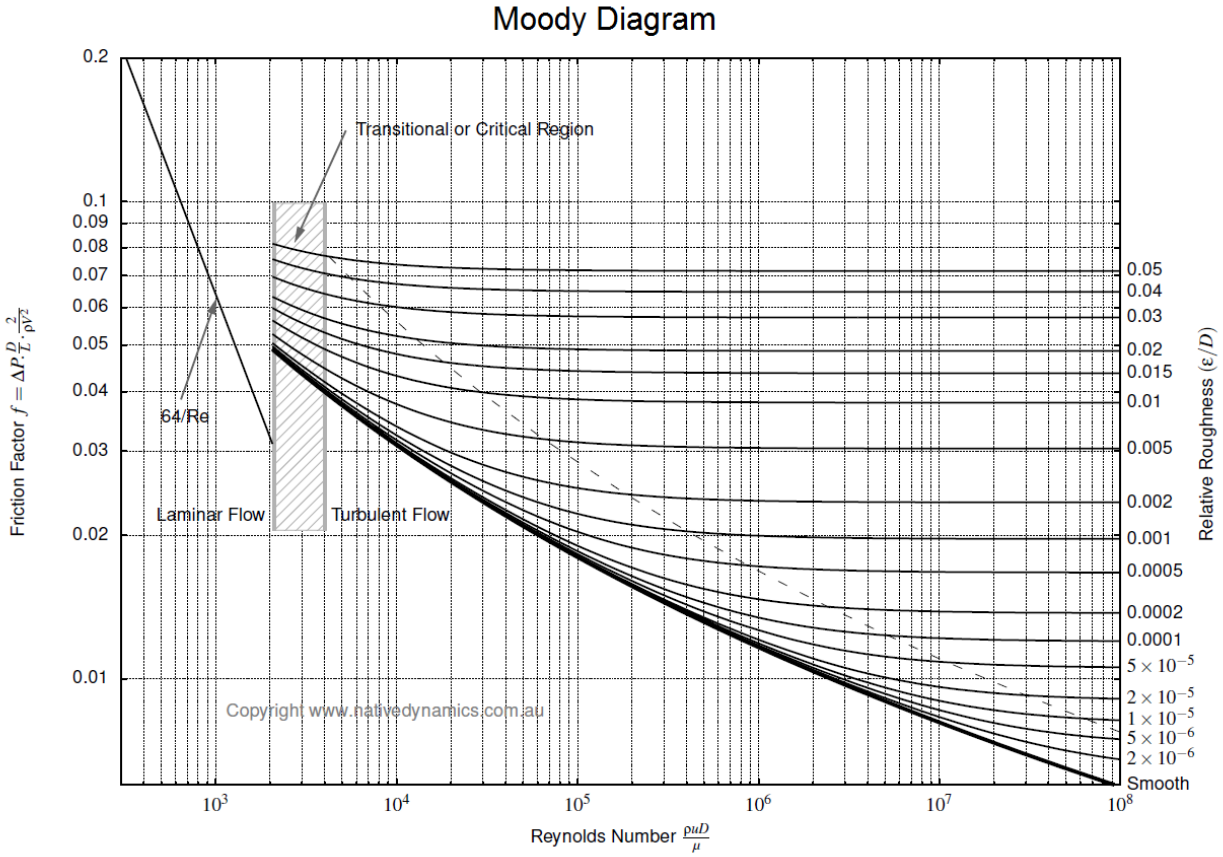

FIGURE 1.6 – Moody diagram for pipe flow (source : *www.nativdynamics.com.au*)

introduced in textbooks either as an efficiency term as compared to the inviscid equivalent, or preferably as the head loss along the considered portion of the flow, normalised by a kinetic energy term based on the bulk velocity. Although convenient for experimentalists, this last definition should still be considered when care when dealing with numerics, because it requires proper averaging (see Ref. [14] for a discussion). We prefer here the definition

$$C_f = 2\left(Re_\tau/Re_b\right)^2, \tag{1.11}$$

which has to be understood differently according to the chosen protocol. For presure-driven flow Re_τ is imposed, but Re_b is not and is understood as a time average of the unsteady Re_b. Conversely for mass-driven flows, Re_b is constant but Re_τ should be defined based on the time-and-space averaged wall-shear stress. For laminar flow, both protocols are equivalent and C_f can be computed analytically. For all laminar shear flows we find that $C_f \sim 1/Re$ with a coefficient specific to the flow geometry and the non-dimensionalisation only. The Moody diagram for pipe flow is depicted in figure 1.6. For high Reynolds numbers in industrial settings, C_f is a constant dependent only on the type of roughness present at the walls. It is this property that justifies the constant coefficients found in all aerodynamics textbook, e.g. the C_x of a car reported in car catalogues. When walls are not rough (which implies either laboratory experiments or low Reynolds number), C_f depends on Re. Again three regimes emerge. The two limiting regimes are the laminar regime, clearly distinct at low Re with the expected $O(1/Re)$ scaling, and a turbulent regime characterised by fits $O(Re^{-\frac{1}{4}})$. The hacked area is traditionally left with a question mark in textbooks and labelled either 'complicated', 'critical', 'uncertain' or an expression hardly clearer : 'transitional'. In the transitional range (according to visualisations) turbulence is spatially and

temporally intermittent. It is the region where mean values do not suffice to shed light on the dynamics of the flow and where the study of fluctuations becomes paramount.

Two *complementary* approaches will be used in this work depending on whether the focus is on the "transitional" regimes themselves, which exist in a limited range of Reynolds numbers, *or* on the transition towards the turbulent state, which is possible as soon as a turbulent state can be defined.

Starting from the turbulent state, we can define the "adiabatic descent procedure", inspired by the experimental methodology used e.g. by Prigent for plane Couette flow, as in figures 1.4 and 1.5. A turbulent state is achieved at a sufficient high value of Re, then Re is decreased in very small steps (or equivalently as a ramp with $dRe/dt < 0$). By analogy with thermodynamic processes this is called an adiabatic decrease (in Re). It allows one to track a given turbulent state in parameter space. It is very robust when the turbulent state is unique, which is the usual case here. This process delivers the full zoology of states present in the transitional range, as well as above it if the initial value of Re is high, and works well in unbounded geometries. It also yields in principle the true critical Reynolds numbers below which no turbulence is found, or at least the critical Reynolds number associated with the finite observation time chosen. Figures 1.4 and 1.5 also highlight the huge lengthscales involved in the collapse process. Such simulations are very CPU-demanding and one can be tempted (or forced) to shorten the domain at equivalent local resolution. Simulations in numerical domains smaller than such lengthscales risk either deforming the associated phenomena or simply missing them.

We can adopt a point of view starting from the well-defined laminar state instead, the "path to turbulence" procedure. There is ample mathematical, experimental and numerical evidence that, for the flows of interest here, the laminar state is always stable with respect to infinitesimal disturbances, no matter what the shape of such disturbance is. However as soon as a turbulent state is realisable for a given Reynolds number, this suggests that certain disturbances of finite amplitude are able to provoke a change of regime. Certain *preferred* paths towards the turbulent state exist in a reproducible way. Out of mathematical convenience, stability theory is often formulated as an initial value problem, consistently with the evolution form ($\frac{\partial}{\partial t} = ...$) of the governing equations. Other approaches can be envisioned, such as the receptivity to noise [15], or to sinusoidal excitations (e.g. resolvent analysis [16]), depending mainly on their potential to match a given experimental (or numerical) protocol. They are not treated here. A large part of the work reported here deals instead with *transition to turbulence as an initial value problem*, based either on the full set of nonlinear equations, on their finite-dimensional truncation in numerical studies, or sometimes on a low-dimensional system of model equations when pedagogically useful. The emphasis is on the determination of physically meaningful initial conditions and the associated trajectories in a suitable *state space*. For such a task the theory of dynamical systems, an intrinsically nonlinear approach well adapted to complex dynamics, is of direct relevance. We will explore the current state of the art in the quest for a description of the transition process in terms of its state space description. Its limitations will also be pointed out with possible self-criticism.

1.5 Linear stability of canonical base flows

Symbolically the nonlinear equation system 1.1-1.2 can be rewritten in the general form :

$$\frac{d\boldsymbol{\mathcal{U}}}{dt} = \boldsymbol{\mathcal{L}}\boldsymbol{\mathcal{U}} + \boldsymbol{\mathcal{N}}(\boldsymbol{\mathcal{U}}) \tag{1.12}$$

where $\boldsymbol{\mathcal{L}}$ is a linear operator and $\boldsymbol{\mathcal{N}}$ contains all nonlinear terms. The meaning of $\boldsymbol{\mathcal{U}}$ does not really need to be made explicit at this stage. It is enough to know that it contains all the independent degrees of freedom of the velocity field. The pressure field p can be determined uniquely (modulo an additive constant) by considering the divergence of Eq. (1.1) and does not need to be considered as an additional field.

We label here "base flow" the steady solution $\boldsymbol{\mathcal{U}_0}$ of Eq. 1.1 consistent with the boundary conditions. As far as trivial solutions with a high degree of symmetry are concerned, they are usually unique. As a steady solution it must verify $\frac{d\boldsymbol{\mathcal{U}_0}}{dt} = \mathbf{0}$. The equation for the perturbation $\boldsymbol{X} = \boldsymbol{\mathcal{U}} - \boldsymbol{\mathcal{U}_0}$ is

$$\frac{d\boldsymbol{X}}{dt} = \boldsymbol{L}\boldsymbol{X} + \boldsymbol{\mathcal{N}}(\boldsymbol{\mathcal{U}}) - \boldsymbol{\mathcal{N}}(\boldsymbol{\mathcal{U}_0}). \tag{1.13}$$

By asssuming that the perturbation $\boldsymbol{X}$ is small enough in a given norm, the above system can be linearised in the neighbourhood of $\boldsymbol{\mathcal{U}_0}$. The linearised system reads in symbolic form

$$\frac{d\boldsymbol{X}}{dt} = \boldsymbol{L}\boldsymbol{X}. \tag{1.14}$$

The issue of the stability of the base flow $\boldsymbol{\mathcal{U}_0}$ with respect to infinitesimal flow disturbances is dictated by a few key properties of the linear operator $\boldsymbol{L}$. Writing down $\boldsymbol{L}$ explicitly is a tedious task. In practice, the use of a numerical discretization often leads to a large square matrix (also referred to as $\boldsymbol{L}$ for simplicity) whose properties can be determined computationally.

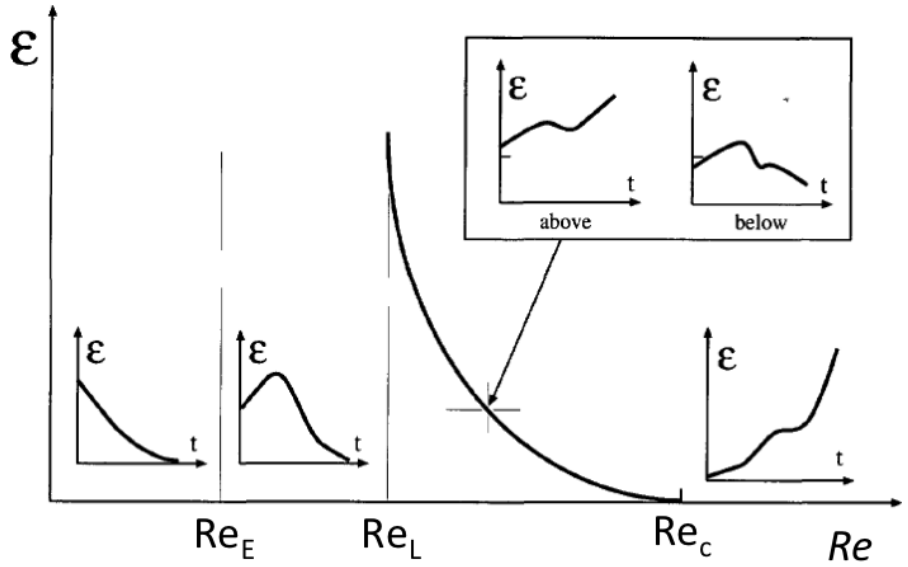

FIGURE 1.7 – Definition of different critical values of the Reynolds number Re_E, Re_L and Re_c. Sketch of typical time series of the kinetic energy ε for several Reynolds numbers, after Ref. [17].

A set of three critical values of the Reynolds number must be considered, depending on the exact notion of stability considered [17]. They are defined graphically in figure 1.7.

The simplest critical value, which also corresponds to the lowest one in the hierarchy, is the *energy Reynolds number* Re_E. It is defined as the highest value of Re below which *all* perturbations to the base flow decay monotonically to zero. By *all* perturbations we mean all shapes as well as all amplitudes. This is hence a nonlinear concept. The Reynolds-Orr theorem leads however to a simplified defining criterion for Re_E invoking only the linear operator $\boldsymbol{L}$.

The usual critical value considered in linear stability theory is the critical Reynolds number Re_L, defined as the smallest value of Re below which at least one class of perturbations grows indefinitely under the action of the linear operator. This is a linear concept only. It corresponds to the smallest value of Re for which the spectrum of $\boldsymbol{L}$ contains at least one eigenvalue with positive real part. In shear flows, unlike e.g. Rayleigh-Bénard convection or classical Taylor-Couette flow, Re_E never coincides with Re_L. Re_L does

not necessarily match the value at which transition to turbulence is observed in experiments and numerics.

The *global* critical Reynolds Re_c, corresponds to the largest value of Re below which *all* perturbations to the base flow eventually return to it. It is a fully nonlinear concept unlike Re_L and Re_E. In other words it is the critical value above which nonlinearity can maintain turbulence provided the right initial condition(s) are supplied. Even if a given perturbation induces turbulence, if the turbulent state relaminarises in finite time with probability 1, there is no guarantee that Re_c has been reached. Re_c is, in the adiabatic limit, the value yielded by the adiabatic descent procedure.

1.5.1 Transient growth

It is crucial to distinguish between finite-time stability and infinite-time stability [18]. The long-time stability is fully determined by the spectrum of $\boldsymbol{L}$, denoted as $Sp(\boldsymbol{L}) = \{\lambda \in \mathcal{C}, \exists \boldsymbol{X} \neq \boldsymbol{0}, \boldsymbol{L}\boldsymbol{X} = \lambda \boldsymbol{X}\}$. In finite dimensions the spectrum of $\boldsymbol{L}$ is discrete and corresponds to the eigenvalues of the associated matrix. It is a classical result that if *all* eigenvalues in the spectrum have strictly negative real parts, then the system is asymptotically stable for long times. The decay of perturbations is also dominated on long times by the least stable eigenvalue (the one with the largest real part). However, transient growth of $||\boldsymbol{X}|| = \sqrt{\boldsymbol{X} \cdot \boldsymbol{X}}$ is also possible even if all eigenvalues of $\boldsymbol{L}$ indicate long-time stability. This arises provided $\boldsymbol{L}$ and its adjoint (defined using the same scalar product as for the 2-norm) do not commute, i.e. $\boldsymbol{L}\boldsymbol{L}^* \neq \boldsymbol{L}^*\boldsymbol{L}$, in which case $\boldsymbol{L}$ is called *non-normal*. Another equivalent measure of non-normality, for invertible operators, is the condition number of the eigenbasis, defined as $\kappa = ||\boldsymbol{L}|| \cdot ||\boldsymbol{L}^{-1}||$, where the matrix norm used here is the usual Frobenius norm. $\kappa = 1$ for normal operators while $\kappa > 1$ for non-normal operators [19]. A symmetric or anti-symmetric operator is for instance normal. A non-normal operator can be diagonalisable but this is not a necessary condition. If it is diagonalisable, then the eigenvectors do not form an orthogonal basis.

A numerically determined point spectrum typical of shear flows, belonging to plane Poiseuille flow at $Re = 10^4$, is displayed in figure 1.8 using dots. Any dot lying above the real axis represents an unstable mode. In the figure almost all dots lie below that line, indicating that damped modes dominate. Only one dot lies above it, and it can be established that no such unstable mode is found when $Re < 5772$ [20]. The pseudo-spectrum $\Lambda_\varepsilon = z \in \mathcal{C}, ||(z\boldsymbol{I} - \boldsymbol{L})^{-1}|| \geq \varepsilon^{-1}$ is a useful generalisation of the spectrum [21].

A popular interrogation emerging from the non-normality property is the following : given the linearised context, what is the initial condition producing the largest transient growth of perturbation kinetic energy ? Let us suppose that the perturbation kinetic energy $E(t)$ is given by $\frac{1}{2}||\boldsymbol{X}(t)||^2$, that the related energy gain at time t is defined as $G(t) = E(t)/E(0)$, and that the optimal gain is given by

$$G_{max} = \max_{\boldsymbol{X},t} G(t). \tag{1.15}$$

For operators that are not asymptotically stable, there is at least one eigenvalue with positive real part : if a given initial perturbation has a non-zero projection in the related eigenspace, then this perturbation will grow indefinitely with time in that direction ; in that case the optimal gain is $G_{max} = \infty$. For stable normal operators, $G_{max} = 1$ since the decay of the perturbation kinetic energy is monotonic. A non-trivial situation occurs when $\boldsymbol{L}$ is stable but non-normal. In such a situation there is potential for energy growth over finite times.

It was determined numerically that G_{max} rises rapidly with the Reynolds number, in fact as $O(Re^2)$ [18]. This result holds apparently regardless of the flow case. It is this result, rather than the non-normal property itself, that justifies why laminar shear flows are so sensitive in practice to arbitrary perturbations such as incoming noise or small geometrical imperfections.

The so-called *optimal modes* are the flow structures achieving maximum growth in finite time. When considered in three dimensions, they correspond invariably to structured arrays of streamwise vortices. If

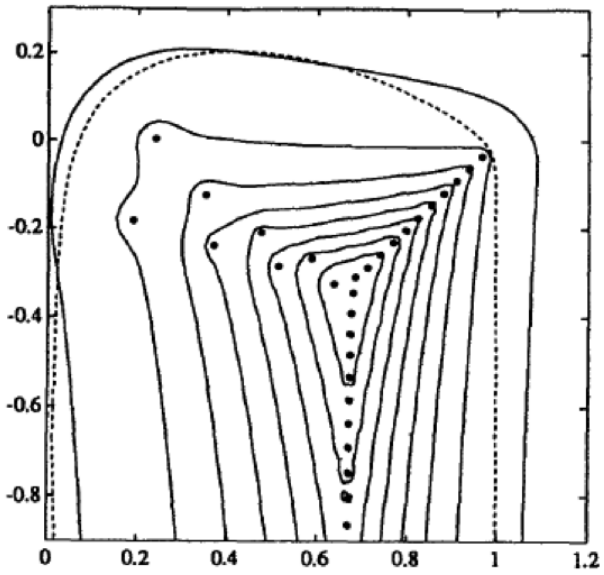

FIGURE 1.8 – Spectrum (dots), pseudo-spectrum for $\varepsilon = 10^{-n}$, n =1 to 8 (solid lines) and numerical range (dashed line) for plane Poiseuille flow at $Re = 10^4$, from Reddy *et al.* (1993) [19].

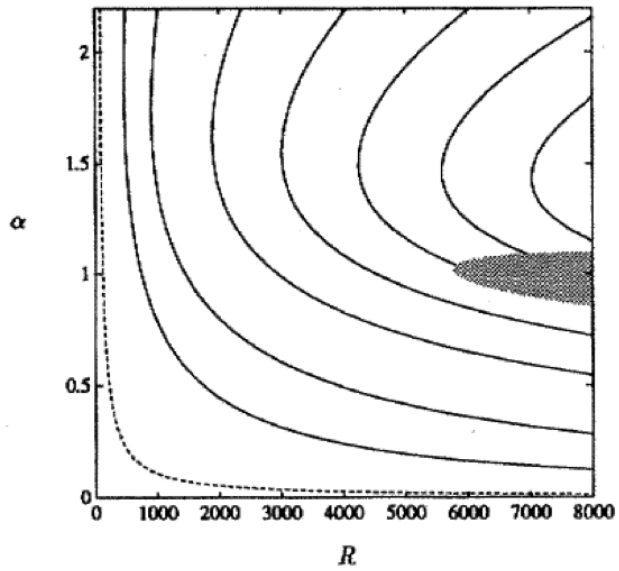

FIGURE 1.9 – Levels of G_{max} in plane Poiseuille flow depending on the axial wavenumber α, and on the Reynolds number R based on laminar the centerline velocity, from Reddy *et al.* (1993) [19]. Dashed line : $G = 1$, dark area : $G = +\infty$, other lines correspond to $G = 5, 10, 20, 30, 40, 50, 60$.

such a flow field is considered as an initial condition in the framework of an initial-value problem, then the output at the optimal time t_{max} is also a structured array of streamwise streaks superimposed on the original array of streamwise vortices. The streaks are defined as spanwise variations of the streamwise velocity field, i.e. an alternation of slow and fast lanes forming a given spanwise wavelength. These opti-

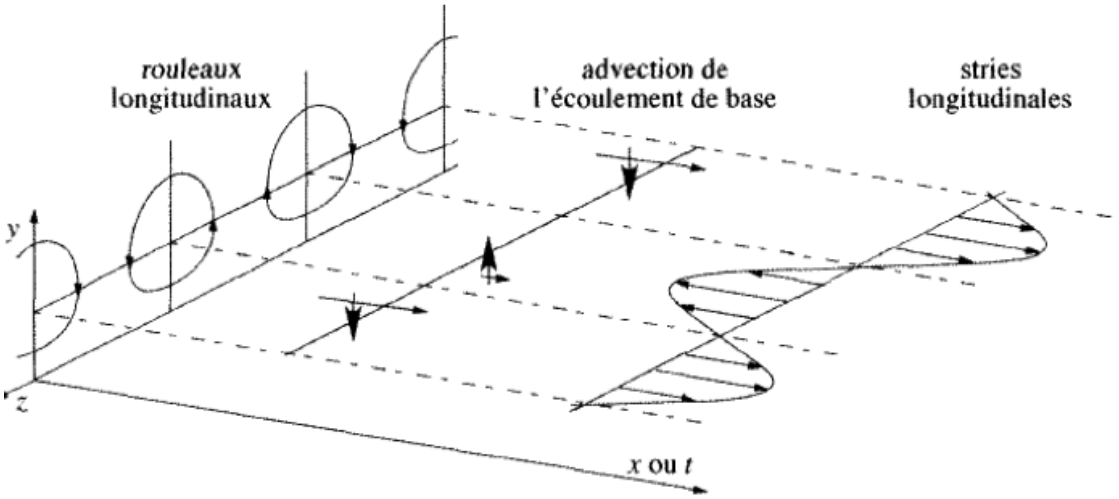

FIGURE 1.10 – Sketch of the lift-up effect from F. Charru's textbook [22] showing the development in time or space of streamwise streaks from streamwise vortices.

mal streaks, as well as the associated vortices are independent of the streamwise variable. The amplitude of the vortices themselves decreases steadily with time whereas the amplitude of the streaks reaches its maximum at $t = t_{max}$. The development of streaks from an initial distribution of streamwise vorticity is labelled *lift-up* to celebrate the fact that streamwise vorticity is able to *lift up* the streamwise velocity isocontours, although by continuity they are associated with *push-down* regions where the fluid is brought down closer to the wall by the neighbouring vortices. If the wall is at rest, upwards motion inside the vortices generates a low-speed streak, whose instability will be emphasized later. This lift-up effect, in the streamwise-independent case, is formally and mathematically similar to the rise of plumes by vortices in the advection of a passive scalar. The difference of the shear flow case with the two-dimensional convection picture is that a third velocity component arises. This allows one to generate a three-dimensional vorticity field out of an initial condition that features only streamwise vorticity. Another way to interpret the lift-up mechanism is that it demonstrates the advection of the base flow by the flow perturbation [23].

The importance of streamwise streaks in transitional as well as turbulent shear flows should not be minimised : they represent the main coherent structures found near the wall in all flows featuring boundary layers. This includes *all* the flow cases investigated here. A velocity field of plane Couette flow is computed using a visualisation routine developed by J. F. Gibson [24] in figure 1.11. The red/yellow lanes correspond to the highspeed streaks whereas the blue lanes, which appear slightly more sinuous, are the low-speed streaks. Streaks can also be found in free jets or wakes. One of the rare "formulas" of the shear flow literature is the mean spanwise wavelength of the streaks, found almost universally to be $\lambda_z^+ \approx 100$. This formula alone justifies the introduction of inner units (the non-dimensionalisation by $\delta_\nu = \sqrt{\frac{\tau_w}{\rho}}$ instead of h). This simple scaling relation can be extracted directly, in a statistical sense, from the small-scale peak present in figure 1.2. The linear framework, more elegantly reformulated as an input-ouput formalism [25], is convenient to explain why streaks emerge, not only when initialised by the optimal mode, but also from a disordered vorticity field and in finite time.

The linear point of view on subcritical transition has certainly put an end to a mathematical mystery. Beyond explaining the universal emergence of streaks in high Reynolds numbers shear flows, it has also

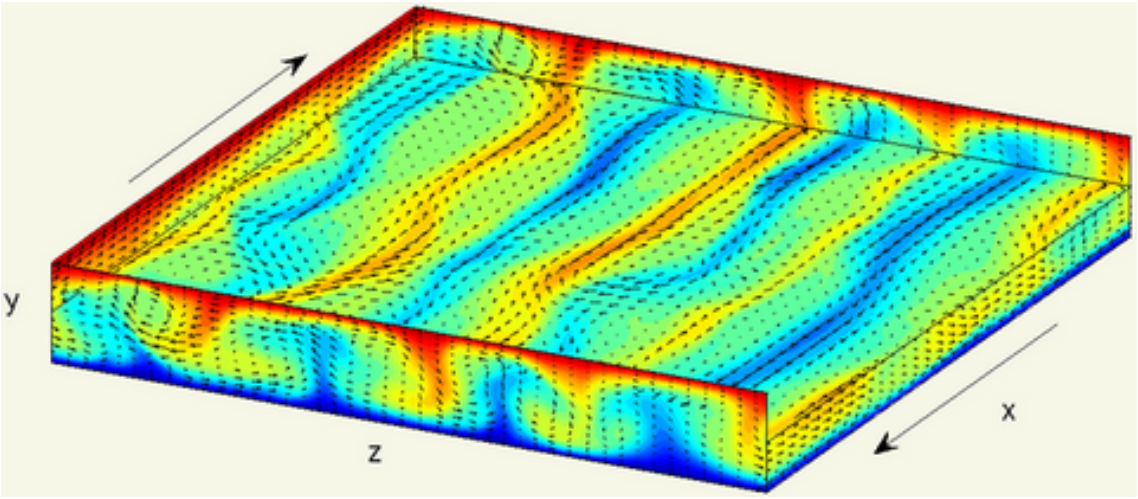

FIGURE 1.11 – Velocity field of plane Couette flow from a computation in Ref. [24]. The red/yellow lanes correspond to the highspeed streaks whereas the blue lanes, which appear slightly more sinuous, are the low-speed streaks.

emphasized the importance of non-normality in generic linear dynamics. This is perhaps welcome after decades of influence from quantum physics, where the emphasis is on symmetric, hence normal operators. However turbulence is a nonlinear phenomenon. A linear theory alone, although it can yield a path towards a turbulent flow, cannot explain the emergence and, more importantly, the ability of a turbulent flow state to sustain itself.

1.5.2 Nonlinear extension

For a linear system of equations, all solutions found independently can be combined linearly to form new solutions. In planar flows, the equivariance of the equations with respect to the two planar directions justifies ansätze of the form $e^{ik_x x+ik_z z}$ when solving the linearised equations. Although general solutions contain a summation of these exponential solutions, linearity allows to focus on each wavenumber separately. Such an assumption leads to the boundary conditions $\boldsymbol{u'}(x+2\pi/k_x, z+2\pi/k_z) = \boldsymbol{u'}(x,z)$ being automatically satisfied, by construction. Historically, after linear concepts have been applied to the study of the stability of fluid flows, it has become very tempting to generalise the system by restoring the neglected nonlinear terms... even if in the nonlinear context, the study of individual exponential ansätze is no longer justified ! Although it is obvious that no nonlinear open flow obeys a strict spatial periodicity condition, there are some cases for which this hypothesis can be justified. On one hand, if the wavelength is sufficiently large, for instance much larger than the correlation length of the system, the natural outflow and inflows are in practice uncorrelated : in such a situation the error committed by recycling outputs into inputs is less problematic. On the other hand, if that imposed wavelength is too short, additional unphysical correlation is added into the system of equations, and we deal with a flow case that cannot be reproduced experimentally. Another case in which spatial periodicity is relevant is the numerical simulation/analysis of localised velocity fields, at least when the spatial decay is sufficiently rapid.

Not only do periodic boundary conditions make the mathematical analysis of open flows mathematically better-posed, they also imply simpler theorems. For instance, the Reynolds-Orr equation governs the time evolution of the energy $e = \frac{1}{2} < \boldsymbol{u'}, \boldsymbol{u'} >$ of the fluctuations. It is obtained by multipying scalarly the equation for $\frac{d\boldsymbol{X}}{dt}$ by $\boldsymbol{X}$ and making ample use of integration-by-parts theorems. In the presence of periodic boundary conditions in the planar variables, it can be verified that $< \boldsymbol{\mathcal{N}}(\boldsymbol{X}), \boldsymbol{X} >= 0$. The

Reynolds-Orr then reads in compact form :

$$\frac{de}{dt} =< \boldsymbol{LX}, \boldsymbol{X} > . \tag{1.16}$$

This equation, also valid in the nonlinear regime, states that the energy amplification is independent of the exact nonlinear terms, provided the energy-conserving property $< \boldsymbol{N}(\boldsymbol{X}), \boldsymbol{X} >= 0$ is verified. By dividing Eq. 1.16 by $|\boldsymbol{u'}|^2 = |\boldsymbol{X}|^2$, this conclusion can be pushed even further : the instantaneous rate of change of the perturbation kinetic energy does not depend on the instantaneous perturbation energy given by $|\boldsymbol{u'}|^2$. Although this has generated controversy [26], it is now clear that this does not make the nonlinear terms less important. The norm of $\boldsymbol{X}$ might not depend on $\boldsymbol{\mathcal{N}}$, but its orientation definitely does, and the term involved in the momentum equations is $\boldsymbol{X}$, not $||\boldsymbol{X}||$.

1.6 Nonlinear concepts

1.6.1 Self-sustaining process

Within the previous linearised framework, the main and perhaps only question addressed deals with the ability of a perturbation to escape, or not, the neighbourhood of the base flow solution. If restoring nonlinearity into the original equations is a welcome departure from linear stability theory, it does not indicate how to deal mathematically with the new nonlinear system. The true change of paradigm occurs when, instead of assessing *how far from the laminar state* the system temporarily lies, one gets interested in *how close to new alternative flow states* the system can get. This new type of interrogation brings back the question of *turbulent state* into the picture. It is mathematically consistent with the possibility that the laminar base flow, when described as a fixed point in state space, has a basin of attraction that does *not* necessarily coincide with the full state space. Now provided other dynamical regimes are possible, there must be a mechanism that maintains their dynamics *away* from the laminar regime *for all times*. Such a mechanism, called simply *self-sustaining process* [27], is necessarily nonlinear. Its identification and validation are not trivial and constitute a mechanistic way of understanding the existence of a turbulent state.

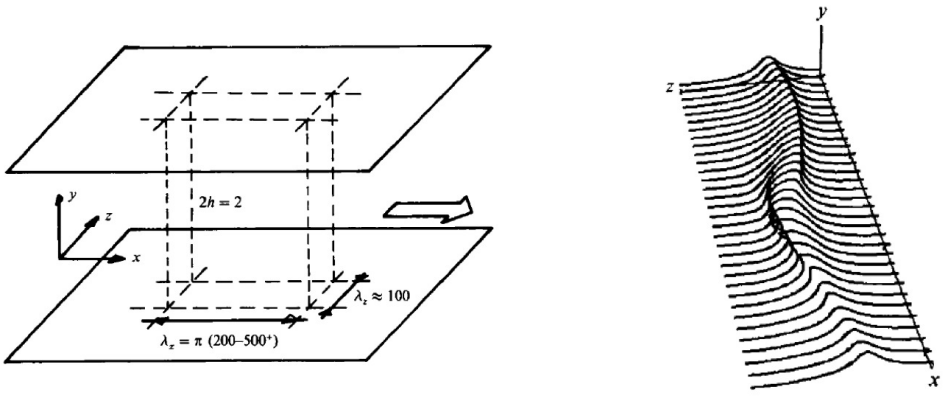

FIGURE 1.12 – Left : Reduction in domain size, taken from Jiménez & Moin [28]. Right : instantaneous wall vorticity highlighting the wavy streak.

Crucial progress in this direction has been made by Fabian Waleffe and co-authors in a series of papers in the second half of the 1990s [9]. Its strategy can be summarised by following their 1995 paper :

— consider a flow case (they chose plane Couette flow) with a linearly stable base flow
— use direct numerical solution to simulate the turbulent regime inside a spatially periodic box,
— decrease carefully both the Reynolds number *and* the box size while keeping the dynamics non-relaminarising as in Figure 1.12,

— when the system seems on the verge of relaminarising, analyse the dynamics over a finite-time segment

The success of this strategy is to yield a new type of flow with its own dynamics, that appears at the same time prone to analysis while being strongly reminiscent of the dynamics observed in wall turbulence simulations. In particular, the velocity field found in plane Couette flow after such a reduction, shown in figure 1.13, possesses long wavy streaks flanked by shorter streamwise vortices, as found in many turbulence simulations at moderate Reynolds numbers.

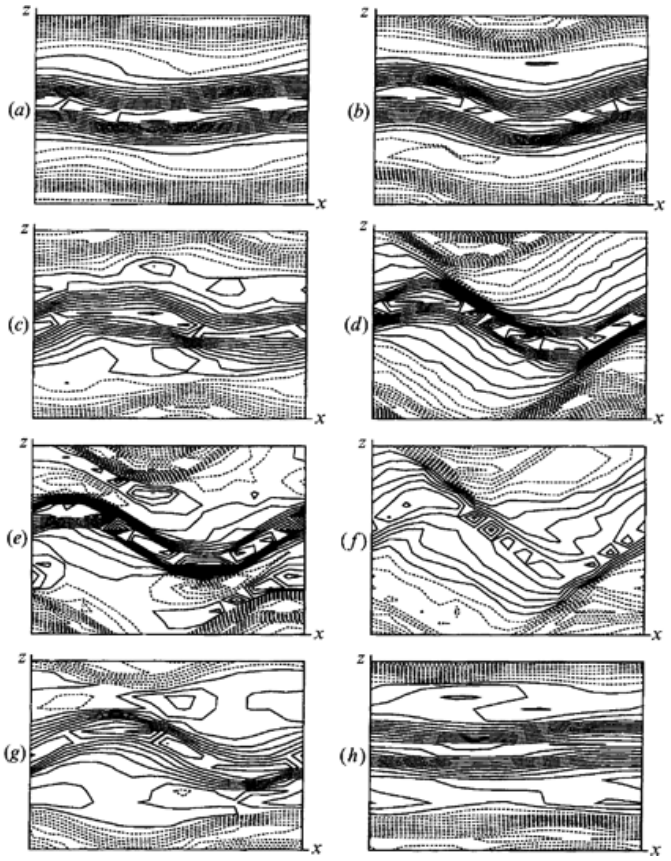

FIGURE 1.13 – From a) to h) : ordered snapshots of streamwise velocity field at mid-gap in pCf, investigated by [9], illustration of one turbulent cycle consistently with the proposed self-sustaining process.

The streamwise streaks are not steady and they are known to undergo so-called bursting events also described as "streak breakdown". It is indeed evident in figure 1.13, where the long sinuous coherent structure in figure 1.13a gets increasingly distorted with time until it almost disappears in figure 1.13f. It then gets regenerated back to the same amplitude as in a), which closes the loop. It is perhaps best understood in terms of vorticity components : a streak is characterised in the xz plane of figure 1.13a as a wave of wall-normal vorticity ω_y. The streak instability starting from figure 1.13b amplifies ω_y [29], up to levels where the nonlinear behaviour of the instability starts to manifest itself : the streak breaks down. Through the advection by the mean shear, ω_y gets tilted in the streamwise direction and its streamwise component ω_x increases in amplitude. Eventually, the lift-up mechanism [18], essentially the advection of the base flow by streamwise vortices, regenerates streaks and restores the original level of ω_y. For the case of a spatially correlated minimal box, this sequence of events illustrates the self-sustaining process of Waleffe as sketched in figure 1.14. Variations on this mechanism can be found in the literature provided a slightly different computational domain is used, however they mainly impact the symmetries of the streak instability without modifying the sequence of events and the approximate period of the process.

As will be see in future chapters, slightly different three-dimensional SSPs can be identified in shear flows yet only in the presence of spatial localisation.

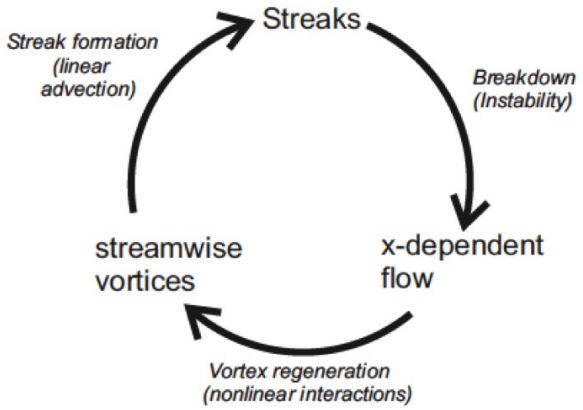

FIGURE 1.14 – Sketch of the self-sustaining process from F. Waleffe [30].

Dynamically speaking, the self-sustaining process is found to be weakly chaotic although the authors once hoped they would reduce to a perfectly cyclic dynamics [31]. This intuitively suggests, by analogy with simple low-dimensional chaotic attractors such as the Lorenz or the Rössler attractor -where the attractor can be covered by unstable periodic solutions-, that an ordered cyclic process is embedded in this chaotic dynamics. It should feature exactly the same ingredients as the wilder self-sustaining process (wavy streaks and rolls). This was confirmed a few years later by G. Kawahara & S. Kida who identified numerically an unstable periodic orbit (UPO) apparently embedded in the turbulent dynamics [32]. This apparent embedding was suggested by both the sequence of events visualised in videos, and by a convincing match between the statistics of the UPO of mean flow, r.m.s velocity fluctuations etc... and those from turbulent simulations. A sequence of events taken along the orbit is displayed in figure 1.15 and favourably compares with the material displayed in figures 1.13 and 1.14 Another convincing feature, although only qualitative, is the fact that the UPO seems intricately linked with the state portraits displayed in Figure 1.17.

The hunting season for other invariant solutions mimicking the turbulent dynamics was then declared open. Waleffe himself completed his description of the state space of plane shear flows by identifying solutions simpler than the UPO of Kawahara and Kida [33]. The associated numerical strategy, not so easily generalisable, assumes a forcing term able to generate wavy streaks via the subcritical instability of straight streamwise streaks. It then makes use of a numerical continuation technique to identifiy a solution that sustains itself without forcing. This method was then used by several groups to yield brand new solutions [34, 35]. It was at the same time understood that formerly found finite-amplitude solutions, notably the so-called Nagata solutions of plane Couette flow [36] originally identified via numerical homotopy, were from the same large family and could be found using similar techniques.

The periodic cell considered first by Hamilton *et al.* [9] was re-considered by P. Cvitanović and coworkers (a by-product of this investigation is the now freely available DNS code $channelflow$ developed by J.F. Gibson). Their investigations shed a clearer light on the complexity of the state space of even that simple flow. Multiple steady states [37], heteroclinic connections [38] as well as periodic orbits [39] were identified and plotted using savant projection systems. These authors pointed out the need for symmetry reduction in order to take into acount systems with advection [40]. That led ultimately to representations of the state space of pipe flow [41, 42], as visualised in an arbitrary Poincaré section in Fig. 1.19.

Although experimental verification of such concepts might seem one step more arduous (but decisive

FIGURE 1.15 – Three-dimensional visualisations of the velocity field along the turbulent-like periodic orbit found by Kawahara & Kida [32].

for the credibility of the theory), careful work worth mentioning has been achieved by a few teams. The original theoretical idea of Waleffe to identify self-sustaining solutions by introducing a forcing term, waiting for the flow to bifurcate and then bringing back the forcing to zero was tried successfully by S. Bottin and co-workers at CEA Saclay. By using wires and beads of increasingly small size, they could confirm that streamwise vortices are indeed crucial elements of possible finite-amplitude solutions of the Navier–Stokes equations [43]. Later, excited by the recent numerical discovery [34, 35] of unstable travelling wave solutions in cylindrical pipe flow, Hof *et al.* [44] used cutting edge time-resolved Particle Image Velocimetry to report on furtive observations of similar travelling wave solutions from at a bulk Reynolds number of Re=2400. Another such travelling wave, analogous to one identified numerically by Pringle & Kerswell [45] was identified in the wake of a decaying turbulent zone by the same experimental group [46] in pipe flow. The concept of self-sustaining process itself was claimed to be observed in the wake of vortex generators in a boundary layer set-up [47]. More recently, focusing on the so-called Kolmogorov-flow driven by a sinusoidal shear profile, a detailed comparison between exact solutions computed from DNS versus those computed from experiments was made possible [48, 49].

It is important to highlight some implications of the strategy used by F. Waleffe, notably the use of smaller and smaller numerical domains in order to "confine" the dynamics. It is not strictly true that such an operation is equivalent to confinement, since the physical domain is still formally infinite. Instead it amounts to strengthening correlations. In this study, the whole flow was interpreted as a *crystalline* structure. Jimenez & Moin used a similar strategy in order to prevent the existence of velocity eddies of size larger than a specified cut-off size [28], i.e. to make turbulence less multi-scale, whereas Waleffe and subsequent authors would focus on lower Re and on making turbulence less "spatiotemporal". Choosing

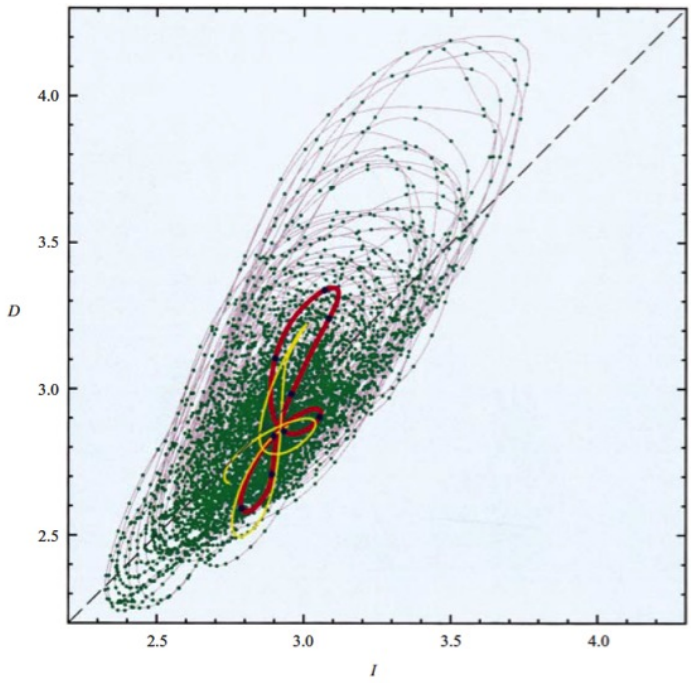

FIGURE 1.16 – State portrait energy input vs dissipation for plane Couette flow, taken from Ref. [32].

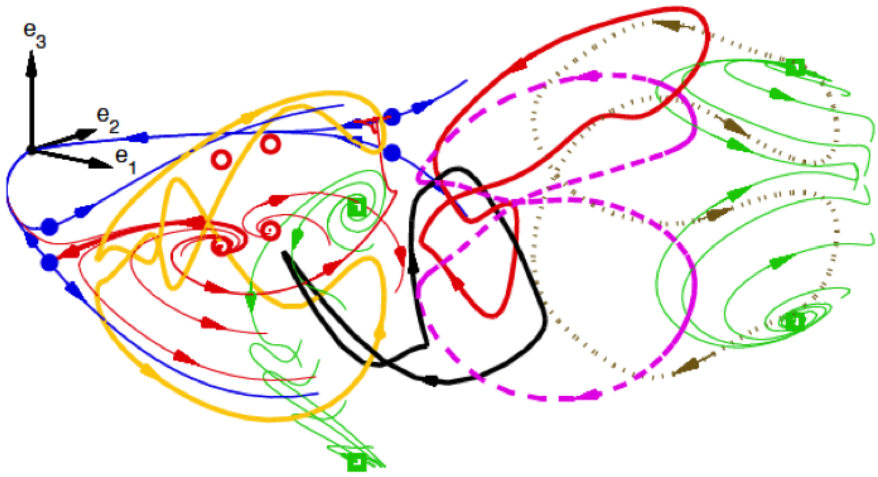

FIGURE 1.17 – Three-dimensional projection of the state space of plane Couette flow, including several fixed points, their unstable manifolds as well as 5 periodic orbits, from Ref. [39].

this cut-off in inner units (the natural unit for streak width in turbulent flows) rather than in outer units allowed them to bypass the reduction in Reynolds number and focus only on the reduction in domain size. This lead to the famous concept of "Minimal Flow Unit" [28], understood as the smallest domain

size able to sustain turbulent motion, or equivalently non-laminar flow (despite the absence of any strict minimisation in the optimal sense).

1.6.2 Finite-amplitude solutions

Let us first define what is meant by "finite-amplitude solution" here in order to remove any ambiguity. The historical perspective is perhaps useful : it starts with the vague turbulent notion of *coherent structure*, a word used from the 1970s to label any shape recognisable in the flow that has some spatial coherence over some time interval, as opposed to the purely statistical investigations of the time [50]. F. Waleffe, aware of the contradictory nature of the concept, introduced the notion of exact coherent structure' (ECS) in order to restore the link with the Navier–Stokes equations. Once that link restored, finding ECS in practice turned into the usual numerical problem of identifying solutions to the discretised Navier–Stokes equations. The adjective "finite-amplitude" is added here in order to emphasize that the solutions are *not* obtained via the other method popular at the time, namely weakly nonlinear analysis, and thus that no assumption is made on the smallness of the amplitude. As soon as the self-sustaining process (SSP) was identified by Waleffe and co-authors, the quest for finite-amplitude solutions in the same flow set-ups became a quest for illustrations of the very same SSP using mathematically well-defined solutions.

There is some ambiguity to the fact that, especially in the numericist's jargon, any unsteady solution $\boldsymbol{X}(t)$ to an initial value problem is precisely also a "solution". Behind the label "finite-amplitude solution", the notion of "simple solution" has been progressively eclipsed. "Simplicity" is not an objective property, however it still makes sense to talk about a hierarchy of solutions starting from the simplest ones.

When focusing on the temporal dynamics, the simplest solutions to the Navier–Stokes equations (or more generally any PDE system) are steady states. For all times t, t' they obey the steady property

$$\boldsymbol{u}(x,y,z,t) = \boldsymbol{u}(x,y,z,t'). \tag{1.17}$$

The next level in the hierarchy corresponds to solutions that are steady in a given moving frame of reference : travelling wave solutions (TWs) are defined by

$$\boldsymbol{u}(x,y,z,t+T) = \boldsymbol{u}(x+c_xT, y, z+c_zT, t), \tag{1.18}$$

for all t and T. The c's are interpreted as phase velocities.

Periodic orbits (POs) are defined as

$$\boldsymbol{u}(x,y,z,t+T) = \boldsymbol{u}(x,y,z,t), \tag{1.19}$$

for all t but for given values of T.

Next in the hierarchy, relative periodic orbits (RPOs) are defined as

$$\boldsymbol{u}(x,y,z,t+T) = \boldsymbol{u}(x+\sigma_x, y, z+\sigma_z, t), \tag{1.20}$$

for all t but for given values of T, σ_x and σ_z. Note that travelling waves are degenerate relative periodic orbits as well as degenerate steady states.

It is possible to describe such special solutions independently of the notion of space. If the system is written under the generic form $\dot{\boldsymbol{X}} = \boldsymbol{F}(\boldsymbol{X})$ with a propagator ϕ^t, then steady states are simply zeros of $\boldsymbol{F}$, or equivalently fixed points of ϕ^t. As for travelling waves and relative periodic orbits, the shifts in space form a vector $\sigma = (\sigma_x, \sigma_z)$ of rank two. Spatial shifts can be reinterpreted as simple application of an operator $\mathcal{T}_\sigma$ on velocity fields. That way a TW can be redefined as any solution, for any $T > 0$ to

$$\phi^T \boldsymbol{\mathcal{U}} = \mathcal{T}_\sigma \boldsymbol{\mathcal{U}}, \tag{1.21}$$

whereas an RPO is defined as a solution to the same equation yet for a specific value of $T > 0$.

Many methods have been used in the past to find exact solutions to the Navier–Stokes equations, especially in the context of subcritical shear flows where the laminar solution, the only one known analytically a priori, is evidently no good description of a sustained turbulent flow. Some of these methods will be described in the next chapter. The original hope is that once a finite-amplitude solution is identified, it might serve as a reduced laboratory to investigate a turbulent flow without the difficulties inherent to very unsteady signals, such as arbitrary time-integration, choice of initial condition, need for ensemble averaging, etc... in other words a laboratory where the dynamics is fully reproducible. Since in the context of turbulence most finite-amplitude solutions of interest are expected to be unstable, a pedagogic cartoon has emerged progressively to describe the dynamics of a turbulent flow : as depicted in Fig. 1.21, the dynamics of the flow is encoded in an ergodic state-space trajectory $\boldsymbol{X}(t)$. The state space is populated by pointwise finite-amplitude solutions in the shape of points and cycles, all unstable except the fixed point corresponding to the laminar base flow. A turbulent trajectory, if any, corresponds to a trajectory staying away from the basin of the laminar state forever and visting the neighbourhoods of the individual ECSs one after the other. All other trajectories eventually converge to the laminar state and are labelled *transient*, possibly *transiently turbulent* if its *lifetime* is deemed sufficiently long. The picture of transition associated with it is two-fold. To start with, only initial conditions located in the right dynamical region are likely to appear turbulent, be it only transiently. Moreover, as the Reynolds number decreases the number of unstable solutions reduces and eventually drops to zero. In such a cartoon the complexity of the state space is mainly determined by the number of unstable solutions. It is worth repeating that this view, although faithful to an original view of turbulence by Hopf [51], and no matter how pedagogically helpful, is only a cartoon. In particular it is unable to shed light on such concerns as the fractality/strangeness of the attractor and is unable to yield any information about the invariant measure of the system.

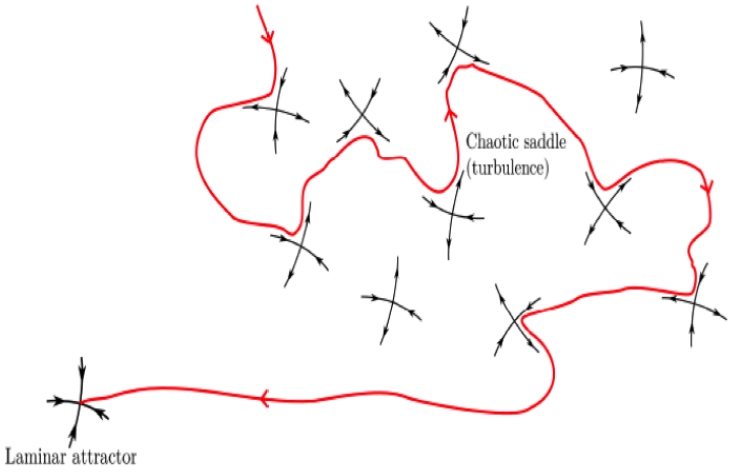

FIGURE 1.18 – Cartoon of the state space in subcritical transition to turbulence. Each cross except the laminar one denotes a locally hyperbolic finite-amplitude solution together with its stable and unstable manifolds. Courtesy of T. K. Kreilos [52].

1.6.3 Cycle Expansions

There is a deeper reason as to why the knowledge of simple exact solutions is important : cycle expansions. The e-book by P. Cvitanović [53] is devoted to a detailed explanation of the mathematics

underlying this very general idea. Suppose an autonomous dynamical system of the form $\dot{\boldsymbol{x}} = \boldsymbol{F}(\boldsymbol{x})$ in arbitrarily high dimension, associated with the flow map ϕ^t. Suppose now also that the system above verifies the *axiom A* property, i.e. that in the neighbourhood of *each* periodic or steady solution, the system can be linearised and decomposed into stable and unstable tangent eigenspaces. This hypothesis rules out central manifolds, non-hyperbolic effects and hence rules out the proximity to a bifurcation point. For a given system, the validity of the axiom A hypothesis is notoriously difficult to predict ; at best it is usually assumed as a hypothesis. Under these assumptions, a formula originally suggested by Gutzwiller [53] expresses the dynamical averages of *any* observable as a weighted average over the *entire* set of periodic orbits of the system. No information other than the location of the periodic orbits, their period and their linear stability is required. [54]. By the dynamical average of an observable $A = A(\boldsymbol{x})$, we mean all the possible moments and cumulants obtained by averaging $A(\boldsymbol{x}(t))$ along an ergodic trajectory $\boldsymbol{x} = \boldsymbol{x}(t)$ from time $t = -\infty$ to $t = +\infty$ [55].

More mathematically, if A^t is an observable evaluated at time t, we can always introduce the transfer operator

$$\mathcal{L}^t(\boldsymbol{x}, \boldsymbol{y}) = \delta(\boldsymbol{y} - \phi^t(\boldsymbol{x}))e^{\beta A^t(\boldsymbol{x})}, \tag{1.22}$$

where $\boldsymbol{x}$ and $\boldsymbol{y}$ are two arbitrary points of state space. β is an auxiliary variable whose main role is to enable one to recover the desired state space average by differentiation. The kernel $\delta(\boldsymbol{y} - \phi^t(\boldsymbol{x}))$ is the Perron–Frobenius operator which transports densities in time (cf Chap. 6 in Ref [53]). Note that taking the trace of a linear operator containing the factor $\delta(\boldsymbol{y} - \phi^t(\boldsymbol{x}))$ is equivalent to considering only the points $\boldsymbol{x}$ where $\delta(\boldsymbol{y} - \phi^t(\boldsymbol{x})) \neq 0$, i.e. periodic orbits whose period is an integer multiple of t. The cycle expansion formula states that

$$tr(\mathcal{L}^t) = \sum_p T_p \sum_{r=1}^{\infty} \frac{\delta(t - rT_p)}{|det(\mathcal{I} - \mathcal{J}_p^r)|}, \tag{1.23}$$

where $\mathcal{I}$ is the identity matrix, $\mathcal{J}_p$ the Jacobian at the system linearised around the periodic orbit of interest, r the multiplicity of the orbit and T_p its prime period.

More intuitively, the above formula is a generalisation of the trace formula $tr(log(\mathcal{L})) = log(det(\mathcal{L}))$ for a matrix $\mathcal{L}$. On the left-hand side of Eq. 1.23 we have the statistical information expressed as function of the right-hand side, i.e. the individual deterministic elements. Indeed the spectral theory applied to the operator $\mathcal{L} = \mathcal{L}^t$ relates its trace to a series of Policott resonances γ_α of multiplicity m_α, i.e.

$$tr(\mathcal{L}^t) = \sum_{\alpha=0}^{\infty} m_\alpha e^{-\gamma_\alpha t}. \tag{1.24}$$

The exponents γ_α are related to the escape rates (for the leading eigenvalue) and correlation functions (for the exponents beyond the leading one), that are all key characteristics about the asymptotics of the system as $t \to +\infty$ [56]. For instance, if averages over the state space Ω are defined by

$$< e^{\beta A} >= \int_\Omega e^{\beta A(\boldsymbol{x})} d\boldsymbol{x}, \tag{1.25}$$

then the average of A is given directly by

$$< A >= \frac{\partial}{\partial \beta} < e^{\beta A} > |_{\beta=0}, \tag{1.26}$$

the standard deviation of A is given by the second derivative with respect to β, etc...

Owing to Eq. 1.23, such information can be evaluated using individual averages over periodic orbits, and only the periodic orbits ! The inclusion of steady states is discussed in [54]. The presence of additional

symmetries is discussed in [53] and results in periodic orbits being generalised into *relative* periodic orbits.

The main limitation in Eq. 1.23 is the infinite number of periodic orbits required to *cover the attractor*. Super-exponential convergence of the main averages versus T is usually observed for low-dimensional systems such as the Lorenz system when only periodic orbits up to period T are considered [57]. Nevertheless in high dimension this still leaves one with a daunting numerical task of determining *all* periodic orbits of period less than T without missing any of them.

Two remarks can be made at this stage. The first one is that unstable periodic orbits are generic and are expected to be found in all dynamical systems displaying chaos. An illustration is given by the construction of the Smale's horseshoe [58]. More than an expectation, the existence of unstable periodic orbits is sometimes listed as one of the conditions defining chaos, together with the condition that they are over the attractor [59, 60]. Beyond the numerical challenge associated with it, the mere identification of a given periodic solution is hence by itself not a theoretical breakthrough. In the context of the flow inside a MFU for instance, UPOs of the kind identified by [61] are in fact expected. UPOs are a consequence of the presence of chaos and do not "explain" chaos. In the same vein, periodic orbits likely to be found embedded within turbulent flows will not *explain turbulence* either. The second one is a matter of feasibility in a finite world : it remains far from clear whether such a heavy numerical machinery is truly progress if the main goal is to compute the mean flow profile. It seems that so far, and for a number of years to come, an efficient numerical solver will be much more efficient in predicting the flow statistics.

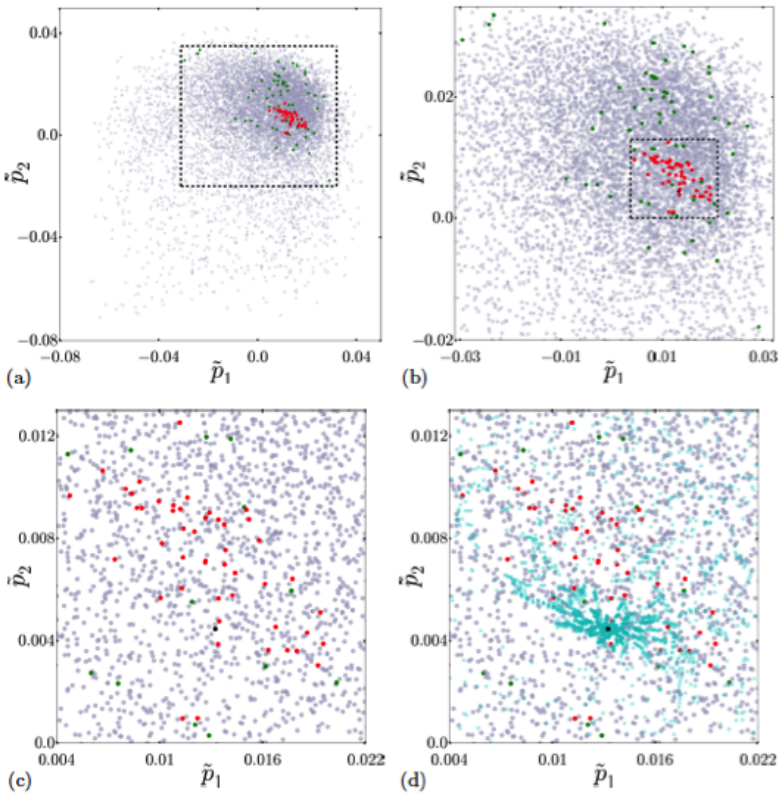

FIGURE 1.19 – a) Projection of a Poincaré section of the state space of pipe flow. Turbulent trajectories (grey) and relative periodic orbits (black, green and red), b) and c) successive zooms. Taken from [42]. d) same as c) with the unstable manifold of one of the periodic orbits depicted in blue.

1.6.4 Chaotic saddles

A large part of the literature on dissipative dynamical systems celebrates the notion of attractor, or equivalently of ω-limit set : the part of the state space that will again be visited by a given trajectory, no matter how many times it has been visited by the same trajectory already. Attractors are consistent with i) the dissipative nature of the Navier–Stokes equations and ii) the notion of sustained dynamical regime. A clearer link between the two notions (attractors and turbulence) emerged in the 1960s pioneered by E.A. Lorenz, initially with thermal convection in mind, for which turbulence is indeed sustained as long as thermal forcing is on. Direct application of this analogy to open shear flows leads to surprising results. At large enough Reynolds number, it is certainly more straightforward to consider turbulence as sustained, although even there some concepts become shaky due to the main advection. This is at least the case in spatially periodic simulations of channels and pipes in which, once initiated, turbulence never dies out. At lower Reynolds numbers, close to the onset of appearance of turbulent dynamics, the situation is less clear. Although some initial conditions seem to lead to a sustained turbulent flow, simulations over longer and longer observation times sometimes reveal relaminarisation. Unless transition is triggered again, the autonomous system stays laminar forever and the turbulent episode is nothing more than a transient. Experimentally (i.e. without periodic boundary conditions) this has a counterpart, easiest understood in pipe flow : a turbulent patch can travel several thousands of pipe diameters and die over the space of only a few pipe diameters [62–64]. In spatially extended systems such as plane Couette flow, although turbulence can spread, it can also recess until the whole flow becomes laminar [65, 66]. This relaminarisation is hence not only a numerical artefact but a genuine physical phenomenon, although again the mechanisms at play in the presence of spatial periodicity might differ from those in free space. Theoretical efforts to understand this relaminarisation phenomena have led to many interesting analogies with other areas of theoretical or applied physics [67]. To begin with, the lifetimes corresponding to multiple laboratory or computer experiments all pointed towards statistical distributions. Moreover the cumulated distributions of lifetimes frequently appear exponential, indicating a *memoryless process*. Although an analogy with radioactivity was unavoidably made, a more fruitful analogy turned out to be classical scattering, seen as a model of idealized unimolecular fragmentation [68]. The same formalism turned out later to be useful in other areas of hydrodynamics, namely fluid mixing [69], [70]. In the scattering picture, trajectories bounce alternatively on an array of hard spheres in a chaotic fashion, until they escape a given region of the associated state space. Despite the lack of dissipation, this picture of state space in figure 1.20 is very close to that depicted schematically in Fig. 1.21. It is structured around not one, but rather several invariant sets. In particular the rate of leakage of a delayed trajectory from the interaction region is claimed to be analogous to the rate of decay of a metastable system. This analogy has given a yet stronger weight to the cartoon of Fig. 1.21 : the lifetime of individual turbulent realisations corresponds to the time it takes for the corresponding trajectory to bounce through the "jungle" of unstable solutions and eventually to escape from it. The more entangled the network the longer the mean lifetime. A formalism of Markov chains has even been developed to account for the memoryless statistics observed [71, 72]. The initial success of this new dynamical picture came however from i) its originality and ii) its ability to incorporate well-chosen elements from dynamical systems theories to explain new features of low-Reynolds number turbulence. A question that remained, however, unanswered by this approach is about the possible divergence of turbulence's mean lifetime as the Reynolds number increases.

1.6.5 Other invariant sets

The historical focus on a set of fixed points and periodic orbits has perhaps slightly shadowed the search for other invariant sets beyond them. Invariant manifolds are as important as fixed points in many dissipative systems. In particular stable manifolds of objects yet-to-be-identified often act as inpenetrable barriers to trajectories, and hence as proper state space frontiers when their codimension is one. This will be the case for the edge manifold that will be extensively reported in the next chapter. It is as yet unknown whether other invariant manifolds can be of interest to the description of the state space for this class of hydrodynamic systems.

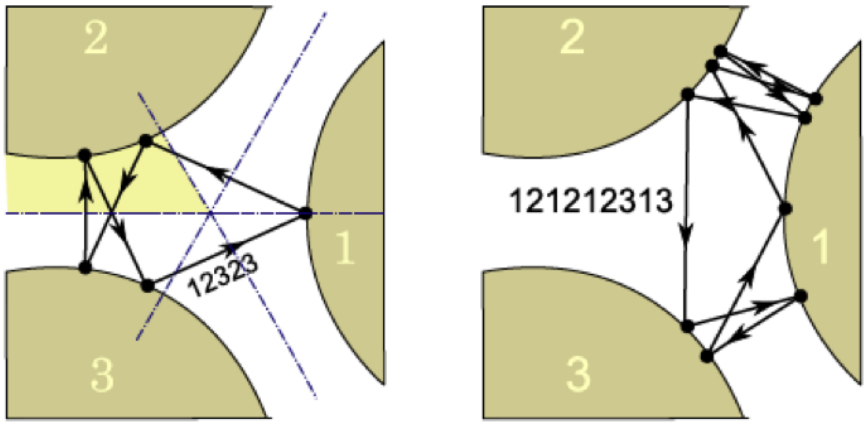

FIGURE 1.20 – Cartoon of two trajectories bouncing periodically between three repelling invariant sets. Taken from *Chaosbook.org*. Any other trajectory leaving the game after a finite number of rebounds is interpreted as a chaotic transient.

Other orbits (understood as 'trajectories') are however of interest. The ECSs reported above correspond almost exclusively to states with both a stable and an unstable eigenspace. As a direct consequence, heteroclinic orbits leaving the neighbourhood of one given state at $t = -\infty$ and connecting with the neighbourhood of another one for $t \to +\infty$ are likely to exist. Their properties are important as they are believed to guide the dynamics of most trajectories. They have been investigated numerically in Refs [73–75].

Homoclinic trajectories are also important as a support for state-space trajectories, however their numerical identification is potentially even richer in consequences. The Smale–horseshoe, a cornerstone of dissipative dynamical systems theories [76][58], states that the existence of a homoclinic orbit from an unstable periodic orbit automatically implies chaotic dynamics. This strong theorem has been used by [77, 78] to justifiy the chaoticity of plane Couette flow in the HKW cell. Interestingly, the Smale Horseshoe theorem is not expected to be valid if the periodic orbit is replaced by a steady state or a travelling wave. Given the number of unstable steady states identified in shear flows at the moment rather than UPOs, one can wonder what implication it has for the dynamics.

Another conceptually easy (but practically heavy) generalisation concerns the inclusion of unstable quasiperiodic states into the same picture. Such new solutions can emerge from Neimark–Säcker bifurcations of periodic orbits, and they can also bifurcate out of the blue. While formally the repelling role played by two-frequency solutions cannot be ignored, it remains to be shown how such information can be quantitatively useful : there is no equivalent of cycle expansions taking two-tori solutions into account. However exact toroidal solutions with more than two temporal frequencies are likely to play an increased role at slightly higher Reynolds numbers where the flow starts to display multiscale properties [79].

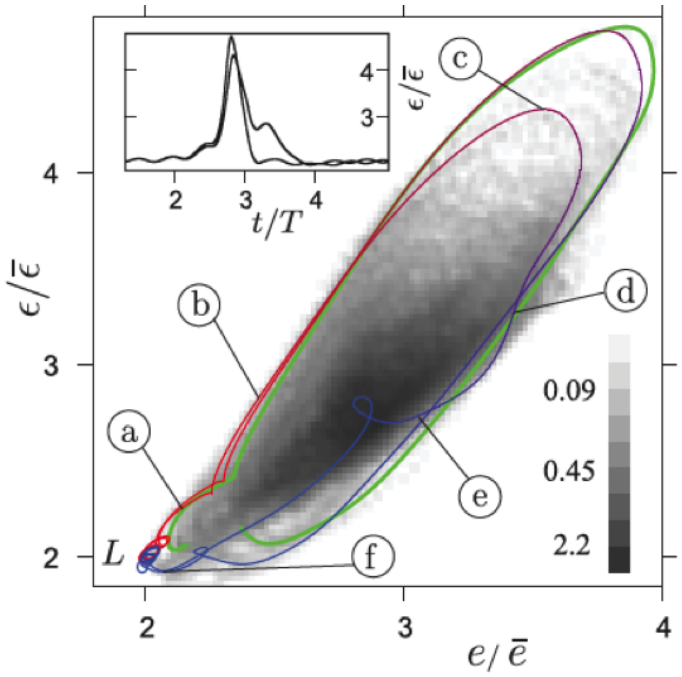

FIGURE 1.21 – Two homoclinic orbits of plane Couette flow starting from a time-periodic edge state (colours), together with the PDF of individual trajectories (grey). Representation in a kinetic energy/dissipation state portrait. From [77].

2

Dynamical systems description

2.1 The edge of chaos

Among the concepts from dynamical systems theories developed in the preceding introductory chapter, the recently formalised concepts of *edge manifold* and *edge state* have been left aside. The present chapter represents a personal opportunity to re-define these concepts from scratch, with the relevant mathematical rigour and with a (hopefully) consistent vocabulary.

2.1.1 The edge as a smooth separatrix

3.1.1.1 Illustration on a low-dimensional model

We consider first, mainly for pedagogic purposes, the two-dimensional autonomous model suggest by O. Dauchot and P. Manneville [17], which we label DM2D. This system is written under the general form $\dot{\boldsymbol{x}} = \boldsymbol{L}\boldsymbol{x} + \mathcal{N}(\boldsymbol{x})$, where $\boldsymbol{x} \in \Omega = \mathbb{R}^2$. $\boldsymbol{L}$ is a typical non-normal matrix suggested by Trefethen [80]. The components of $\boldsymbol{\mathcal{N}}$ consist of quadratic forms that conserve energy such that $< \boldsymbol{\mathcal{N}}(\boldsymbol{X}), \boldsymbol{X} >= 0$ for all $\boldsymbol{X}$ in line with the Reynolds-Orr theorem. These two operators read respectively :

$$\boldsymbol{L} = \begin{bmatrix} s_1 & 1 \\ 0 & s_2 \end{bmatrix}, \quad \boldsymbol{\mathcal{N}}(x_1, x_2) = \begin{bmatrix} x_1 x_2 \\ -x_1^2 \end{bmatrix}.$$

A state portrait of the DM2D model is displayed in figure 2.1 for the parameters $s_1 = -0.1875$ and $s_2 = -1$.

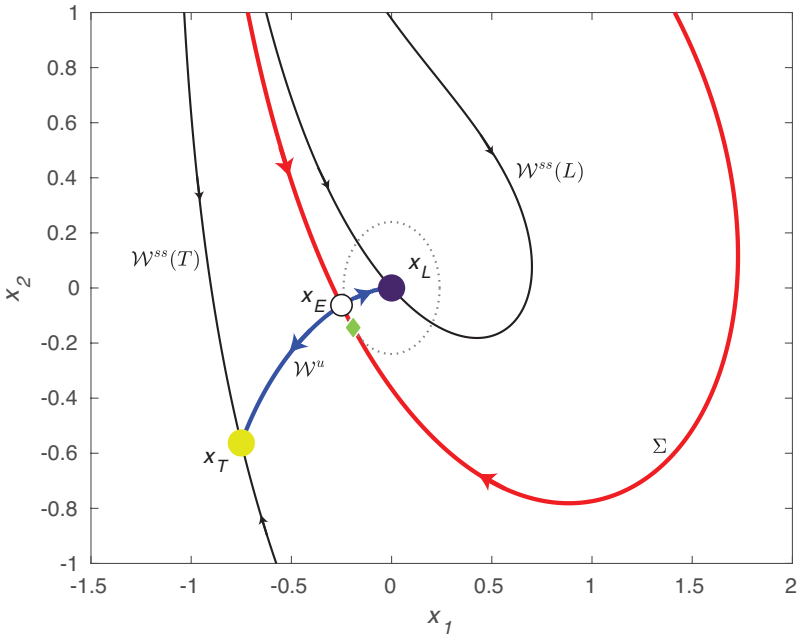

FIGURE 2.1 – State space of the DM2D model [17]. The laminar state $\boldsymbol{x}_L$ and the turbulent state $\boldsymbol{x}_T$ are represented together with their respective superstable manifolds, $\mathcal{W}^{ss}(L)$ and $\mathcal{W}^{ss}(T)$. The dividing line in red represents the edge manifold and coincides with the stable manifold of the *edge state* $\boldsymbol{x}_E$, $\mathcal{W}^s(\boldsymbol{x}_E) = \Sigma$. The blue trajectories form the oriented unstable manifold of E, $\mathcal{W}^u(\boldsymbol{x}_E)$. The green diamond corresponds to the minimal seed (see Section 3.3). Taken from Ref. [81].

The description of the state space is straighforward : two attracting fixed points $\boldsymbol{x}_L$ (the "laminar state") and $\boldsymbol{x}_T$ (the "turbulent state") coexist. The fact that the turbulent state has no proper "turbulent" dynamics does not matter much for the present illustration. By construction $\boldsymbol{x}_L$ is linearly stable, and it can be checked analytically that $\boldsymbol{x}_T$ is also linearly stable. Each attractor hence possesses its own

attraction basin, respectively $\mathcal{B}_L$ and $\mathcal{B}_T$. Their intersection is non-empty and we define the *edge manifold* as the intersection of their closures :

$$\Sigma = \overline{\mathcal{B}_L} \cap \overline{\mathcal{B}_T}, \tag{2.1}$$

displayed in red in figure 2.1. Trajectories starting at initial time from any point in Σ stay on Σ, hence Σ is an invariant set for the dynamics [82]. In addition, all such trajectories converge to a third fixed point labelled $\boldsymbol{x}_E$. We have the identity $\Sigma = \mathcal{W}^s(\{x_E\})$. $\boldsymbol{x}_E$ is labelled the "edge state", and it is here a point of zero dimension. It should not be confused with the "edge manifold" Σ (sometimes simply referred to as "edge") which here has dimension 1, in other words Σ is a hypersurface of codimension one. As the governing parameter s_1 is decreased, the two attractors $\boldsymbol{x}_E$ and $\boldsymbol{x}_T$ merge together and disappear at the same time, leaving the laminar state $\boldsymbol{x}_L$ alone (as fixed point) in the state space.

Within the DM2D model, the transition process from the laminar state to the turbulent one is already rich enough to be compared to the basic transition process as observed in hydrodynamical systems :

— initial conditions close inside $\mathcal{B}_L$ can approach $\boldsymbol{x}_E$ transiently but end up in $\boldsymbol{x}_L$
— initial conditions close inside $\mathcal{B}_T$ can approach $\boldsymbol{x}_E$ transiently but end up in $\boldsymbol{x}_T$
— the closer the initial condition to Σ, the longer the transient visit to $\boldsymbol{x}_E$.

This indicates that $\boldsymbol{x}_E$, although unstable with respect to two-dimensional disturbances, is stable and attracting within Σ and unstable in any direction transverse to Σ. Numerically, $\boldsymbol{x}_E$ can be hence found by a simple one-dimensional search (labelled also *shooting method* in the early Japanese literature). Such a search only requires initial conditions within a one-dimensional segment that intersects Σ somewhere. The concept is illustrated in figure 2.10. This is an iterative process terminated once the two initial conditions one either side of Σ are considered close enough. Note that in dissipative systems this algorithm *always* identifies an edge state, regardless of the associated dynamics.

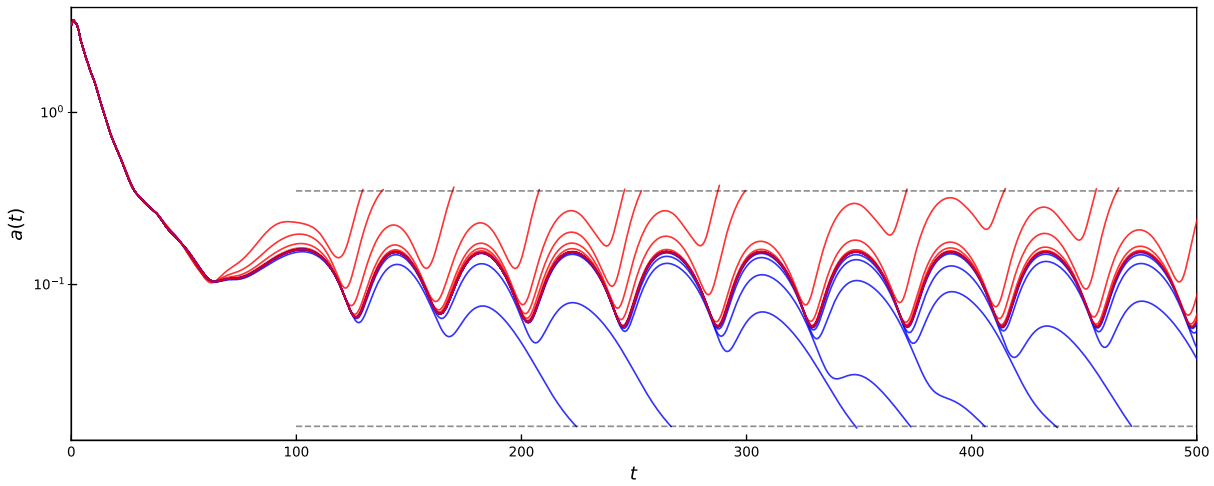

FIGURE 2.2 – Illustration of the "classical" iterative bisection process (courtesy M. Beneitez). Grey dashed lines : lower and upper bounds chosen for an observable $a(t)$. The sets of red and blue curves bracket an edge trajectory from t =0 until at least t =500.

3.1.1.2 The edge seen as a Lagrangian Coherent structure in high dimension

It is visually clear from figure 2.1 that the manifold Σ divides the state space into two complementary parts. No initial condition located strictly within one attraction basin can end up in the other basin, which makes Σ a barrier to transport. In addition, the hyperbolic nature of $\boldsymbol{x}_E$ is responsible for repelling

all nearby trajectories, even those infinitesimally close to Σ. All these conditions are strongly reminiscent of the physical concept of *hyperbolic Lagrangian Coherent Structure*, where *Lagrangian* refers to the tracking of individual trajectories [83]. The original frame for which LCSs were developed is also motivated by hydrodynamics, namely the finite-time transport of fluid particles by known time-dependent fluid flows [84, 85]. In particular, in steady velocity fields, repelling LCSs essentially mean material barriers to transport. Other applications, for instance chemical reactions, have also been considered [86]. The class of systems under study are however very different from the current context in transition : the dynamics are always conservative, there are no attractors, the trajectories can be computed in either forward or backward time, and the dimension of the state space (which coincides with the physical space) is very low, typically two. Besides, the system is in general non-autonomous due to the time dependence of the vector field. In most applications of Lagrangian concepts, the state space associated with Lagrangian tracers (governed by an equation $\dot{x} = v$) and the physical space coincide. In the Eulerian point of view relevant to the present transition problem, both spaces differ radically in their dimension.

There are several definitions used to identify repelling LCSs. We consider here only two of the simplest quantifiers : Finite-time Lyapunov exponents (FTLEs) and Lagrangian Descriptors (LDs).

Finite-time Lyapunov exponents

Finite-time Lyapunov exponents (FTLEs) have been popularised as a tool for the identification of LCSs in [84, 87]. Let $C^t_{t_0}$ be the (positive definite) Cauchy-Green tensor defined by

$$C^t_{t_0} = (\nabla \phi^t_{t_0})^* \nabla \phi^t_{t_0}, \tag{2.2}$$

where $(\cdot)^*$ represents the Hermitian transpose and the derivatives ∇ are with respect to state space variables. The Cauchy-green tensor has size $n \times n$, and its entries are usually computed using second-order centered finite-differences [83]. If $\tau = t - t_0 > 0$, the average growth rate over the time interval $(t_0, t_0 + \tau)$ around an initial condition x_0 is given by $\sqrt{\lambda(t_0, t_0 + \tau, x_0)}$, with λ the largest eigenvalue of the diagonalisable matrix $C^t_{t_0}$. The present system is autonomous hence $t_0 = 0$ without loss of generality. The leading finite-time Lyapunov exponent of the system at position x_0 is given by

$$\Lambda(x_0, \tau) = \frac{1}{\tau} \log \sqrt{\lambda(0, \tau, x_0)}. \tag{2.3}$$

The ridges in the field of the leading FTLE at time τ can be used as a diagnostic of a hyperbolic LCS [83, 88]. Hyperbolic LCSs refer to attracting and repelling distinguished invariant manifolds [84], with only the forward time FTLEs relevant for the identification of repelling LCSs [89]. FTLEs can be computed in arbitrarily high dimension using the recent scalable algorithm based on Optimally Time Dependent (OTD) modes, which are themselves determined from a minimization principle [90]. Under generic conditions these OTD modes converge exponentially fast to the eigendirections of the Cauchy-Green tensor associated with the largest eigenvalues, i.e. the largest finite-time Lyapunov exponents [91].

Lagrangian Descriptors

Lagrangian Descriptors (LDs) are a more recent diagnostic for Lagrangian coherence introduced in [92, 93] and its theoretical framework further developed in [94]. Like FTLEs, LDs are based on the integration of a given observable along trajectories, however they do not request any differentiation of the flow map with respect to the initial condition. The original quantity of interest is

$$M(x_0, t_0, \tau) = \int_{t_0 - \tau}^{t_0 + \tau} g(x(t)) dt, . \tag{2.4}$$

The observable g can be defined as

$$g(x(t)) = \sum_{i=1}^{m} |f_i(x, t)|^p, \tag{2.5}$$

where the f_i's are the components of the velocity field f, and $p \in (0, 1]$ and $\tau \in \mathbb{R}^+$ are two parameters. $p = 0.5$ is a good choice in practice. Eq. 2.4 can be split into its forward and backwards contribution [86, 95]. For the present autonomous system, again $t_0 = 0$ without loss of generality, and these contributions write hence respectively

$$M(x_0, \tau)^+ = \int_0^\tau g(x(t))dt, M(x_0, \tau)^- = M(x_0, \tau) - M^+(x_0, 0, \tau). \tag{2.6}$$

Due to the dissipative nature of the system, numerical backwards integration is ruled out for numerical stability reasons, only M^+ can be considered here. Since our focus is on stable manifolds rather than unstable ones it is sufficient to focus on the computation of $M^+(x_0, t_0, \tau)$. The abrupt change also means that the derivative of M^+ transverse to the boundaries is discontinuous. These singular features in LD plots are often connected to the stable and unstable manifolds of saddle points. Depending on the case, it is also useful to quantify abrupt changes of M^+ via the L^2-norm of its gradient

$$B(x_0, \tau) = \left[\sum_{i=1}^{n} \left(\frac{\partial M^+}{\partial x_{0,i}}(x_0, \tau) \right)^2 \right]^{1/2}. \tag{2.7}$$

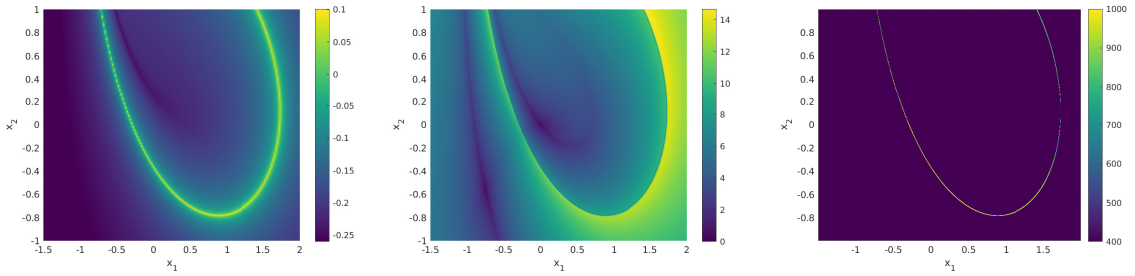

FIGURE 2.3 – State space of the DM model represented using isolevels of a) the leading FTLE Λ b) M^+ and c) $B = ||\nabla M^+||$. In each case the time horizon is $T = 60$. The edge manifold Σ is highlighted by the ridge in a) and c).

Other diagnostics for LCSs are routinely used, see [88] for a comparative review. Alongside the diagnostics based on a scalar field, such as FTLEs and LDs, other approaches based on transfer operators or dynamic Laplace operators seek coherent structures by formulating rigorous mathematical coherence principles (see e.g. [88, 96]). These diagnostics generally display limited scalability and are not considered here.

3.1.1.3 Illustration on hydrodynamic examples

The first pioneering use of the concepts of edge manifold and edge state in hydrodynamics is probably due to S. Toh and T. Itano [97]. The system they investigated is plane channel flow in a computational cell relatively close to that considered in [28]. Their pedagogic sketch, displayed in figure 2.4 shares many ressemblances with figure 2.1. The edge state identified in their study was claimed to be travelling wave solution. It was later re-interpreted, based on a longer computational, as a very long (relative) periodic orbit [98]. Eventually, it was demonstrated using better resolution and even longer edge tracking that the edge state in that system is in fact neither steady nor periodic or quasiperiodic, but apparently chaotic [99]. What was originally interpreted by Toh & Itano as the instability of the edge state was in fact part of the edge state dynamics itself. Note that in the same lab in Kyoto, G. Kawahara and S. Kida also used the same computational method in their 2001 paper on periodic orbits but in plane Couette flow : the edge state identified is the "gentle" periodic orbit visible in state portraits of the previous chapter.

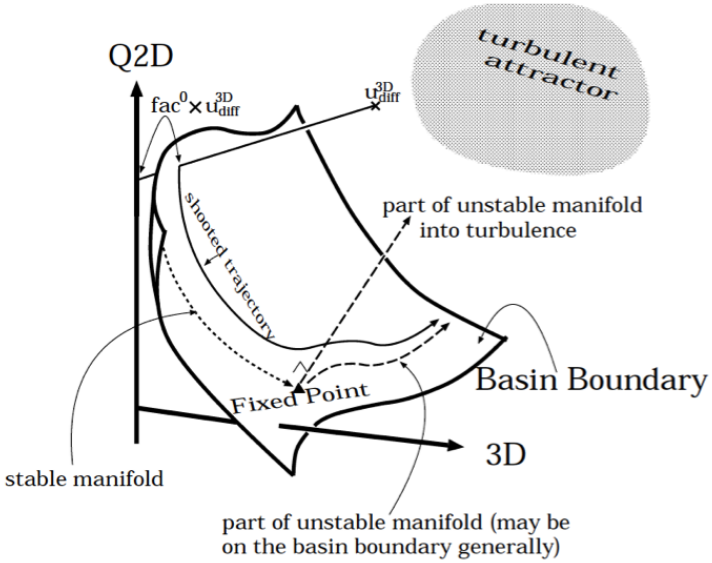

FIGURE 2.4 – Sketch of state space from Toh & Itano 2001 [97]. The dividing hypersurface labelled "Basin Boundary" represents the edge manifold.

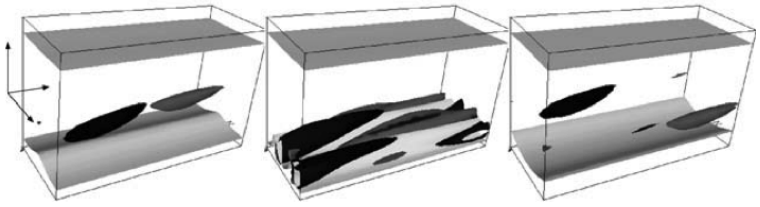

FIGURE 2.5 – Three-dimensional snapshots of the unsteady velocity field for the relative periodic edge state, as identified in channel flow by Toh & Itano 2003 [98]. Light grey : isocontours of streamwise velocity, darker colours : isocontours of the vortex criterion Q coloured by the sign of the streamwise vorticity.

2.1.2 Concept of edge state in chaotic saddles

In the previous example of the DM2D model, all fixed points but the edge state are attractors, and the edge manifold appears smooth. As previously mentioned, a key property of transitional shear flows close to their onset is the finite lifetime of the *turbulent* dynamics, observed both in experiments and in computations [100]. This property appears incompatible with the definition of a "turbulent" attractor, hence the only attractor left in this picture is the laminar state. The notion of attraction basin hence needs to be generalised to that of a separatrix between *short transients* and *supertransients* [67]. The generalisation works in practice since, for observation times shorter than the mean lifetime, the dynamics is indistinguishable from the bistable dynamics detailed earlier. Similarly, most usual quantities such as Lyapunov exponents, correlation functions etc.. can be computed over finite times only [67]. Severe practical problems arise however if the observation time is longer or comparable to the mean lifetime.

There has been a strong interest in transient chaos by theoreticians, going back perhaps as early as the foundations of complex dynamics and Fatou's dust in iterative maps in the early 20^{th} century. Fatou's dust is the union of the attraction basins of periodic points in simple maps such as the tent map, which is known to have the structure of a Cantor set and whose construction is illustrated in figure 2.6.

There is a direct analogy with the edge manifold in smooth differential systems. Since the turbulent

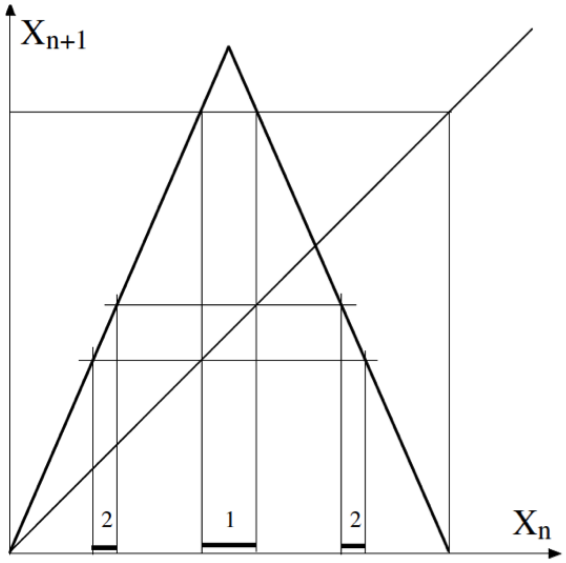

FIGURE 2.6 – Iterative construction of the Cantor set of Fatou's dusts of the tent map (courtesy P. Manneville).

dynamics itself does *not* define an invariant set, the edge manifold is regarded as the only remaining non-trivial invariant set of the system. It can hence be sought directly as a set characterised by infinite lifetimes, i.e. the ridge in a lifetime landscape as in figure 2.7. Most related algorithms use the idea that any segment joining two regions of the state space with different lifetimes *must* straddle the edge. Luckily they do not differ from standard bisection algorithms [101–103].

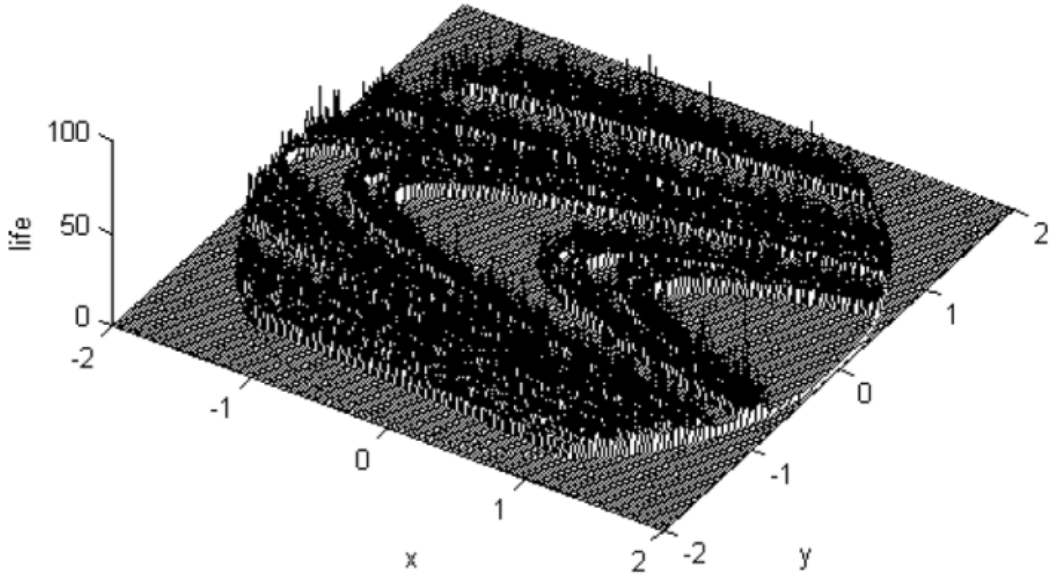

FIGURE 2.7 – Chaotic saddle of the Henon attractor revealed by the ridge in the lifetime landscape. [103].

Until 2005 the edge state was reported under very different names such as "chaotic saddle". The introduction of the word *edge* (in fact, originally *edge of chaos*) dates back to the reference paper of J. Skufca, B. Eckhardt and J. Yorke in 2006, who focus on a 9-dimensional Galerkin model of subcritical

transition. It has remained popular ever since. We would like to emphasize the distinction between the *edge* Σ (the manifold/separatrix/barrier) and the *edge state* E, which is the limit state of a trajectory within Σ. E is sometimes labelled the *relative attractor* on Σ. Note that, although the turbulent state is often considered unique, no principle warrants the uniqueness of the edge state for a given system. In a few cases several distinct edge states have been identified for the same set of parameters.

It did not take long until the above concept was used in a genuine Navier–Stokes context, starting with pipe flow [104–106], in situations where the mean turbulent lifetimes are either finite or unbounded. From a dynamical point of view, the edge state can host relatively simple time variations or look chaotic, however the time variations look modest compared to the associated turbulent dynamics. Experience suggests that the chaoticity of edge states is the exception rather than the rule. From a structural point of view, the perturbation velocity field associated with edge states possesses a few robust features : streamwise rolls and streaks are always present, just as for the turbulent state (see figure 2.8). Edge states are never strictly two-dimensional and display streamwise variations for finite Re. These elements are all consistent with the SSP picture of F. Waleffe [107]. As Re goes to infinity (provided the numerical domain is unchanged), the corresponding coherent structures evolve towards a two-dimensional flow different from the laminar one, whereas the streamwise-dependent part becomes dominated by a wave part traveling at constant speed. It was later realised [108] that this is perfectly consistent with the Vortex-Wave Interaction picture suggested by P. Hall and co-workers in the 1980s to address the question of high-Re shear turbulence [109]. This theory involves critical layers, whose thickness scales like $O((\alpha Re)^{-\frac{1}{3}})$, such that they become singularly thin in the high-Re limit [110]. This apparent issue will be mentioned again in the last section of this chapter when dealing with localised edge states.

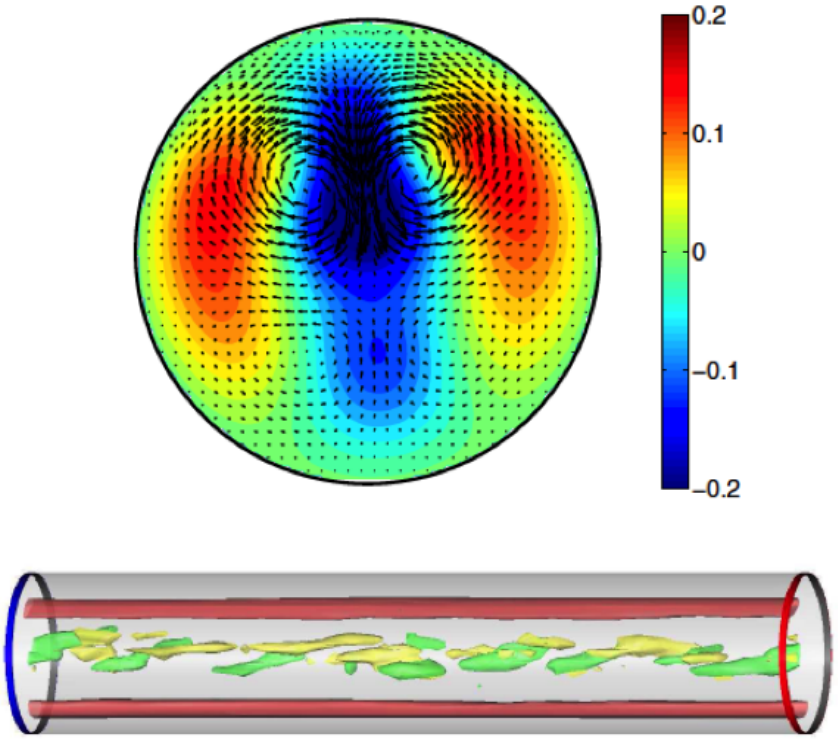

FIGURE 2.8 – Snapshot of the edge state in pipe flow with parameters $Re = 2875$ and domain length $L = 5D$, from Ref. [105]. Top : cross-sectional velocity field, bottom : three-dimensional side view (flow from left to right).

2.1.3 Edge tracking techniques

A posteriori verification

The methods to identify numerically edge states will be referred to as "edge tracking techniques". Several methods coexist in the hydrodynamic literature with their pros and cons, although edge tracking tends to be dominated by the "classical" bisection method. The first edge states in shear flows were found accidentally even before the separatrix concept emerged. It simply turned out that, out of the multitude of finite-amplitude solutions identified numerically (no matter how), some of them have the edge state property that their stable manifold divides the state space into two separate parts. The simplest finite-amplitude solutions to date usually emerge in saddle-node bifurcations, and form pairs with one "lower-branch solution" and one "upper-branch solution" (the distinction is usually based on the perturbation kinetic energy). If one of these states has, even for a bounded parameter range, strictly one unstable eigenvalue (equivalently one unstable Floquet multiplier if the state has time periodicity), then it is very likely to be an edge state because its stable eigenspace has codimension one ($dim(E^u) = 1$). This is the case for instance with the steady lower-branch Nagata state, the first finite-amplitude solution found in plane Couette flow [111]. It was verified multiple times that i) slight perturbations to the edge state lead either to turbulent or laminar dynamics depending on the sign of the perturbation, ii) classical bisection finds this steady solution as the edge state, and iii) for low enough Re this is the only such state for the corresponding numerical parameters [112]. Conversely, finite-amplitude solutions with two or more distinct instability directions ($dim(E^u) > 1$) are not eligible as edge states, however they can belong to Σ or not.

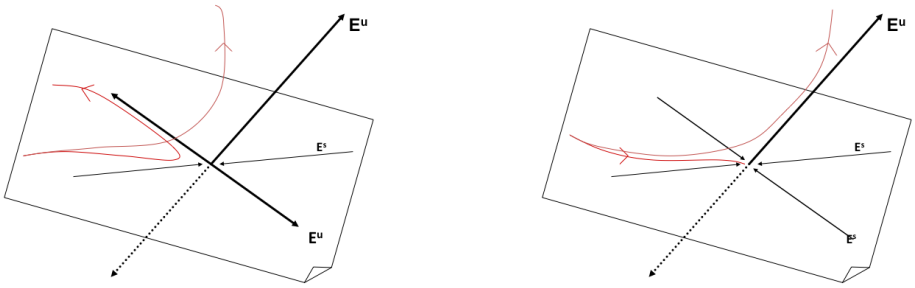

FIGURE 2.9 – Sketch of local stability near hyperbolic points. a) $dim(E^u) > 1$ b) $dim(E^u) = 1$. Only in the case b) can the fixed point be an edge state.

Bisection techniques

The core of popular edge tracking techniques is the bisection process. Geometrically speaking, a one-dimensional state space segment is first identified such that it straddles the laminar-turbulent separatrix Σ. The straddling property is identified simply by monitoring whether the flow is laminar or turbulent after some observation time. The segment is iteratively shrunk until it coincides with a state on Σ as in figure 2.10. The process is always convergent as soon as the length of the segment can shrink to zero, irrespective of the dynamics obtained. It occurs however in practice that machine precision is reached before the bisection has led to the desired or expected dynamics. In such a case the process is simply *restarted* by considering another pair straddling Σ (usually chosen from the end of the previous steps). Most searches employ this restarted technique in order to access the true asymptotic state without being fooled by finite arithmetic.

A common misunderstanding consists in claiming that edge tracking algorithms fail to converge if

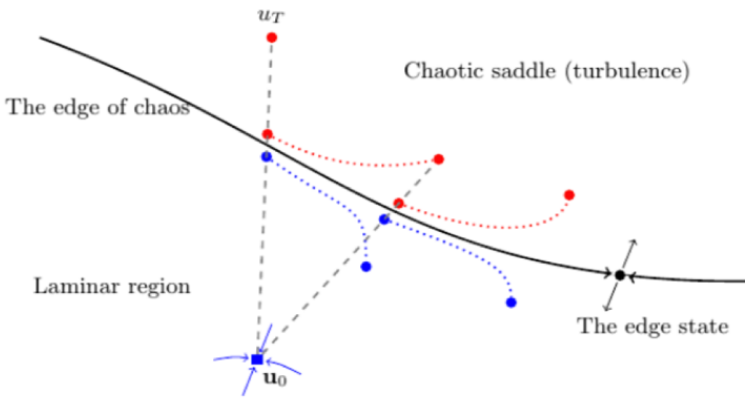

FIGURE 2.10 – Sketch of edge tracking from Ref. [113]

the end result is dynamically "complex". In addition, the seducing advantage of simple edge states is the possibility to monitor the convergence towards them. If the edge state is instead a chaotic relative attractor, it is much more delicate to assess quantitatively when the asymptotic state is 'reached' or to claim convergence.

Each bisection algorithm can be summarised as a recursive loop :

Step 0 $k = 0$, choose a perturbation to the laminar flow $\boldsymbol{u}_0$

For k=0,1,2,... repeat until machine precision is reached :
Step 1 $\boldsymbol{u}_k(t = 0) = \lambda_k \boldsymbol{u}_0$

Step 2 $\lambda_{k+1} = \frac{1}{2}\left(min(\lambda_k, \lambda_{k-1}) + max(\lambda_k, \lambda_{k-1})\right)$

Step 3 if $\boldsymbol{u}_k(t)$ ever becomes turbulent (even transiently), $\lambda_{k-1} \leftarrow \lambda_k$ and $\lambda_k \leftarrow \lambda_{k+1}$

else $\lambda_k \leftarrow \lambda_{k+1}$.

Bisection algorithms differ according to the method chosen to select the final observation time.

The "classical" bisection technique used here is based on the choice of one observable $a = a(t) = a(\boldsymbol{x}(t))$ together with the choice of *bounds* a_L and a_T. It is then assumed, based on physical intuition, that the dynamics has no choice but to relaminarise if $a(t) < a_L$, or no choice but to go turbulent if $a(t) > a_T$. A transient time is usually excluded at the beginning of each run before the previous property $a_L < a(t) < a_T$ is checked for. Note that a good choice of (a_L, a_T) can in practice really accelerate the process by several orders of magnitude. Ideally the choices $a_L = min\{a(\boldsymbol{x}), \boldsymbol{x} \in \Sigma\}$ and $a_T = max\{a(\boldsymbol{x}), \boldsymbol{x} \in \Sigma\}$ are ideal, but such information is not necessarily available beforehand. If the amplitude of the edge a_E is known (even when time-dependent), this can lead to further improvements

in speed.

One of the issues with classical bisection algorithm is that each step is longer than the previous one. The time needed for each iteration diverges in principle as the relative attractor is approached. This is due to the increasing transient time spent in the neighbourhood of the relative attractor before the bounds are reached. Restarting from states ever closer to E can limit this divergence but not fully prevent it. The interpretation of Σ as a Lagrangian Coherent Structure can here provide a solution : bisection now refers to the classical maximisation (or minimisation) of a given state space functional, in the hope to locate ridges in a given landscape. This functional can be for instance the leading FTLE computed over a specified time horizon τ. It can also be, when using Lagrangian Descriptors, the gradient B^+ of M^+ introduced in Eq. 2.7 for a specified time horizon τ.

The performances of these three different bisection algorithms have been compared in figure 2.11a for the simple two-dimensional DM2D model introduced earlier. All three algorithms converge exponentially

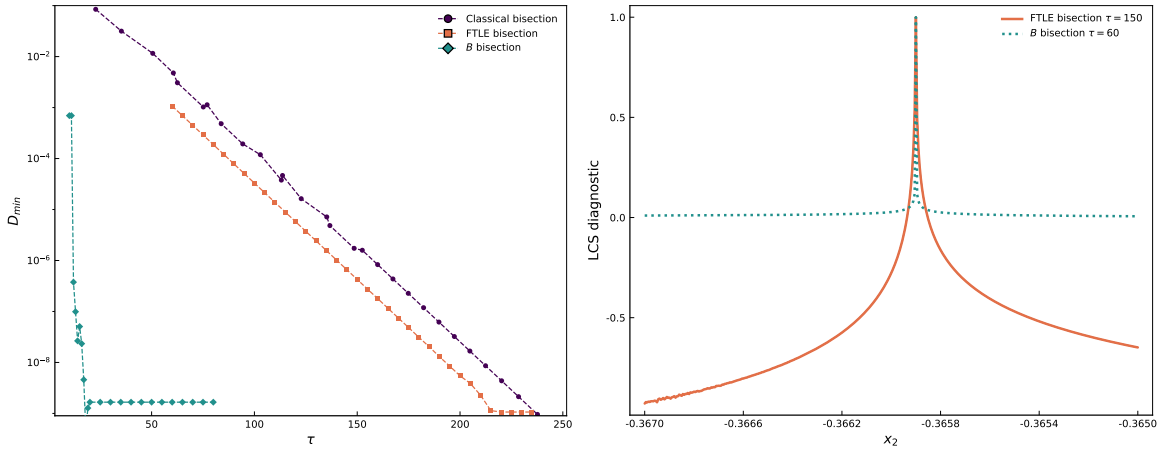

FIGURE 2.11 – DM2D model. Left : convergence in log scale of the there types of bisection versus the horizon time τ. Right : LCS diagnostics as a function of x_2.

fast towards the edge state E. The FTLE-based bisection outperforms the classical bisection algorithm although the improvement is not spectacular. The LD-based method, however, is much faster than the two other ones. This suggests the use of such a variant of the bisection technique for future studies. We note that the ridge structure on Σ characterises geometrically the edge manifold only when the turbulent state is a simple fixed point. The computations above have been generalised to investigate the structure of Σ in minimal flow units of plane Couette flow at $Re = 400$. There the landscape of both FTLEs, M^+ and B is slightly more difficult to apprehend. In particular, turbulence for these parameters is transient : following the Λ-lemma [114], the edge manifold crosses the straddling segment multiple times. This leads to the jagged landscape depicted in figure 2.12. It is not clear whether in such cases the new bisection techniques offer any advantage compared to the original method considered by Skufca *et al.*.

Feedback control methods

Bisection algorithms are conceptually simple but, because they are based on multiple simulations, they can be costly and slow. Indeed one bisection requires 2^n individual runs until machine precision ε_M is reached at n^{th} iteration, i.e. $n \sim -log(\varepsilon_M)/log2$, at which point the process needs to be restarted M times as long as no simple edge state has been reached. The total cost is hence of $Mn \geq 100$ runs at least, with each run getting longer as accuracy improves. For instance, in [115], each bisection required a total of $Mn \approx 400$ runs, which corresponds to $\approx 10^6 - 10^7$ CPU hours. This high cost makes parametric studies infeasible in practice. Other numerical methods have been suggested as alternatives to the bisection-rootfinder combination, e.g. iterative adjoint optimisation methods [112, 116] though they

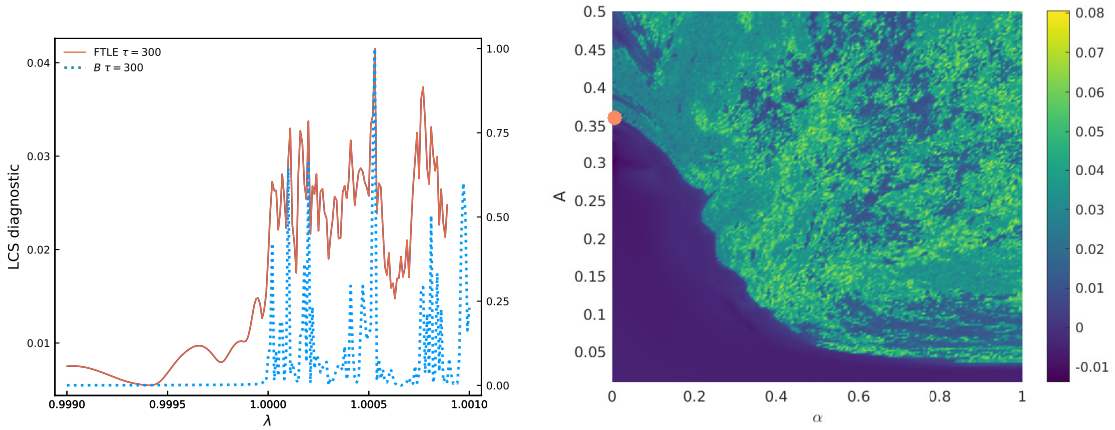

FIGURE 2.12 – Plane Couette flow computations. Left : One-dimensional landscape of state space rendered using LCS indicators (FTLEs, B) for $\tau = 300$. Right : two-dimensional cut through state space visualised using iso-levels of FTLEs. A and α are two coordinates centered on the laminar state and defined in Ref. [81].

involve significant mathematical and computational complexity.

Since the goal is to pinpoint and converge towards one of the unstable regions of the state space, refined control strategies can achieve a similar task. This is done by introducing into the original system a *control* term that counteracts the edge instability and is able to stabilise unstable states without altering them significantly. Several theoretical control strategies have been suggested in the past in order to converge towards unstable states, some of the notable ones are Pyragas delay-based control [117] and Selective Frequency Damping [118]. The former is heavy to implement in high dimension because of memory requirements and suffers from some limitations regarding convergence. The latter is easy to implement and is convenient at least for steady states. However it turns out not to converge in shear flows, because eigenvalues with zero imaginary part are not stabilised (see e.g. [119]).

We propose a remarkably simple linear feedback control able to constrain the dynamics to the edge manifold, and to stabilise invariant solutions that are stable within it. This scheme has been applied to track unstable chimera states in systems of non-locally coupled phase oscillators [120, 121]. In its most simple form, the control scheme makes one of the system parameters μ state-dependent by imposing a linear relation between the parameter and an observable $A(t)$.

$$\mu(t) = \mu_0 + \kappa(A_0 - A(t)) \tag{2.8}$$

For the shear flow problems we will identify μ with Re and A with some pre-defined perturbation energy

$$A(t) = \int_{r_i}^{r_w} (u^2 + v^2)\, r \,\mathrm{d}r \,\mathrm{d}\theta \,\mathrm{d}z \,. \tag{2.9}$$

Geometrically, the resulting dynamics can be understood by considering its representation in the (μ, x) plane. For $\kappa = 0$ we are back to the uncontrolled system, where for a fixed choice of the parameter the dynamics is constrained to a vertical line in the (μ, x) plane, determined by the choice of the parameter. The equilibria for each fixed parameter $\mu > 0$ are selected as the intersections with the corresponding vertical line. The equilibria on the upper branch of the parabola are dynamically stable, while those on the lower branch are unstable (cf figure 2.13a) . By choosing the pivot point (μ_0, x_0) fixed and varying the control gain κ we can now sweep the stable equilibrium of the controlled system along the parabola, until the straight line becomes tangential to the parabola and both equilibria disappear in a saddle-node bifurcation (cf figure 2.13b).

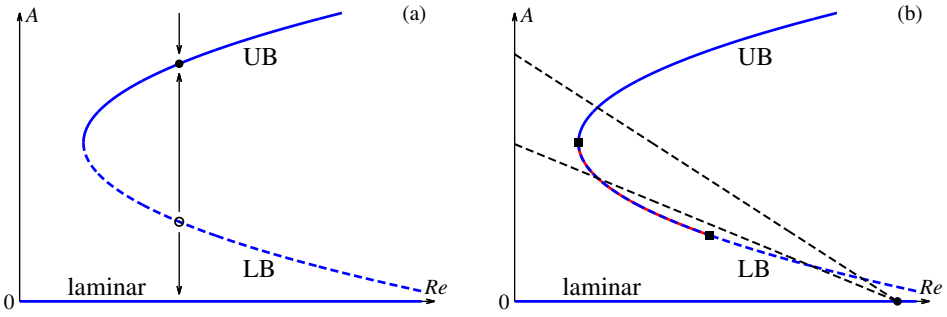

FIGURE 2.13 – Sketch in an (A, Re) representation of the stability of the uncontrolled (a) and controlled system using the feedback control method (b) based on the constraint (2.8) corresponding to the dashed slanted lines. The labels 'UB' and 'LB' refer to the upper and lower branch in the uncontrolled system, respectively. In fig. (b) the dashed slanted line is rotated around a pivot point at a given rate, allowing the unstable fixed point on LB to be tracked dynamically.

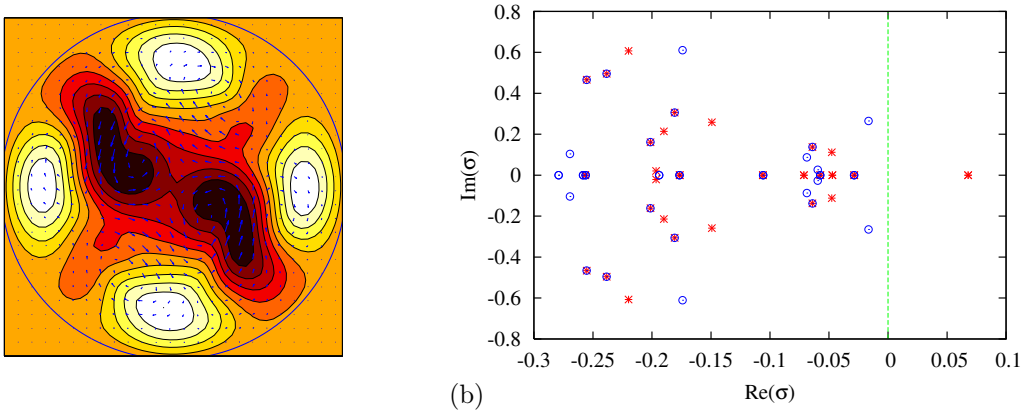

(a) (b)

FIGURE 2.14 – (a) Cross section of the stabilised TW solution with $\alpha = 1.25$ and $m_0 = 2$. Streamwise velocity perturbation in colour (from dark to white) and cross-stream components (vectors). (b) Eigenvalue spectrum for the TW solution with (blue circles) and without control (red crosses).

This control scheme was applied to the case of pipe flow investigated in ref. [106]. Within a few hours of computation it manages to stabilise the lower-branch travelling solution which is the edge state for that system. Not only does it identify this unstable state for one parameter value, but it can trace a large part of the corresponding branch of TWs in the same computation. Although computationally very appealing, the suggested method converges exactly only when the edge state does *not* display any oscillatory instability. It would be desirable to explore further the properties of this control scheme as well as the possibilities to use unconverged results combined with another algorithm [122].

2.2 Edge state dynamics in terms of finite-amplitude solutions.

In the present section, we consider a finite-time segment from an edge trajectory computed in pipe flow, and analyse how the edge fluctuations are structured by the presence in state space of neighbouring finite-amplitude solutions. This analysis is based on classical recurrence analysis traditionally used in chaotic theory and signal processing [123].

2.2.1 Recurrences

We begin by defining the notion of spatial shift by considering a velocity field, independently of the time t at which it is considered. $\sigma = (\sigma_\theta, \sigma_z)$ is a pair containing the values of the shifts in the axial and azimuthal directions respectively (the generalisation to Cartesian coordinates is trivial and intuitive). Let $\boldsymbol{T}_\sigma$ act on $\boldsymbol{u}$ such that

$$(\boldsymbol{T}_\sigma \boldsymbol{u})(r, \theta, z, t) = \boldsymbol{u}(r, \theta + \sigma_\theta, z + \sigma_z, t). \tag{2.10}$$

Several types of finite-amplitude solutions are identified during this study. In particular, travelling wave solutions (TWs) are defined by

$$\boldsymbol{u}(r, \theta, z, t + T) = (\boldsymbol{T}_\sigma \boldsymbol{u})(r, \theta, z, t), \tag{2.11}$$

with $\sigma = (c_\theta T, c_z T)$ for a specific couple (c_θ, c_z) and for all t and T. Relative periodic orbits (RPOs) are defined by the same relation (2.11) for all t, which however holds only for given values of T, σ_θ and σ_z.

We define now a recurrence function depending on the two time arguments t_i and t

$$r(t_i, t) := \frac{|\boldsymbol{X}(t) - \boldsymbol{T}_\sigma \boldsymbol{X}(t_i)|}{|\boldsymbol{X}(t_i)|} \tag{2.12}$$

Identifying all the minima in t of the recurrence function yields r_{min}, a function of only t_i, defined as

$$r_{min}(t_i) := \min_{t > t_i} \{\, r_i(t) : \frac{\partial r_i}{\partial t} = 0 \,\}. \tag{2.13}$$

The signal of r_{min} is depicted in figure 2.15 for $\sigma = (0, 0)$. The value of $\sigma_\theta = 0$ is motivated by computational simplicity. The value $\sigma_z = 0$ is selected arbitrarily to alleviate, in the case of travelling waves, the degeneracy between σ_z and the time period. $r_{min}(t_i)$ features an alternation of relative lows and highs, with low values reaching 10^{-1}. Note that such values are substantially lower than the corresponding r_{min} found in turbulent runs for the same system, which rarely dip under $0.2-0.3$.

The main idea of recurrence analysis is that local minima of $r_{min}(t_i)$, associated with a time T such that $r_{min}(t_i) = r(T, t_i)$, correspond to furtive approaches to RPOs with a period close to T. Such RPOs would in fact correspond to exact zeros of the recurrence function r. Such zeros can be identified numerically within machine precision, using adaptations of classical rootfinding techniques. Rootfinders are iterative algorithms which need an initial condition, and the state corresponding to each dip of r_{min} is precisely a good choice of initial condition. The classical Newton method, by far the most used rootfinder in this context, seeks for instance zeros of the functional

$$g : \boldsymbol{X} \to |\phi^T(\boldsymbol{X}) - \boldsymbol{T}_\sigma \boldsymbol{X}|^2. \tag{2.14}$$

in a $(N+3)$-dimensional state space. N is the dimension of X, 3 refers to the additional scalar unknowns T, σ_z and σ_θ and ϕ^T is the nonlinear propagator over a time horizon $T > 0$. If convergence fails, the Newton algorithm can be complemented by a globalisation technique such as the Hookstep [124] or the double dogleg step [125]. For the case displayed in figure 2.15, a different TW solution has been found for almost every dip, and it was verified that the TWs look visually close to the initial condition given to the Newton solver. Closer inspection has revealed that one special TW is recurrent in this search (modulo azimuthal shifts), namely the TW labelled $S1$.

This investigation validates the sketch below (see figure 2.16) where the dynamics *along* the edge manifold Σ can be described as a hyperbolic *saddle*, i.e. a networks of connected hyperbolic points guiding the dynamics. In the direction *transverse* to Σ the dynamics is dominated by the two attractors of the system, the laminar and the turbulent state, which are outside Σ. Asymptotic convergence towards a given finite-amplitude solution belonging to Σ, i.e. towards an edge state, is possible only if, among the list of states sitting on Σ, one of them possesses a stable manifold of codimension one. This is consistent

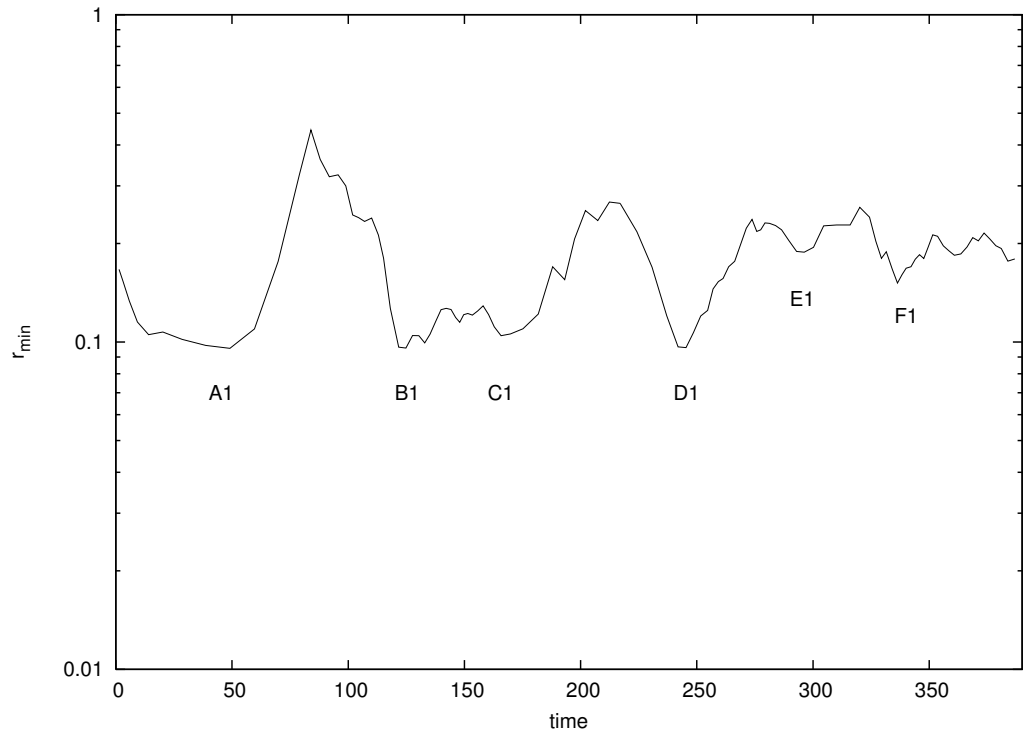

FIGURE 2.15 – Residual $r_{min}(t_i)$ from [106]. Labels indicate the dips of r_{min} likely to yield good initial conditions for a subsequent Newton search.

with the sketches in figure 2.9.

The imposition of well-chosen discrete symmetries in the computations can help to identify more exact solutions, because it can reduce the number of unstable eigenvalues. Intuition is unfortunately a poor guide here and one relies mostly on luck. In the case of pipe flow for instance, luck was bypassed by the knowledge of one special case. A TW has been found in a former study [126] with axial wavenumber $\alpha = 1.25$. It possesses the $\mathcal{R}_2$ symmetry, i.e. it is π-periodic in the azimuthal coordinate rather than 2π-periodic. When its eigenvectors are restricted to the symmetric subspace invariant under $\mathcal{R}_2$, only one eigenvalue is unstable. This TW fullfills the conditions to be an edge state according to figure 2.9a. Indeed it was identified as an asymptotic edge state using the classical bisection method. A surprise arose however : depending on the initial condition chosen for the bisection with $\mathcal{R}_2$ symmetry, either that TW is found, or another (new) solution labelled $C3$. This is attested to by the recurrence function r_{min} shown in figure 2.17, where the convergence to a TW is clear. The convergence to a well-defined attractor such as $C3$ does not prevent the transient approach to other states. This is for instance the case with the TW labelled $A3$, identified using the recurrence function in figure 2.17, and displayed in figure 2.18 together with $C3$.

Edge tracking was employed in the examples above as a *tool* to reveal new exact solutions. These solutions belong by construction to Σ and their identification allows one to construct, stone after stone, a better representation of the topology of Σ. The main advantage of this approach over e.g. homotopy, is the simplicity of the concept. Moreover, the solutions found are guaranteed to be weakly unstable (else they would not have been found) and have a dynamical role that is already understood. The edge tracking method, if complemented with a good continuation solver, yields more than edge states. Continuation allows one to track edge states (and other more unstable states) down to the saddle-node bifurcation from which they are born, and to trace the upper branch as well. This is shown in figure 2.19 as an example drawn from pipe flow. This whole diagram of new solutions [127] was started from the knowledge of one

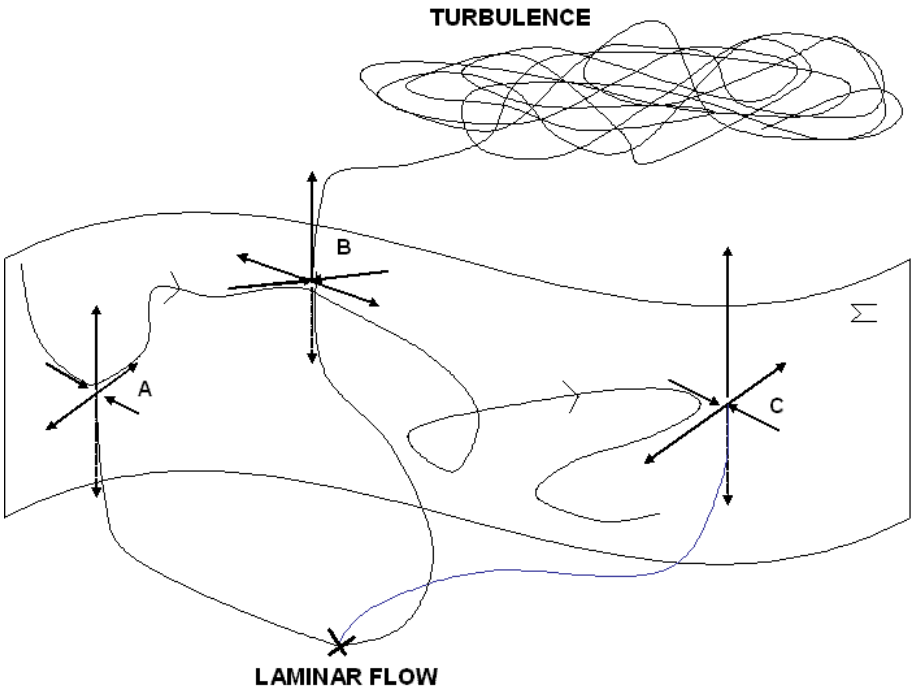

FIGURE 2.16 – Illustration of the hyperbolic saddle structure of the edge manifold in state space, taken from Ref. [106].

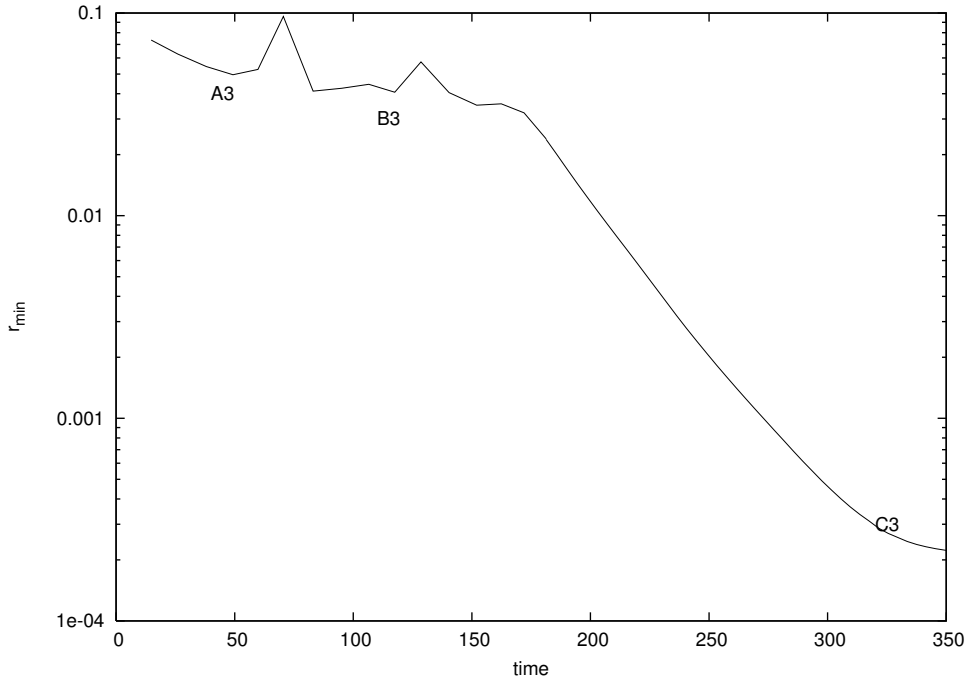

FIGURE 2.17 – Residual $r_{min}(t_i)$ from [106]. Edge trajectory restricted to the subspace invariant by the $\mathcal{R}_2$ symmetry. $\alpha = 1.25$.

edge state only with $\mathcal{R}_2$ symmetry. The other solutions were found by changing the index of the azimuthal

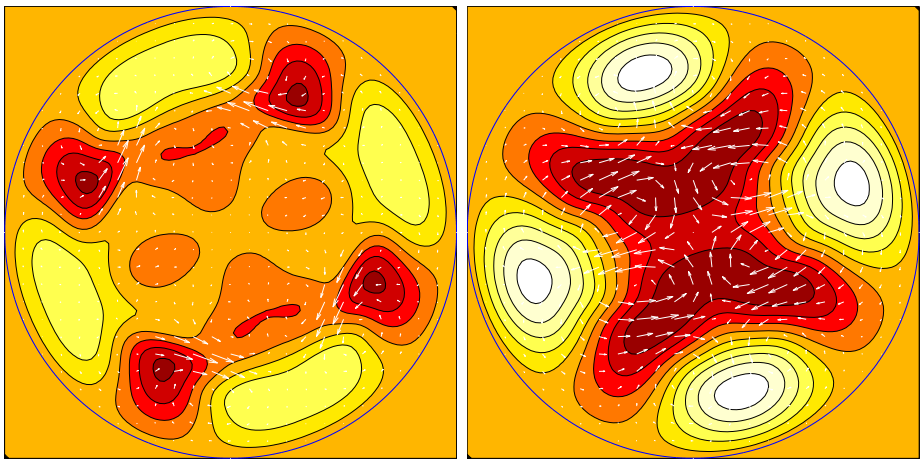

FIGURE 2.18 – Residual $r_{min}(t_i)$ from [106]. Cross-section of TW solutions $A3$ (left) and $C3$ (right). Isovalues of streamwise velocity perturbation superimposed with quivers for the transverse velocity field. $\alpha = 1.25$.

symmetry and by applying numerical arclength continuation.

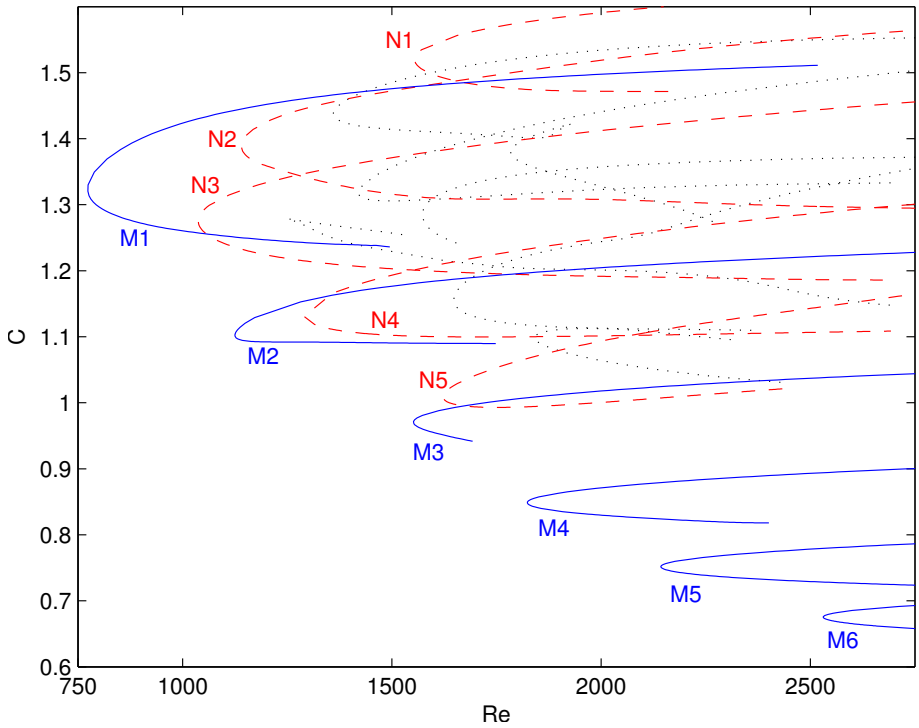

FIGURE 2.19 – Bifurcation diagram c (streamwise phase velocity) vs Re for travelling waves solutions in pipe flow with $\alpha = 1.25$ and different values of the azimuthal symmetry index m [127].

These findings suggest a full method in order to identify whole new families of exact solutions of the Navier–Stokes equations. It requires only a timestepper and the evidence that the dynamics is bistable, (with a laminar point as an attractor and another turbulent attractor)... and some luck too. The method can work as well if the attractor is a chaotic saddle, provided its mean lifetime is long enough with respect to the time to approach the edge state along the edge. Then if the system possesses an exact coherent state as an edge state, the bisection algorithm will asymptotically converge to it from *suitable* initial

conditions. This was the case in Refs. [106] and [128] in pipe flow, Ref. [129] in plane Couette flow, Ref. [130] in plane Poiseuille flow, Ref. [113] and Ref. [131] in ASBL (the list is non exhaustive). Convergence can be accelerated using an efficient rootfinder adapted to high dimension. Compared to the homotopy methods used beforehand, the present method offers the important advantage that the dynamic role of these solutions in state space is known by construction.

Numerical continuation of these solutions in R (or in α) invariably reveals that the branch of the original edge state turns around in a fold at some finite parameter value. It appears then that the edge state is a lower-branch solution and that the other solution is an upper-branch solution, the two originating from the same saddle-node bifurcation. Application of this technique in the pipe flow instance of figures 2.17, conducted for several values of the azimuthal wavenumber m, has led to many new branches of TW solutions, as in fig. 2.19. Together with the related investigations in [45], [132], [133] or [134], more than 20 different families of travelling waves have been found so far in spatially periodic pipe flow ; all are exact solutions to the Navier–Stokes equations within numerical accuracy. Together they all contribute to the structure of the state space of turbulent pipe flow [126]. The new information is that the dynamics on the edge is organised around the lower-branch solutions only.

2.2.2 Chaoticity of edge trajectories

The sketch of the topology of the edge manifold in figure 2.16 is very comparable in spirit to the random walk picture suggested for the turbulent attractor/saddle in the previous chapter. It is (at least *a posteriori*) no surprise for the case of a turbulent saddle, where the stable manifold of the edge state appears dense in the state space. However this is not a trivial result in the usual case where turbulence is an attractor, as evidenced by the counter-examples when the edge state is a simple relative attractor. The main implication of the dynamics sketched in figure 2.16 is the possibility that the edge dynamics be chaotic. While this has been speculated many times, the chaoticity of generic edge trajectories has never been properly demonstrated. We suggest here to focus on a given flow case in which the edge state is known to be dynamically unsteady and to test its chaoticity by using standard Lyapunov analysis, i.e. by computing its Lyapunov exponents $\lambda_1, \lambda_2, ..., \lambda_r$. Lyapunov exponents are defined as the infinite time limit of FTLEs defined earlier :

$$\lambda_i = \lim_{T\to\infty} (\lambda_{t_0}^{t_0+T})_i \tag{2.15}$$

independently of t_0.

The computation of the FTLEs is achieved using the side-computation of Optimally Time-Dependent (OTD) modes [91]. The flow case chosen for this demanding computation is the minimal flow unit of pPF in a computational domain with $L_x^+ \times L_z^+ = 200 \times 100$ [135–137] illustrated in figure 2.20. The mass flux is kept constant and the centerline Reynolds number for the laminar flow is $Re_{cl} = 7,200$ corresponding to $Re_\tau = 120$. This computation required at least $80,000$ outer time units of edge tracking for the convergence of the $r = 40$ first exponents. The spectrum is shown in figure 2.21(left). There are at least 6 exponents that are strictly positive, which validates the former hypothesis that the edge state is chaotic. More can be deduced from this computation : one exponent dominates the spectrum whereas all other exponents (including the negative ones) form a continuum. It is interesting to compare this spectrum to the Lyapunov spectrum corresponding to the turbulent regime of channel flow, as computed in Ref. [138] in a comparable computational domain and comparable Reynolds number Re_τ of 80 (although with a less good numerical resolution). There the exponents formed one continuum without any dominant value. The number of positive exponents was also reported to be 166, a number expected to rise for higher Re_τ and better resolution. We now turn our attention to the dimension of the underlying attractor, defined according to the Kaplan-Yorke conjecture [139] by

$$D_{KY} = j + \frac{1}{\lambda_{j+1}} \sum_{i=1}^{j} \lambda_k \tag{2.16}$$

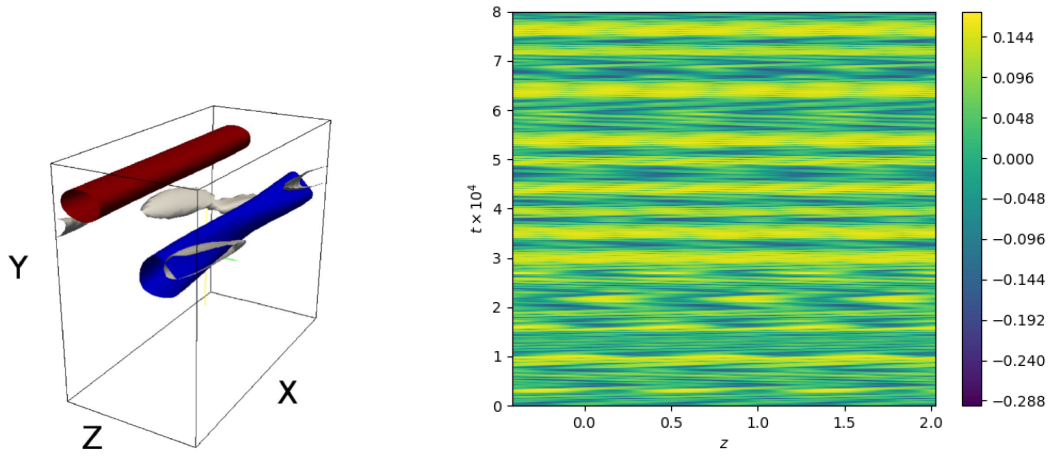

FIGURE 2.20 – Edge state in minimal flow unit pPf for $Re_\tau = 100$. Left : 3D snapshot of isolevels of streamwise velocity perturbation. Right : space-time diagram [137] of $< u >_x (y = -0.5, z, t)$ (three copies concatenated together).

where

$$\sum_{i=1}^{j} \lambda_k \geq 0$$

and

$$\sum_{i=1}^{j+1} \lambda_k < 0,$$

The computation of D_{KY} for the edge state at $Re_{cl} = 7,200$ suggests $D_{KY} \approx 22.5 \pm 0.1$ as can be deduced from the change of sign of $\lambda_1 + ... + \lambda_k$ in figure 2.21 (right). As with all strange attractors that number is non-integer. For the turbulent case, the corresponding Kaplan-Yorke dimension is close to 360 [138], a number likely to increase with a higher computational resolution.

Conditions for turbulence to be transient

One interesting trend appeared during the investigation of this edge state. As previously mentioned, it is customary to define the computational domain in outer units whereas the original study of Jiménez and Moin [28] originally considered a scaling in inner units, making the box size in outer units Re-dependent. In the investigation of [137] different box sizes were tested in inner units, most of them slightly smaller than in Ref. [28], for instance $L_x^+ = 200$ instead of 300. One of the consequences was that the turbulence turned transient no matter how high the value of Re_τ (as far as 180). This suggests that, unlike speculated in early works, the finite lifetime is not only a trivial consequence of low Reynolds numbers. For periodic domains defined in inner units, the finiteness of the lifetimes becomes apparent when the domain size $L^+ = L \times Re_\tau$ itself becomes small enough once measured in outer units. This suggests that the transient character of these turbulent flows is linked, consistently with the $2h \approx 100\delta_\nu$ concept [9, 10], to the confinement by the domain size. In other words, *turbulence in periodic domains is transient when the dynamics is spatially correlated.* This is perfectly consistent with the common observation that, at fixed domain size, turbulence relaminarises only at low enough Re. Since full spatial correlation is the property that justifies the dynamical systems approach at odds with genuine spatio-temporal turbulent flows, one is left wondering how much the transiency phenomenon (at least in MFUs) is a consequence of the periodic domains only. Note a similar dilemma in the case where turbulence takes place in a triply periodic domain too [140]. All these results suggest to investigate the transiency phenomenon in the

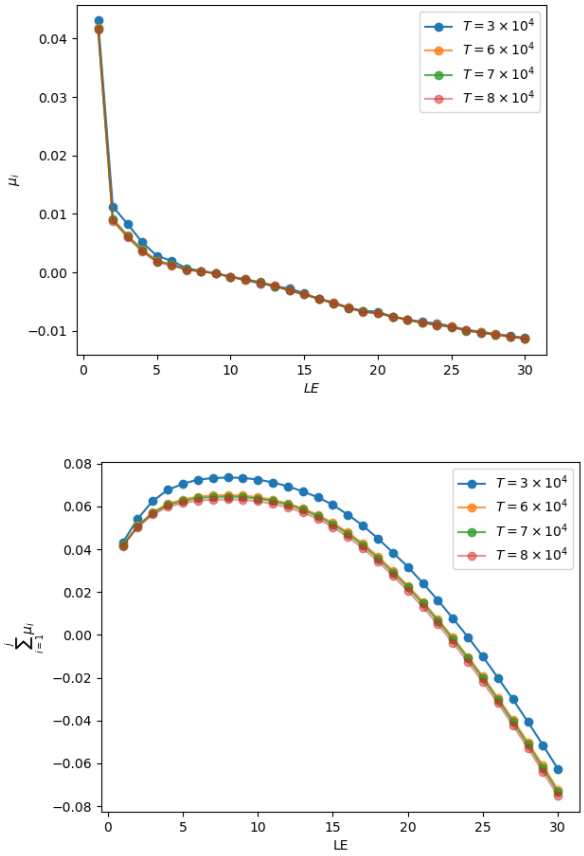

FIGURE 2.21 – Left : Lyapunov spectrum $\{\mu_i\}_i$ for minimal flow unit pPf for $Re_{cl} = 7,200$. Right : sum of Lyapunov exponents $\sum_{i=1}^{k} \mu_i$ versus k.

absence of finite-size effects.

2.3 Minimal states

2.3.1 Theoretical concept and limitations

The relative attractor on the edge manifold Σ is not the only place of interest in the state space. Geometrically speaking, it is interesting to investigate how close Σ gets to the laminar attractor. This supposes the choice of metric, usually related to the energy norm, such that the problem amounts to finding

$$argmin\{|\boldsymbol{x}|, \boldsymbol{x} \in \mathcal{B}_T\}, \tag{2.17}$$

where $\mathcal{B}_T$ is the basin of attraction of the laminar state. In the toy problem suggested by Dauchot and Manneville in figure 2.1, the point M closest to the laminar fixed point is represented, using a green diamond, as the tangency point between Σ and the smallest ball centered on the laminar state that touches Σ [141]. M differs from the edge state and does not form an invariant set. The associated physical question concerns the critical perturbation energy i) below which no transition to turbulence is possible, and ii) above which transition is possible provided the right initial condition is chosen. A given perturbation is associated to this global minimum of the critical energy landscape. It is called the *minimal*

seed or equivalently the nonlinear optimal disturbance. It must by construction belong to Σ which is the boundary of $\mathcal{B}_T$, as a consequence of which it can not induce transition by itself : optimal transition requires in practice an infinitesimal perturbation of the minimal seed. A popular question in the 1990s was to identify how the energy of the minimal seed E_c scales with the Reynolds number. Experimental evidence suggests that the optimal threshold should decrease with Re, making transition for identical initial disturbances more likely at higher Re. Although simple dimensionless analysis suggests a scaling $E_c = O(Re^{-2})$ independently of the flow type [142], many studies including analytical ones suggested other power-law alternatives of the kind $E_c = O(Re^{-\gamma})$ with $\gamma > 1$ [143, 144]. Solving the optimisation problem 2.17 is a direct way to determine how the critical energy or other quantities depend on Re. Although the definition of the norm to be minimised is straighforward, one slightly more ambiguous issue is to define a quantitative scalar indicator of the transition phenomenon itself.

A simplified sketch of the state space is shown in figure 2.22, with an emphasis on the minimal seed M. The laminar state is the point O, the edge state is represented for simplicity as a saddle point S, and the turbulent attractor itself does not need to be represented explicitly. The case where turbulence is not an attractor has not been fully investigated as of now. We emphasize that, as for the whole dynamics picture, the concept of minimal seed is intrinsically linked to the framework of initial value problems. Determinining the minimal background disturbance likely to maintain non-laminar flow is another problem. Another possible issue, relevant to experiments where localised disturbances are considered, is to consider disturbances applied for a finite duration. This is again a different problem that would call for different mathematical approaches. We will detail below two numerical approaches to the initial value problem (2.17) and describe the transition path to turbulence starting from the neighnourhood of such initial conditions.

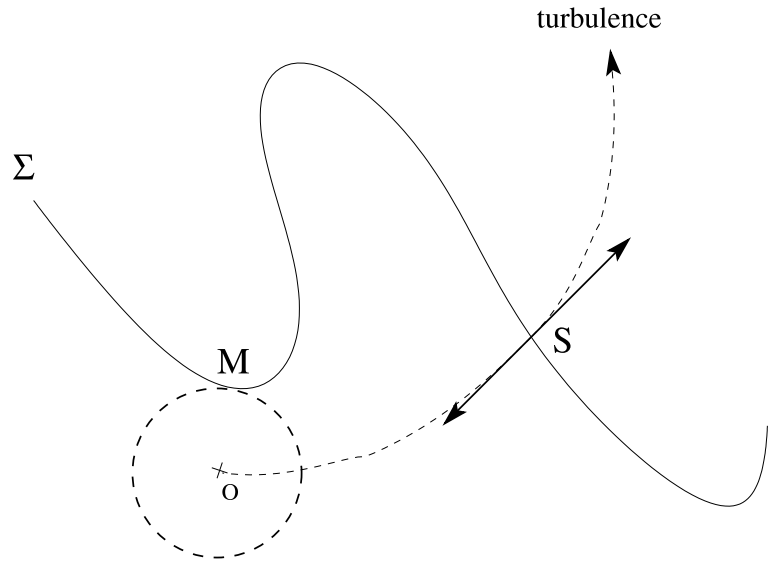

FIGURE 2.22 – Sketch of the state space with an underlying energy metrics, where O is the laminar state, S the edge state on the edge manifold Σ, and M the minimal seed.

2.3.2 Optimal oblique transition

During the 1990s and 2000s a large body of the numerical literature in shear flows dealt with the concept of linear optimal perturbations (LOP), those maximising the gain due to the linearised operator [18]. There is no direct theoretical link between LOPs and the minimal seed concept, a fully nonlinear concept. In particular LOPs can be computed in different specific subspaces corresponding to different symmetries, such as different wavenumbers, whereas the minimal seed is a global minimiser in state space.

However it is intuitively plausible that a transition path starting from the lowest possible amplitude would share features in common with the linear mechanisms, those commonly observed for low-amplitude (in theory infinitesimally low) disturbances. It was hence assumed for simplicity in [145] that the perturbation velocity field of the minimal seed $\boldsymbol{U}_{opt}$ could be decomposed as a sum of LOPs $\bar{\boldsymbol{U}}_i,\ i = 1, ..., m$, computed each for a different wavenumber :

$$\boldsymbol{U}_{opt} = \sum_{i=1}^{m} A_i \bar{\boldsymbol{U}}_i. \tag{2.18}$$

The norm to be minimised is the perturbation kinetic energy

$$||\boldsymbol{U}_{opt}|| = (\frac{1}{vol(V)} \int_V |\boldsymbol{U}_{opt}|^2 dV)^{\frac{1}{2}}, \tag{2.19}$$

where V denotes both the computational domain and $vol(V)$ its three-dimensional volume. A scalar measure of transition remains to be defined. The main idea here exploits the sketch of fig. 2.22 : a perturbation in the neighbourhood of Σ must, if it leads to transition, approach the edge state S, which has a well-defined energy E_S. Minimising the energy of $\boldsymbol{U}_{opt}$ is hence equivalent to maximising the ratio E_S/E_c i.e. the energy gain. This leads in the space of the $\{A_i\}$ to an minimisation of the energy needed to reach, not the turbulent attractor, but the edge state S. This is a much better defined optimisation problem, since the critical energy to reach the edge state is precisely a byproduct of the classical bisection process. For m given, we can indeed define formally the mapping $(A_1, ..., A_m) \rightarrow E_c(A_1, ..., A_m)$. In this definition, E_c is the perturbation kinetic energy of the state obtained by rescaling $\sum A_i \bar{\boldsymbol{U}}_i$ using the classical bisection algorithm. A simple m-dimensional Newton solver is then used to make $\nabla_i E_c$ vanish, i.e. to find the explicit minima of the mapping $\{A_i\}_i \rightarrow E_c$. Note that this is a fully nonlinear approach even if LOPs are involved, and the equations used in the optimisation are the fully nonlinear ones. The finiteness of m (m=2 or 3 in practice) makes it only a low-price reduced approach, yet. Since LOPs are not localised in physical space, a short summation of them shares similar properties. This implies that only non-localised minimal seeds can be sought using this method, therefore the approach is restrained to minimal flow units only.

The optimal condition found in plane Couette flow for $m = 2$ is found to feature the modes $(1, 1)$ and $(1, -1)$ with equal amplitude. This result holds for all computational domains and Reynolds numbers tested. This is exactly the *oblique wave* identified earlier in Ref. [146]. This perturbation used nonlinear interactions to generate a mode $(2, 0)$ as well as $(0, 2)$. The optimal mode with $(k_x, k_z) \sim (0, 2)$ corresponds to a pair of streamwise vortices, known to be associated with a strong linear gain via the lift-up effect. This alone justifies that the oblique wave transition path is an efficient one in terms of energy gain. The present results complement this intuition by proving that this path is in fact *nonlinearly optimal*, at least for $m = 2$. The threshold energy of the oblique waves is shown in figure 2.23 as a function of Re. The exponent γ resulting from the optimisation is $\gamma = 2$. This result corrects in passing the numerical evaluation $\gamma = 2.5$ from [147], the mismatch being attributed to different numerical resolutions.

The flow field resulting from the optimisation with $m = 3$ -based on the LOPs associated with wavevectors $(1, 1)$, $(1, -1)$ and $(1, 2)$ - is displayed in figure 2.24. Its structure is itself very similar to the oblique wave identified for $m = 2$, and its perturbation energy is only 1% less than E_c found for $m = 2$. The corresponding transition scenario is shown in figure 2.25 as a sequence of three-dimensional plots of the wall-normal velocity field. The initial condition corresponding to $\boldsymbol{U}_{opt}$ magnified in amplitude by a factor $(1 + \tilde{\varepsilon})$, with $\tilde{\varepsilon}$ smaller than 10^{-4}. The different phases of the transition process unfold as follows. From $t = 0$ to $t = 10$, the oblique wave pattern gets strongly distorted by the shear. It turns rapidly from an initially upward-tilted shape to a downward-tilted one, as an illustration of the linear Orr mechanism in shear flows [18]. This is associated with the transient growth of the oblique modes. After $t = 10$, the structures elongate in the downstream direction and the disturbance is dominated from $t = 20$ on by streamwise vortices with a small but noticeable streamwise undulation. After $t = 40$, the dynamics slows down dramatically and the spatial structure of the perturbation hardly changes until $t = 220$, as an unstable steady state solution located on the edge is being transiently approached. The duration of

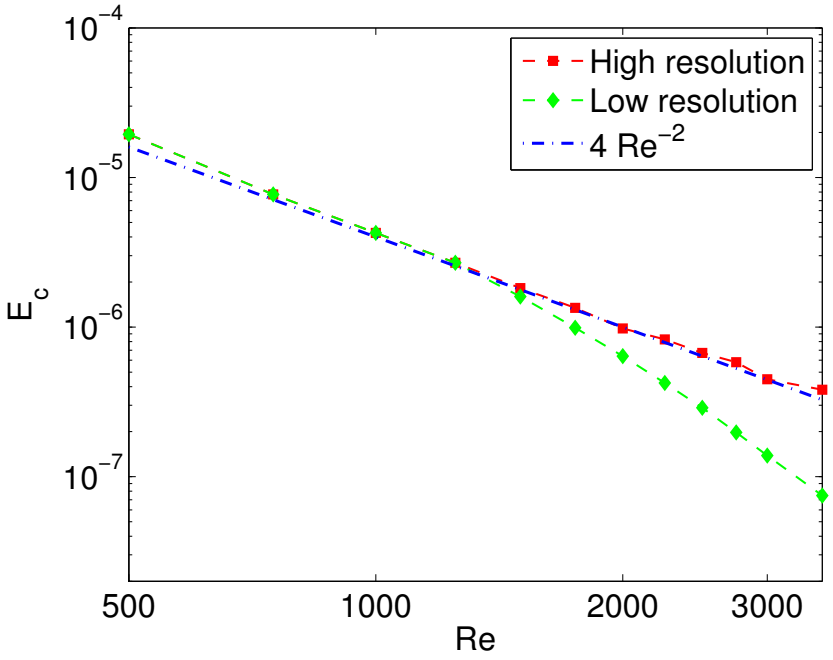

FIGURE 2.23 – Threshold energy E_c for the oblique scenario ($m = 2$) as a function of the Reynolds number Re, for a computational domain of size $L_x = 4\pi$, $L_z = 2\pi$. The results obtained using low numerical resolution, similar to Ref. [147] (green line), are compared to well-resolved simulations where the number of grid points increases with Re (red line). The latter is well approximated by the function $4Re^{-2}$.

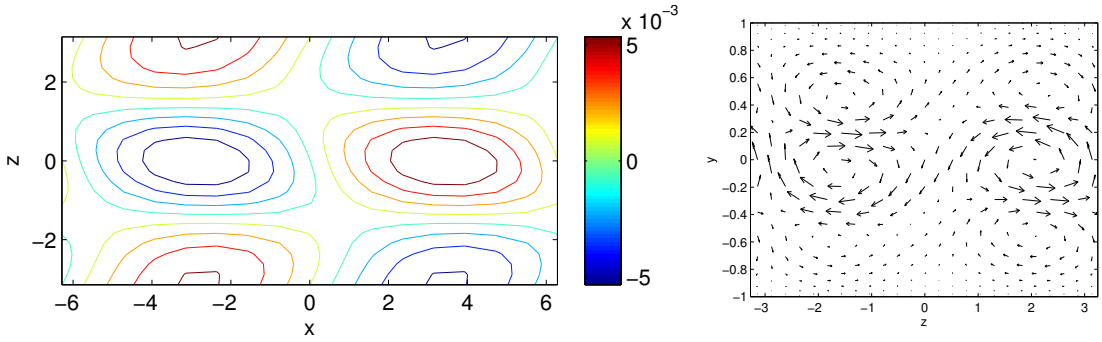

FIGURE 2.24 – (Color online) Initial condition of minimal energy leading to turbulence for $m = 3$. The state is the superposition of three linearly optimal modes with wavenumber $(k_x, k_z) = (1, \pm 1)$ and $(1, 2)$, where the complex amplitudes are determined by the optimisation procedure. Streamwise velocity in the mid-plane $y = 0$ (left), cross-stream velocity field in a section $x = 0$ (right).

the transient approach increases with decreasing $\hat{\varepsilon}$. Near $t \approx 240$, the low-speed streaks start to distort and the velocity field becomes rapidly unsteady. By $t \approx 270$ it has all the qualitative features of the turbulent flow reached at $Re = 400$ from other initial disturbances : elongated streamwise structures, stronger velocity fluctuations, stronger unsteadiness.

2.3.3 Variational technique

The former approach is difficultly exploitable with higher values of m. A natural alternative is to perform a more classical nonlinear adjoint optimisation, yet in the full state space of dimension $n \gg m$,

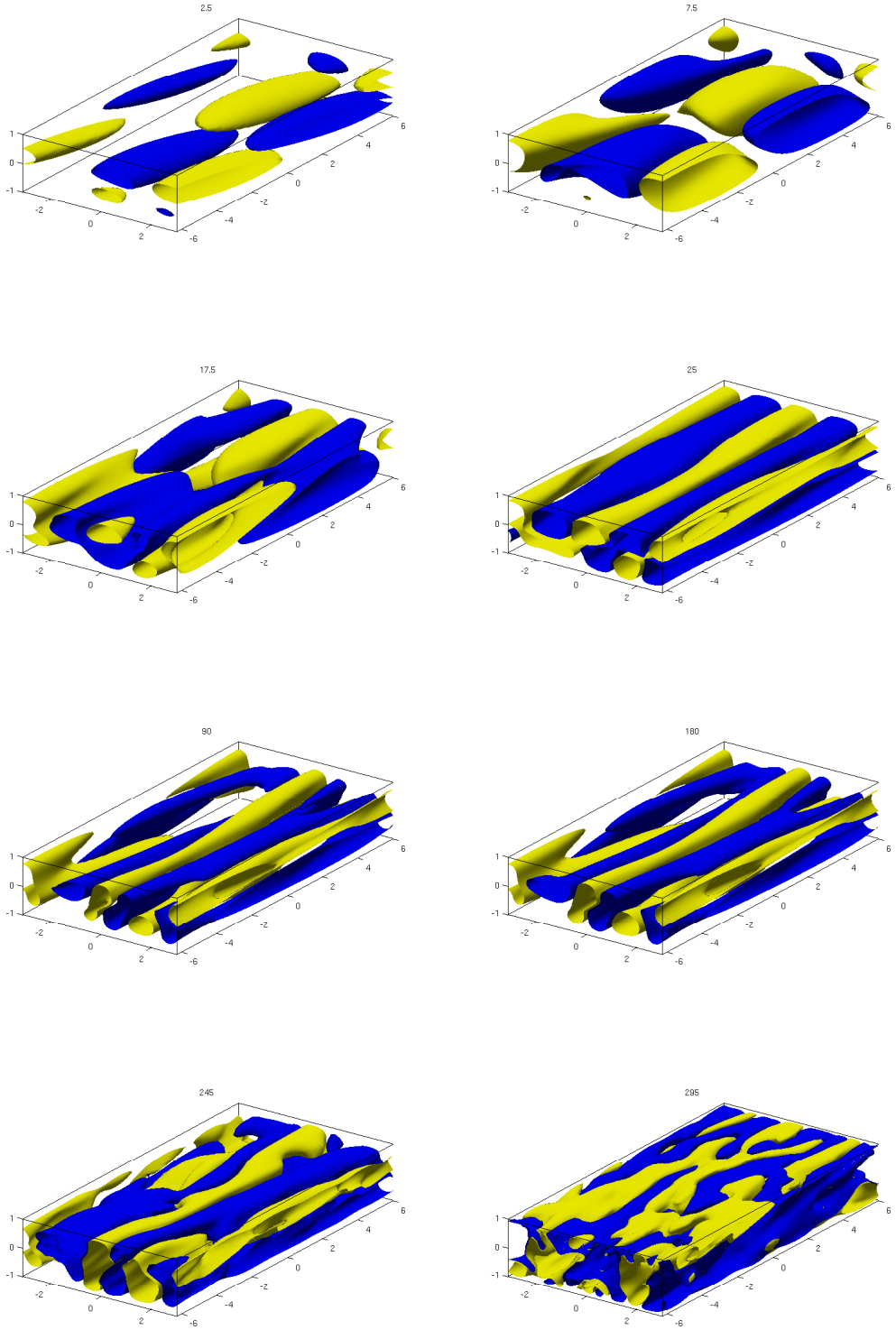

FIGURE 2.25 – Three-dimensional view of the time evolution of the wall-normal velocity, $v = \pm 4 \times 10^{-3}$, along the trajectory T_{opt} initiated by the minimal perturbation M with amplitude $(1+\hat{\varepsilon})$ (see text). From top to bottom and from left to right, $t = 2.5,\ 7.5,\ 17.5,\ 25,\ 90,\ 180,\ 245,\ 295$.

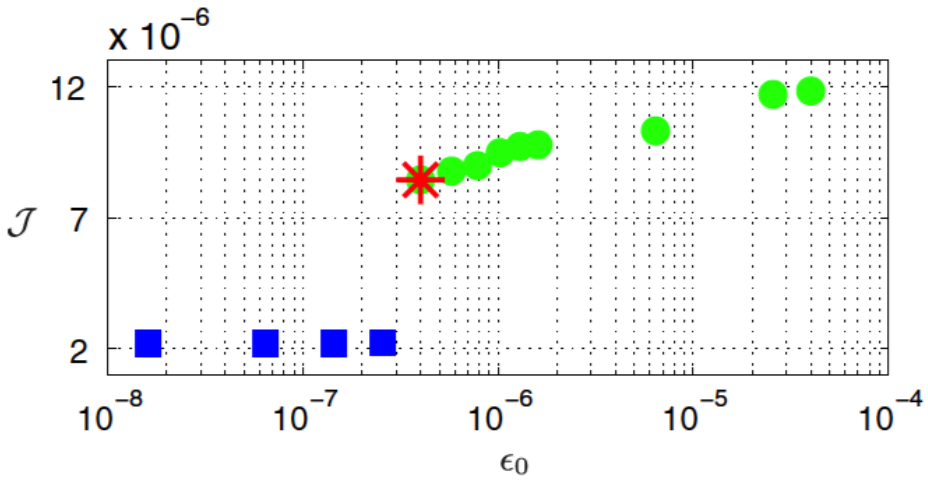

FIGURE 2.26 – Optimised objective function versus intial energy ϵ_0. from Monokrous *et* al. [148]. The energy is found using classical bisection. Blue : relaminarising cases, green : transitioning cases.The minmal energy threshold corresponds to the red star.

with n of order 10^6. Adjoint optimisation is an iterative process that requires the differentiation of a scalar Lagrangian function with respect to all the variables of the problem. It turns out that the the mapping E_c used in Ref. [145] is not straightforward to differentiate, therefore other indicators of the transition must be chosen. A standard choice used in all works by R.R. Kerswell, S. Cherubini and co-authors relies on the energy gain G, making nonlinear optimals genuine nonlinear generalisations of the linear concept of the LOPs. In the work carried out in Refs [148] and [149], the integral viscous dissipation was preferred, defined by :

$$\mathcal{D} = 1 + \frac{1}{Re}\frac{1}{2L_xL_z}\int_V \frac{\partial u_i}{\partial x_j}\frac{\partial u_i}{\partial x_j}dxdydz, \tag{2.20}$$

where u still denotes the perturbation velocity field. The objective function maximised by the constrained optimisation algorithm is the total time-averaged dissipation

$$\mathcal{J} = \frac{1}{T}\int_0^T \mathcal{D}(t)dt. \tag{2.21}$$

A trajectory reaching the turbulent state at finite time T is expected to display a value of $\mathcal{J}$ larger than for a laminarising trajectory. The main advantage of $\mathcal{J}$ over the energy gain G is that $\mathcal{J}$ contains an average contribution of positive $D(t)$ at all times, and saturates for large T in a monotonous way. In contrast to $G(t)$, it neither undergoes rapid variations nor pronounced overshoots when approaching the edge. Besides, maximising $\mathcal{J}$ amounts to maximising the area between 0 and $D(t) > 0$ in the interval $[0 : T]$. This implies for $\epsilon_0 > E_c$ that the algorithm seeks the trajectory reaching high dissipation in the *fastest* way. It was verified visually in [150] that the optimisation does not appear to depend on the choice of functional.

The optimisation algorithm relies on two steps : first an energy shell characterised by E_0>0 is selected, on which the adjoint optimisation is performed together with the additional constraint $E = \epsilon_0$ (for the definition of the energy used in Ref. [149] E does no feature the factor $1/vol(V)$ any longer). Then E_0 is varied (as in the bisection process yet with less accuracy) until the maximal value of $\mathcal{J}$ displays an change of trend, indicating that turbulence is no longer reached for ϵ_0 low enough, as in figure 2.26 from the actual data.

The adjoint optimisation algorithm can now be furtively described. It looks iteratively for stationary points of the Lagrange functional , where optimality is fulfilled with respect to the various design variables. The Lagrangian functional $\mathcal{L}$ is defined by

$$\mathcal{L}(\boldsymbol{X}) = \mathcal{J}(\tilde{\boldsymbol{u}}) - \ll \boldsymbol{v}, \partial_t \boldsymbol{u} - \boldsymbol{NS}(\boldsymbol{u}, p) \gg \\ - \ll q, \boldsymbol{\nabla} \cdot \boldsymbol{u} \gg - \lambda(\epsilon(\tilde{\boldsymbol{u}}) - \epsilon_0). \tag{2.22}$$

(the product $\ll \cdot, \cdot \gg$ denotes here the spatial scalar product $< \cdot, \cdot >$ together with time integration). The direct variables in the optimisation are contained in a large vector $\tilde{\boldsymbol{u}}$ containing the perturbation velocity field $\boldsymbol{u}(\boldsymbol{x}, t)$ and the pressure field $p(\boldsymbol{x}, t)$, and is considered in a suitable space of functions defined on $V \times [0 : T]$. The dynamical constraints to be satisfied include the governing equations and the energy shell constraint :

i) $\partial_t \boldsymbol{u} = \boldsymbol{NS}(\boldsymbol{u}, p)$ at all times (the momentum equation)

ii) $\boldsymbol{\nabla} \cdot \boldsymbol{u} = 0$ at all times (the incompressibility equation),

iii) $E = \epsilon_0$ at $t = 0$ (the energy shell constraint).

Differentiating $\mathcal{L}$ with respect to the adjoint variables $\boldsymbol{v}$, q and λ leads to the above constraints. Differentiating $\mathcal{L}$ leads however to a new set of equations. It includes the adjoint Navier–Stokes equations that are linear in $\boldsymbol{v}$ and need to be integrated backwards in time, as well as compatibility conditions to close the loop. The algorithm is convergent for a given value of ϵ_0.

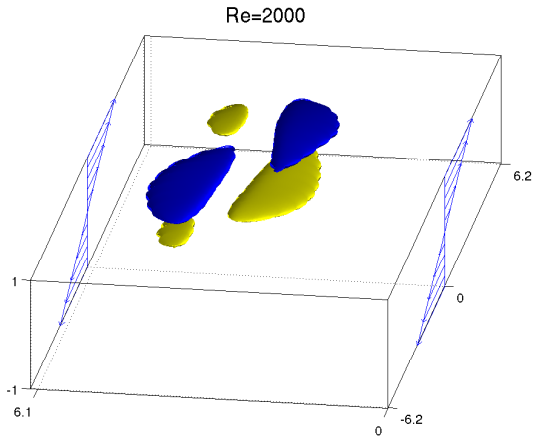

FIGURE 2.27 – Minimal seed for plane Couette flow at $Re = 2000$. Iso-levels of streamwise perturbation velocity. The laminar base flow profile is sketched for visual guidance.

The minimal seed M obtained in pCf for $Re = 2000$ is displayed in figure 2.27. The checkerboard structure typical of oblique waves can be recognised, again with a non-perfect symmetry. However it is now localised spatially and surrounded by laminar flow. It is indeed intuitive that, since energy is now an extensive quantity, a localised velocity field represents a better candidate than a non-localised one for an "efficient" transition process. The optimal transition path starting from a small neighbourhood of M is now displayed in figure 2.28, again by using a sequence of still visualisations of the perturbation velocity field in a plane $y = -0.5$. The early times prior to $t = 80$ feature evidence for the Orr mechanism but are not analysed here. Between $t = 80$ and $t \approx 138$ a sinuous streaky structure is transiently visited, identified

with the edge state (S in the sketch of figure 2.22). A rapid instability of the streaks manifests itself in the form of intense small-scale wall-normal motions at the tips of the streaks. Their breakdown produces even smaller-scale turbulent fluctuations that form a front aligned with the streamwise direction. The front moves in the spanwise direction until the whole flow becomes and remains turbulent.

2.3.4 Dependence on Re

The dependence of the threshold energy E_c versus Re is displayed in figure 2.29. The emerging power-law scaling has an exponent of $\gamma \approx 2.6$, larger than the exponent $\gamma = 2$ obtained for oblique waves. It is tempting to interpret this steeper exponent as the same exponent as for oblique waves, with a Re-dependent correction associated with a spatial localisation that gets more pronounced as Re is increased. This requires however a deeper study involving most likely larger computational domains. The present results highlight the importance of large computational domains in the presence of spatially localised dynamics. It features in passing evidence that the edge state, which is dynamically visited along the optimal transition path, displays itself spatial localisation. The localisation of edge states forms the subject of the next section.

2.4 Spatial localisation of edge states

2.4.1 Motivation

There are two main reasons to revisit all the previous theory of edge states in the absence of finite-size effects. The first one is unphysical : it is the limitation inherent to the choice of periodic computational domains. Many of the bifurcations occuring with respect to the computational box size, or the Reynolds number, appear as a by-product of the periodic boundary conditions chosen... even though the governing equations are the true ones from hydrodynamics. The second reason is simply the experimental evidence that, in a given range of Reynolds numbers, the coherent structures of the turbulent regime are indeed found to be spatially localised. For instance pipe flow features localised puffs [151] as the only possible turbulent state when $1800 \leq Re \leq 2500$ approximately. It makes sense to expect the liminal perturbations leading to puffs to be also spatially localised. An auxiliary motivation is that experimentalists can be tempted to excite the flow in a localised fashion ; even if no localised turbulent structure sustains forever in the regime of interest, the transition from localised to delocalised features coherent structures characterised by laminar-turbulent interfaces. All these reasons have pushed researchers in subcritical transition to favour larger computational domains (without necessary changing numerical method) in an effort to reduce the impact of the periodic boundary conditions. As often, this conceptual progress has been made possible by some technical progress, notably the ever-increasing computational power, and notably by the development and spreading of parallelisation techniques (MPI). Performing edge tracking in larger domains is only a matter of computing power. The characteristics of the edge tracking algorithm(s) remain unchanged, and there is no strong reason to consider other observables for the bisection process. However, we stress that choosing an extensive quantity (e.g. perturbation kinetic energy or cross-flow energy) is a wiser choice than an intensive one, at least if domain changes are to be carried out. For the classical bisection described earlier, the choice of the bounds a_L and a_T can reveal practically crucial because of the more costly simulations.

To our knowledge the first localised edge states have been computed in pipe flow and shown at the Newton Institute in September 2008 by three different teams, Marburg together with Barcelona [152] at the same time as the team in Bristol [153]. The discovery was quickly extended to pCf [154–158] and later to other flows. The conclusion from *all* edge tracking computations so far is deceptively simple : edge states appear localised in each direction provided there is enough space for localisation to proceed, with no exception. Importantly for what follows, the choice for longer computational domains only makes spatial localisation possible, but it does not imply it from first principles : the physical reason why a

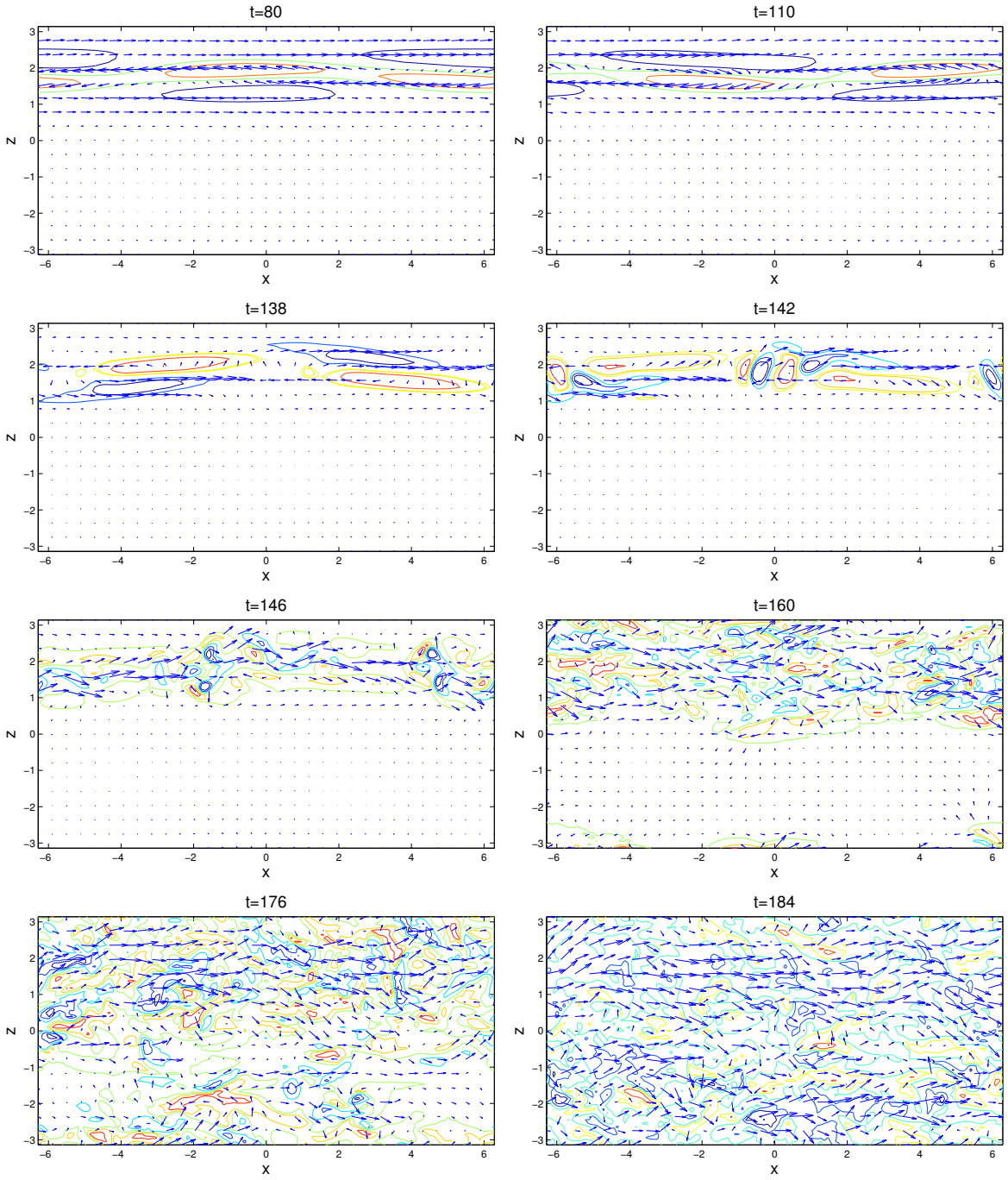

FIGURE 2.28 – Velocity field in the plane p_y : $y = -0.5$. u_y : colours, (u_x, u_z) : arrows. Iso-contours of u_y normalised by their maximum, where $\max u_y = 0.0055$ (t=80), 0.0117 (t=110), 0.052 (t=138), 0.1023 (t=142), 0.2329 (t=146), 0.3333 (t=160), 0.3273 (t=176), 0.5473 (t=184).

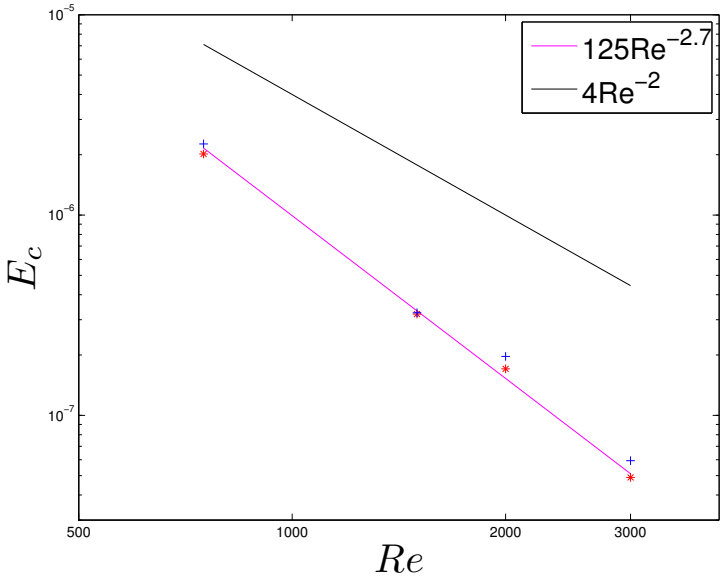

FIGURE 2.29 – Energy threshold E_c vs. Re for $Re = 750, 1500, 2000, 3000$. The fit $125Re^{-2.7}$ is compared to the fit $4Re^{-2}$ obtained for the Oblique Wave scenario for the same computational box (data from Duguet, Brandt & Larsson (2010)).

given flow state "prefers" to be localised requires a deeper explanation that is still pending and will be discussed in the conclusions. A few representative examples will be considered below, together with a description of the associated dynamics, in order both of increasing localisation and complex dynamics.

2.4.2 One-dimensional localisation

Striped edge state in channel flow

We begin with the localised edge state which, although not historically first, hosts the simplest dynamics. It was found and reported recently in three-dimensional computational domains of plane channel flow with extension in one direction only. The computational domain is a paralleloid, however it is not trivially aligned with the usual x and z directions of the flow (denoted x' and z' in the pedagogical sketch of figure 2.30). Instead it makes an angle θ with the streamwise direction. This "tilted domain" was first suggested by Tuckerman & Barkley [159] in order to reproduce numerically, at a cheaper price, the oblique laminar-turbulent patterns found in experiments of pCf. It was described initially as an extended MFU domain, the extension being along one dimension only [159]. It was later generalised without difficulty to simulations of Taylor–Couette flows and plane Poiseuille flows, both known to host oblique turbulent stripes in well-tuned parameter ranges [160–162]. The classical bisection algorithm has been run using the channelflow code [163] with the total perturbation energy as the extensive observable and a well-chosen pair of bounds. The algorithm converged easily towards a constant energy signal, which is the signature of a TW solution and is displayed in figure 2.31. This TW was converged down to accuracy $r_{min} < 10^{-12}$ using the Newton solver included in the *channelflow* code.

The spatial structure of the solution, shown in figure 2.32a for $\theta = 45°$ and $Re = 720$ is the first property of interest. There is an active core characterised by vortices and streaks. They are approximately aligned with the physical streamwise direction although a small tilt angle is perceptible. Outside this zone the flow is streak-free and almost laminar except for the presence of a smooth secondary flow reconnecting with the laminar flow far enough from the active core. The robustness of the spatial localisation with respect to an increase in domain size has been tested in figure 2.32b by comparing different

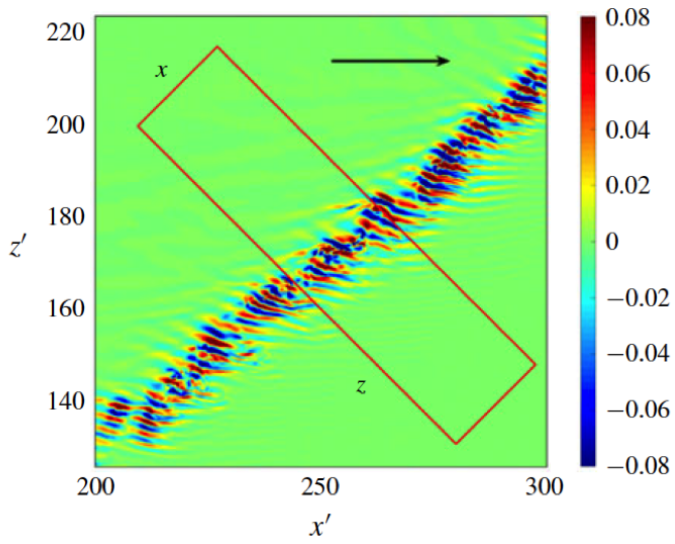

FIGURE 2.30 – Sketch of tilted periodic domain for pPf.

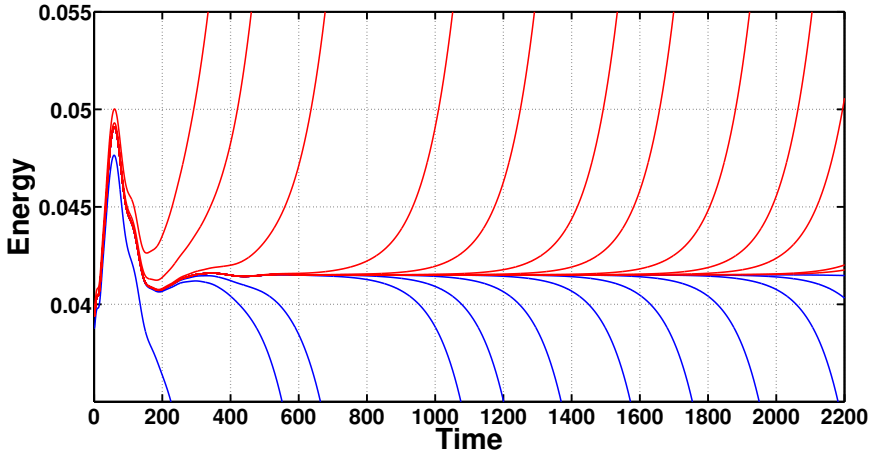

FIGURE 2.31 – bisection Energy $Re = 720$, domain $= 40h \times 2h \times 10h$.

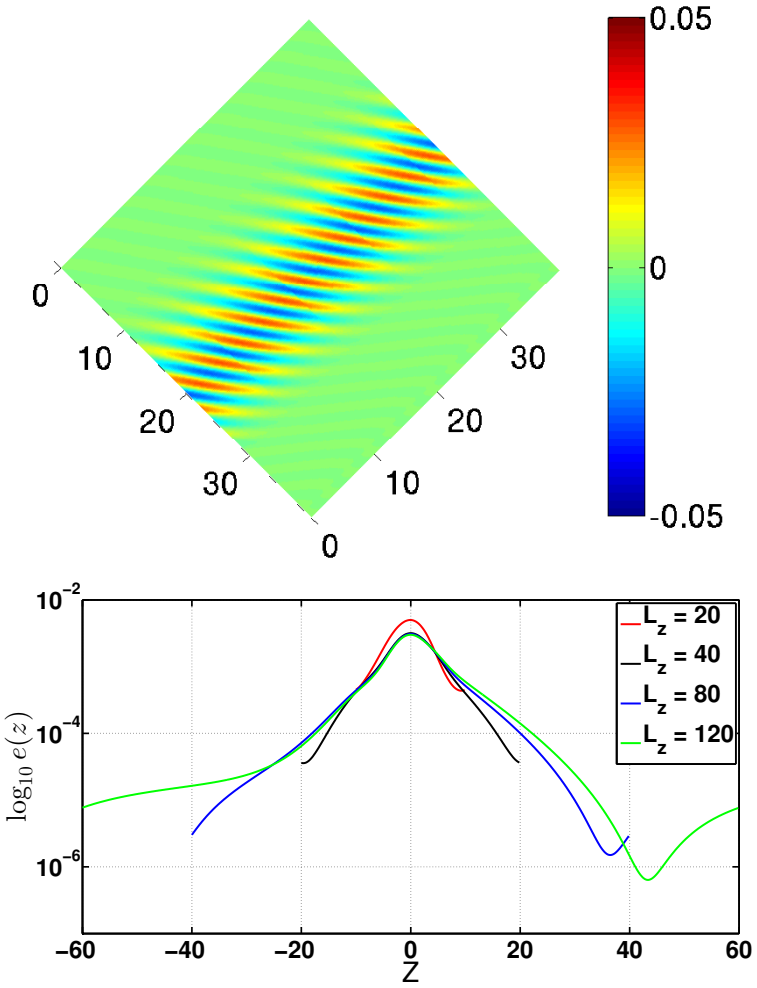

FIGURE 2.32 – a) Edge state (several wavelengths concatenated b) Energy $e(z)$ for an edge state $Re = 720$ for increasing domain sizes. Localisation appears as a robust feature of edge states in large enough domains.

converged states, computed for different values of the long domain direction L_z, whereas L_x has been fixed to various values between 2 and 10. Here as in all other shear flows investigated, localisation turns out robust. The tails of the velocity field are exponential for all components, a result also found valid in the corresponding localised turbulent regimes [162]. There is another robust feature that distinguishes however these localised edge states from their turbulent counterparts : localisation of edge states is valid for all values of Re whereas the turbulent states are only localised in a finite range of Re, bounded by Re_{cl} approximately 2000 in the case of pPf [161].

Another recent discovery worth a deeper investigation concerns the relevance of Waleffe's SSP to the present exact states. For small computational domains it is an undisputed fact that Waleffe's SSP rules out the dynamics and structures of all exact states [33, 135]. This is justified by the fact that the SSP itself was deduced from the detailed analysis of the turbulent dynamics in MFUs. As spatial localisation is added to the picture, the interaction between streaks, rolls and waves predicted theoretically happens to be violated : as seen in figure 2.32a, the streaks in the active part do not display the streamwise undulations characteristic of the SSP. They are however not streamwise-independent either since both streak tips upstream and downstream feature some light tilting (related to the presence of a large-scale

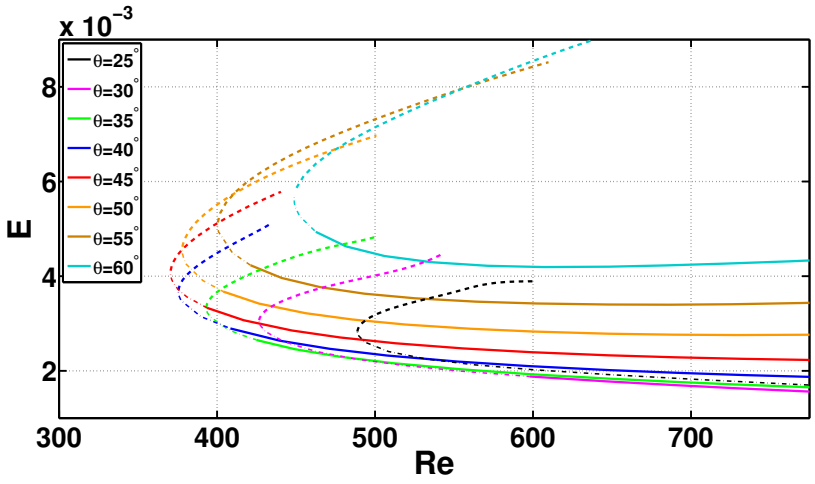

FIGURE 2.33 – Bifurcation of TWs as function of Re for different angles.

flow [130]. It is plausible that the feedback of the streak on the streamwise vorticity, the darkest phase in Waleffe's picture, is modified in the presence of localisation and does not even feature the streak instability phase that precedes it. As a supplementary element for discussion, we can mention that other steady localised solutions with the oblique property have been recently identified in pCf [164]. They are not edge states and emerge from modulational instabilities of MFU states. These other new solutions, unlike the edge states of pPF, do feature streamwise undulations. It is then an open question how many variants of the SSP can exist in the presence of localisation, and what the implications are as far the relevance of these solutions to transition is concerned.

Similar TWs have been converged for other values of the angle θ. The range of values of θ for which TWs have been found widens with increasing Re. Arclength continuation has been applied to the TWs obtained for all angles, starting from initial states obtained for $Re = 720$. The structure of the bifurcation diagram for the TWs is shown in figure 2.33. It is confirmed that for a fixed value of L_x, all TWs emerge in saddle-node bifurcations at marginally low values of Re. The value Re_{SN} of the lowest saddle-node bifurcation is less than 400, well below the value of 660 where turbulence can no longer sustain in such computational domains as well as in experiments [161, 165]. Among the many TW solutions ever identified in MFUs of pPf, these are the ones appearing at the lowest values of Re We understand that, unless new solutions are found at even lower Re, the state space of plane Poiseuille restricts to the laminar basin for $Re < Re_{SN}$, and gets populated by more and more different unstable TW solutions as Re increases beyond Re_{SN}. These solutions, together with a myriad of RPO states bifurcating from them [130], are understood to form the backbone of a chaotic saddle, with a real attractor forming only beyond $Re \geq 660$.

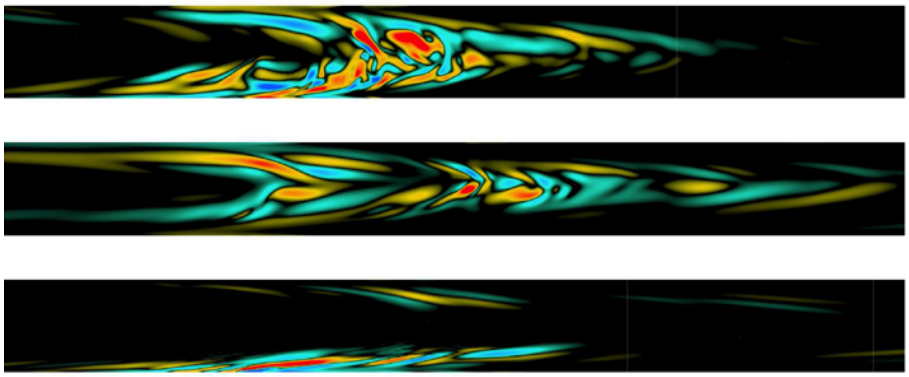

FIGURE 2.34 – Instantaneous meridian cuts of the axial perturbation vorticity field for edge states of pipe flow for Re=2000,3000 and 6000 (from top to bottom). The axial dimension has been scaled by a factor of two and only $25D$ of the total domain is shown.

Localised edge state in pipe flow

Localised edge state in pipe flow were computed initially in Refs [152] and [153] without any imposed discrete symmetry. The bisection method in each study is strictly similar to the one used in the corresponding non-localised case. Only the streamwise length of the computational domain was increased, from e.g. $5D$ in Refs [105, 106] to $33.51D$ and 50 to $100D$ in Refs [152] and [153], respectively. The results mimic those from the preceding plane Poiseuille case : whatever the value of Re investigated, the edge state identified is localised axially. For the values of Re in the transitional range, where turbulent puffs are found ($1800 < Re < 2500$ approximately), the edge state ressembles its turbulent counterpart, as shown in figure 2.34(top) for $Re = 2000$. As Re is increased beyond that range, the edge state stays axially localised and starts to localise also within the cross-section. As is most evident for $Re = 6000$, ultimately the edge state is best described solely as a finite-amplitude *near-wall disturbance* without any need to be related to the turbulent puffs of the transitional range. A crucial difference with plane Poiseuille lies however in the temporal dynamics : all signals suggest chaotic dynamics. In a direct analogy with the shorter domains of pipe flow [106], an attempt to stabilise the dynamics by imposing a discrete symmetry $\mathcal{R}_3$ was performed in Ref. [153] : the dynamics of the energetic observable stayed erratic as long as the edge state could be tracked. Fortunately, this attempt was ignored by Avila *et* al. who, unaware of this lack of success, tried to impose a discrete $\mathcal{R}_2$ and observed convergence to a localised RPO state [128]. This state is quantitatively very similar to a TW, except for a temporal modulation of very small amplitude, observable at the downstream tip only [11, 166]. Note that a similar state has been also observed in a low-resolution bisection in Ref. [153] and initially interpreted as a TW. This state is displayed at the bottom in figure 2.35a using isolevels of streamwise velocity perturbation, compared to its corresponding upper-branch state and to a non-symmetric turbulent puff. Several studies of this RPO state are worth mentioning at this point. The first one is related to the origin of the localisation property : a path in parameter space was found, from the point of view of bifurcations, that relates the non-localised travelling waves of former studies to the present RPO state [167]. As far as we know no localised TW has been found in pipe flow. The second set of results concerns the emergence of complex behaviour in pipe flow [128, 168]. The scenario for the onset of chaos in pipe flow (all in the context of the imposed $\mathcal{R}_2$ symmetry) follows a route slightly different from the usual cascade of bifurcations leading from the base flow to the turbulent state. Here the story unfolds not from the base flow, which is linearly stable, but from the RPO-branch of the edge state. Following down this branch in Re leads classically to a saddle-node bifurcation at $Re = Re_{SN} \approx 1428$. After the fold, increasing Re leads now to a cascade of supercritical bifurcations from the upper-branch state, also found in the non-localised cases of Refs. [169] and [170]. The type of cascade seems to depend on the details of the flow case, e.g. torus breakdown in pipe [128] versus period doubling in [169]. The chaotic attractor born at $Re \approx 1540$ is not the end of the story as in the typical Ruelle–Takens scenarios from textbooks. The chaotic attractor grows in size

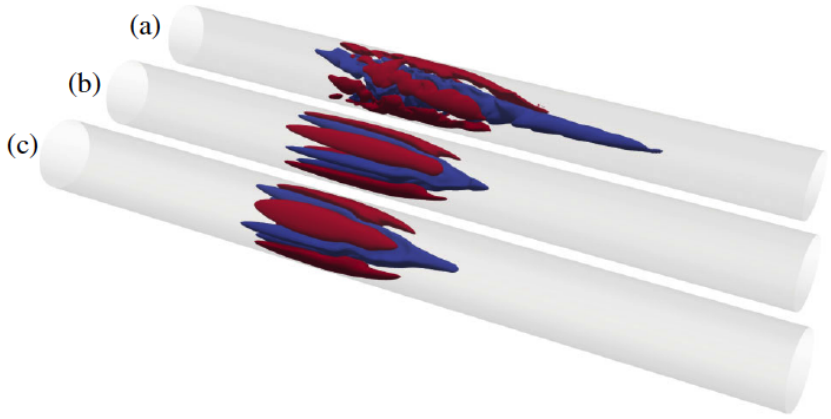

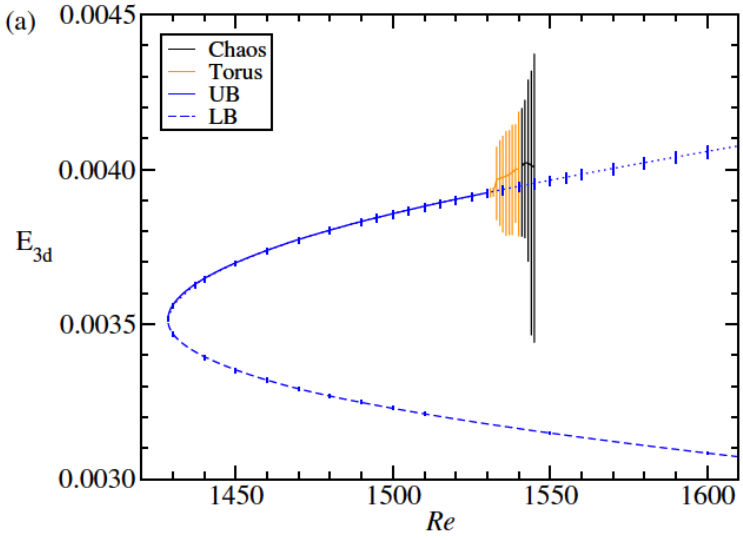

FIGURE 2.35 – a) from top to bottom : turbulent state (puff), upper-branch and lower-branch RPOs for pipe flow at Re= (iso-levels of streamwise velocity perturbation. b) bifurcation diagram for the RPO branch.

until it touches the stable manifold of the edge state, i.e. the edge manifold. At this point located at $Re = Re_{bc} \approx 1545 \pm 1$ a boundary crisis occurs : the attractor turns into a saddle and lifetimes become finite. Close to the boudary crisis the mean lifetimes scale as $(Re - Re_{bc})^{-1}$ and decrease with increasing Re, before they grow again for yet higher Re [171]. The rest of the story requires even larger domains and will be detailed in the next chapter.

Summing up the pipe flow case, the edge state is again robustly localised yet with a more complex dynamics. As with smaller computational domains the edge dynamics is still of relatively low dimension, so low that a well-chosen restriction to a symmetry subspace (via the imposition of a discrete symmetry) is enough to stabilise a simple RPO state as the edge state. Again in a perfect analogy with smaller domains, a detailed bifurcation study of the RPO state (technically unfeasible as such starting from a chaotic state) reveals the dynamical origin of the chaotic behaviour of the corresponding turbulent state. Assuming that the localisation of the edge state is understood (e.g. via the amplitude modulation suggested in Ref. [167]), this justifies directly the localisation of the turbulent puffs. Besides, the transient chaos so often celebrated in pipe flow finds its origin in a boundary crisis of the upper branch state. Such a scenario starts again with the knowledge of an edge state and relies on the luck of identifying a simple tractable edge state of TW or RPO type.

Localised edge states in ASBL

The third flow case considered here is the Asymptotic Suction Boundary Layer (ASBL) flow. As for plane Couette or plane Poiseuille flow, the simulation of ASBL in periodic domains requires the knowledge of two numerical parameters L_x and L_z, the streamwise and spanwise wavelengths of the computational domain, respectively. An additional parameter compared to the other confined planar flows is the wall-normal extent L_y, although it is expected that the results should not depend on L_y once it is large enough, because the base flow is uniform at a sufficiently far distance from the wall located at $y = 0$. Although this can be considered physically artifical, one-dimension spanwise extension can be enforced by choosing $L_z >> L_x$, with the values of L_z varied between 4π and 6π. In a similar vein one could also choose $L_x >> L_z$ as well as tilted domains as in pPf/pCf, although this has not been considered. The present edge tracking computations have all been performed for fixed parameters $Re = 500$ and $L_z = 40$, while the parameter L_x has been varied in small steps [131, 172].

Classical edge tracking has been performed using the code SIMSON developed at KTH, with the cross-flow energy as scalar observable. As for some parameters of pPf (including those in Refs. [98, 99, 173] the energy signal on the edge displays large peak-to-peak variations typical of *bursting* dynamics. We stress that, unlike initially believed by Toh & Itano in their 2001 paper [97], the bursts are intrinsic parts of the edge state and do not belong to its unstable manifold : they do not represent an instability of the edge state but are part of its dynamics. This implies looser bounds for the bisection and eventually longer simulations. The long periods of these bursts makes Newton convergence technically impossible even when the edge state seems to be an RPO. Space-time diagrams typical of converged solutions are represented in figure 2.36. The first three frames correspond to three different asymptotic dynamics obtained for the same set of parameters from different initial conidtions. It represents evidence that edge states need not be uniquely defined. The two first frames correspond to two symmetric counterparts and are a consequence of the equivariance of the system with respect to $z \leftarrow -z$ flips. For the first case, the active core where the streaks are present shifts to the right (i.e. increasing z) after each burst in a periodic fashion ; for the second case the shifts occur towards the left (i.e. decreasing z). The third one displays alternate shifts towards the left and the right, also in a periodic fashion yet with a slightly shorter time period. The fourth case displayed has been found for a different streamwise wavelength L_x of 4π. It features very similar shifts in both direction, but the direction of the shifts appears erratic as in a random walk. The mechanics behind the shifts has been analysed in Ref. [131] and turns out to represent a generalisation of the scenario found in related MFUs [113], where low-speed and high-speed streaks periodically cross and exchange roles, therefore appearing as drifting in the spanwise direction.
It was decided to investigate intermediate values of L_x between 4π and 6π to understand the dynamical origin of the chaotic edge states. Since none of the states can be converged using a rootfinder and because

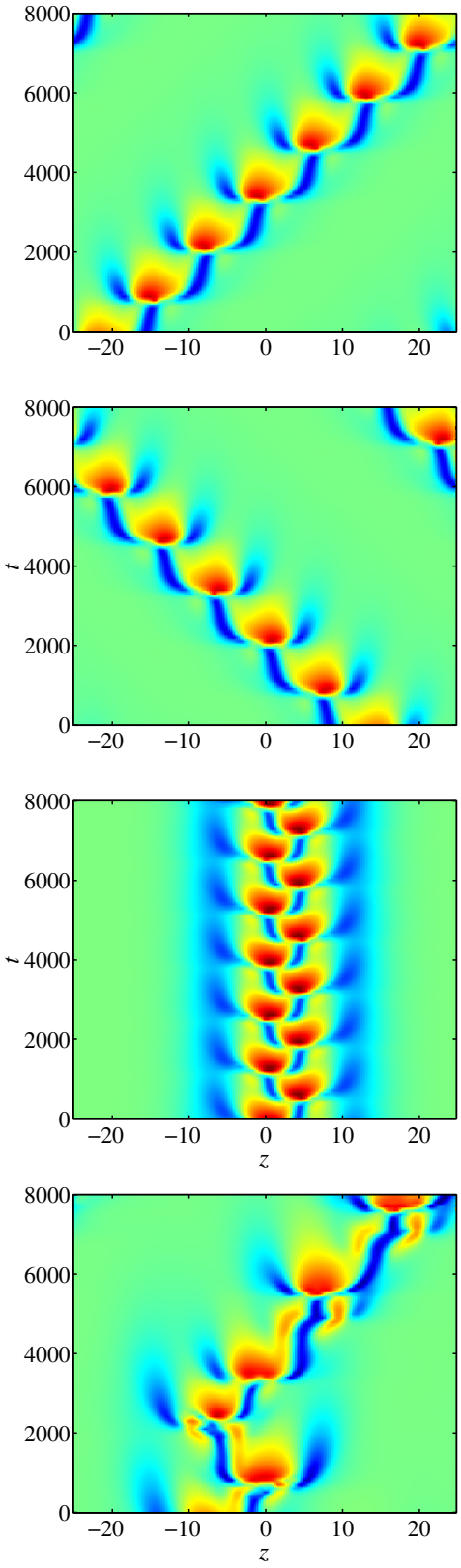

FIGURE 2.36 – Space-time diagrams of cross-flow energy for edge states in wide domains of ASBL [172], $Re = 500$, $L_z = 400$, $L_x = 6\pi$ except for the last frame where $L_x = 4\pi$. The branches for the Left-shifting and Left-Right-shifting states are represented with red squares and blue circles, respectively. Larger symbols represent stable (filled) and unstable (empty) states, whereas erratic behaviour is denoted with smaller symbols.

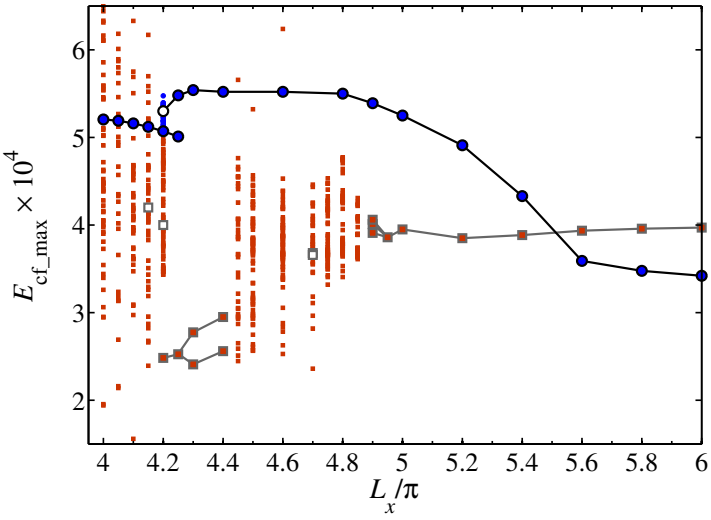

FIGURE 2.37 – Bifurcation diagram for edge states in wide ASBL : cross-flow energy versus L_x [172].

of multistability, several new edge tracking computations had to be performed independently for each new parameter. This computationally expensive series of edge computations revealed unsuspected complexity. This is summarized in the incomplete bifurcation diagram of figure 2.37. In this diagram, coloured circles denote RPOs : blue circles represent the states shifting alternatively left and right, represent red circles the ones shifting in one direction only. All the other states are chaotic. Some of them feature clear transient yet recurrent approaches towards one type of periodic state. It was established in Ref. [172] using first-return maps that chaos emerges in various ways, including type-III intermittency [174]. Such a complex wealth of dynamical scenario makes it clear that the picture with the edge state as a uniquely defined saddle point is naive.

It is interesting to investigate the fate of supraliminal perturbations, i.e. initial perturbations that are close to the edge state and belong to the turbulent basin $\mathcal{B}_T$. Formally speaking, this corresponds to investigating the one-dimensional unstable manifold of the edge state(s). In practice the tracking of an unstable manifold in high dimension is a delicate task (see e.g. [75, 175]. Fortunately, there are robust features common to most supraliminar perturbations. When the turbulent state is spatially localised (e.g. in the transitional range) the transition form the edge state to the turbulent state proceeds as a *local* phenomenon. When the turbulent state is not localised, which corresponds to all parameters beyond the transitional range, the transition proceeds in two stages [152, 153] : an initial rapid phase of local transition is followed by a slower phase of front propagation where turbulence invades laminar flow around it. This can also be seen in figures 2.28 in pCf as well as in figure 2.38 in ASBL. In a few exotic situations, the transition process can involve both localisation on the way towards the edge state and delocalisation on the way from the edge state. This is the case for instance for supraliminal noisy perturbations [153].

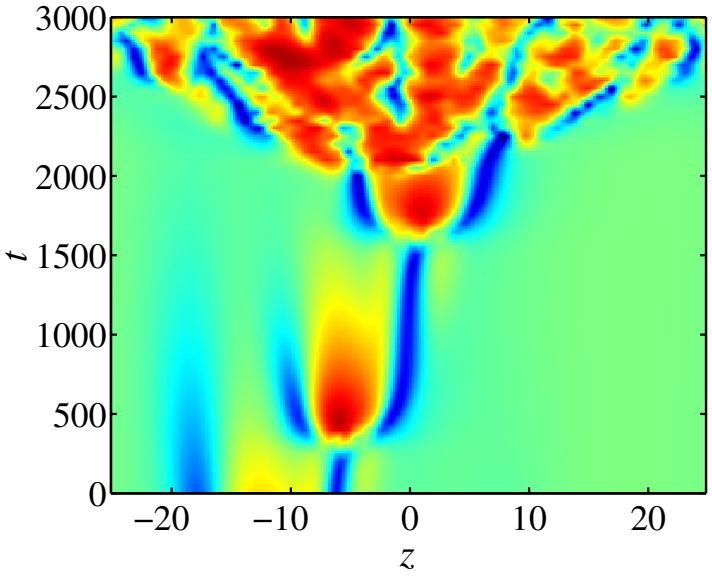

FIGURE 2.38 – Space-time diagram illustrating the delocalisation during the transition process initiated by the edge state in ASBL.

2.4.3 Two-dimensional localisation

2.4.4 plane Couette flow

The investigation of the one-dimensional localisation of edge states might seem natural for pipe flow, whose geometry has an "effective dimension" of one. Its relevance is a priori less convincing for planar flows, as attested by the dependence of the results on the parameter L_x. This had lead some researchers to denigrate edge states as "spurious" solutions. This is erroneous since edge states are true solutions of the Navier–Stokes equations. Nevertheless the physical relevance of formerly found solutions to experiments is, because of the of periodic boundary conditions involved in their computation, debatable. A truly robust picture of edge states exists however (in the sense that it does not depend on any input parameter). The generalisation from one-dimensional to two-dimensional localisation of edge states is theoretically straightforward. It is robustly attested in all shear flows provided the two planar dimensions (say x and z) present a sufficient extension with respect to the wall-normal direction y. The real practical challenge is the computational cost of the many individual simulations and the difficulty to reach an asymptotic state. This high cost explains why so few full computations of localised edge states have been performed to date, let alone Newton convergence and/or parametric investigations.

The first instance of such computations can be found in Ref. [154] as well as [157] for plane Couette flow. The largest dimensions considered for the computational domain in Ref. [154] are $L_x = 400$ and $L_z = 100$ in units of the half-gap h. These dimensions are large enough to warrant unambiguous localisation of the velocity field in x and z as appreciable in figure 2.39 for $Re = 375$. Halving the box dimensions also yields a state describable as localised, with an active core comparable in terms of dimensions : this suggests that the localisation is, again, a robust feature independently of the box size for large enough domains. The dimensions $L_x = 400$ and $L_z = 100$ can be compared to those of the computational box for the MFU, for instance $L_x = 5.51$ and $L_z = 2.51$ in Ref. [24], for which no localisation is detectable at least for $Re \approx 400$. No physical rule of thumb has emerged so far to distinguish between localised and non-localised cases, but evidence suggest that $L_{x,z} > 50$ is sufficient in practice. From a dynamical point of view the edge state in pCf appears chaotic as judged from global energy signals. Some efforts have been undertaken to provide one with a description of the edge trajectory in terms of finite-amplitude solutions. Although transient approaches to apparent steady states have been noted, no convergence towards an exact solution was established. Only later did J.F. Gibson and E. Brand identify a steady state solution with a localised structure similar to that of the edge state in Ref. [154], however that solution turned out neither to be an edge state nor to even lie on the edge manifold. More work is required to have a perfectly deterministic picture of the dynamics on the edge.

Moving towards higher Re suggests that edge states get narrower in z but also longer in x, see figure 2.39 for $Re = 1000$. This suggests that higher Re require even longer numerical domains. At this point it is worth remembering that Vortex Wave interaction theory predicts the emergence as $Re \to \infty$ of a critical layer whose thickness scales as $(\alpha Re)^{-\frac{1}{3}}$ [108]. The emergence of such a singular layer is confirmed in MFUs where the streamwise wavelength α remains $O(1)$, however in the present computations with localisation there are several wavelengths α contributing. Choosing the largest wavelength as $\alpha = 2\pi/L_x \sim Re^{-1}$, the thickness of a possible critical layer is $(\alpha Re)^{-\frac{1}{3}} = O(1)$ and no critical layer needs to be considered [176]. Choosing α representative of the $O(1)$ wavelengths found in the active region makes the "local" occurence of critical layers possible. This is the case for instance for the localised edge state found in pipe flow at $Re = 6,000$ and $10,000$ (resp. Figs 9 and 10 in Ref. [153]).

2.4.5 ASBL

An analogous edge tracking computation has been considered in ASBL, seen as a model for a boundary layer flow without the technical complications due to spatial development [115]. No additional discrete symmetry was imposed. The present computation made use of a PRACE allocation of several million CPU hours exclusively dedicated to this project. Unlike the previous pCf computation, the bisection was

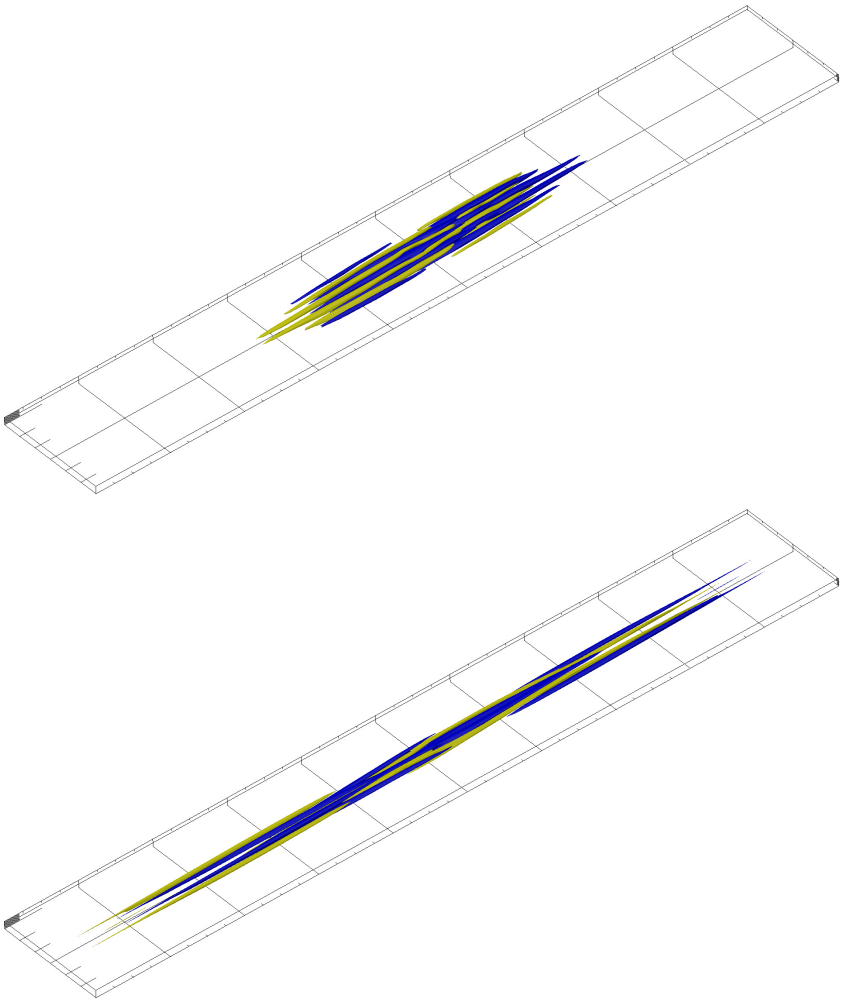

FIGURE 2.39 – Localised edge states in pCf for Re =375 and 1000 from [154]

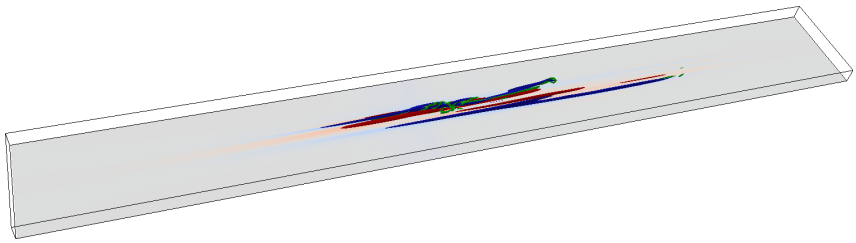

FIGURE 2.40 – Snapshot of the localised edge in ASBL for $Re = 500$. Isolevels of streamwise velocity perturbation (red/blue) with isolevels of $\lambda_2 < 0$ (grey).

pushed as far as possible, with the hope that if a simple relative attractor exists it will not be missed. No simple state was eventually found for the parameters tested ($Re = 500$ notably) therefore the edge trajectory is claimed by default to be chaotic. The geometric parameters are $L_x = 800$ and $L_z = 100$, whereas L_y is kept to 15. It has been verified that the spatial structure of the edge state (shown in figure 2.40) changes little for $Re = 500$ when these dimensions vary.

A two-dimensional space-time diagram (x, t) of the cross-flow energy was constructed in a manner similar to those of figure 2.36, with the explicit aim of performing qualitative comparisons. This diagram, displayed in figure 2.41 happens to look surprisingly close to the chaotic edge state found for $L_x = 4\pi$ in figure 2.36d : the main structure is localised in z over a support of approximately 20 units of δ_0^*. It drifts alternately towards $z > 0$ or $z < 0$ with changes of direction over timescales of $O(10^3\delta_0^*/U_\infty)$. Each change in the numbers of active streaks correlates well with a burst of the cross-flow energy. Such changes of direction were already found to be typical of ASBL in smaller computational domains [131, 172]. Here they similarly involve the crossing of low- and high-speed streaks preliminary to energy bursts. However these bursts and drifts were found neither in large-domain pCf nor in MFU of pCf. The qualitative conclusion from this global comparison is speculative but optimistic : edge states in large computational domains are invariably localised and are robust coherent structures, however they keep dynamically the same main features as their MFU counterparts. This is true with respect to bursts and drifts as well as for critical layers, local wavelength selection etc... More computations would be needed to confirm this speculation. If confirmed, this implies that the investigation of edge states in spatially correlated systems, presents a physical interest despite their lack of robustness with respect to geometric parameters. Instead it can be used as a cheaper *laboratory* to understand the more complex yet robust dynamics of localised edge states for the same flows.

The last crucial property of edge states concerns their relevance to the transition process. It is understood that, by definition, only perturbations to the laminar flow with a very specific amplitude are attracted by the edge state. For trajectories initiated very close to the minimal seed, transient visits to the edge state were detected and even exploited to find new exact solutions [112]. This is not surprising given the saddle nature of the edge state but that property is not expected to hold beyond its linear neighbourhood. However, does the edge state play a role of any importance for generic initial conditions, in the absence of any bisection process ? This has been tested by focussing on a large domain of ASBL where different instances of noisy velocity fields (with different amplitudes) were imposed as initial conditions at $t = 0$ [115]. Some initial conditions lead to an incipient turbulent spot and some lead to laminarisation. However *all* trajectories, when visualised in the state portrait of figure 2.42, displayed a clear transient approach to the same state space region where the edge state is located, similar to the approach to a simple hyperbolic saddle point. A state portrait based on energetic quantities is not a rigorous projection and these results should only be seen as an indication that the edge state plays the role of an unavoidable toll station in a high-dimensional state space.

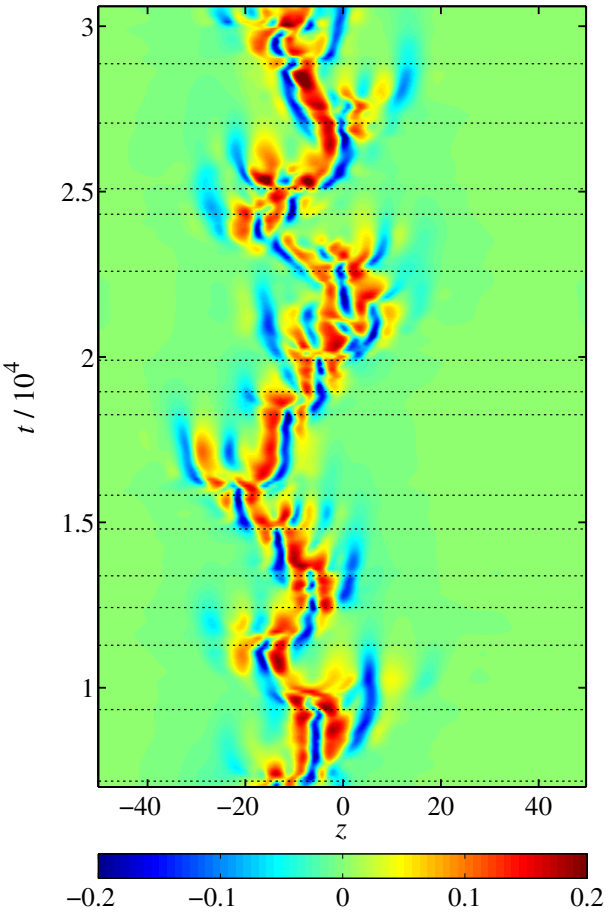

FIGURE 2.41 – Space-time diagram for the localised edge in ASBL at $R = 500$. The dynamics is qualitatively comparable to figure 2.36d.

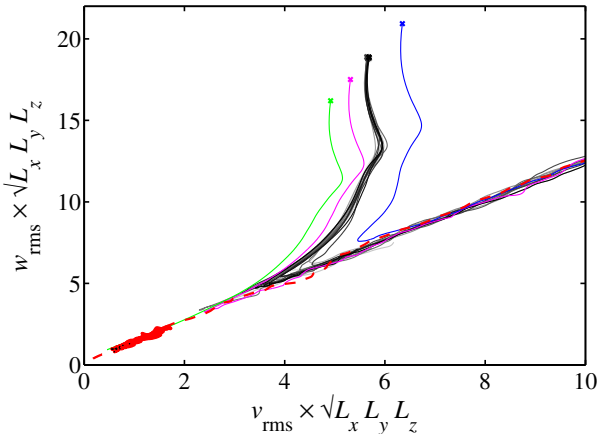

FIGURE 2.42 – State portrait of ASBL during transition initiated by 20 different noisy initial conditions. [115]. Edge state : red solid line. The axis denote the r.m.s. averages of the wall-normal and spanwise velocity components, normalised by the domain size in order to account for the different computational domains used.

2.5 Conclusions

This section has mainly focused on the concept of edge states and its development in the context of parallel shear flows in the last 10 years. Edge states correspond to relative attractors for the dynamics of edge trajectories, the trajectories constrained to lie on the laminar-boundary state space boundary Σ [97, 177]. Edge states are not unique and do not necessarily host simple dynamics, instead they can support low-dimensional temporal chaos [106]. Chaotic edge states appear even as the generic rule rather than as an exception. The computational algorithms used to find them rely usually on the classical bisection based on energy bounds, although new variants based on Lagrangian concepts and/or feedback control can be envisioned. The principal success in the exploitation of edge states lies in their property of spatial localisation independent on the physical parameters. The localisation property emerges in practice as soon as the computational domain is large enough [154]. This makes edge states *physically robust* objects since their existence and dynamics no longer depends on numerical parameters such as the computational domain size or the numerical discretisation. The same robustness concept applies as well to minimal states, the initial perturbations of smallest energy likely to trigger actual transition [178]. In some sense, edge states and minimal states are hence the most relevant instance, if not the only one, of application of dynamical systems theory to shear flows. Other concepts such as e.g. periodic orbits have so far only been identified in MFUs. They are therefore intimately connected to periodic boundary conditions and the property of MFUs to capture only spatially correlated dynamics. There is still hope to construct a fully robust dynamical systems theory for localised turbulent states, whose simulation does not rely on a specific choice of domain size. Turbulent puffs in pipe flow appear as the best candidate for such a task and encouraging results have appeared recently [75]. At the time where the present conclusions started to emerge, there was growing evidence that more knowledge on the dynamics of localised states was required, that the study of transitional shear flows in periodic domains was reaching its limits... but also that the current numerical facilities has reached the stage of development where they could shed some light on some open questions. The next chapter is dedicated to the dynamics of localised structures in transitional shear flows. In particular it explores the recent contribution of large domain numerical simulations to the study of transitional regimes of shear flow turbulence.

3

Spatiotemporal aspects of subcritical transition

3.1 Transition as a phase transition

The previous chapter was devoted to the question of the coexistence of the laminar and the turbulent regimes in state space. The present chapter attacks the question of laminar-turbulent coexistence from the point of view of their coexistence *in physical space*. These are two different questions that request very different angles of attack, different philosophies as well as different methodologies... and lead to different results. The state space coexistence implies, when dealing with extended systems, the possibility to achieve different regimes at different places but at a single time. These different "phases" are then separated by interfaces, whose competition rules the dynamics of the flow. Moreover, it is a well-known peculiarity of subcritical flows that, in a well chosen range of parameters, the different phases can also coexist in a sustained fashion. There is a clear analogy with the language used in equilibrium thermodynamics when dealing with different phases. The general analogy between the laminar-turbulent problem and the thermodynamics of phase change was probably proposed first by Yves Pomeau in the 1980s [179]. It rapidly developed into a school of thought around people such as P. Manneville, F. Daviaud and many others. As soon as the different phases are well defined, interpreting the transition from laminar to turbulent as a genuine phase transition becomes paramount. The use of a vocabular imported from the world of statistical physics becomes very tempting despite many caveats. For instance, should laminar–turbulent transition correspond to a continuous or a discontinuous phase transition ? And of which order ? Some of the concepts from equilibrium thermodynamics do not export very well towards the field of dissipative non-equilibrium physics. Since the laminar phase is defined without any fluctuations, a fruitful analogy must consider it as an absorbing state, whereas the turbulent state contains its own fluctuations. The concept of edge corresponds to a third regime that has the property of being unstable and not realizable. For a phase transition to make sense, a control parameter must be chosen, in general taken to be the Reynolds number Re under one of its numerous incarnations. The question of which order parameter to use is more arduous. There is no free energy associated with the Navier–Stokes equations to rely on to define the type of transition in the spirit of Ehrenfest. Free energies can also be defined as limiting distributions by using the principle of large deviations but this has not yet been exploited deeply in the turbulence context, because of limitations in terms of volume of data. Instead it was chosen to use as order parameter an intensive quantity akin to a *density of turbulence*, namely a turbulent fraction that can be estimated from data (also called intermittency factor). An important question that has stirred the community in the last ten years concerns the universal and the continuous/discontinuous character of the transition using this formalism. The present chapter mentions these issues, but not only. It does not only focus on the onset of the turbulent regime but on the full transitional range, where the turbulent fraction is not necesarily small, but simply finite. Moreover, D. Barkley developed recently a low-order PDE model for pipe flow. The way he derived the model from phenomenological facts [180] is based on a constructive criticism of the simple one-component phase transition picture. This criticism invokes the need for large-scale flows to be included in the picture. The present chapter is an opportunity to investigate large-scale flows, to re-define the concept and to use it for a better understanding of morphogenesis of laminar–turbulent patterns. This chapter begins with the spatiotemporal description of the transitional regimes of pipe flow, followed by planar flows. Spatially developing boundary layer flows are treated only in the next chapter.

3.2 One-dimensional shear flows

We begin with the description of pipe flow, whose effective dimension is one. This makes the phenomenology geometrically simpler to describe. The comparison with laboratory experiments. is also *a priori* simpler. By default the forcing protocol corresponds to constant mass flux. We choose hence the bulk-based Reynolds number $Re = U_b D/\nu$ as the governing parameter. Laminar pipe flow is linearly stable for all Re, hence the laminar regime is always a possibility. A relevant bifurcation diagram for pipe flow should, for simplicity, refer only to regimes observable in the so-called thermodynamic limit of infinite domains over infinite observation times. It should feature laminar flow only when this is the only possible regime, otherwise it should indicate the turbulent regime. A sketchy diagram (taken from [181])

condensing much of the information available ten years ago is displayed in figure 3.1 for pedagogy. It suggests that only the laminar flow can be observed, sufficiently far down the pipe, provided $Re < 2050$. Sustained turbulent states are only observed above this value. Two specific turbulent states exist : the first is referred to as *spatiotemporal intermittency* (STI) and features only spatially sparse turbulence. The other corresponds to the high-Reynolds number regime where turbulence, if seeded locally, expands continuously. This regime is characterised by *expanding slugs*. At any location sufficiently far downstream, the flow will eventually become turbulent in a sustained manner, and the turbulent state is locally indistinguishable from its prediction in periodic computations [180].

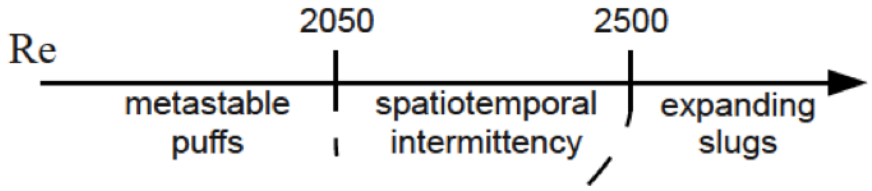

FIGURE 3.1 – Qualitative bifurcation diagram for pipe flow as a function of the Reynolds number Re (from [181]).

3.2.1 Localised puffs

In its sparest incarnation, the STI regime consists of individual coherent structures called turbulent puffs. Puffs are localised in the streamwise direction and remain coherent over their cross-section [182].They were already identified in Reynolds' experiment [183] and described as "flashes", or also as "streaks" in Ref. [184]. The localisation of turbulent puffs makes them relatively easy to trigger one by one using localised perturbations, e.g. transverse impulsive jets as in figure 3.2. However, puffs can also form from other types of upstream perturbations, including permanent ones [185]. The apparent stability of puffs (seen as unsteady objects) over short times suggests that they are manifestations of a turbulent equilibrium [151, 186], naively thought to be a metastable one. In fact, and this is one of the main findings in transition during the years 2000s, individual puffs appear stable only on the timescales typical of short pipe experiments, but they are never in equilibrium : either they relaminarise after a finite time [62, 63, 187–189], or they proliferate [13, 180, 184, 186, 190]. Observing the instability of a puff is hence only a matter of time. Despite this property, the ratio between the lifetime of the puffs by the typical timescale of the turbulent fluctuations inside them is always reported to be very large. It hence makes sense to study puffs as equilibrium regimes over intermediatly long timescales, and to look for a self-sustaining process (SSP). The situation was similar in small periodic domains, where Waleffe's self-sustaining process (SSP) did not prevent the turbulent state built on a chaotic saddle of relaminarising. However, the SSP of localised states turns out to differ structurally from that of Waleffe, precisely because of the spatial localisation.

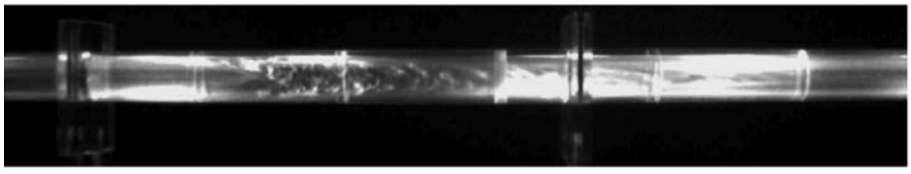

FIGURE 3.2 – Puff in experimental pipe flow for $Re = 1800$ visualised by Mearlmaid Pearlessence illuminated by a vertical sheet of light [191]. Flow from left to right.

.

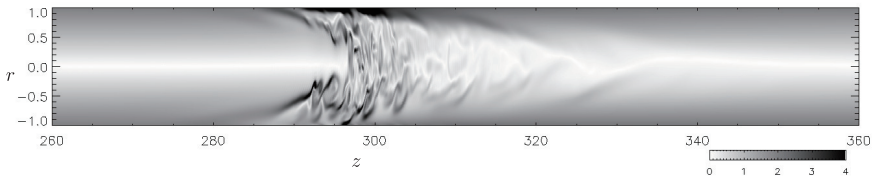

FIGURE 3.3 – Puff in numerical pipe flow for $Re = 2000$ visualised by isolevels of absolute vorticity. Flow from left to right. From Ref. [192]

.

The total vorticity field inside a meridian plane of a puff is shown in figure 3.3, with the flow from left to right. The less coherent part corresponding to the 'turbulent' zone (between x=285 and 320 in units of the pipe radius) has a well-reported arrowhead structure. The fluctuations closest to the pipe wall are those located most upstream and are relatively large-scale. Since they are in a zone of low velocity, their propagation velocity is slower than that of the mean structure. From the point of view of the puff, these wall structures are "left behind". They correspond to the tails of streaks generated within the turbulent zone itself. The strongest velocity gradients, also visible in figure 3.3 because of the strong levels of absolute vorticity, occur at the steep upstream interface between the fluctuations. Since they are located in a faster zone of the flow, these small-scale structures have a propagation velocity which is positive in the frame of the puff : these small-scales structures catch up with the puff, thereby contributing to its re-energization. This has led Shimizu & Kida [193] to suggest a simple cyclic SSP to explain the puff's long lifetime : the production of small-scale turbulence is the result of the shear instability of the vortex layer corresponding to the tails of the low-speed streaks (cf figure 3.4). These streaks are the signature of the lift-up effect due to the vortical activity close to the wall (due to the turbulence), and the loop is closed. As for periodic domains, it is intuitive that if any of these links fails to occur fast enough, the loop is broken, the puff fails at sustaining and relaminarises. Note that this SSP is not two-dimensional since it involves the azimuthal direction, without which there is no transverse modulation and no low-speed streak. This cyclic mechanism differs effectively from that of Waleffe [30] : the spatial localisation of the fluctuations is crucial to ensure enough shear upstream from the puff and to give rise to the shear instability (labelled for simplicity "KH" like the Kelvin-Helmholtz instability). This difference has not yet been much emphasized. Note that it is consistent with the PDE models suggested by Barkley [180, 194]. In the deterministic part of these models, localised states exist at values of the Reynolds number smaller than those where the homogeneous steady states bifurcate. Necessarily such localised states need a specific mechanism to sustain themselves against viscous dissipation as well.

3.2.2 Turbulence proliferation

Puff splitting

Since the natural organisation of the turbulent regime at low Re is precisely a series of localised puffs, it makes sense to investigate the proliferation phenomenon by starting from a single turbulent puff first. Unlike Fourier modes and other delocalised initial conditions, choosing a localised initial condition has the important advantage of being experimentally reproducible. There is a deeper justification to this choice. As shown in the previous chapter, edge states, which are invariant sets of the system, possess the localisation property as soon as they are computed in large enough domains (or, in other words, when they are computed in the absence of finite-size effects). Minimal states also share this property. These special perturbations are well defined mathematically ; they are not rigorously unique but do not rely on a long list of parameters. In addition they are, by construction, robust to domain changes. Initialising the system at initial time with such perturbations is a consistent, non-parametric way to excite the flow with only little perturbation energy. For pipe flow the choice to start from the edge state was considered natural for instance in order to excite slugs in Refs [152] and [153], whereas localised minimal seeds were considered in Ref. [195].

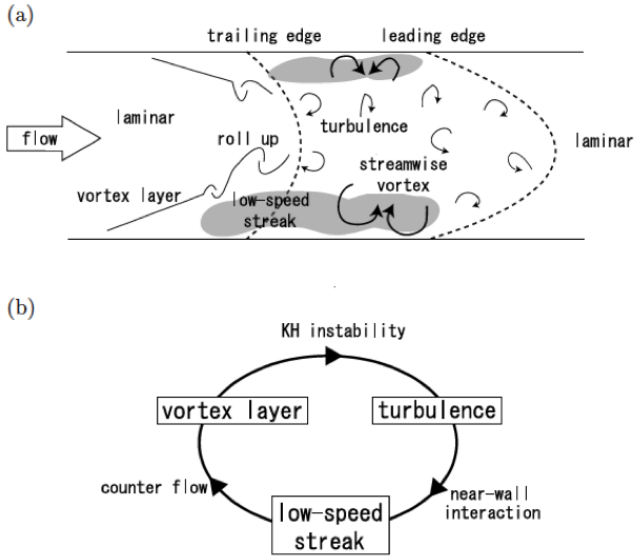

FIGURE 3.4 – Sketch of the Self-Sustaining Process for localised states in pipe flow (taken from Ref. [193])

.

The mechanisms of proliferation are relatively well described qualitatively in the early pipe experiments of Lindgren [184]. Their quantification in the immediate neighbourhood of the critical point can be found in Ref. [13]. In this regime turbulence proliferation corresponds qualitatively to the "splitting" of individual puffs, or rather to their *duplication* or *self-replication* (in the sense that the turbulent fraction is supposed to increase), if we are to borrow vocabulary from biology and pattern formation [196].

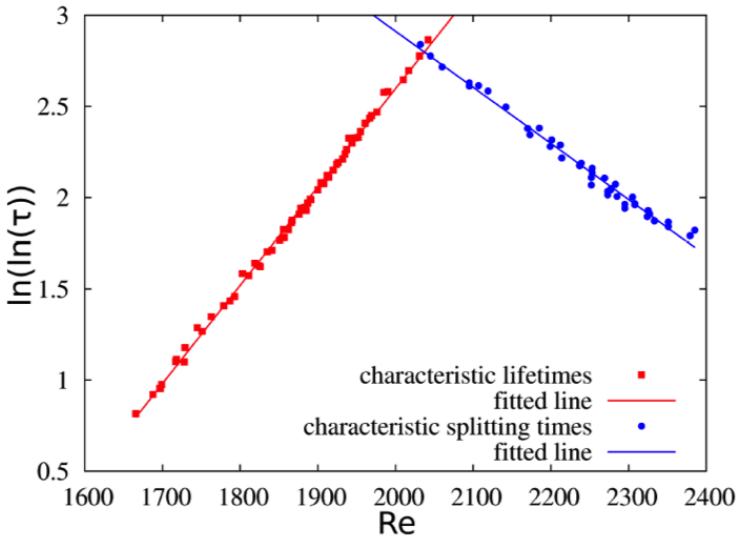

FIGURE 3.5 – Mean lifetimes and splitting times versus Re in pipe flow. Taken from [197].

.

In this plot (reproduced in figure 3.5 in double log data following Ref. [197]) the mean lifetime and the mean splitting time are plotted versus the Reynolds number. The mean lifetime increases super-exponentially with Re while the mean splitting time decreases also in a super-exponential manner. Both mean values cross at a given value of Re where the probability to decay balances exactly that of splitting.

Above this value of Re, turbulence spreads statistically. This single plot, beyond the impressive statistical database needed to achieve it, represents a real conceptual progress since it offers at last, after almost 130 years of investigation, a rigorous definition of the critical point for pipe flow.

The dynamics of the splitting process [192] is shown as a still movie in figure 3.6. The representation makes use of $r \approx 0.8$ surfaces, where fewer small-scale fluctuations are present and where the streaks dynamics is particularly clear. The initial puff fluctuates in length with some vorticity intermittently shed downstream at a fast pace (comparable to the turn-over time $O(D/U)$). The splitting process proceeds in several steps and is successful only if all steps have occurred in a fast enough sequence. First a low-speed streak undergoes a statistically atypical elongation in the downstream direction (1^{st} to 5^{th} frame) considered to be a rare event. Then the associated flow destabilises downstream. This gives rise to a new puff a distance of roughly 40 radii downstream of the initial puff (9^{th} frame). Depending on the quantity chosen, it is possible to detect that the puff grows in length before effectively splitting into two turbulent parts. Whether the puff first elongates and then splits, or first splits and only later nucleates a new puff, is not entirely clear and deserves more investigation. The link with extreme value theory and Gumbel distributions [198], like for the relaminarisation process [199], deserves as well a deeper look.

What makes the description of the STI regime relatively simple in the approximate range $Re \in (1800 : 2350)$ is, beyond the one-dimensional geometry inherent to the pipe set-up, the quantized nature of the proliferation rules themselves. Each puff yields, at the next instant, either the same puff, two puffs, or no puff at all. This set of probabilistic rules lends itself very well to a description in terms of cellular automata, known in the presence of an absorbing state to reproduce well STI dynamics [200]. For slightly larger values of Re however, i.e. from 2350 to approximately 2700, an emerging trend competes with the quantized dynamics : continuous expansion. For $Re \geq 2700$, most expansion events can be described as continuous.

Continuous expansion

Although laminar-like holes and interrupted growth sequences can still be found as rare events [201], the flow tends to a uniformly turbulent flow as time increases. It is tempting to try to define a second critical value of Re around 2700 but this is not as effective as in the case of the first critical point. Moxey & Barkley [12] have for instance defined an intermittent factor γ (otherwise called "turbulent fraction" in other flows) by thresholding the local perturbation kinetic energy. In principle one would wish to define the second critical point at the value of Re where γ reaches 100%. The dependence on the threshold does not make this definition very accurate yet, although it is again consistent with a transition from STI to full-fledged turbulence at around $Re \approx 2600 - 2700$. Using the second moment of the distribution of laminar lengths is another option used by the same authors, with similar conclusions.

The hydrodynamic mechanisms responsible for the elongation of a puff (i.e. in this regime a *slug*) are not clear as of now. As pointed out in Ref. [192], most dynamical events of importance take place at the leading edge. They are related to the production and the fast propagation downstream of vortical disturbances : when the fluctuations born upstream (whatever their origin) overtake the puff before any decay, this results in a temporary elongation of the puff. The same mechanism can well occur for an already well elongated slug. This can be labelled *leading edge growth* since the presence of the trailing edge does not seem crucial as long as there is a turbulence production mechanism.

Two different variants of leading edge growth have been identified qualitatively in the space-time diagrams from Ref. [153] : for $Re = 3000$ for instance, there is no production of turbulent kinetic energy at the downstream front (only at the upstream one), the leading edge can be described as *diffusive* as for puffs at lower Re. For $Re = 6000$ in turn, there is strong production of turbulent kinetic energy at the downstream front, as visualised by the vigorous small-scale vorticity present near the wall. The existence of these two types of leading edge fronts have later been confirmed, first in the Barkley model [180] then in DNS [202]. They have been labelled respectively "weak" and "strong" fronts. The transition from weak

to strong fronts in terms of probabilities is gradual as Re increases, with only strong fronts selected at high Re.

Although this has been considerably less investigated, an additional mechanism for slug elongation at the trailing edge has also been reported in Ref. [153]. It can be labelled by analogy "trailing edge growth" since it requires a trailing edge but, apparently, no leading edge. It is illustrated in figure 3.7 for $Re = 4500$. This mechanism is a direct extension of the SSP of Shimizu & Kida to the higher-Re regime, outside the standard puff regime. Once the vortex layer upstream has shed Kelvin-Helmholtz vortices in what seems like a standard three-dimensional shear instability, these vortices propagate with a positive velocity downstream. The trailing edge growth mechanism relies on the idea that the value of the streamwise advection velocity obeys a non-trivial distribution. While the fastest vortical disturbances travel fast enough to enter the turbulent zone, the slowest ones do not manage to catch up with the puff and are left behind it as it propagates. As a consequence there are remains of turbulent fluctuations just upstream of the turbulent zone. This possibly nucleates new turbulence that forms a new trailing edge interface, in a mechanism of growth by aggregation.

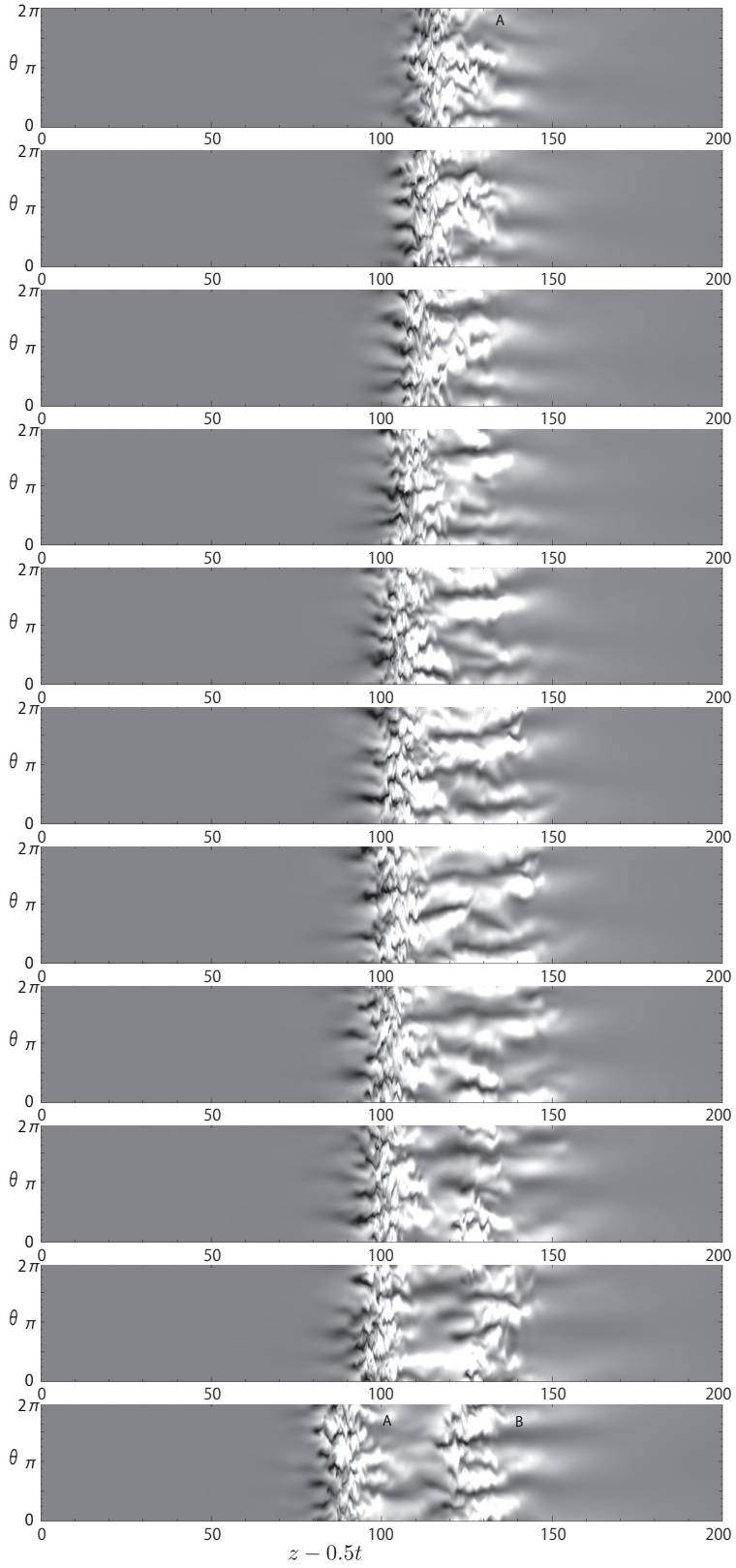

FIGURE 3.6 – Sequence of events leading to puff splitting in numerical pipe flow for $Re = 2300$ visualised by isolevels of absolute vorticity at $r \approx 0.8$ at a frame velocity equal to the bulk speed. Flow from left to right. [192].

.

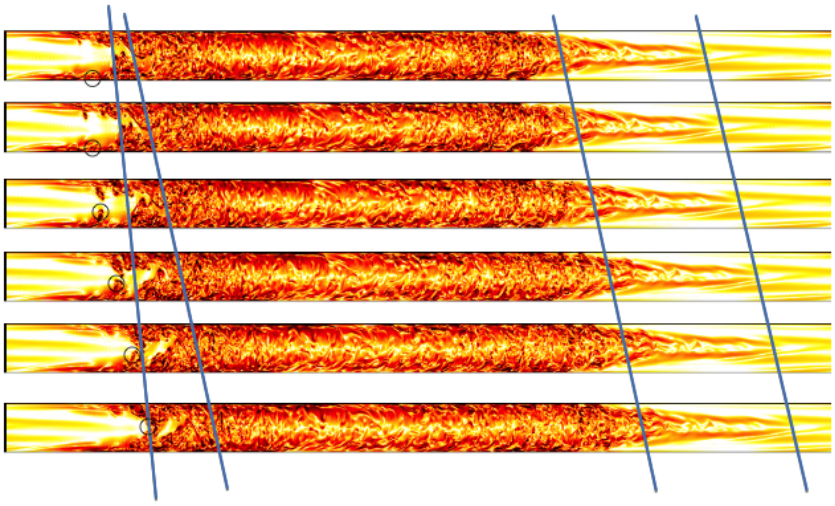

FIGURE 3.7 – Sequence of events leading to trailing edge growth of slugs in numerical pipe flow for $Re = 4500$ visualised by isolevels of absolute vorticity. Flow from left to right. Taken from Ref. [153].

3.3 Two-dimensional shear flows

3.3.1 Experimental approach

The structuration of the transitional regimes is notoriously more challenging when the effective dimension is two rather than one. This includes all flows with two neutral directions, be they planar or not. The first historical mention of laminar-turbulent patterning occured, as often, in an experimental investigation ofTaylor-Couette flow. It appeared first in conference proceedings [203] and later as a part of a long article in which D. Coles [204] describes the many regimes of Taylor-Couette flow. A photograph from the experimental campaign is included here in figure 3.8, where a simple turbulent helix can be recognised amidst the flow. It was also mentioned before publication in the lecture notes of R. Feynman [205]. This special flow case was baptized with humour "barber-pole turbulence" or, for geometrical reasons not yet understood, "spiral turbulence". In this thesis, the wording 'oblique stripe pattern' will be preferred, with the convention that 'oblique' refers to a non-zero angle with respect to the mean (streamwise) flow direction. At the time it was not clear whether this coherent structure, obtained when the two cylinders are nearly exactly counter-rotating, was a consequence of the end walls or not, or whether several wavelengths could be captured at once. Further experiments with different aspect ratios [206–209] and numerics [210, 211] have eversince provided ample evidence that the helical-shaped turbulence is an intrinsic regime of the flow and exists also in the presence of periodic boundary conditions.

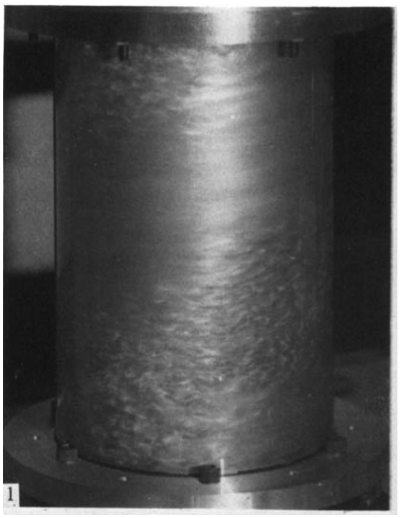

FIGURE 3.8 – Experiments by D. Coles [204].

There are some clear advantages yet also difficulties associated with the Taylor-Couette configuration that explain the frequent choice for plane Couette flow as a decent alternative. One of the undisputed advantages is the closed geometry. Difficulties include the fact that exact counter-rotation leads to laminar-turbulent patterns only in the limit $\eta \to 1$, where η is the radius ratio. Since a set-up with $\eta \approx 1$ is difficult to engineer accurately, this implies a specific tuning for the angular velocities of the cylinder and a complicated parametric dependence. Beyond the engineering issues, having non-equal angular velocities implies a non-zero flow rate and hence advection of the patterns. Also, for η far from 1, the natural azimuthal periodicity strongly influences the wavelength selection. This is at odds with the initial motivation of investigating two-dimensional patterns in the absence of finite-size effects. All these reasons combined together lead to the choice of plane Couette flow as a simpler candidate for the study of subcritical transition. Experimentally speaking, plane Couette flow with zero mass flux is difficult to achieve. Since the experiments of Tillmark [212] and Daviaud [213] all pCf apparatuses are similar and follow the sketch in figure 3.9. For technical reasons, the working fluid must be a liquid and the two walls must consist of a single flexible belt guided by two co-rotating cylinders. Most of the theoretical progress

of the 1990s has been achieved using the apparatus at CEA Saclay, notably in the experimental studies of F. Daviaud [213], J. Hegseth [214], O. Dauchot [215, 216], S. Bottin [43, 65, 217], A. Prigent [209, 218, 219]), and later R. Monchaux at ENSTA [220–223].

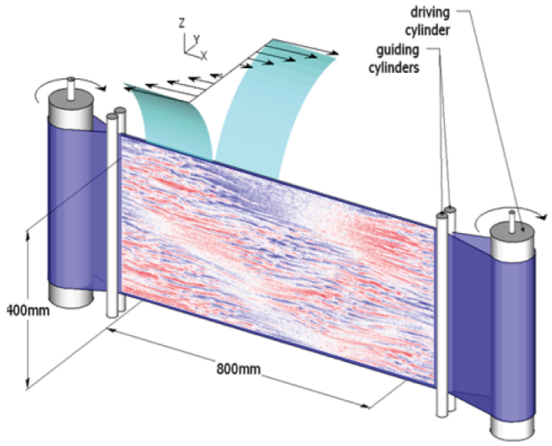

FIGURE 3.9 – Sketch of experimental pCf apparatus, taken from Ref. [223].

The transitional range of pCf, parametrised by the Reynolds number $Re = U_w h/\nu$ based on the half-gap h and the velocity of the walls $\pm U_w$, does not appear in experiments to depend quantitatively on the dimensions of the apparatus or of the numerical domain. Its bounds lie within the interval $Re \in (280 : 410)$. Meanwhile turbulence seems sustained statistically above $Re = 325$ [43, 65, 66, 217, 224, 225]. However, there are differences. The domain used in S. Bottin's experiments [217] has dimensions $L_x \times L_z = 35 \times 190$, expressed in units of the half-gap h. The STI regime has been found and well described, but it features no order, only laminar and turbulent patches without a clear organisation. The set-up used by A. Prigent has dimensions $L_x \times L_z = 340 \times 770$ in units of h. The upper transitional range, for $Re \geq 340$ at least, is much more ordered than in the smaller set-up. It is shown in figure 3.10 and can be qualified as *the patterning range*. The range of values of Re below it, that includes the critcial point around $Re = 325$, is again less ordered. Understanding how the transitional range is structured for diverging domain sizes and observation times ("in the thermodynamic limit") has motivated the use of direct numerical simulation for pCf.

A conceptually simpler flow case is plane Poiseuille flow (pPf), especially for experimentalists, since in contrast with pCf it only features rigid static walls. Like pipe flow, it possesses a non-zero flow rate in the laboratory frame. This issue implies that long observation times require long channels, with a special emphasis on the technically demanding plate parallelism. Transitional plane Poiseuille flow had remained a curiosity in the 2000s and until very recently, only tackled numerically by T. Tsukahara and co-authors and later experimentally [226], and thought to be a simple generalisation of pCf. It turned out later that the two flows have subtle differences when it comes to pattern formation and the existence of a critical point. There was however a recent explosion in the number of experimental studies of the transitional range of pPf [165, 227–230], backed by associated numerical studies [14, 161, 162, 231–234]. Both pressure-driven and mass-driven pPf have been considered depending on the authors, implying either Re_τ or Re_{cl} as the genuine governing parameter. We note as well emerging studies in a companion flow, namely zero mass flux plane Couette-Poiseuille flow [235, 236].

3.3.2 Numerical approach

Theoretical efforts to understand the organisation of these shear flows in the transitional ranges are not many. The spatial structure of the turbulent "spirals" was qualititatively understood in the early

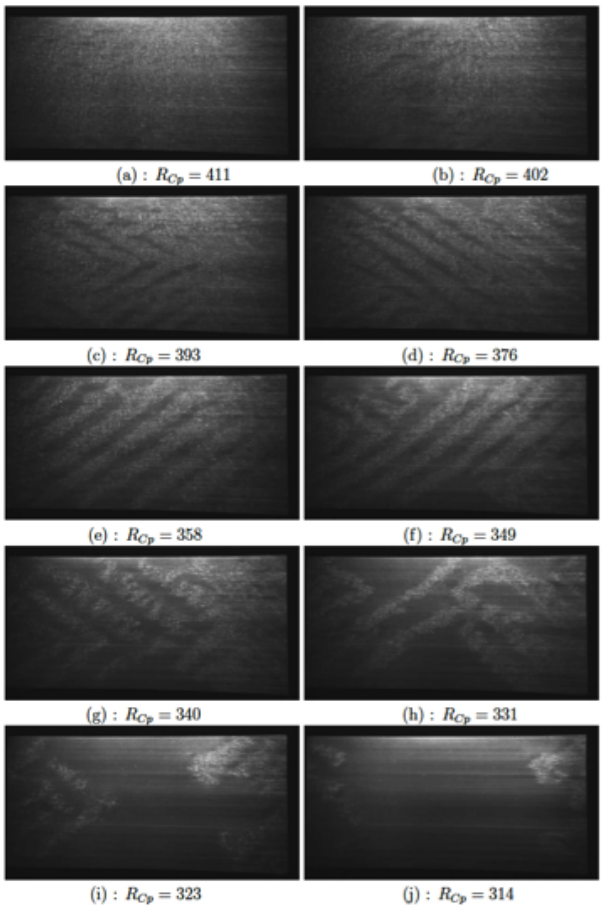

FIGURE 3.10 – Adiabatic descent in plane Couette flow, Experiments by A. Prigent [224]

works of Coles [203], athough it is not clear that these works were well recognised in their time. Pomeau and Hayot [237] attempted to explain the presence of laminar gaps in Taylor-Couette experiments from the feedback by the pressure forces, whose consequence is to halt the progression of the turbulent interface. Hegseth [214] has written about the importance of the spanwise vorticity in the formation of the intermittent state. The numerical work of Tuckerman & Barkley [159, 161, 238] has been carried out almost exclusively in oblique tilted domains. Laminar-turbulent patterns emerge in the turbulent regime without difficulty provided the dimensions of the domain are large enough. The range of values of Re in which they are found is compatible with experiments. These studies lead to a good understanding of the structuration of the mean flow. The main drawback is that the angle and the wavelength of the patterns are imposed input parameters.

In parallel a series of PDE models, where most of the modelling hypotheses concern the wall-normal structuration, have been developed over two decades by P. Manneville in the hope to reproduce laminar-turbulent patterns at a cheaper computational cost [239–241]. It was eventually confirmed that this approach is qualitatively valid provided the reduction in the wall-normal direction is not too severe [241]. The resulting computational model [242] does not lend itself easily to analytical predictions, but can be used as a low-order proxy of generic shear flows. The cheaper cost allows one, rather than to simply compute faster, to reach domain sizes unavailable by DNS and to eventually conclude about the continuous/discontinuous character of the transition [243]. This is detailed in Section 4.4.

In the context of the 2000s, although puffs in pipe flow had been properly reproduced numerically,

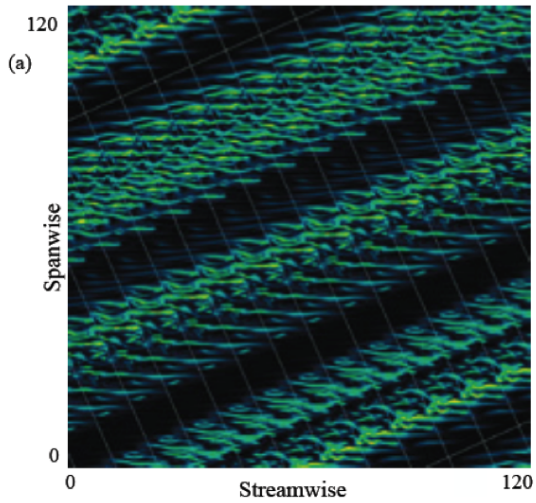

FIGURE 3.11 – Numerical simulation of laminar-turbulent patterns in pCf by L.S. Tuckerman and D. Barkley [159] perfomed in a tilted domain (2005). Several copies concatenated together displayed in the usual streamwise-spanwise coordinates. Instantaneous perturbation kinetic energy shown in the mid-plane. Domain angle : 24°, original dimensions $10h \times 2h \times 40h$.

a proper numerical simulation of the transitional laminar-turbulent patterns of pCf or TCf was still lacking. The simulations in a tilted slender domain of Tuckerman and Barkley [159] capture the long-wavelength modulation of turbulence flow with an imposed angle. The qualitative match with experiments is however not fully satisfying. For instance the signed orientation of the turbulent stripes observed in Prigent's experiments [224] can by construction not be reproduced.

plane Couette flow

Owing to the computational power of the machines available at KTH Stockholm, numerical simulations in a domain with $L_x \times L_z = 800 \times 356$ (still in units of h) were performed over observation times ranging from 2×10^3 to 2×10^4 h/U_w. The simulation is based on the spectral code SIMSON which assumes Fourier modes in x and z, i.e. periodic boundary conditions in x and z. For $310 \leq Re \leq 410$, for any initial condition (spot, edge state, noise, turbulent field from another value of Re) the flow evolves towards a state of laminar-turbulent coexistence, with interfaces always oblique with respect to the mean flow. The instances where the interface is locally not oblique all result in rapid relaminarisation or in a rapid evolution of the flow, suggesting that non-oblique interfaces are simply unstable. The development of a turbulent pattern from a noisy initial condition is documented in figure 3.12 for $Re = 350$. The noisy flow field was selected because it allows for a faster convergence to the final turbulent flow field. The early *receptivity* stage is well visible in the animated plots : streaks emerge rapidly from the noise at every location due to the lift-up effect. After $\approx 100 - 200$ time units the streaks have decayed in amplitude everywhere, except at a few random locations where streak breakdown occurs : this is the stage of *spot nucleation*. The third phase is slower and corresponds to *front propagation* : the spots grow, usually in an oblique fashion, split, reconnect, merge... until a statistically steady pattern with weakly varying turbulent fraction settles. We note in passing that the high resolution typical of spectral methods is comparable to the spatial resolution achievable nowadays in experimental PIV. The comparison of the streamwise velocity field from DNS (figure 3.12c) vs. experiments (figure 3.13) is excellent and leaves no doubt that the governing Navier-Stokes equations are well adapted to the hydrodynamic phenomena of interest.

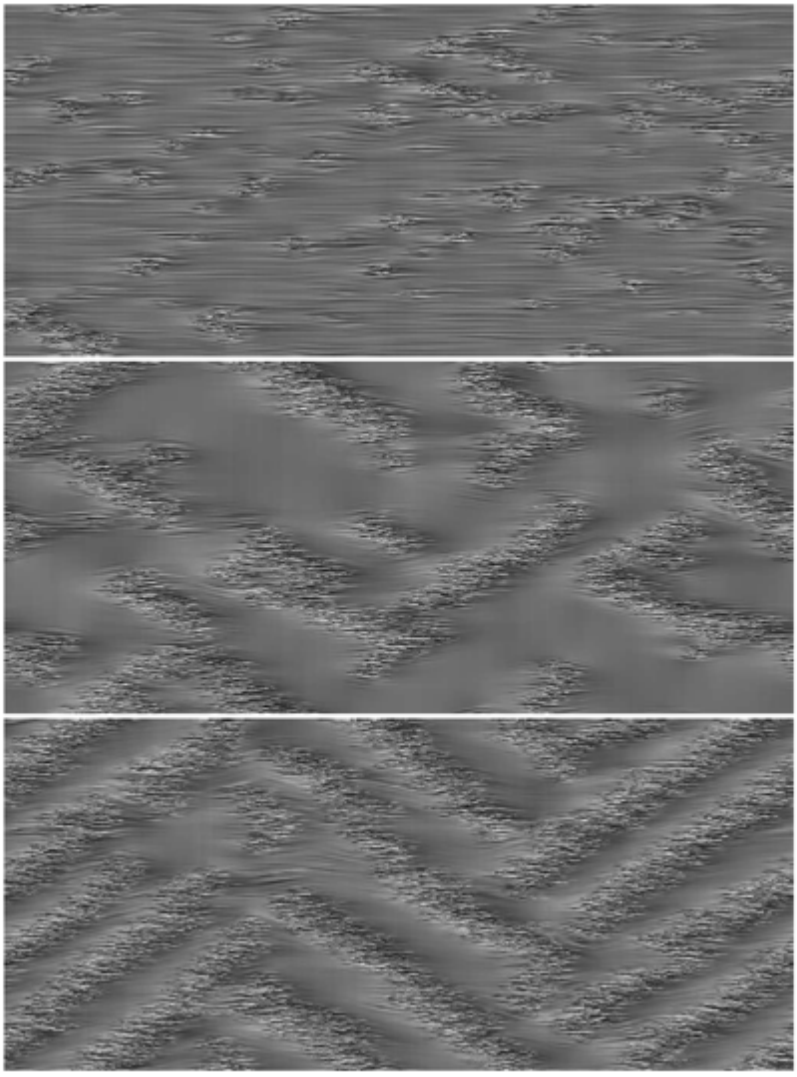

FIGURE 3.12 – Development of a turbulent pattern at $Re = 330$ starting from a noisy initial condition. Streamwise velocity field in the mid-plane $y = 0$ at time $t = 200$, 1865 and $20,000$.

plane Poiseuille flow

A similar computational series of runs was carried out in plane Poiseuille (pPf) driven by a fixed pressure gradient [14]. This time, unlike the protocol followed in pCf, a genuine adiabatic descent was performed by lowering the governing parameter Re_τ in small steps. A computational domain with $L_x \times L_z = 250 \times 125$ was considered initially (expressed in units of the half-gap h). As Re_τ decreased, the mean spacing between stripes was observed to increase, until for $Re_\tau = 55$ it was decided to restart the process from a noisy initial condition but in a larger domain with $L_x \times L_z = 500 \times 250$ in order to avoid accumulating finite-size effects. Instantaneous representations of the wall shear stress (averaged between the two walls) is shown in figure 3.14 for Re_τ=100,80,60 and finally 40 in figure 3.15. As in pCf an oblique and irregular stripe pattern is present for all values of $Re_\tau \leq 90$; it invariably forms whatever the initial condition. It is hence interpreted, at least in the upper transitional range, as a modulational instability of the homogeneous turbulent state [209]. The snapshot at Re_τ=40 stands out as all stripes point in the same direction. This phenomenon was pointed out in Ref. [244] and analysed as a macroscopic bifurcation. For $Re_\tau \geq 50$ the network of oblique stripes is tight and rigid, both orientations are equally possible and are in competition at all times. As Re_τ is lowered below 50, one of the two orientations gets beaten

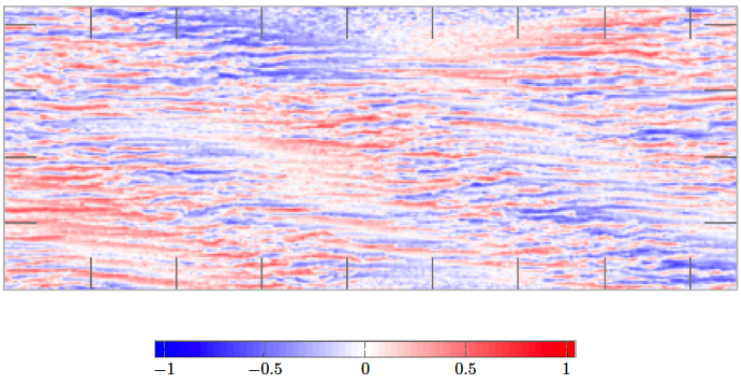

FIGURE 3.13 – Experimental velocity field (u_x, u_z) of turbulent stripes in pCf obtained using Particle Image Velocimetry (2020). From Ref. [223].

in finite time by the other one. As a consequence past a size-dependent transient all stripes propagate downstream in the same direction and move freely like particles in a gas [165, 245–247]. The existence of this *lower transitional range* with a different dynamics [234] has as of yet no equivalent in pCf.

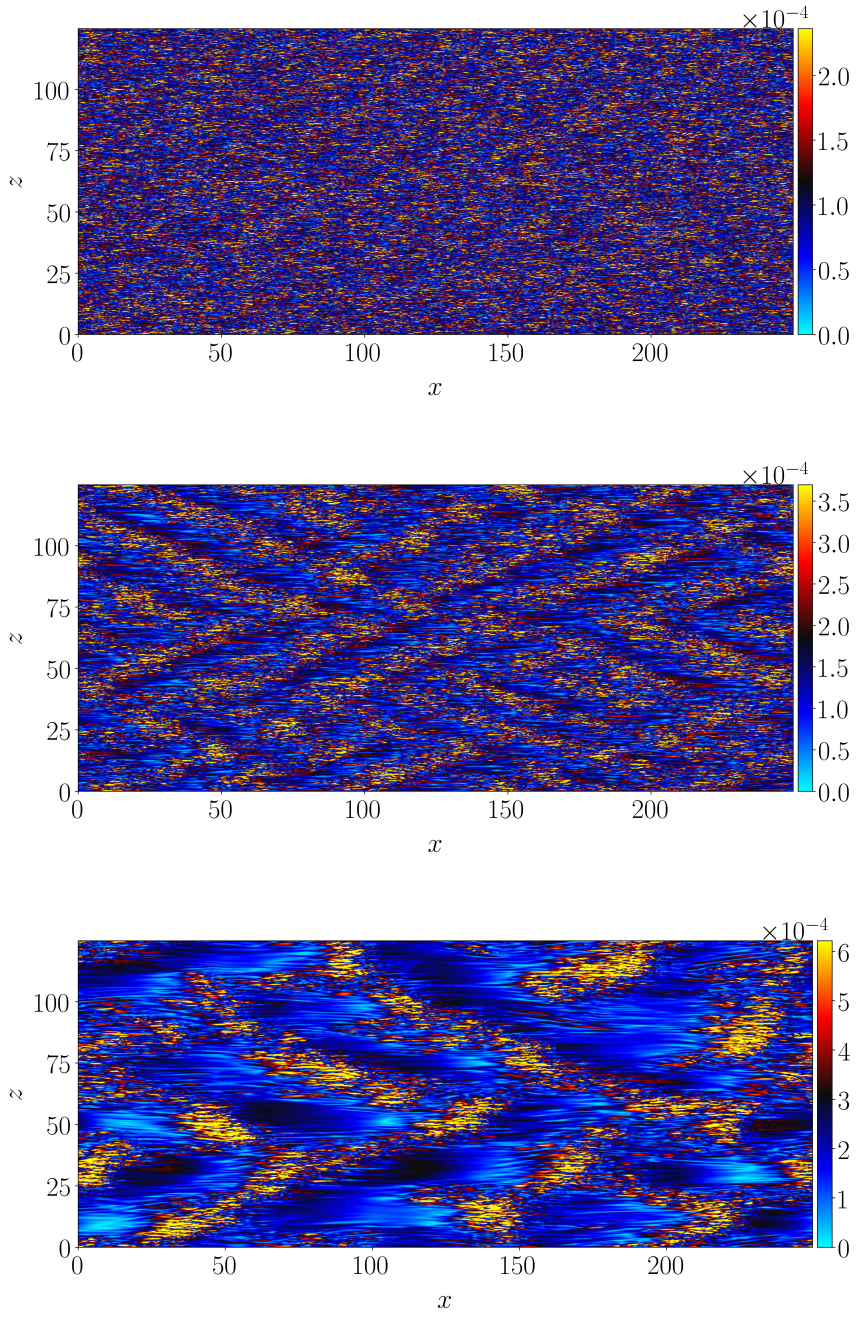

FIGURE 3.14 – Pressure-driven pPf for Re_τ=100, 80 and 60. Isolevels of the instantaneous wall shear stress fluctuation $\tau'(x, z, t)$. Domain length $L_x = 250h$. From Ref. [14].

3.3.3 Bifurcation diagrams

Qualitative diagrams

Qualitative bifurcation diagrams can be deduced from the database obtained earlier. The protocol chosen to determine these bifurcation diagrams is always the same and is standard in the presence of hysteresis : the starting point is the featureless regime (no matter how it was found) and the exploration is

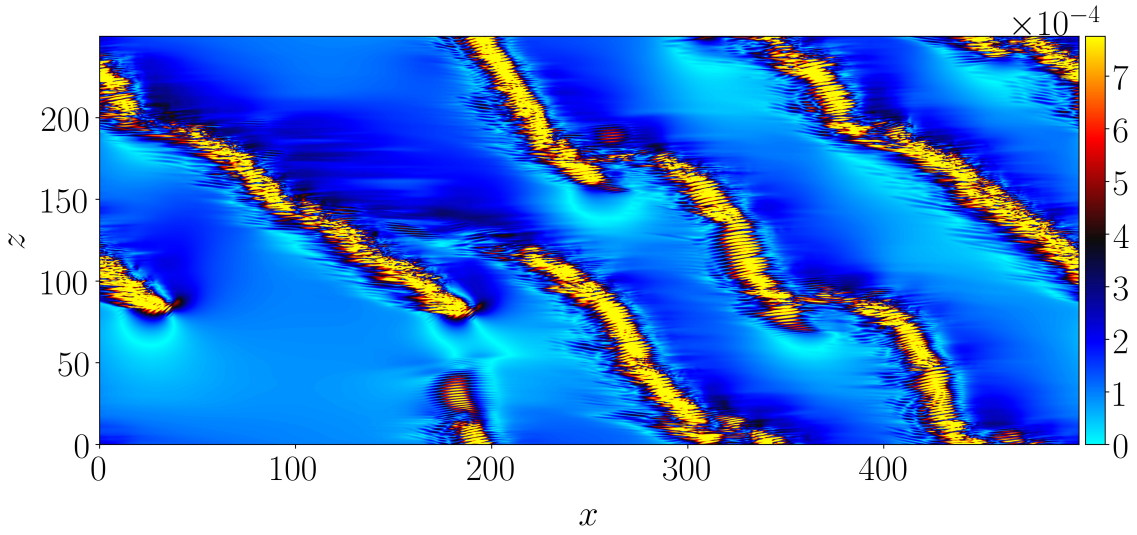

FIGURE 3.15 – Pressure-driven pPf for $Re_\tau = 40$. Isolevels of the instantaneous wall shear stress fluctuation $\tau'(x, z, t)$. Domain length $L_x = 500h$. From Ref. [14]

carried out by *quasi-adiabatically* reducing the Reynolds number. The descent is in practice never strictly adiabatic, and the easiest way is to choose small enough steps in Re with long enough plateaus between parameter changes. In analogy with figure 3.1 for pipe flow, the qualitative bifurcation diagrams for pCf and pPf are represented along a unidimensional axis in figure 3.16, respectively top and bottom.

Several comments can be made at this stage. These two flows have in common the presence of an STI/pattern regime lcoated between the laminar and the turbulent ones. As an order of magnitude the width of the STI zone occupies one quarter of the value of the critical value Re_g. But these two flows also display clear qualitative differences. The fact that the numbers do not match is secondary and can be assigned to the historically different definitions of Re (as discussed in Refs [238, 248]). There are also clear qualitative differences. In pCf the STI zone seems to consist of one part only, whereas in pPf there is a change of behaviour for Re_τ slightly above 50 as pointed out only recently by Shimizu & Manneville [244] and mentioned on the previous page.

Wavelengths and angles

On a more quantitative basis, as far as pCf is concerned the pattern range lies approximately in the interval $Re \in (330 : 410)$. As far as pressure-driven pPf is concerned, it is restrained to $Re_\tau \in (50 : 90)$. We see in figure 3.12c that several values of the unsigned angle as well as several values of the wavelengths coexist within the same snapshot. This should act as a warning : wavelengths and angles might not be uniquely determined by Re. This is only one of the reasons why angles and wavelengths have not been much documented so far. Another reason is simply that such statistics have been sufficiently dominated by finite-size effects.

More recent computational data has been gathered for the patterns of pressure-driven pPf [14]. Wavelengths and angles have been extracted using several standard methods from image processing. Streamwise/spanwise wavelengths are reported versus Re_τ (occasionally denoted Re_τ^G) in figure 3.17a, whereas angles are reported in figure 3.17b and compared with recent available experimental/numerical data. Despite the good quantitative match, a solid trend emerges : the angle θ gets steeper as Re decreases, culminating with $\theta \approx 45°$ close to the critical point Re_τ. Analyzing the wavelengths λ_x and λ_z shows that they both evolve similarly with Re for $Re_\tau \geq 60$. Consequently the ratio λ_z/λ_x and the angle

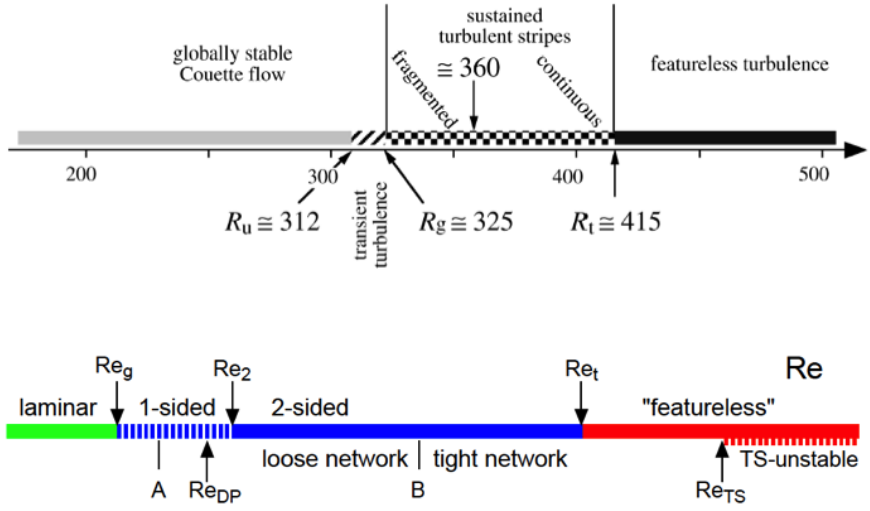

FIGURE 3.16 – Qualitative bifurcation diagrams for pCf (top) and pPf (bottom) (from Refs. [248] and [244], respectively).

$\theta = \arctan \frac{\lambda_z}{\lambda_x}$ stay approximately constant for $Re_\tau \geq 60$. The increase of the angle $\theta = \arctan \frac{\lambda_z}{\lambda_x}$ for $Re_\tau \leq 55$ is linked to an increase in the wavelength λ_z for $Re_\tau \leq 55$ that is no longer compensated by an increase in λ_x. This suggests yet another possible bifurcation point, that lies strictly between the usual thresholds Re_g and Re_t, and more precisely in the interval $(55, 60)$.

Barkley and Tuckerman [238] have suggested, from the streamwise momentum balance expressed in the laminar zones, one of the rare quantitative formulas of this field as a link between angles and wavelengths. If θ refers to the angle between the stripes and the streamwise direction, Λ is the wavelength of the patterns, then

$$\frac{Re \sin\theta}{\lambda} \approx \pi, \tag{3.1}$$

where λ, λ_x and λ_z (respectively the wavelength, the streamwise wavelength and the spanwise wavelength) are connected geometrically via

$$\frac{1}{\lambda^2} = \frac{1}{\lambda_x^2} + \frac{1}{\lambda_z^2}. \tag{3.2}$$

Eq. (3.1) suggests, consistently with e.g. figure 3.12c, that for fixed Re steeper stripe angles are associated with sparser turbulence. Statistics gathered from many published papers (as of 2011) have been gathered in Ref. [249] in an effort to directly verify the validity of Eq. 3.1. They are displayed in figure 3.18. A clear visual conclusion is as follows : the larger the domain size considered (both experimentally or numerically speaking), the more valid the formula.

Turbulent fraction

The instantaneous turbulent fraction is simply the percentage of the wall covered on average by turbulent motion. In line with experimental studies [217], it can be defined using standard thresholding of appropriate wall quantities. Using for example the wall-normal velocity at the centerplane $v = v(y = 0)$

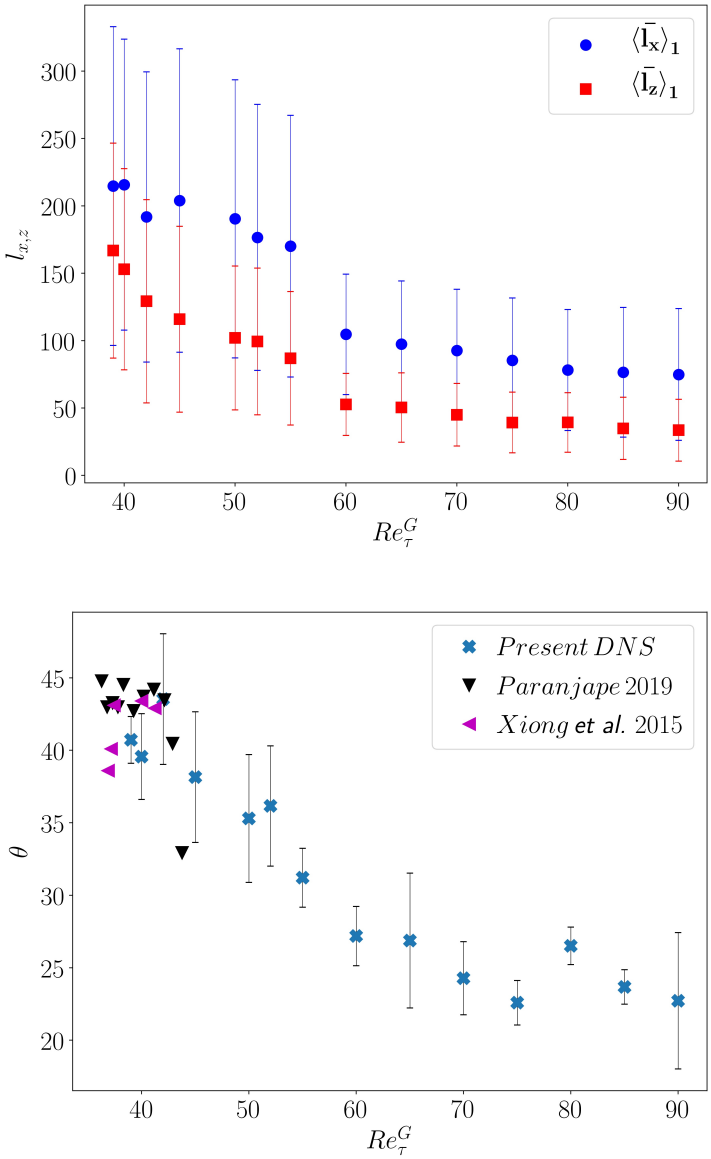

FIGURE 3.17 – Statistics of (top) : streamwise and spanwise wavelengths denoted respectively l_x and l_z, and (bottom) : angle θ with respect to the streamwise direction in pPf, taken from Ref. [14]. Comparison to angles reported in Refs [233] and [165].

(which vanishes exactly for laminar flow) leads to the instantaneous definition of the turbulent fraction $F_T(t)$ as

$$F_T(t) = \frac{\int \delta(v^2(x,z) > a) dx dz}{\int dx dz}, \tag{3.3}$$

while the time-averaged turbulent fraction, an order parameter, is classically defined by

$$< F_T >= \lim_{T \to \infty} \frac{1}{T} \int_0^T F_T(t) dt. \tag{3.4}$$

Equivalently other definitions can be used, without any clear influence on the results. We begin by describing the bifurcations of $< F_T >$ for pCf. The mean value of F_T versus Re, gathered in principle over

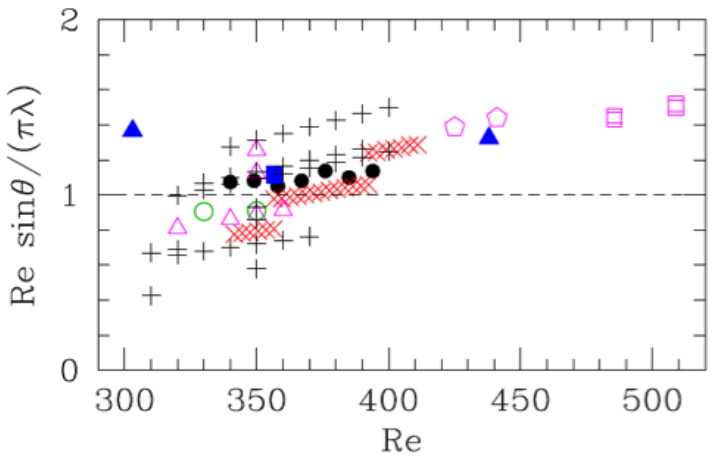

FIG. 16. (Color online) Re sin $\theta/(\pi\lambda)$ for turbulent-laminar patterns in experiment and computations in various wall-bounded shear flows. Experimental measurements by Prigent *et al.* (Ref. 3) of plane Couette flow (full black circles) and Taylor–Couette flow (red crosses). Experimental measurements of rotor-stator flow by Cros and Le Gal (Ref. 10) (full blue triangles). Simulations of plane Poiseuille flow by Tsukahara *et al.* (Refs. 20 and 21) (full blue square). Simulations of Taylor–Couette flow by Meseguer *et al.* (Ref. 24) (hollow magenta pentagons) and by Dong (Refs. 22 and 23) (hollow magenta squares). Simulations of plane Couette flow by Duguet (Ref. 16) (hollow green circles), by Philips and Manneville (Ref. 19) (hollow magenta squares), and by Barkley and Tuckerman (Ref. 13) (black crosses).

FIGURE 3.18 – Statistics gathered from many numerical and experimental studies as of 2011, compiled by [249] together with original caption with references therein.

inifinite times, are reported in figure 3.19, together with the values of F_T at intermediate times (corresponding to the time of nucleation). We note that the turbulent fraction at intermediate times grows continuously with Re, indicating that more and more spots get nucleated as Re increases. The values of $< F_T >$, on the other hand, display a clear discontinuity near $Re \approx 325$. This is perfectly consistent with the experimental results of Bottin *et al.* [43, 217] who also predicted a discontinuous transition from measuring $< F_T > (Re)$. The discontinuity at large times constrasts with the continuity at intermediate times. It shows that for $Re < 325$, nucleated spots shrink and collapse, whereas for $Re > 325$ a growth process takes place and the array of initial spots needs to mutate into a proper network of mature turbulent stripes before statistical equilibrium is reached. The good match, both quantitative and qualitative, between simulation and experiments is only partial : although the diagrams of $< F_T(Re) >$ match well, the oblique stripes from figure 3.12 have no experimental counterpart in Ref. [217] whereas they compare qualitatively well with Prigent's experimental visualisations. Perhaps more importantly, the match between computational and experimental results, although encouraging, does not imply that finite-size effects have been mastered. On the contrary, both studies [66] and [217] suffer from similar limitations due to finite-size effects.

The analysis of $< F_T >$ in pPf is slightly more difficult for several reasons : there is no solid experimental data for comparison, and there are additional bifurcations. It was chosen to compute $< F_T >$ based on the observable $E_v = \int v^2 dy/2$. It is illustrated versus Re_τ in figure 3.20 for different values of the thresholding. As for pCf though, the trend is monotonic : $< F_T >$ decreases with decreasing Reynolds number. Consistently with the observations above and in Ref. [244], a bifurcation occurs near $Re_\tau = 50$, visible in all curves via a change of convexity. As already pointed out in Ref. [12], the values of $< F_T >$ depend strongly on the choice of thresholding, despite the lack of strong qualitative difference. The amplitude of the fluctuations around the mean value of F_T increases around Re_τ =50 and decreases for

lower Reynolds numbers.

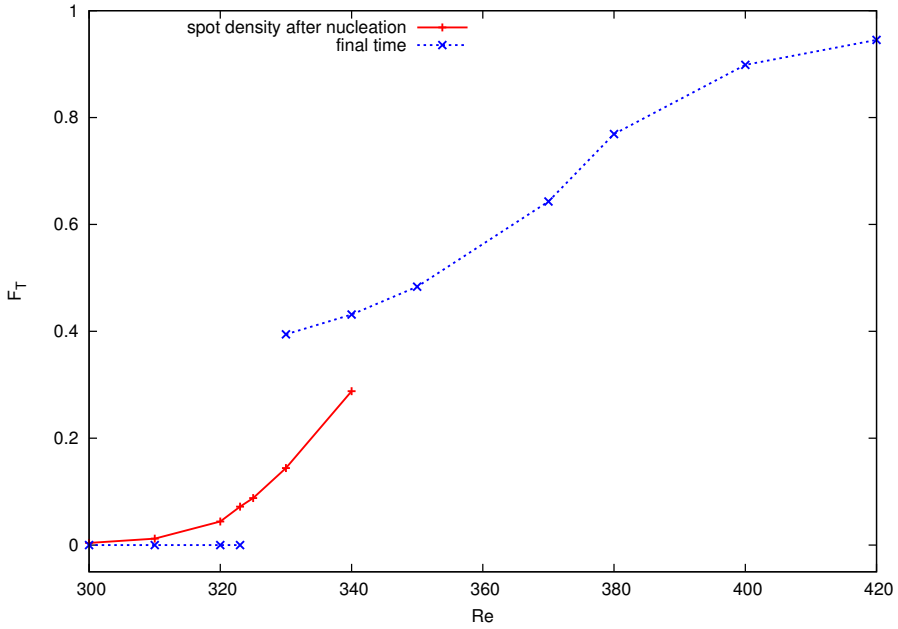

FIGURE 3.19 – Turbulent fraction F_T as a function of Re in pCf : The dotted (blue) line corresponds to the value at equilibrium, whereas the full (red) line corresponds to the turbulent fraction at nucleation time. From [66].

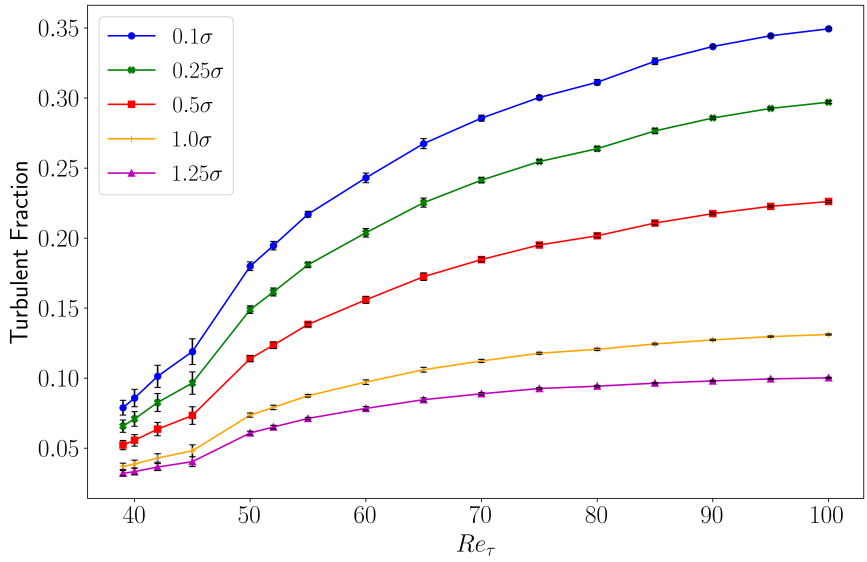

FIGURE 3.20 – Turbulent fraction F_T as a function of Re_τ in pPf, based on the observable $E_v = \int v^2 dy/2$, with error-bars based on the standard deviation $\sigma(E_v)$. Different cut-off values have been used, each of the form $< E_v > +\alpha\sigma(E_v)$. Same database as Ref. [14]. Courtesy Pavan Kashyap.

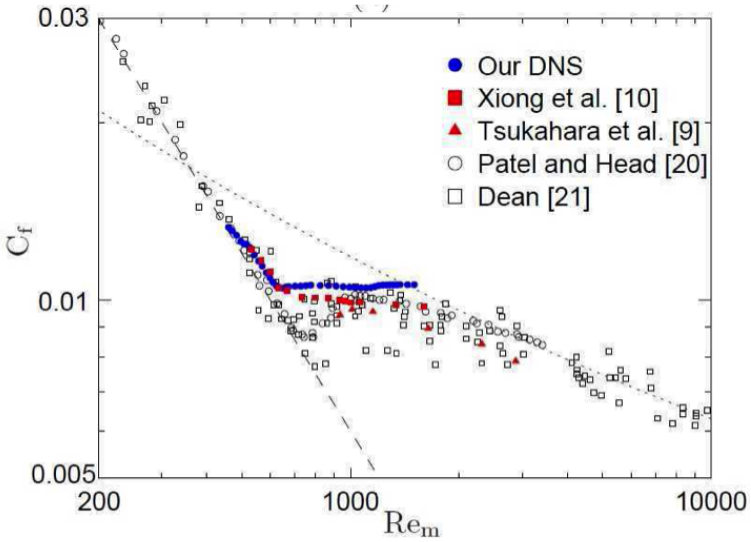

FIGURE 3.21 – Friction factor C_f vs bulk Reynolds number Re_m in plane channel flow [244].

Friction factor

It is also possible to return to the original Moody diagram (also named Fanning for channel flow) for the mean friction factor $C_f = C_f(Re)$, where by convention Re is understood as the bulk Reynolds number Re_b. We note that C_f can be rewritten as $C_f = 2(Re_\tau/Re_b)^2$ independently of the chosen protocol. For pressure-driven pPf, C_f is shown in figure 3.21 taken from Ref. [244]. The laminar branch $C_f \sim Re^{-1}$ as well as the experimental Prandtl law $C_f = O(Re^{-\frac{1}{4}})$ have been indicated for clarity. Two regimes intermediate between the laminar and the turbulent one are found. The first regime, in order of decreasing Re, is the pattern regime with the two competing orientations, in the approximate interval $700 \leq Re_m \leq 1600$, i.e. $50 \leq Re_\tau \leq 90$. It is characterised in a first approximation by constant C_f. Note that, almost 100 years after the determination of the first Moody diagram, this is a new result. Statistics in smaller domains had not yet revealed this property of constant C_f, which might then be a property of the thermodynamic limit only. The second regime occurs for $Re_\tau \leq 50$ only, and features a value of C_f much closer to its laminar counterpart. This is the regime with one dominant orientation, characterised by finite-length stripes in weak interaction with another [14, 165, 234, 246].

The direct implications of a conserved quantity (here C_f) are not yet known. $C_f = cst$ implies mathematically that the variations of Re_τ and those of Re_b are linked in a linear way. The value of C_f in the pattern regime seems in a first approximation to be the same for all shear flows and is found to be very close to 0.01. This number could well be a *universal constant* of the patterning regime with a weak case-dependence, analogous in that respect to the von Kármán constant for developed turbulent flows [250]. Another analogy, certainly naive and incomplete but closer to the realm of phase transitions, is the (p, v) diagram for a van der Waals mixture [251]. The constitutive law of a van der Waals mixture is given by $(p + \frac{a}{v^2})(v - b) = RT$. As the volume available to the confined gas is progressively increased, the transition from liquid to gas proceeds through a plateau in the pressure. The value of the pressure at the plateau is determined by the equality of the chemical potentials of the two pure phases. Note that the van der Waals gas is a classical example of thermodynamically isolated system, hence of equilibrium statistics, in contrast with the present non-equilibrium example of a shear flow. In addition, the phase transition in a van der Waals mixture is the typical example of first-order phase transition, a concept which does not have a strict analog in the hydrodynamic case because free energies are not defined. Nevertheless there is a rich potential to explore from this analogy in terms of nucleation and front propagation [179]. For instance the notion of Gibbs plateau is intrinsically linked to the existence of a latent heat, and it would

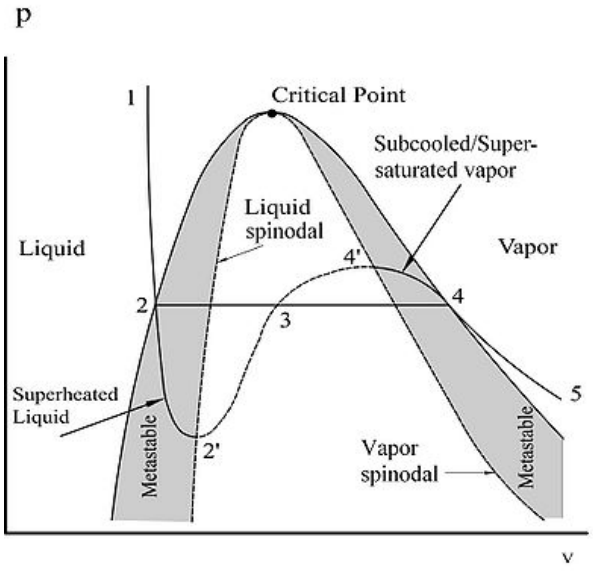

FIGURE 3.22 – Thermodynamic (p,v) diagram for a van der Waals mixture.

be interesting to test how far such cross-disciplinary analogies can be pushed. Another example is the relevance of the concept of unstable edge state to the present picture : is there for instance a robust link between the unstable branch in the thermodynamic diagram of figure 3.22 and the edge branch ?

3.4 The directed percolation hypothesis

3.4.1 Concept and motivation

As demonstrated earlier and summarised in figure 3.23, the turbulent fraction in pCf seems to undergo a discontinuity at a critical Reynolds number close to 325. This conclusion relies on a comparison between the experiments of S. Bottin [217] and direct numerical simulation [66]. Are there however any

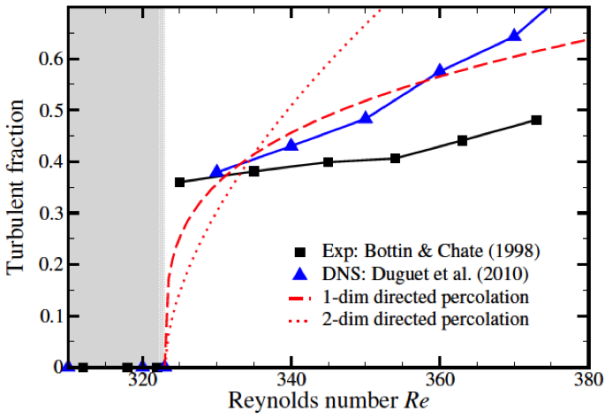

FIGURE 3.23 – Turbulent fraction F_T as a function of Re : Comparison between the experiments of S. Bottin [217], direct numerical simulation [66], and theoretical expectation from directed percolation theory (continuous transitions). Taken from Ref. [252].

analytical theories to rely on ? Nucleation theory is intrisically a first-order transition theory, and it is a priori relevant to explain how laminar-turbulent fronts start to move, but its inability to support any sustained laminar-turbulent coexistence makes it poorly adapted. In contrast, the series of experiments and numerical simulations in the 1990-2000s [43, 63, 188] has highlighted the possibility to have on-site relaminarisation at least for localised turbulent structures. Moreover, a few computational works, e.g. Xiong *et* al. [233] have reported bifurcation diagrams based on other (intensive) observables, e.g. the product ReC_f in channel flow. Their results suggest a continuous transition for this choice of order parameter rather than the discontinuous transition put forward until 2010. Looking back in the earlier Taylor-Couette literature, a few studies actually also suggest results for $F_T(Re)$ consistent with continuous rather than discontinuous transition [208, 253]. In principle, such results become robust in the so-called thermodynamic limit of infinitely large domains over infinite observation times. The inconsistency between these results suggest remnant finite-size effects, but how is that possible given the huge domains considered ? As an illustration, the typical size of a minimal flow unit is $O(1)$ while the largest domains used so far [66, 224] included at least 10^4 such "subdomains", a priori a large enough number even in the absence of any reference. The concept of "subdomain" is relatively fuzzy, nevertheless it proves useful when modelling complex phenomena using cellular automata. This is the ideal size for the correlated sub-systems such that a network of such connected subsystems behaves like the macroscopic system. B. Hof and co-authors questioned the relevance of the MFU concept when it comes to determining the ideal size of a sub-system over which there is a finite probability to relaminarise. They hypothesized correctly that the correct size of a "sub-unit" for transitional shear flows should correspond more to the natural wavelength of laminar-turbulent stripes rather than that of minimal flow units. In other words, STI should correspond to the interaction of neighbouring stripes rather than streaks. Using this point of view, if the turbulent flow can accomodate an arbitrarily low density, then by definition of "continuity" F_T should be continuous near zero (i.e. in the low-density regime). This is bad news in practice both for experimentalists and numericists, because it makes the determination of the continuous/discontinuous nature of the transition even more demanding in terms of domain size. Moreover, at equivalent front propagation speed, larger domains imply longer transition times too.

More is known if fluctuations are taken into account. Grassberger [254] and Janssen [255] have considered the case of a system with two states, one with fluctuations (our turbulent phase) and the other unique and absorbing, i.e. linearly stable and without fluctuations (our laminar phase). Moreover they have assumed no long-range order, a positive scalar order parameter (the turbulent fraction or the kinetic energy). In such circumstances when the effective dimension is one (e.g. in pipe flow), the system must undergo a phase transition which not only is continuous, but belongs to the *universality class of directed percolation*. In two or more effective dimensions (as for planar flows) both continuous and discontinuous phase transitions are possible. Belonging to a universality class is, from a physicist's point of view, a very strong property : it brings phenomena from different area of physics together through a set of unifying scaling relations. Like most critical phenomena, directed percolation is defined by a set of three independent critical exponents that depend only on the effective dimension. Suppose that the critical point is located at the value of the control parameter $R = R_c$, that $\varepsilon = R - R_c$ (possibly including a division by R_c), that the positive scalar order parameter is denoted ρ and its ergodic average $< \rho >$. We denote also by $P(l > L)$ and $P(t > T)$ respectively the cumulative probability distributions of finding a laminar subdomain of size l larger than a given L, or of duration t larger than a given T. Critical phenomena are characterised by the following scaling relations [256, 257]

$$\rho(\varepsilon = 0, t) \sim t^{-\alpha} \tag{3.5}$$

$$< \rho(\varepsilon) > \sim \varepsilon^{\beta} \tag{3.6}$$

$$P(l > L) \sim L^{-\mu_\perp}, \tag{3.7}$$

$$P(t > T) \sim T^{-\mu_\parallel}. \tag{3.8}$$

Equation (3.5) is valid at $\varepsilon = 0$ only, it actually allows one in practice to locate R_c and hence to define $\varepsilon = R - R_c$. Equation 3.6 expresses the continuity of the transition. Equations 3.7 and 3.8 are related to the distribution of large laminar gaps both in space and in time. The values of the critical exponents α, β, $\mu_\perp$ and $\mu_\parallel$ in one and two dimensions are respectively (within 3 digits of accuracy) 0.159, 0.276, 1.784 and 1.84 in 1D, 0.45, 0.583, 1.204 and 1.549 in 2D [258]. Genuine experimental evidence for systems behaving in this way is scarce, mainly due to the eternal limitations by finite-size effects. Physical systems closest to achieving such a critical scaling include for instance one-dimensional thermal convection [259], and in two dimensions electroconvection in nematics [258]. In transitional shear flows, although that idea had been around since Pomeau's 1986 article [179], convincing evidence for directed percolation (DP) at the onset of the turbulent regime was lacking until the work of Lemoult *et al.* [225] in one effective dimension (based on both experiments and numerics).

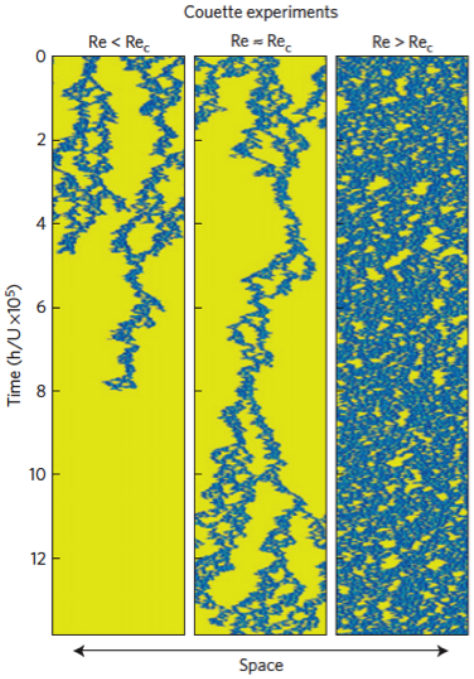

FIGURE 3.24 – Space-time diagram from [225]. From left to right : $\varepsilon < 0$ (transient), $\varepsilon = 0$ (critical) and $\varepsilon > 0$ (sustained STI).

The experimental scaling relations in Ref. [225], corresponding to an axially short Taylor-Couette set-up with a radius ratio very close to unity, are displayed in figures 3.24 and 3.25. Convincing evidence for DP in two-dimensional fluid systems, with a complete set of exponents, is so far restricted to the simulations of Chantry in a sinusoidal shear flow [243, 260] (with reduced resolution). Figure 3.27 is taken from Ref. [243], and it illustrates the domain size necessary to accomodate the relevant STI structures close to $\varepsilon = 0$, in comparison with domains used formerly in the literature (including Refs. [43] and [66]). It illustrates pegagogically why the numerical domain used in Ref. [66], which could accomodate only a maximum of 5 to 6 stripes at onset, necessarily suffered from finite-size effects.

Note that an algebraic fit of the form $F_T \sim (R - R_c)^\beta$ alone is in general not sufficient to validate the critical scaling hypothesis. This hypothesis is inseparable from the $F_T \ll 1$ framework, in other words from a 'dilute' regime where turbulence is scarce. An example of such misleading statistics can be found in [244] for the study of pressure-driven channel flow. Their figure 10 alone could suggest that the scaling $F_T \sim (R - R_c)^\beta$ is well verified in the range $R \in (1000 : 2500)$, which would be a very wide range. However the cumulative distributions of laminar gap size were computed in the same numerical domain in

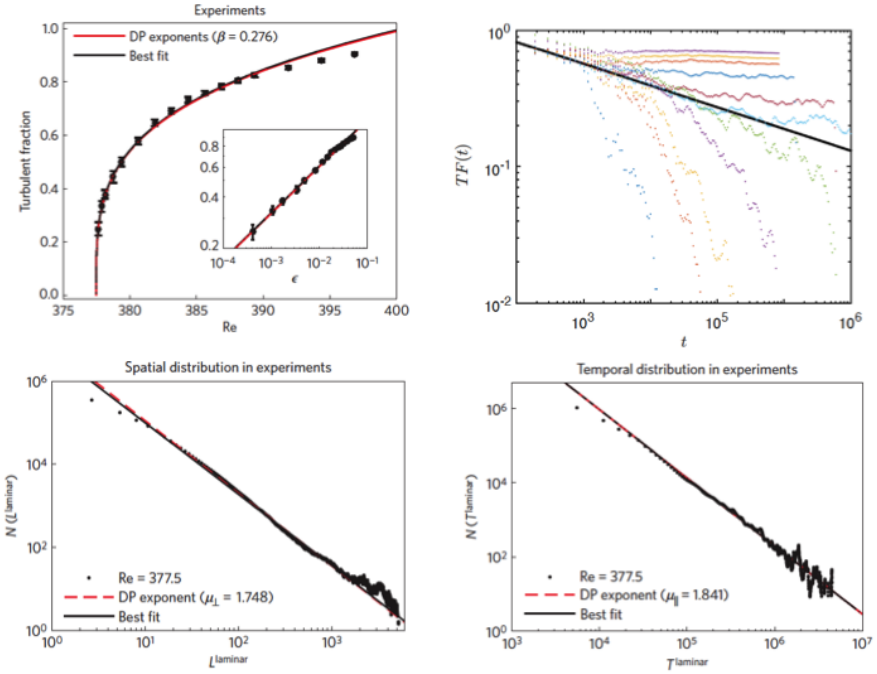

FIGURE 3.25 – Statistics in the experiment of [225]. From top to bottom, from left to right : equilibirum turbulent fraction $< F_T >$ vs. Re (inset : $< F_T >$ vs. ε), instantaneous turbulent fraction $F_T(t)$ vs t, CDF of laminar gap size, and CDF of laminar interval duration, all in log-log scale.

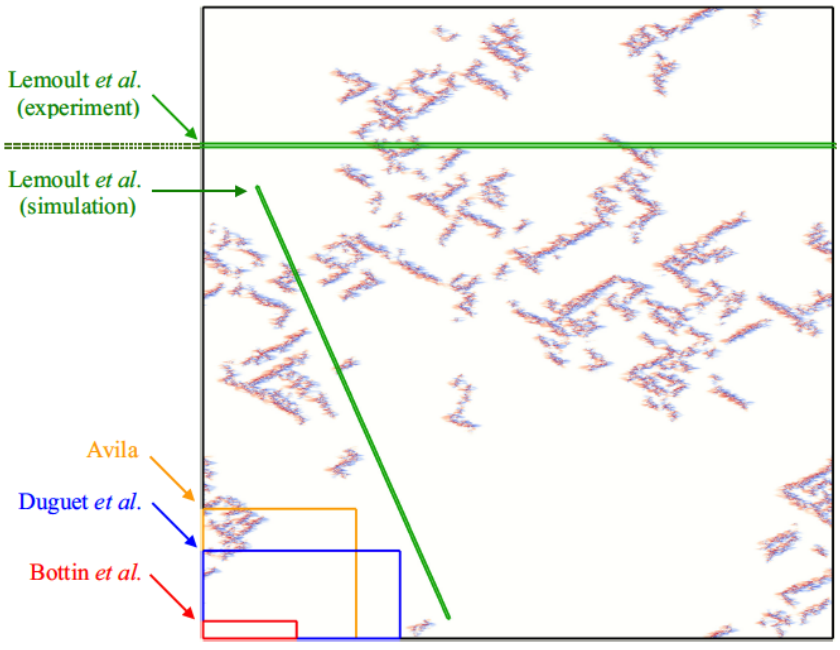

FIGURE 3.26 – Comparison of two-dimensional domains of shear flows [243], including references such as [65, 66, 225, 261].

Ref. [14]. Such distributions are expected to be algebraic close to the critical point, however they appear exponential for all parameters investigated. This demonstrates that a credible algebraic scaling for the turbulent fraction alone has no validity if the scaling relations are not all verified simultaneously. We illustrate this subtle point using two flow cases, namely pPf from Ref. [14] and aCf from Ref. [262]. The latter has been artificially widened in order to reduce finite-size effects due to the confinement [263]. For both flows the investigated distribution is compatible with an algebraic scaling of the form $F_T \sim \varepsilon^{\beta}$ with values of β compatible with DP theory (see figure 3.20 for pPf, and figure 3.28(top) for aCf). Figure 3.27 shows clearly that the distribution of laminar gaps in the streamwise direction of pPf is exponential for all parameters considered, as in standard STI regimes. This is in contrast with the case of aCf where, as Re is varied, figure 3.28(bottom) suggests a cross-over from an exponential towards an algebraic distribution, in other words a transition from an STI to a laminar regime via a critical scaling. The illustration of this point shows more generally that the parameter range where the DP scaling is expected to be valid is always very narrow. Moreover, this DP range differs markedly from the range of Re characterised by laminar-turbulent patterns.

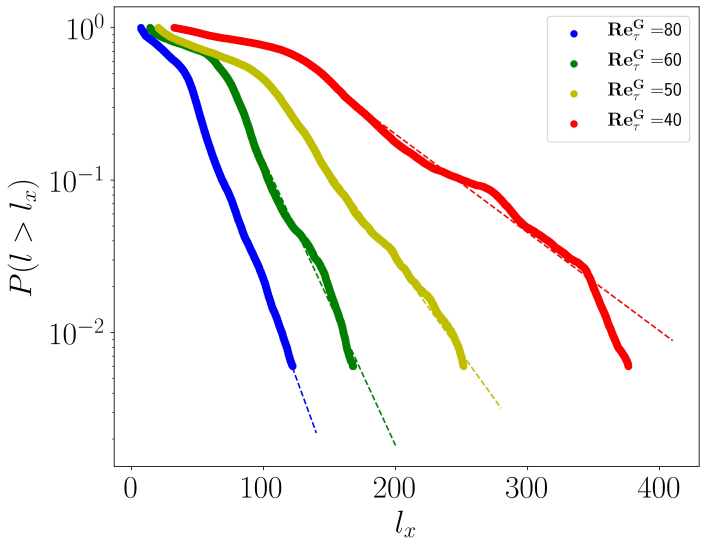

FIGURE 3.27 – Laminar gap statistics in computational pressure-driven pPf from [14]. The exponential statistics suggest that the critical point is still out of reach.

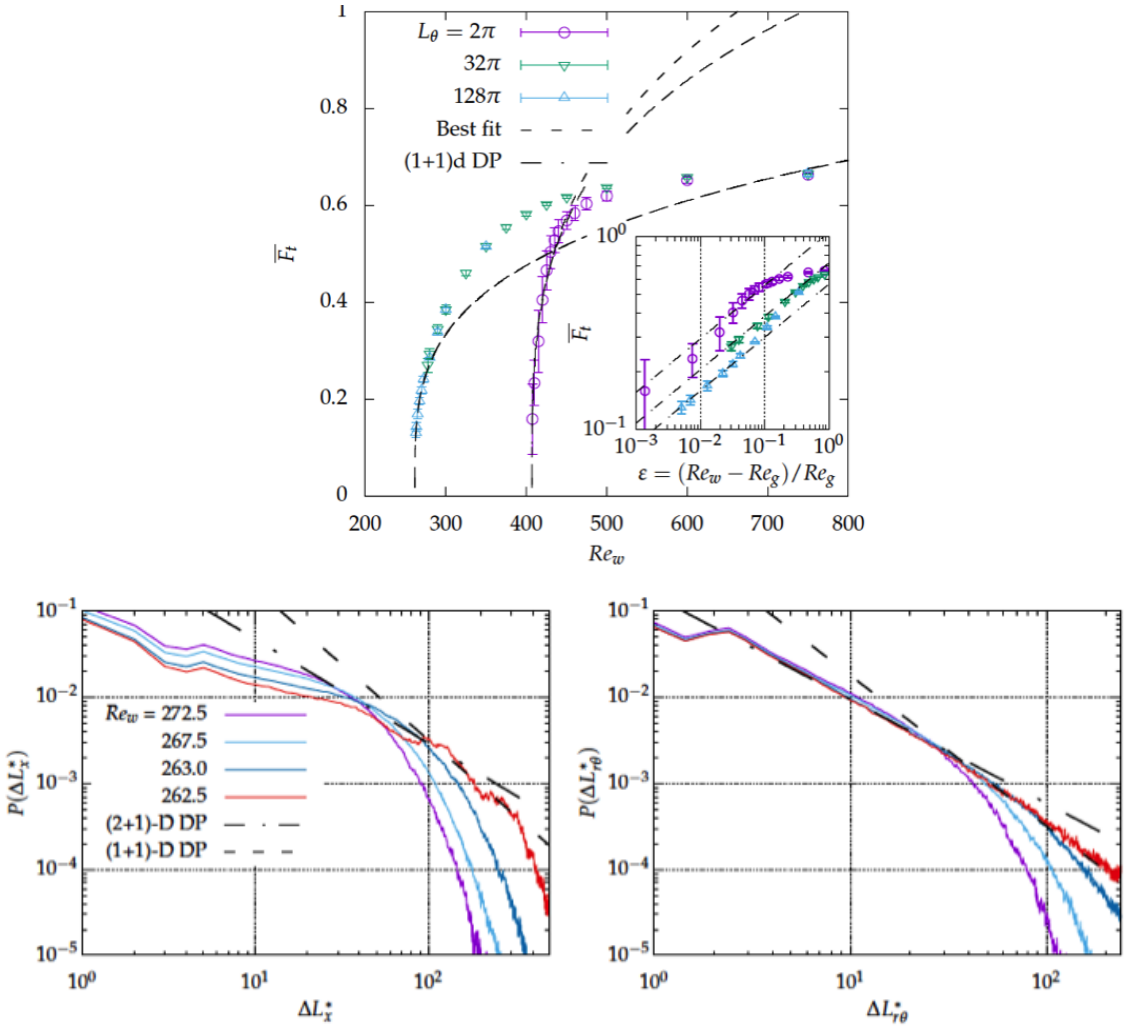

FIGURE 3.28 – Turbulent fraction vs. Re_w (top) and laminar gap statistics in the numerical simulations of aCf from [262], both in the axial (bottom left) and azimuthal direction (bottom right). The azimuthal extent has been artificially extended up to 128π. Unlike figure 3.27 the present cross-over from exponential to algebraic statistics suggests the proximity to the critical point.

3.5 Large-scale flows

3.5.1 Motivation

One of the most striking manifestations of the laminar-turbulent coexistence in the planar case is the obliqueness of the coherent structures. Such a property is intrisically *large-scale*, since at smallest scale the coherent structures are mainly streaks known to be aligned with the streamwise direction. We hence need to define a large-scale component for the velocity field. The mean flow, understood as the temporal average of the velocity field, is the first candidate for a large-scale flow, since the smallest scales corresponding to turbulent fluctuations are usually absorbed by averaging. In the case of banded turbulence, the mean velocity field has been computed and modelled by Barkley & Tuckerman [238]. The limitation inherent to the mean flow is its absence of time-dependence and hence of dynamics. The common alternative is to extract the large-scale component directly from the velocity by using spatial filtering. Spatial filtering approaches are routinely used in higher-Re turbulent flows for scale-by-scale energy budgets (see e.g. [264, 265] for pPf), in the presence of a multitude of scales. It is also central in the computational concept of Large Eddy Simulation, when scales below a given cut-off value are modelled instead of being simulated [266]. The low values of Re typical of the transitional regime are less complex. Owing to a spectral gap property, the more basic distinction between "large" and "small" velocity scales is sufficient for the present purpose of explaining the morphogenesis of stripes and spots in wall shear flows.

A relatively simple computational experiment demonstrates the role played by large-scale flows in the formation of oblique stripes. The main trick is to play with the periodicity of the computational domain in order to annihilate precisely the large-scale flow, in order to understand what is lost in its absence. Suppose, as in Refs [267] and [238], that the computational domain of plane Couette flow is extended in the spanwise direction ($L_z \gg 200$) but not in the streamwise direction ($L_x \approx 10$, comparable to MFUs). As a consequence of this *confinement* no large-scale flow can form with low wavenumber k_x. The spreading of turbulence in this system was analysed in Ref. [267] based on a statistical approach. Spatial proliferation occurs only above a critical Reynolds number $Re = Re_z \approx 310$. No marked intermittency is present for $Re > Re_z$. As an alternative, consider now the case (as in Ref. [238]) where the extension is in the streamwise direction only and not spanwise, i.e. $L_x \gg 200$ but $L_z = 10$. The expansion of turbulent patches occurs only above $Re = Re_x \approx 400$ in a slug-like fashion (fronts moving in the streamwise direction with well determined front speeds). In these two configurations, the dynamics of the turbulent fluctuations is heavily influenced by the choice of the numerical domain. These domains been considered because they are free of large-scale flow. When compared to the case ideally unaffected by finite-size effects (where both dimensions L_x and L_z are simultaneously large), the transitional range is found in an Re-interval of approximately 320–410 [66]. This range of values are numerically very compatible with the values of Re_x and Re_z. This suggests that the sustainment properties of the stripe patterns, including their infamous obliqueness, require a two-dimensional large-scale flow, with both components in x and z.

For the case of a simple steady parallel stripe pattern of plane Couette flow, the large-scale velocity integrated from wall-to-wall is depicted in figure 3.29 using white arrows. The steadiness of the pattern implies that the large-scale flow matches the mean flow considered in [238]. It features two-dimensional jets along each side of the stripes, flowing in opposite directions on either side. The large-scale flow is most prominent where a laminar–turbulent interface can be identified : it is weaker inside the turbulent zones and falls down to zero in laminar domains. The same properties of the large-scale flow around stripes are found in all other extended planar flows, such as pPf and cPf [14, 233, 269]. The case of pipe or duct flows will be mentioned later.

3.5.2 Large/small scale coupling

We base our analysis on the existence of two distinct characteristic scales. The small scales $O(h)$ correspond to the coherence of the turbulent fluctuations inside a turbulent patch (streaks). The large scales can be associated with the diffusive tails of the streaks and can be anticipated to scale like $O(hR)$.

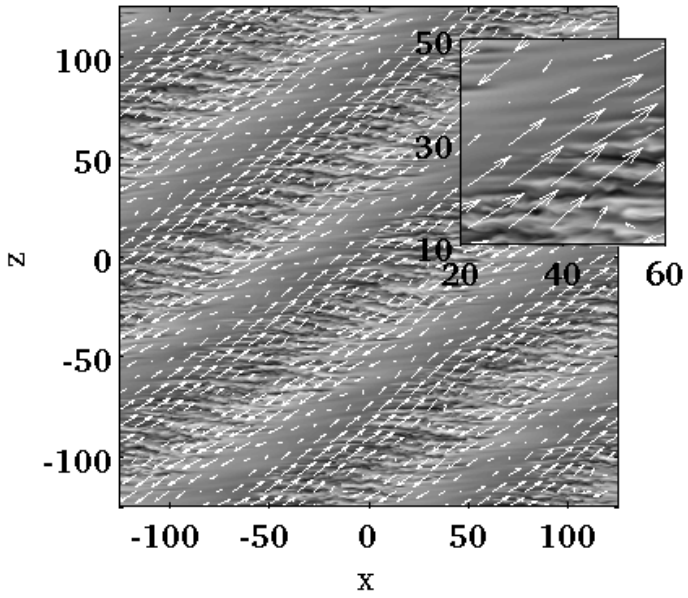

FIGURE 3.29 – Unfiltered and y-integrated large-scale velocity field of pCf for $Re = 350$, from [268].

The hypothesis $R \gg 1$ justifies the names "large" and "small" scales, however we make an additional hypothesis of scale separation, i.e. we assume the existence of a range of intermediate scales Λ between $O(h)$ and $O(hR)$ in which there is (ideally) no energy. We separate the flow field $\boldsymbol{u}$ into small scales $\tilde{\boldsymbol{u}} = H\boldsymbol{u}$ and large scales $\boldsymbol{U} = L\boldsymbol{u}$ such that

$$\boldsymbol{u} = L\boldsymbol{u} + H\boldsymbol{u} = \boldsymbol{U} + \tilde{\boldsymbol{u}}. \tag{3.9}$$

The large-scale flow $\boldsymbol{U} = L\boldsymbol{u} = G \star \boldsymbol{u}$ is frequently defined using the plane-isotropic Gaussian low-pass Gaussian kernel G :

$$G(x,z) = \frac{1}{\sqrt{2\pi}} e^{-\frac{(x^2+z^2)}{2\Lambda^2}}. \tag{3.10}$$

The high-pass filter is defined simply by the convolution kernel $I - G$. Although this decomposition can be carried out *a priori* for any flow field, the scale separation hypothesis is crucial in making it robust with respect to the choice of Λ. In practice, in units of h, the value of Λ can be chosen anywhere in the interval $(20 : 60)$ for most shear flows. $\boldsymbol{U}$ includes the laminar base flow as well as the large-scale modulations typical of STI. The residual $\tilde{\boldsymbol{u}}$ contains the rest, including what intuitively corresponds to the turbulent fluctuations.

We denote y-averaging with a bar $\bar{(.)}$. The incompressibility condition leads to the two-dimensional divergence-free condition in the xz-plane :

$$\partial_x \bar{U}_x + \partial_z \bar{U}_z = 0. \tag{3.11}$$

The momentum equation in the wall-normal (y) direction can be simplified using the scale separation hypothesis. It results in a coupled system of PDE for the large and small scales, respectively :

$$\left(\partial_t + \boldsymbol{U} \cdot \nabla\right) U_y = -\partial_y P + R^{-1}\nabla^2 U_y - L\left(\left(\tilde{\boldsymbol{u}} \cdot \nabla\right) \tilde{u}_y\right) \tag{3.12}$$

$$\left(\partial_t + \boldsymbol{U} \cdot \nabla\right) \tilde{u}_y = -\partial_y \tilde{p} + R^{-1}\nabla^2 \tilde{u}_y - H\left(\left(\tilde{\boldsymbol{u}} \cdot \nabla\right) \tilde{u}_y\right) \tag{3.13}$$

The second equation for the small scales can be simplified at the laminar–turbulent interface, which can be defined as a place where $\tilde{u}_y$ is small enough without being zero. This hypothesis leads to $H\left(\left(\tilde{\boldsymbol{u}} \cdot \nabla\right) \tilde{u}_y\right)$

being negligible, such that the second equation expresses now the simple advection of $\tilde{u}_y$ by the large-scale flow $\boldsymbol{U}$. We also note the presence of the small-scale presure gradient $-\partial_y \tilde{p}$ which does not generate any large-scale flow.

3.5.3 Spot structure

We begin by assessing the structure of the large-scale velocity field around an incipient turbulent spot, at early times before it proliferates. The emphasis is on the far field, which implies particularly large computational domains of size $L_{x,z} > 10^3$ and hence large memory requirements. In the case of plane Couette flow, a robust large-scale quadrupolar structure has been observed in earlier spot simulations [270, 271]. Fluid is sucked inward into the spot in the streamwise direction and ejected out of the spot in the outward spanwise direction as in figure 3.30 (left). As for spots in Poiseuille flow, the large-scale flow is found to differ in topology. The velocity field shown in figure 3.30 (right) is dipolar, consistently with the fact that the spot moves in the streamwise direction with respect to the mean fluid velocity. To our knowledge this dipolar structure had not been inferred from earlier spot simulations [272].

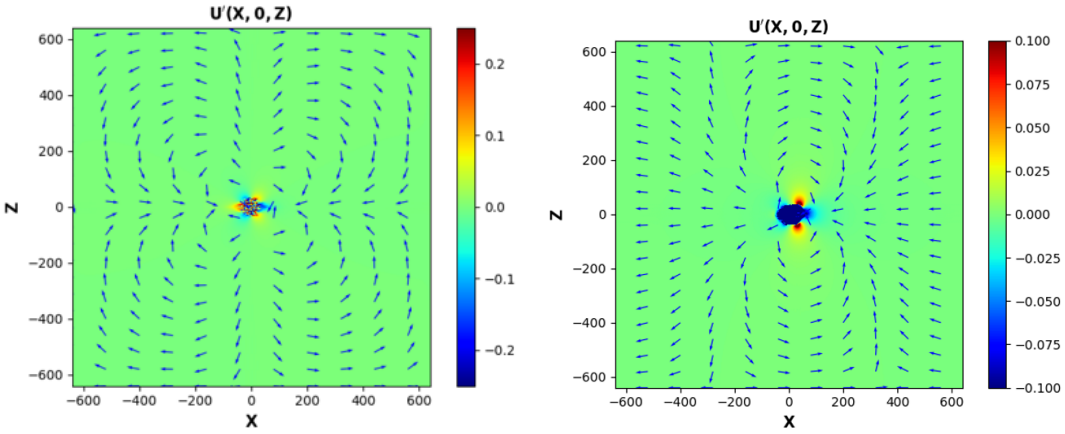

FIGURE 3.30 – Incipient spots in shear flows. Wall-to-wall integrated velocity field in the xz plane. Left : pCf for $Re = 400$, right : pPf for $Re = 3200$.

The far field velocity field can be extracted directly from the above simulations [273]. In contrast to the exponential scaling found e.g. for the localised steady state of Brand and Gibson [274], the velocity field decays algebraically with the distance from the spot. The analytical study of Ref. [275] aims at deriving this algebraic law directly from properties of the linearised Navier-Stokes operator. It is now confirmed by simulations that, independently of time and of the Reynolds number, the quadrupolar velocity field of pCf has its two in-plane components decaying like r^{-3}, with $r = \sqrt{x^2 + z^2}$ the distance from the center of the spot (see figure 3.31). The robustness of this scaling has been probed by reproducing the same spot in different computational domains of increasing size and with varying numerical resolution. For pPf as well as cPf, the decay is also algebraic but with an exponent -2 rather than -3.

These exponents match exactly those predicted for the velocity field of multipoles [273] in two spatial dimensions merely by kinematic theory. In this naive planar model sketched in figure 3.33, the spot corresponds to a two-dimensional distribution of vorticity $\omega(r, \theta)$ (in polar coordinates), strictly localised in the plane, so that the two-dimensional flow is irrotational outside $r > a$ (where a is larger than the size of the region where turbulent fluctuations are found). This is indeed verified approximately in our simulations when the y-integrated wall-normal vorticity ω_y is considered as visible in figure 3.32. The associated two-dimensional flow $(\bar{U}_x, \bar{U}_z)$ has been shown to be divergence-free in the plane in Eq. 3.11. It thus derives from a two-dimensional stream function Ψ verifying $\nabla^2 \Psi = \omega$. The solutions to this equation

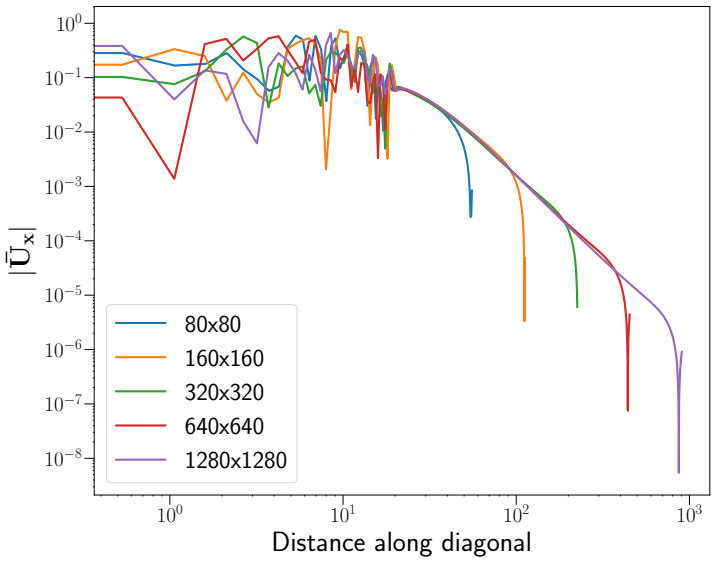

FIGURE 3.31 – Tails of y-integrated streamwise velocity $\bar{U}_x$ in pCf for $Re = 400$, measured along the diagonal $x = z$, shown in increasingly large computational domains (log-log coordinates) [273]. The solid line corresponds to an algebraic fit of exponent -3.

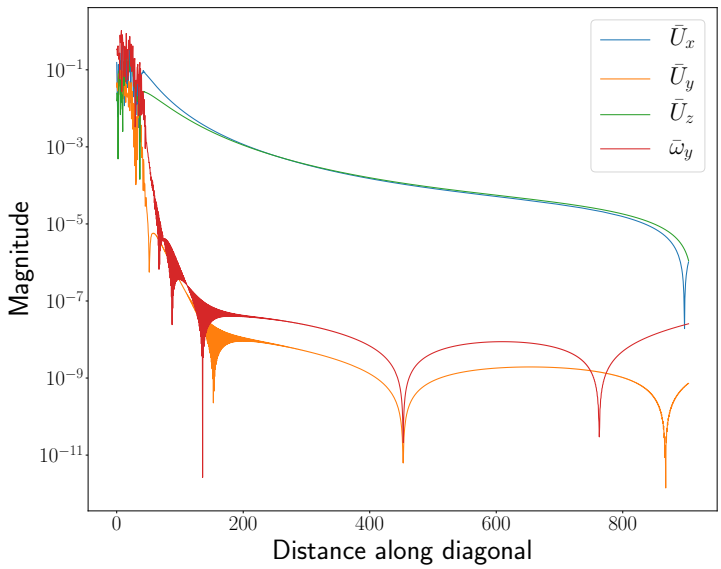

FIGURE 3.32 – Tails of y-integrated wall-normal vorticity $\bar{\omega}_y$ in pCf for $Re = 400$, measured along the diagonal $x = z$, shown in lin-log scale.

can be expanded in the far-field as Taylor series with respect to the small parameter $1/r$. This gives rise

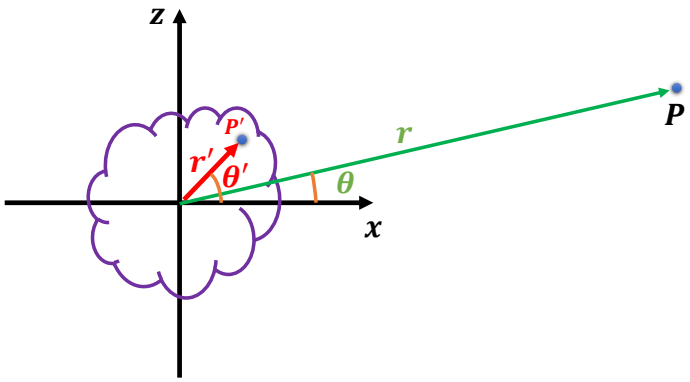

FIGURE 3.33 – Sketch of the two-dimensional kinematic model for spots.

classically to a multipolar expansion of the form

$$\Psi(r,\theta) = \sum_{k=1}^{\infty} \frac{1}{r^k} f_k(\theta) \tag{3.14}$$

$$= \frac{f_1(\theta)}{r} + \frac{f_2(\theta)}{r^2} + ... \tag{3.15}$$

The term in Eq. 3.15 corresponding to monopoles has been discarded for being unphysical. The velocity field deriving from this streamfunction can hence be expanded in the far field as the sum of a dipole (decaying as r^{-2}), a quadrupole (decaying as r^{-3}), and higher-order terms. Unlike Ref. [275] this kinematic approach makes no use of the momentum balance. It suffices to justify the algebraic nature of the decay of the velocity field as well as the exponents found. The upstream-downstream symmetry of the two-dimensional flow field $(\bar{U}_x, \bar{U}_z)$ in plane Couette flow has the effect of cancelling the dipolar component. This explains why, in this flow, the quadrupolar component dominates the flow with an algebraic decay rate steeper than in pressure-driven flows.

Generalising this kinematic theory to three dimensions turns out more tricky. In three dimensions, even when taking the confinement by the walls into account the exponents found do not match the measured exponents. This issue has been noted also in recent studies of the dynamics of pointwise swimmers in the Stokes regimes in active matter studies [276].

3.5.4 Stripe development from spots

From the point of view of *morphogenesis*, we can analyse the growth of a given spot, as it turns with increasing time into an oblique stripe of finite length [268]. The transient and time-dependent character of the velocity field is hence crucial in the present context. Moreover, whatever the shear flow type considered, spots at early times are symmetric, hence the emergence of oblique stripes requires a breaking of symmetry.

The growth of a turbulent patch is shown in Fig. 3.34 for $Re = 360$ along with the corresponding large scale flow $\left(\bar{U}_x, \bar{U}_z\right)$. The streamwise ends of a such a turbulent patch are characterised by so-called overhang regions where locally turbulent flow on one wall faces nearly laminar flow near the other wall, visible in figure 3.35. These regions correspond to a mismatch in the flow rates $\bar{U}_x \neq 0$, whereas $\bar{U}_x = 0$ everywhere else. As a consequence $\partial_x \bar{U}_x \neq 0$ in the overhang regions. Hence $\bar{U}_z \neq 0$ by virtue of Eq. 3.11. The resulting total large-scale flow is thus locally oblique with respect to the streamwise direction. This suggests that newly nucleated streaks at the tips of the spots are simply *advected by the large-scale*

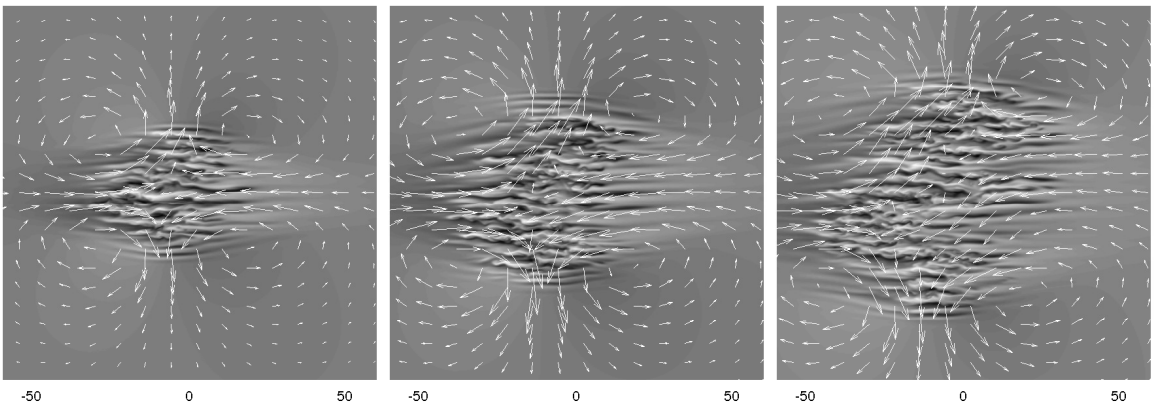

FIGURE 3.34 – Obliquely growing spot in plane Couette flow at $R = 360$ (grey : streamwise velocity in the midplane) and associated y-integrated large-scale flow $\left(\bar{U}_x, \bar{U}_z\right)(x, z)$ (arrows). From left to right : $t = 200,\ 300$ and 400. Simulations in a periodic domain with $\Lambda = 500$ and $1536 \times 33 \times 2048$ spectral modes. Only the subdomain $[-60 : 60] \times [-60 : 60]$ is displayed here.

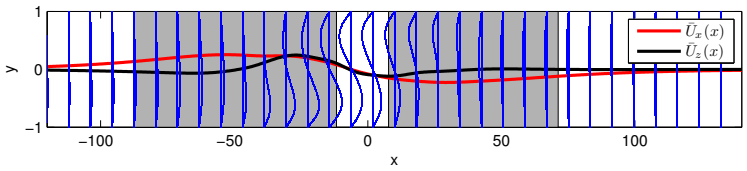

FIGURE 3.35 – PCF from [268]. Cut in the z direction.

flow, which itself has a non-zero angle with respect to the streamwise direction. As a consequence of the non-zero angle between $\boldsymbol{U}$ and the streamwise direction, the growth of the spots is distorted by the presence of the large-scale flow and proceeds obliquely as well [268].

We can now suggest a mechanism to explain the emerging obliqueness of stripes. A forming stripe pattern should be seen as an initial array of growing turbulent spots that consist of small-scale streaks of finite streamwise extent. The main mechanism for the expansion of turbulence in the spanwise direction proceeds via the stochastic nucleation of new streaks [267]. The small fluctuations of $\tilde{u}_y$ near the interface, the signature of newly nucleated streaks, are advected in the direction of $\boldsymbol{U}$, which is oblique with respect to the x direction. The local orientation of $\boldsymbol{U}$ hence determines the direction in which the turbulent patch elongates every time a new streak is added in a nucleation event.

The angle θ measured for turbulent stripes hence appears as a large-scale quantity. Stochasticity of the streak generation process acts on the large-scale flow as intrinsic noise that can even break the symmetry $\theta \leftrightarrow -\theta$ after a sufficiently long time. The global labyrinthine aspect of spots observed at late times results from a random sequence of symmetry breakings occuring at the extremities of the developing spot. For larger values of $R \geq 380$, streaks start to elongate in the streamwise direction while their spanwise rate of nucleation increases rapidly [267]. Those combined effects accelerate the spreading of the turbulent spot while the obliqueness of the turbulent interfaces is qualitatively preserved. As the spot continues to grow, other such discrete extreme events (named "budding" in the study of Ref. [277]) can allow for the outgrowth of additional stripes. The resulting field can be described as a labyrinthine spot shown in figure 3.36 [66]. The success of this approach is unfortunately limited by its inability to predict accurately the angle of the resulting laminar-turbulent interfaces.

The mechanism above has been the subject of experimental verification including a series of experiments carried out in the Paris region. In the context of pCf, the experimental study by Couliou and

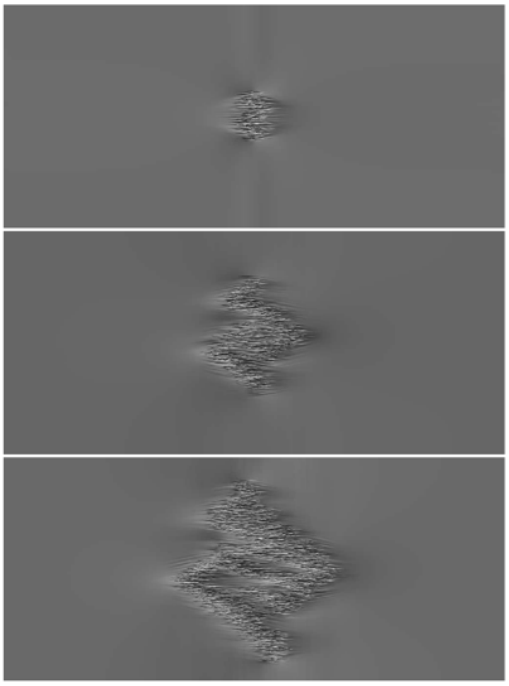

FIGURE 3.36 – Labyrinthine development of a turbulent spot in pCf for $Re = 350$. From top to bottom : t=201, 1043 and 2102 h/U_w.

Monchaux [220, 221], based on Particle Image Velocimetry, as mimicked the numerrcal strategy of Ref. [268]. The spectral gap hypothesis is satisfied. The quadrupolar structure of the velocity field and its orientation shown in figure 3.37 are consistent with the numerical predictions, although y-averaging cannot be performed from planar PIV data.

Experimental investigations of other shear flows have been performed as well using the same methodology, in pPf [278] as well as more recently cPf [269]. The structure of the large-scale flow around the pPf spot was initially described as quadrupolar although the lack of upstream/downstream symmetry suggests the presence of a dipolar component, consistently with Ref. [273]. The far field predictions are however far from being verified, and the nature of the decay of the velocity field can not be assessed from this experimental data. Given the short spanwise extent used ($L_z = 7.5h$) this is not really a surprise, and much wider domains are required to verify these predictions.

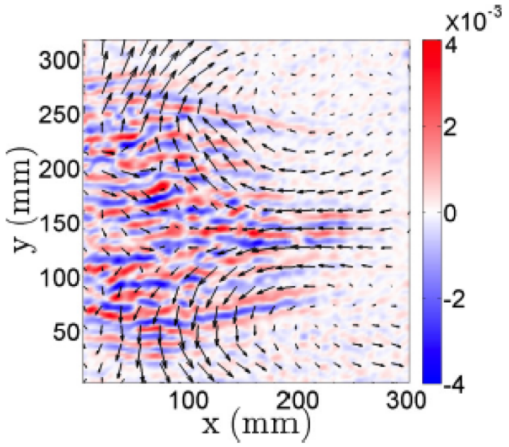

FIGURE 3.37 – Large-scale around a turbulent spot in experimental pCf, from Ref. [221].

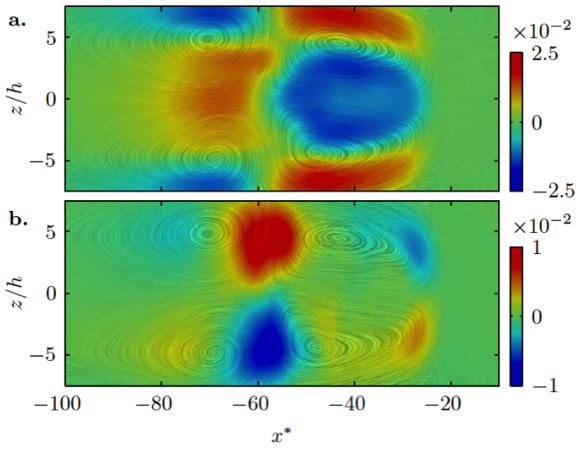

FIGURE 3.38 – Large-scale around a turbulent spot in a narrow channel of width $L_z = 10$ from Ref. [227] : streamwise velocity component (top), spanwise velocity component (bottom).

3.5.5 Helical spots in annular flows

In this subsection we wish to explore the limits of the previous theory by examining a few flow cases where the spanwise extent can be conveniently varied. We focus on shear flows inside an annular geometry consisting of two coaxial cylinders. The radius ratio r_i/r_o is denoted as η. The geometry (and terminology) is common to the Taylor-Couette family but the flow is forced axially rather than azimuthally. Two flow cases are actually considered : annular Poiseuille flow (aPf), where an axial pressure gradient is applied, and annular Couette flow (aCf), where the inner cylinder moves axially with a steady positive velocity. In the $\eta \to 1$ limit, aPf coincides with pPf whereas aCf coincides with pCf, they hence display exactly the same phenomenology as far as the transitional range is concerned. For finite η, e.g. here $\eta = 0.8$, by varying Re and making sure that the domain is long enough it is not difficult to identify a transitional range characterised by helical stripes wrapped around the inner cylinder. These stripes are directly comparable with the oblique stripes of pPf once unwrapped and mapped onto a planar domain. In particular the large-scale flow can again be computed, and it displays the same property of being parallel to the laminar-turbulent interfaces. However the pitch angle of the stripes apparently decreases together with η. Lowering η below 0.5 for aCf, or 0.3 for aPf, brings unexpected results : the helical patterns are no longer found. For $\eta = 0.1$ the flow is still characterised by localised structures, however their dynamics features mainly splitting and decay, in a way much more reminiscent of cylindrical pipe flow than of pPf.

The theory invoked for the growth of the patterns [268], based on the presence of a large-scale flow, can again be used here in its steady version. It is actually simpler since it is based solely on the two-dimensional divergence-free property of the large-scale flow. Written in cylindrical coordinates consistent with the annular geometry, incompressibility is written :

$$\partial_x u_x + \frac{1}{r}\partial_r(r u_r) + \frac{1}{r}\partial_\theta u_\theta = 0. \tag{3.16}$$

An angle α with the streamwise direction can, as before, be defined by

$$\tan\alpha(x,\theta,t) = \left| \frac{\overline{U_\theta(x,\theta,t)}}{\overline{U_x(x,\theta,t)}} \right|. \tag{3.17}$$

where

$$\overline{(\cdot)} = \frac{\int_{R_i}^{R_o} r(\cdot)\,\mathrm{d}r}{\int_{R_i}^{R_o} r\,\mathrm{d}r}. \tag{3.18}$$

The key point is that the azimuthal extent of 2π can be interpreted as a large number in units of the gap $d = r_o - r_i$, if η is close to 1. Fig. 3.40 displays the inner and outer perimeters, resp. $L_{zi}(\eta)$ and $L_{zo}(\eta)$, in units of d as the radius ratio is varied. When $L_{zi}/d \gg 1$, the flow in the gap behaves as a planar flow. Otherwise the situation is closer to pipe flow with an effective dimension of one and no large-scale azimuthal flow. The intersection of an arbitrary line $L_z = \lambda_z^c$ with the curves $L_{zo}(\eta)$ and $L_{zi}(\eta)$ in Fig. 3.40 defines two values of η, respectively η_1 and η_2. This leads to three distinct ranges of values for η :

— for $0 < \eta \leq \eta_1$, there is no space for large scales in the azimuthal direction, neither at the inner nor at the outer wall. As a consequence $\overline{U_\theta} = 0$ for all r, and $\partial_x \overline{U_x} = 0$.
— for $\eta_2 \leq \eta \leq 1$, azimuthal large scales can form at both inner and outer walls : $\partial_\theta \overline{U_\theta} = -\partial_x \overline{U_x}$ with $\overline{U_\theta} \neq 0$. The situation is then analogous to the planar case where oblique laminar-interfaces can be sustained.
— for $\eta_1 \leq \eta \leq \eta_2$, the situation is mixed : azimuthal large scale flows cannot be accommodated at all locations in the cross-section. A probabilistic approach is required.

Since the exact values of η_1 and η_2 depend on the threshold λ_z^c, the qualitative conclusions above need to be verified numerically. Figure 3.41 shows, for $\eta = 0.2$, two values of Re for which the two types of inclinations ($\theta = 0°$ and $\theta \neq 0$) coexist spatially. Two antagonist effects likely to deviate from the planar

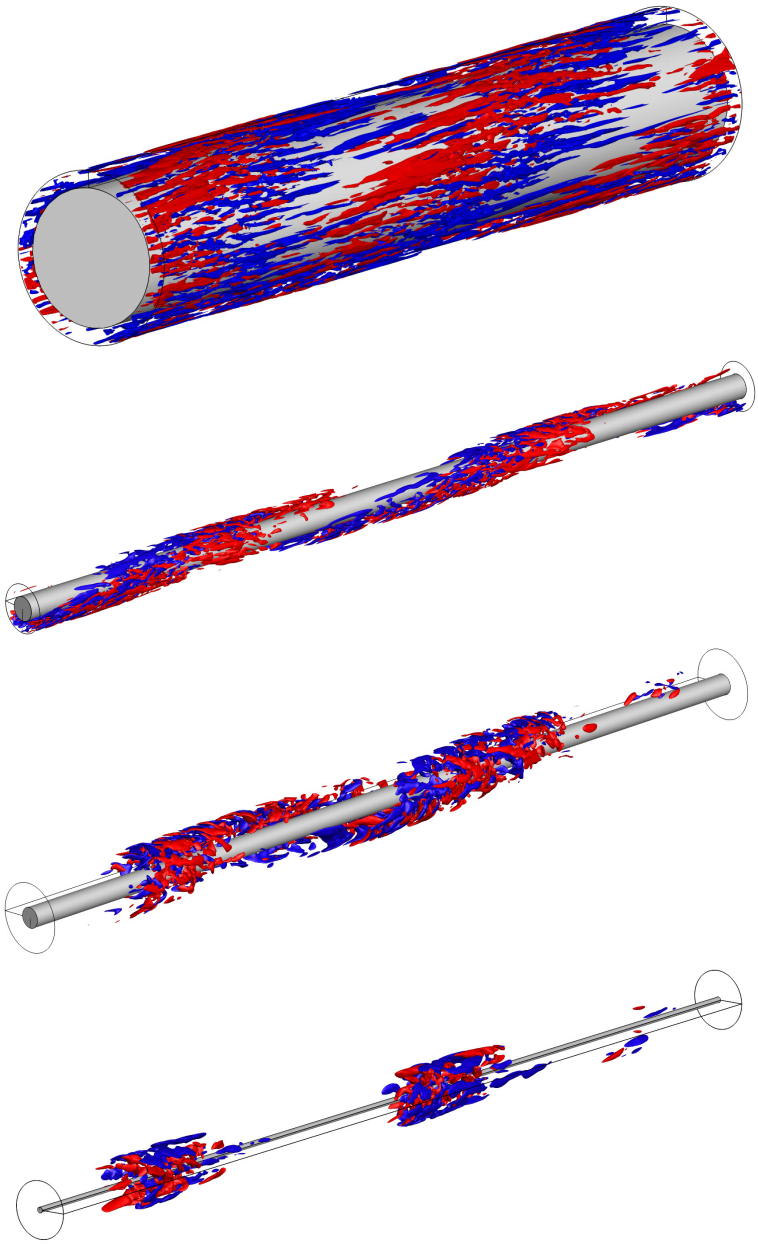

FIGURE 3.39 – Localised coherent structures in Annular Pipe Flow (aPf), from top to bottom : $\eta = 0.8$ and $Re_\tau = 72$, $\eta = 0.5$ and $Re_\tau = 56$, $\eta = 0.3$ and $Re_\tau = 56$, $\eta = 0.1$ and $Re_\tau = 52$. Three-dimensional isolevels of streamwise velocity fluctuations.

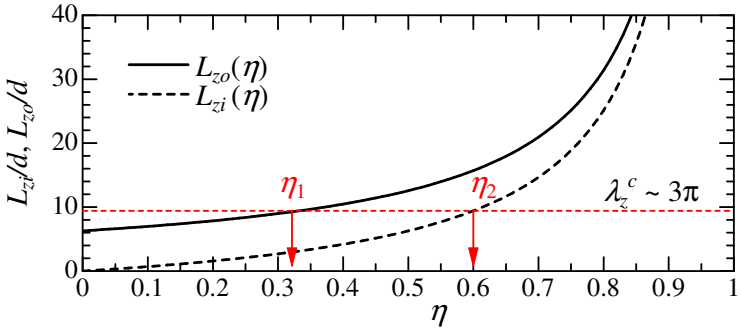

FIGURE 3.40 – Azimuthal length as a function of radius ratio.

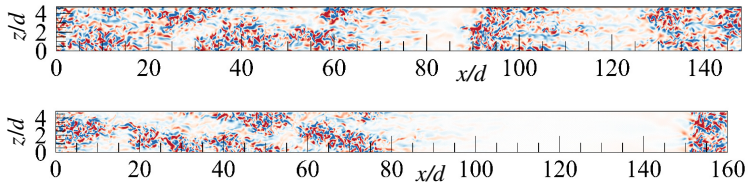

FIGURE 3.41 – Localised coherent structures in APF, $\eta = 0.2$. From top to bottom : $Re_\tau = 56$ (top) and $Re_\tau = 52$ (bottom). Two-dimensional isolevels of radial velocity close to mid-gap.

case compete here : wall curvature and azimuthal confinement. They are a priori linked together by the geometry. The two related parameters can however be made independent if the outer perimeter L_z is chosen such that $L_z > 2\pi$. This is achieved in practice by simulating the same regimes in an artificial domain with an azimuthal wavenumber $\beta = 2\pi/L_z$ input as a non-integer. This numerical trick has been considered in Refs. [263],[262] in the context of aCf. We can focus for instance on the case $\eta = 0.5$. When $L_z = 2\pi$, no laminar-turbulence is found whatever the value of Re. However for $L_z \gg 2\pi$ the flow for $\eta = 0.5$ features a transitional range characterised by clear oblique/helical stripe patterns. This rules out wall curvature as a possible explanation why oblique interfaces do not form. However it validates the idea that regular oblique patterning in a given Re-interval is the rule once azimuthal confinement by periodic boundary conditions is weak.

3.5.6 Boundary layer flows

While the annular examples above were opportunities to test the robustness of the theory with respect to azimuthal confinement, its robustness with respect to wall-normal confinement needs to be also addressed. In the planar case with two plates (pPf or pCf), a two-dimensional divergence-free property was established in Eq. 3.11 for the velocity field integrated from wall to wall. The crucial mathematical step to Eq. 3.11 is the property $[u_y]_{y=-h}^{y=+h} = 0$, in other words the fact that the wall-normal mass flux is zero (due to wall impermeability in pCf and pPf). This property can be violated in the case with one wall only, i.e. boundary layer flows. This is illustrated in the Asymptotic Suction Boundary Layer flow (ASBL). For this flow, in the absence of a top wall the integration in y of Eq. 3.11 can be carried out between the lower wall (by convention at $y = 0$) and any wall-normal position y^*, yielding

$$\partial_x \bar{u}_x + \partial_z \bar{u}_z = -u_y(y^*) + u_y(0), \tag{3.19}$$

where $\bar{u}_i = \int_0^{y^*} u_i(x, y, z, t)dy$ is the equivalent of the wall-integrated flow in the original Eq. (3.11). As a consequence, the loss of streamwise flow rate experienced when entering a localised turbulence patch in the x direction does no longer have to be balanced by a spanwise flux like in contained shear flows.

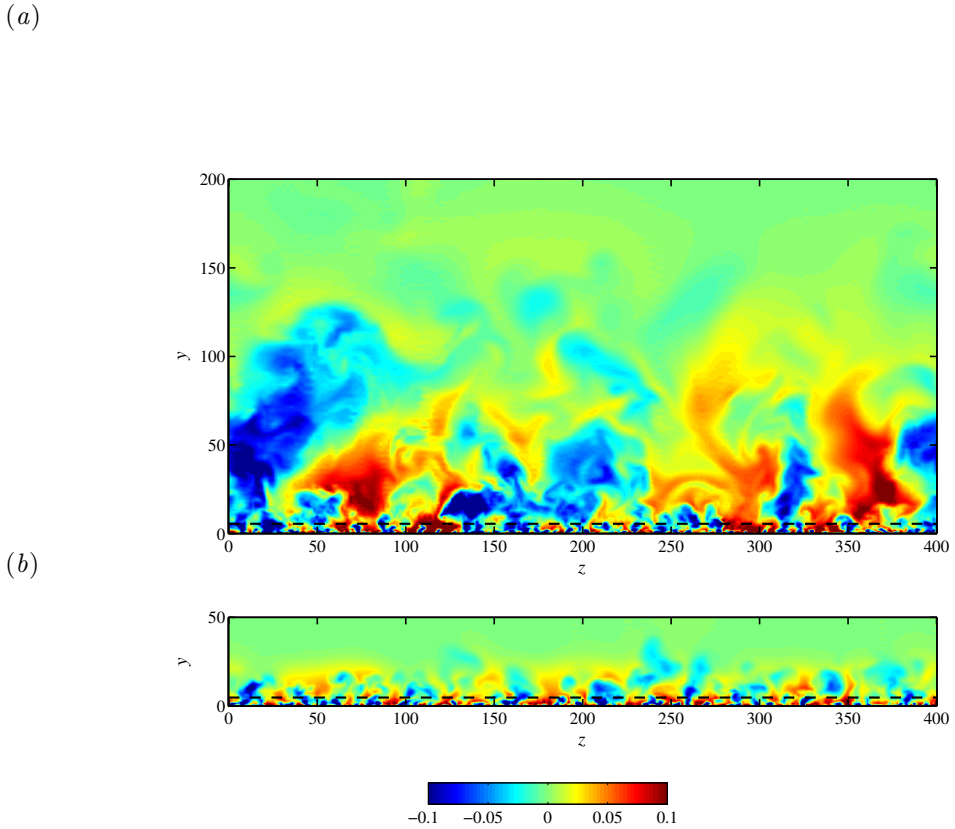

FIGURE 3.42 – Two-dimensional yz-plane visualisations of the streamwise velocity fluctuations u' in ASBL for (a) $Re = 333$ and (b) $Re = 260$ computed using R1 resolution. Only part of the wall-normal extent of the domain is shown. The black dashed line marks the height $y^+ = 100$. The values of the time-averaged 99% boundary-layer thickness are $\delta_{99} \approx 155$ and 27 for $Re = 333$ and 260, respectively. Computations obtained using moderate resolution [1]

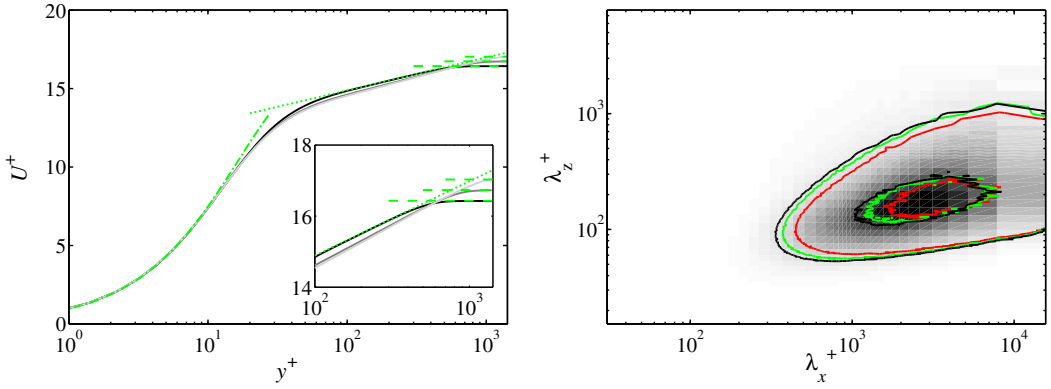

FIGURE 3.43 – (a) Mean streamwise velocity profiles for $Re = 270$, $Re = 280$ and $Re = 290$ in ASBL, with the lighter colours corresponding to increasing Re. The green dot-dashed line corresponds to the modified linear law. The green dotted line represents the empirical log law $u^+ = \frac{1}{\kappa} \ln y^+ + B$ for $Re = 270$ with $\kappa = 1.1$ and $B = 10.7$. (c) Two-dimensional premultiplied energy spectrum $\phi_{uu}^+(\lambda_x^+, \lambda_z^+)$ at position $y^+ = 12$ for $Re = 270, 280$ and 290

This loss of streamwise flow rate can instead be balanced by a wall-normal gradient of momentum or by both wall-normal and spanwise gradients. In the absence of clear rule, we simply state that oblique laminar-turbulent interfaces are not generic in ASBL, whereas in channel and Couette flows they are. This conclusion is true independently of Re. Direct numerical simulation in computational domains both large and high (i.e. L_y large too), with well-adapted numerical resolution, has shown that there is indeed no ordered laminar-turbulent coexistence in ASBL even arbitrarily close to the onset of its turbulence regime [1]. In other words *ASBL does not possess any transitional range*. Moreover, all elements point towards a clear violation of the directed percolation hypothesis : transition seems discontinuous in the sense that the turbulent fraction directly goes from 100% to 0% as Re is decreased below the critical point $Re = 269 \pm 1$. The value of this critical Reynolds number has been verified experimentally in a recent study. It falls within only 1% of the numerical value [279, 280]. An element of justification is found in turbulent statistics : for $Re = 270$ (just above onset) the turbulent regime verifies the logarithmic law of the wall, whereas this is far from true for any of the classical contained flow such as pipe or channels near their critical point. Turbulent ASBL is hence multiscale for all Reynolds numbers from onset.

In order to verify that the mechanism suggested here to discard sustained laminar-turbulent coexistence in ASBL applies in practice, a numerical manipulation of the flow has been implemented. Similarly to Ref. [281], the non-zero fluctuations of the wall-normal and spanwise velocity are brought to zero at a given distance from the wall using a volume force. This mimics a "ceiling effect", whereas it is expected that truly confined flows would exhibit a transitional range, just as pCf or pPf do. If V_S is the suction velocity (independent of y), the additional body force writes $\boldsymbol{F} = (0, -\lambda(y)(V_S + u_y), -\lambda(y)u_z)$, with $\lambda(y) = S((y - y_s)/d)$. The function S is chosen as

$$S(u) = \begin{cases} 0\,, & u \leq 0\,, \\ 1/\left(1 + e^{(1/(u-1)+1/u)}\right), & 0 < u < 1\,, \\ 1\,, & u \geq 1\,, \end{cases} \tag{3.20}$$

The parameters values tested correspond to $y_s^+ = 100$ and $d^+ \approx 80$. The distance of $100\delta_\nu$ corresponds to the mean streak spacing for all shear flows, or in other words to the Kolmogorov length of inhomogeneous shear flows. It is believed that choosing a similar wall-normal extent would leave out any scale larger than this cut-off value, make the flow monoscale and hence make it susceptible to develop large-scale modulations. The results are encouraging, and at least the main hypothesis turns out to be correct : although the flow ultimately relaminarises for $Re = 280$, it develops transient interfaces during the relaminarisation process. Importantly, these interfaces (visualised furtively in figure 3.44) appear unambiguously oblique with respect to the streamwise axes. For $Re \geq 290$ the flow does not relaminarise

FIGURE 3.44 – Two-dimensional xz-plane visualisations with wall-normal damping for $Re = 280$ in ASBL. Streamwise velocity at $y^+ \approx 12$.

and other furtive oblique interfaces are easily identified [1]. However, with the choice of filtering function and the parameters used no sustained STI or pattern regime was identified so far.

3.6 Multiphysics extensions

The range of Reynolds numbers corresponding to the transitional range for planar shear flows is relatively narrow. Moreover, it does not correspond to a very wide range of applications. Most flows encountered in everyday applications, because of the typical lengthscales and velocity scales involved are characterised by Reynolds numbers of the order of 10^5 or more, where full-fledged turbulence is the rule. It is however possible, and relevant in a large range of realistic applications, to consider shear flows in the presence of an additional force F such that the transitional range is pushed to such high Reynolds numbers. In primitive variables formulation, the non-dimensional incompressible equations read

$$\frac{\partial \mathbf{u}}{\partial t} + (\mathbf{u} \cdot \nabla)\mathbf{u} = -\nabla p + \frac{1}{R}\nabla^2 \mathbf{u} + \mathbf{F} \ , \tag{3.21}$$

$$\nabla \cdot \mathbf{u} = 0 \ , \tag{3.22}$$

where p is the pressure field, $\mathbf{u}$ is the velocity field and $\mathbf{F}$ is an external force (of module F) which can be added to damp turbulent fluctuations. For purely shear-driven flows, $\mathbf{F} = 0$. For patterns to be pushed towards higher R, the additional force of interest should have a tendency to damp turbulent fluctuations. If the Reynolds number is denoted R for simplicity, the range of R where patterns can be observed can be noted *a priori* $[R_g(F) : R_t(F)]$. Equivalently, for a given value of the governing parameter R, patterns are sustained within a range $[F_t(R) : F_g(R)]$. The force F can alternatively be seen as a way to control turbulence in applications when strong unsteadiness is considered as undesirable.

A first example from the literature is found in plane Couette flow with global spanwise rotation (RPCF). Cyclonic spanwise rotation is known to damp turbulent fluctuations [283]. In this case we can define F as a measure of the rotation rate, for instance the non-dimensional rotation number Ro propotional to the rotation rate $\Omega < 0$ -not to be confused with the Rossby number inversely proportional to it-. It was verified experimentally [282] that RPCF has a linearly stable laminar regime. Under suitable excitation, a regime of localised turbulence exists in a well defined range of values of R and F. For fixed F, when R is increased, as documented in figure 3.45 one encounters first a regime of spots within a laminar environment, then a patterned regime, an intermittent one and eventually turbulence. That sequence is qualitatively similar to that encountered for $F = 0$ when increasing R. It was verified using large numerical domains that this phenomenology is well captured numerically [284] for R up to 6000, as shown in

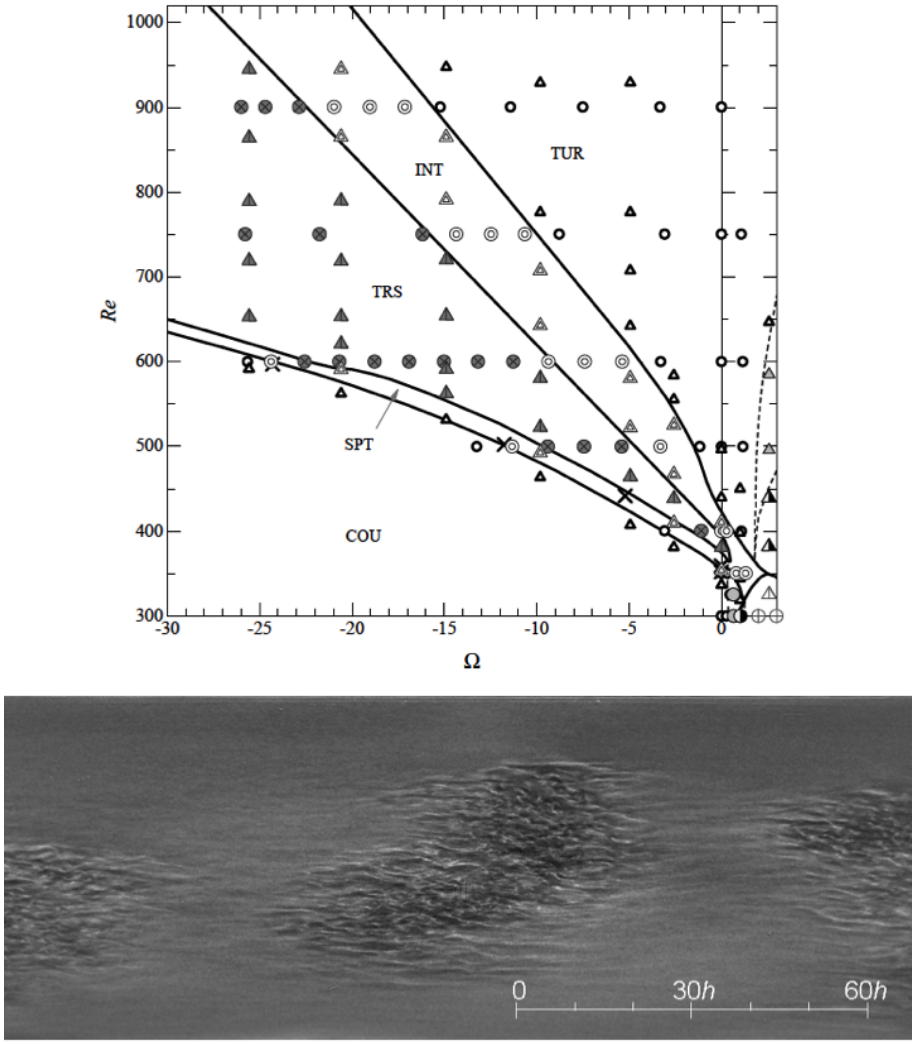

FIGURE 3.45 – Top : Experimental parameter space (Ω, Re) for negative rotation Ω [282] (COU : laminar Couette flow, SPT : spots, TRS : turbulent stripe patterns, INT : intermittent turbulence, TUR : turbulent flow). Bottom : snapshot of the spot regime

FIGURE 3.46 – Stripe pattern in DNS of RPCF.

figure 3.46 . Above $R = 6000$ the phenomenology changes. The value of R in Ref. [284] was pushed as high as $R = 20,000$ with relevant numerical resolution. Laminar-turbulent patterns are still found but only at a small distance from the wall. Further away from the wall the flow is characterised by turbulent fluctuations without any dominant large-scale structure. We witness in figure 3.47 the emergence as R increases of *near-wall stripes* of increasingly small thickness. Moreover, the stripes on either wall are no longer steady as in pCf, instead they travel in opposite directions with velocities $O(1)$ corresponding to the large-scale velocity if not to the mean flow velocity. This new regime is very expensive to simulate and equally difficult to achieve experimentally with large dimensions. As a consequence, the parameter space remains to be properly explored.

Note that another related example is the classical Taylor-Couette flow when both cylinders rotate in opposite directions. This is not a surprise since Taylor-Couette is viewed as a limiting case of spanwise rotating pCf when the radius ratio tends towards unity. When this aspect ratio is close to 1, it is known that helical laminar-turbulent patterns can be found [207, 218, 253, 261].

A second area of application of the above concept is found in the presence of stable density stratification. Such applications abound in geophysics both in the atmospheric and oceanic contexts. Former investigations in small enough periodic domains have revealed a trend for turbulent regimes to relaminarise for strong enough density gradient [285, 286]. In analogy with the observations for pure shear flows, it was tempting to speculate that laminar-turbulent coexistence would be possible, for neighbouring parameters, provided large enough domains are used. This has been verified again in Ref. [284] in a symmetric ("open") channel geometry that turbulent-laminar stripe patterns could be maintained at higher R, with a grossly constant turbulent fraction, provided the stratification parameter (the Richardson number) would be increased with the same rate. As for RPCF, at really high values of R patterns do not occupy the full gap width, they are located at a close distance from the wall amidst turbulent fluctuations. The value of R in Ref. [284] was pushed also as high as $R = 20,000$ with the relevant numerical resolution. The two systems are yet not equivalent. For instance, it is believed that internal waves, made possible, can be excited at the right frequency by the large-scale modulations or by turbulent fluctuations, and start to interfere with the turbulence itself. Despite more recent continuations of this work [287–289] this scenario lacks as of now a proper investigation.

The last application of interest is found within the context of electrically conducting fluids in the presence of an imposed magnetic field. Applications of low-magnetic Reynolds number magnetohydrodynamics are frequent in industry when liquid metals are involved, e.g. in electromagnetic brakes or in the growth of semiconductor crystals. Similarly to stratified flows, there was former evidence, from simulations in small periodic domains, that the application of a magnetic field could make turbulent flows relaminarise [290, 291]. A similar approach was undertaken in Ref. [284] using much larger computational domains, for the case of plane Poiseuille flow, again for R up to 20,000. The force F is parametrised by a Hartmann number. The orientation of the magnetic field was chosen aligned with either x, y or z. The only clear case, from the point of view of the formation of laminar-turbulent patterns, corresponds to the

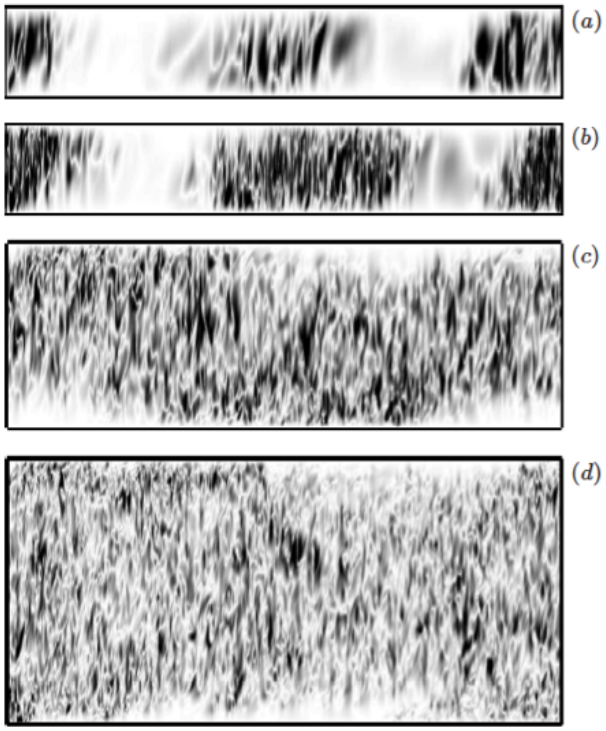

FIGURE 3.47 – RPCF in (x, y) section as Ro is increased. Isolevels of absolute value of wall-normal velocity. Values of Re and Ro and L_x from top to bottom : $(350, 0, 250)$, $(750, -0.02, 250)$, $(6 \times 10^3, -0.116, 48)$ and $(2 \times 10^4, -0.2, 25.1)$.

spanwise magnetic field. There again, laminar-turbulent patterns appear robust to increasing F until the laminar-turbulent coexistence is found only by the wall. More recent investigations of these regimes have pointed out similarities and a few discrepancies with non-magnetic cases in duct geometries [292, 293].

These separate investigations have been carried out with the aim of identifying features in common. Beyond the immediate message that laminar-turbulent patterns are robust to increases in F (provided F has the property to dampen out turbulent fluctuations), it represents an opportunity to measure the wavelengths of the patterns over a much wider range of R than is possible for $F = 0$, namely almost two decades from $R = 300$ to $20,000$. These wavelengths are represented for a large class of patterns from various sources in a two-dimensional cluster plot (Λ_x, Λ_z) in figure 3.48(left). Although R varies by almost two decades, wavelengths vary over hardly a factor of 4 (an exception is represented by the MHD case Mzh at $R = 20,000$ which displays a smaller wavelength, may be influenced by the choice of the numerical domain). Although a very slow dependence of Λ_x and Λ_z on Re is not strictly ruled out, the present results rather suggest a lack of direct dependence, i.e. $\Lambda_x, \Lambda_z = O(1)$. This is in contrast with the small scales which, as is clear from e.g. figures 3.47 but also figure 3.46, shrink with increasing Re as in all turbulent flows. A reduction to inner units has been performed in the spectrum of figure 3.48b, for the cases with increasing density stratification. Such cases are seen in figure 3.48a to have similar large-scale wavelengths (as indicated by the labels PP, S80 and S183). According to the classical wall turbulence theory, for featureless turbulent flows the near-wall peaks of the spectrum should collapse around $\lambda_z^+ = 100$. This is the case here, to acceptable accuracy, even in the patterning regime. The large-scale peaks, however, do not scale at all in inner units and the outer unit suggestion from figure 3.48a is much more adequate. We conclude that, whereas *small-scale structures scale in inner units, large-scale patterns scale in outer units*. Such a result would not have been exploitable from pure shear flow data only.

The last teaching from this very global comparison concerns the correlation between the imposed (resp. measured) Reynolds numbers depending on the choice of protocol. The friction Reynolds number Re_τ is plotted in figure 3.49 versus the bulk Reynolds number Re defined for each case, in log-log coordinates. Although no accurate power-law fit dominates this plot, a linear relation of the kind $Re_\tau = O(Re_b)$ is compatible with the data. Recall that for pure shear flows such a relation was suggested from the largest-domain investigations, in correspondence with the relation $C_f = cst$. A simple extrapolation of this law to the data of figure 3.49 suggests again that, at least *as a rule of thumb, laminar-turbulent patterns are characterised by a constant friction factor*, also whenever additional forces are present in the budget.

3.7 Conclusion

The last decade has been important for the study of transition to turbulence from a spatiotemporal point of view, mainly because numerical facilities are now a full alternative to the more classical experimental approach. In particular, large computational domains are now feasible using numerical simulation. The global issue of whether transition obeys the equivalent of a phase transition is now essentially solved : as far as the turbulent fraction as a function of the Reynolds number is concerned, continuous transition is the rule, with critical exponents compatible with the scenario of directed percolation [225, 260]. Quantitative evidence for this universal scenario requires however large computational domains that remain extremely costly to simulate, even as of 2021. However, understanding that such requirements are in order represents already an important theoretical progress. For pipe flow, the spreading of turbulence results from puff splitting events, and for higher Reynolds number from the growth of slugs [153, 180, 202]. For planar flows such as plane Couette flow and plane Poiseuille flow, the spreading of turbulence proceeds from a sequence of events leading from receptivity to streak growth, to localised spot nucleation to spatial proliferation [14, 66]. The role played by large-scale flows in the proliferation process is now better understood : being generated at the level of the laminar-turbulent interfaces, the large-scale flow simply advects the weakest perturbations at the interface in a direction necessarily oblique to the streamwise direction. The resulting growth is hence dominated by the oblique elongation of the nucleated patches of turbulence [268]. This mechanism has been validated by analysing its actual limits. It breaks down in

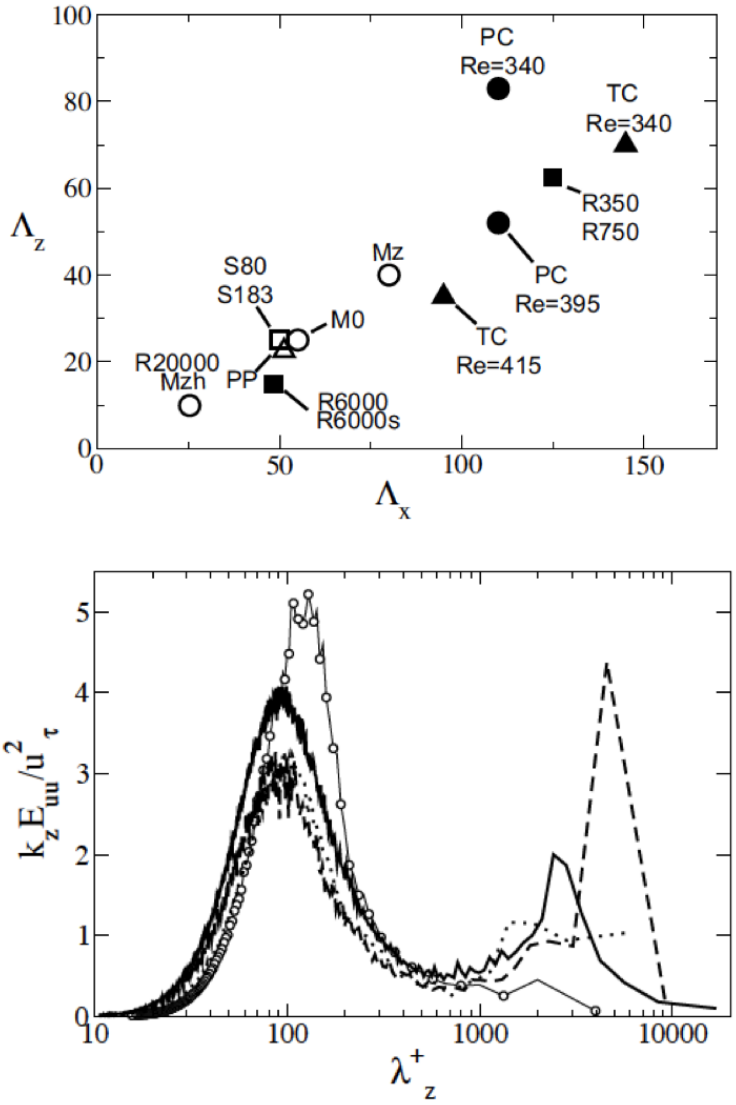

FIGURE 3.48 – Top : location of modulation wavelengths of the patterns in (Λ_x, Λ_z) space for various cases listed in Ref. [284]. Bottom : energy spectrum for the density stratified cases PP, S80 and S183, with lengths displayed in inner units.

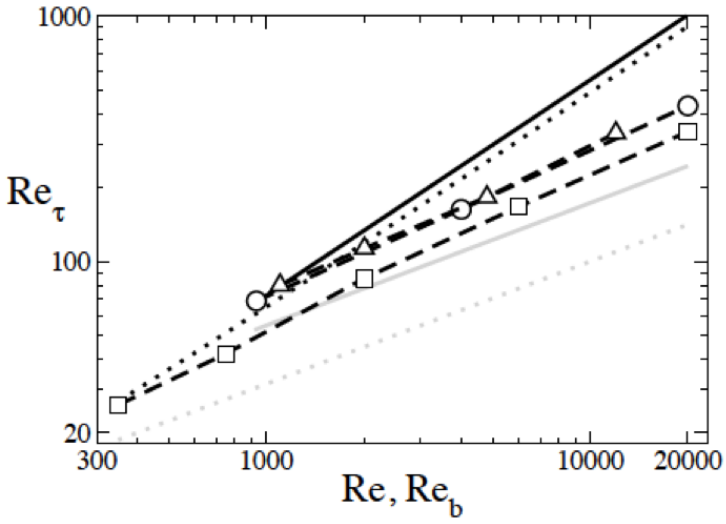

FIGURE 3.49 – $(Re_\tau - Re_b)$ relation for many different flow cases together in the transitional regime.

two cases : in annular flows [263, 294] because of the azimuthal confinement that rules out large-scale flows [295], and in boundary layer flows because the flow is not confined in the wall-normal direction. The mechanistic reasons why large-scale modulations form in the transitional range are still not fully understood. Several competing theories exist, mainly motivated by low-order models : Turing instability [296] modified with noise, crystallisation of turbulent puffs [297] or simply excitability [180], but a deeper investigation is needed to distinguish between all these credible scenarios from real data. Interestingly, the notion of transitional range appears irrelevant in the parallel boundary layer flow (ASBL), which hosts no laminar-turbulent patterns and features a wholly discontinuous phase transition. The case of boundary layer flows is shown to differ strongly from the channel geometries because of the absence of wall confinement [1]. The next chapter is dedicated to a deeper theory of transition applicable to spatially developing boundary layer flows.

4

A transition theory for spatially developing boundary layer flows

4.1 Phenomenology of Blasius boundary layer transition

Boundary layer flows are, simultaneously, among the most obvious hydrodynamic examples of solid/fluid interaction, and a complicated case of transition to turbulence. The simplest example is probably the Blasius boundary layer flow, because of its two-dimensional steady solution, and this chapter is concerned about the nonlinear stability of this base flow with respect to incoming disturbances. Unlike e.g. Couette flow, whose academical origin is hard to hide, the Blasius flow configuration is prevalent in many real applications including aeronautics, propulsion and aerodynamics. This explains why experimental studies abound, in particular those based on wind tunnels experiments. The present chapter aims at unifying recent results obtained by attempting to apply the concepts stemming from dynamical systems theories to the Blasius boundary layer flow.

4.1.1 Flow set-up

The Blasius flow corresponds to the steady flow developing above a semi-infinite plate that starts at some origin $x = 0$. Despite the steadiness hypothesis, the flow experiences spatial development, such that tracers advected by that flow are constantly slowing down. Besides there is always entrainment of fluid from the region outside. The spatial development can be interpreted as the combined advection and viscous diffusion of the spanwise vorticity. It emanates from the leading edge, which acts as a singular source of vorticity.

We begin by presenting the 'ideal set-up' and then confront it with more realistic cases comparable to wind tunnel conditions. The 'ideal' Blasius set-up is illustrated in figure 4.17(top). The velocity at the plate is exactly zero when the plate is still, whereas at an infinite distance above the plate the velocity vectors are oriented in the streamwise direction, and have constant amplitude U_∞. Owing to viscous diffusion the displacement thickness grows with the distance x from the leading edge as $\sqrt{x}$. This flow does not depend on any physical control parameter [298]. Reynolds numbers are based either on x or on the layer displacement thickness δ^*, and they change with x. The displacement thickness is defined classically from the streamwise velocity base flow profile $u(x, y)$ as

$$\delta^*(x) = \int_0^\infty (1 - \frac{u(x,y)}{U_\infty})dy \tag{4.1}$$

Such Reynolds numbers are interpreted as a coordinate system rather than as a governing parameter. Numerically however, it is important to specify the value of the Reynolds number at the upstream end of the computational domain $Re_{\delta_0^*} = U_\infty \delta_0^*/\nu$, with δ_0^* corresponding to δ^* evaluated at this point. The laminar solution is given, for $x > 0$ sufficiently large, by the solution of the Blasius O.D.E. [298]. This equation rules the dynamics of the streamfunction, considered as a function of the reduced variable $y/\sqrt{x}$ only, under additional hypotheses such as steadiness and lubrication ($x \gg y$). The laminar Blasius solution has no analytical expression but it is easily integrated numerically. It is not strictly valid immediately close to the leading edge, however it constitutes an excellent approximation of the real laminar solution as soon as $Re_x = xU_\infty/\nu \geq 200$. The linear stability (in time or in space, or both) of the steady Blasius solution is a difficult mathematical problem. Under the lubrication hypothesis it is however possible to "freeze" the base flow locally as if the spatial development was too slow to matter. Under such conditions the system can be linearised around the base flow solution $\boldsymbol{u_0}$, and an ansatz of the form $e^{\alpha t}$ is admissible. The linear stability computed under these assumptions is displayed in figure 4.2. Linearly unstable modes correspond to the zone $\mathcal{R}(\alpha) > 0$. They exist for $Re > 519$ [18]. These modes have finite streamwise wavenumber $k_x \neq 0$ and $k_z = 0$, they are localised inside the boundary layer, travel uniquely downstream, consist of co-rotating spanwise vortices and are called Tollmien-Schlichting waves. In real experiments these waves appear via wavepackets that also grow in length with x [299] A large series of experiments are dedicated to exciting these waves, to the way they lose their stability with respect to three-dimensional disturbances and finally transition to a turbulent flow far enough downstream. This is the so-called *classical transition scenario* usually present in most textbooks.

The realistic set-up is very similar to the ideal one, yet it incorporates sources of inhomogeneity that are responsible for the transition as observed in realistic wind tunnel experiments [300]. This is sketched in figure 4.17(bottom). The potential sources of flow disturbance can be of various physical origins : incompressible vortical disturbances, acoustic waves, incoming turbulence, tripping wire, wake of a grid [301], etc... They are located typically "upstream" but not necessarily upstream of the leading edge, nor upstream of the computational domain if the latter starts at a finite value of $x = x_0$. In a simplified picture the sources of disturbance are rather located upstream of the zone where transition happens : laminar flow is considered under the influence of permanent disturbances of finite amplitude, while the turbulent flow further downstream is not subject to disturbances. In particular, the permanent character of the disturbances takes the system a priori away from the realm of initial-value problems. The reason why such a distinction needs to be made between ideal and realistic set-up is the following : the transition scenario might differ from the classical one provided the finite-amplitude disturbances are strong enough [302–305]. We base the present investigations on the underlying idea that the flow is destabilised by incoming turbulence that might be caused by either an upstream grid, or by any other non-specified reason. In order to keep the flow conditions well defined, the in-coming turbulence is considered as temporally permanent, spatially decaying with x, isotropic and homogeneous, and it is characterised by two parameters : the turbulence intensity Tu and the integral lengthscale of the decaying turbulence, L. Only the effect of Tu will be considered in what follows, with $Tu > 0$ defined classically by

$$Tu = \frac{1}{\sqrt{3}}\sqrt{u_{x,rms}^2 + u_{y,rms}^2 + u_{z,rms}^2}. \tag{4.2}$$

The sketch in figure 4.17 illustrates the three main transition scenarios found as Tu is increased from low levels ($Tu < 1\%$) to high levels, via intermediate levels (everything inbetween) :

— For low enough Tu, the classical transition scenario is at play : the initial receptivity phase converts the weak disturbances into nascent TS waves which grow and later destabilise into Λ–shaped vortices. These vortices eventually break down into sustained turbulence further downstream.

— For intermediate Tu, the scenario is called *bypass transition* [307] : the receptivity phase leads to the spatial growth of coherent streaks (also called Klebanoff modes), and the transition is provoked by the destabilisation of these streaks.

— For large enough Tu ($Tu > 6\%$) free-stream turbulence breaks initially into smaller structures, which later destabilise into turbulent spots.[308])

The present aim is to generalise the knowledge on edge states to better understand their role in the bypass process. The presence of TS waves in one of the scenarios interferes with the concept of edge state in a puzzling way that has not been addressed before. The high amplitude regime is not investigated here, but it has also been investigated in a possible relation with minimal seeds [309, 310].

4.1.2 Bypass scenario

The bypass scenario was initially identified in experiments, and it has eversince been validated in several numerical simulations. A rapid but more detailed description of the process is useful to determine the "ingredients" needed for a nonlinear theory of transition. Pedagogic experimental visualisations from Ref. [302] are displayed in figure 4.4. They correspond to the same flow yet with different upstream grids and different values of Re at the level of the grid. These visualisations show sudden bursts of turbulence nucleating randomly on an well-ordered array of straight streamwise streaks. The presence of streamwise streaks is consistent with computational observations. For instance in figure 4.5, the excitation by free-stream turbulence is achieved by mimicking a synthetic turbulent flow upstream [303].

The receptivity stage upstream, that turns decaying turbulence into active streaks, is not fully understood. It is essentially based on linear mechanisms but does not feature any instability. It does not differ from the lift-up provided there is streamwise vorticity upstream. The first manifestation of nonlinear behaviour lies probably at the level of the first solitary streak breaking down, i.e. when the first incipients spot gets nucleated. This is where the analogy with edge state scenarios from the previous chapter become tempting (despite the lack of an obvious initial-value problem context). In the case of plane Couette flow, it was demonstrated in Ref. [149] how the occurrence of a streaky edge state and its linear instability were the essential nonlinear steps justifying the search for exact solutions (although

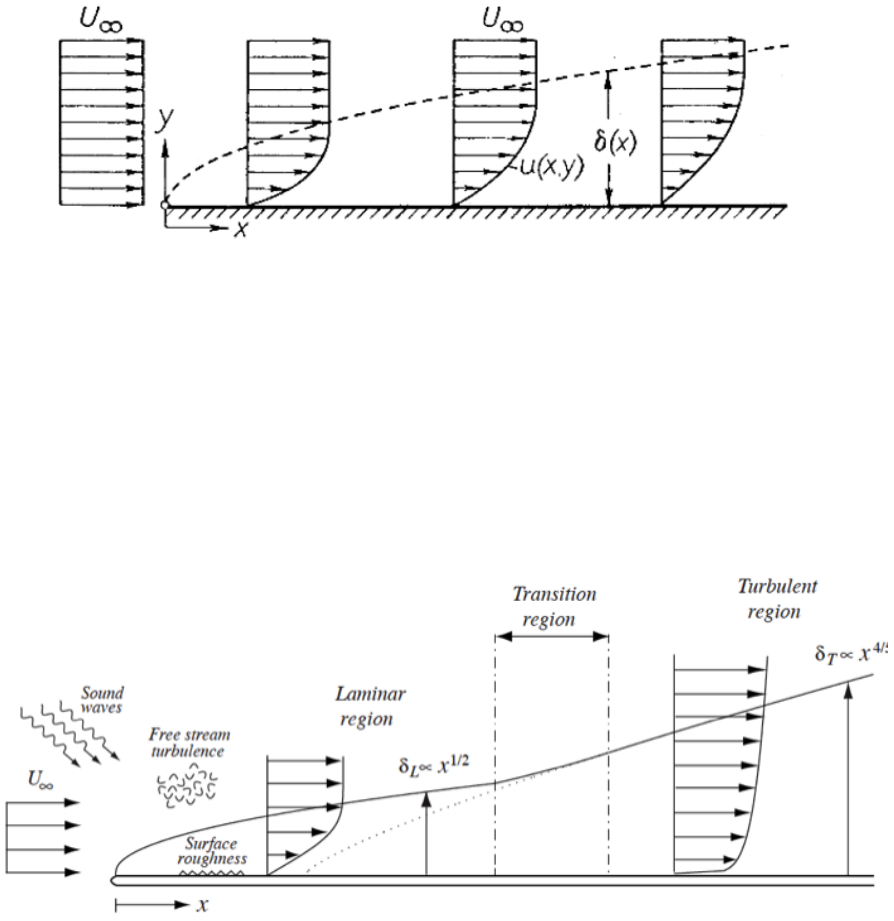

FIGURE 4.1 – Sketches of Blasius boundary layer flow in the laminar (top) and transitional cases (top). From Ref. [306].

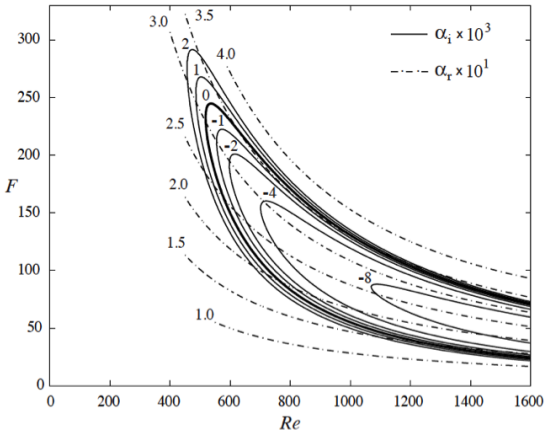

FIGURE 4.2 – Stability of the Blasius flow in a frequency-Reynolds number diagram (F, Re). Solid lines : iso-real part of the related eigenvalues, Dashed lines : iso-imaginary part. From Ref. [306]

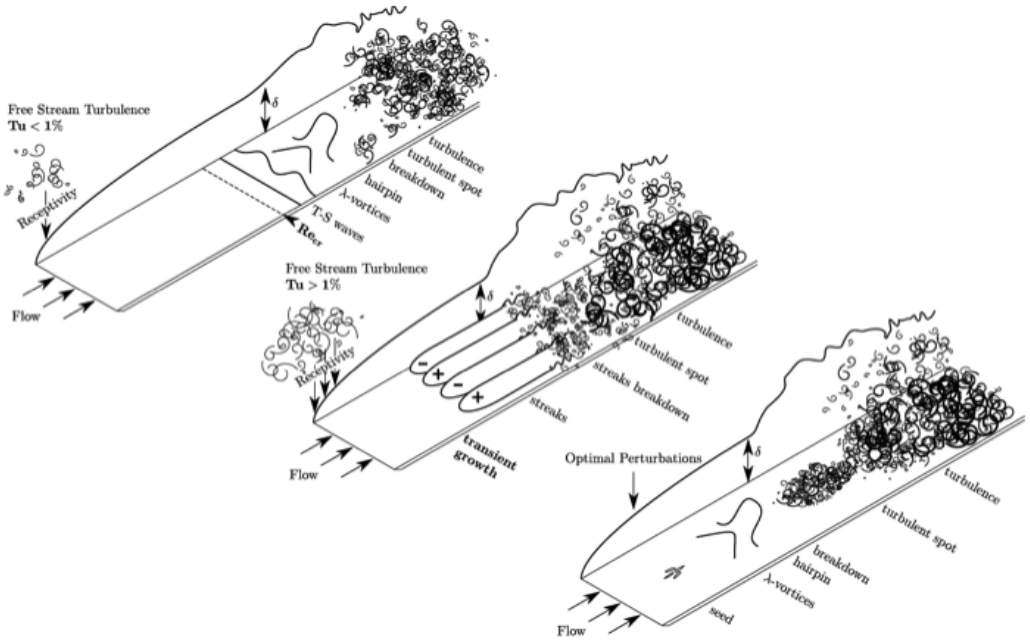

FIGURE 4.3 – Sketch of transition in Blasius boundary layer depending on the incoming turbulence level Tu. From Ref. [311].

the instability of the edge state can also be investigated in a linearised fashion). As in planar flows, the nonlinear approach consists first in identifying numerically a relevant and non-trivial base flow, then in analysing its stability and predicting the structures responsible for the breakdown of the streaks.

The edge state, being defined as an invariant set, is the ideal candidate for such a base flow. Scrutinising figure 4.5 leads to additional information on the edge state to be sought. It is clear from this figure that the early nucleation of spots is a local phenomenon. It make hence sense to consider the *growth of a*

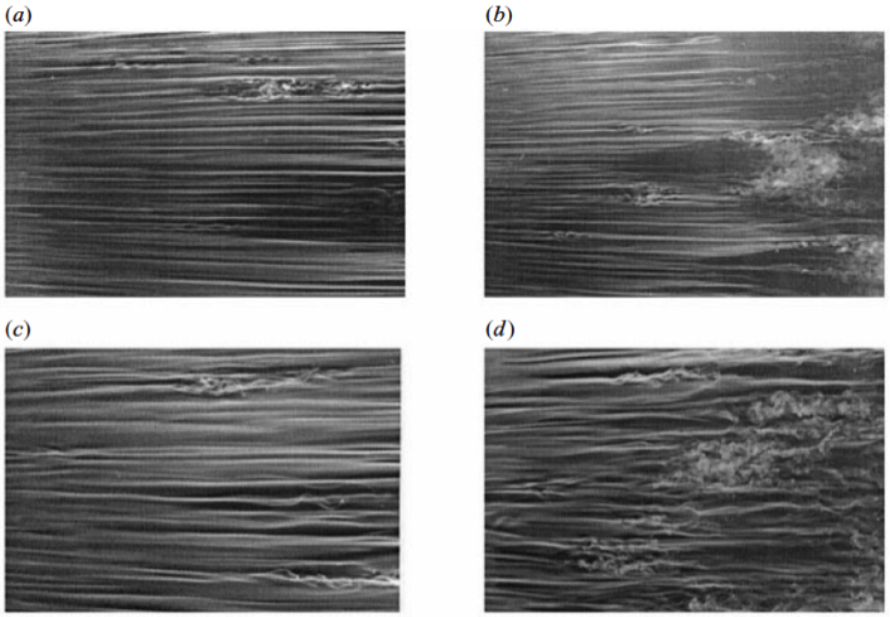

FIGURE 4.4 – Visualisations of the bypass process for several entrance grids and flow speeds. Experiment from Ref. [302].

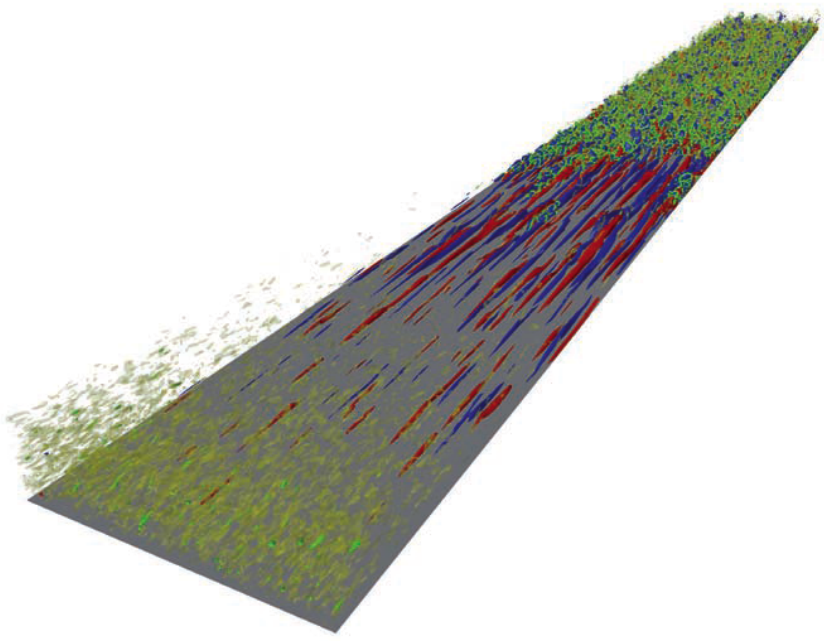

FIGURE 4.5 – Visualisation of the bypass process from Ref. [303]. Isovalues of streamwise velocity fluctuations, together isolevels of $\lambda < 0$ (green).

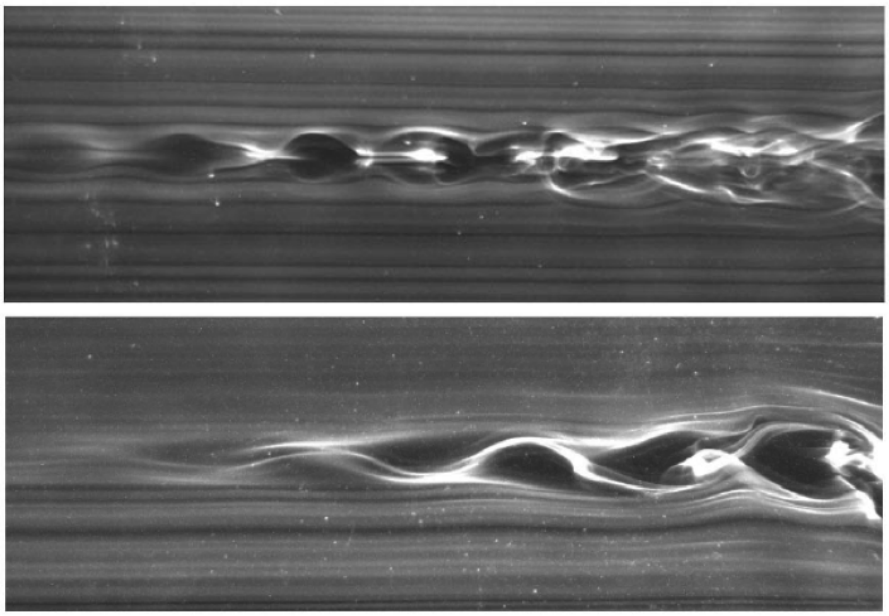

FIGURE 4.6 – Instabilities of streaks generated in an experimental boundary layer flow, of varicose (top) or sinuous (bottom) typeFrom Ref. [312].

localised disturbance on a localised streak of finite length in order to free oneself from the dependency on the chosen wavenumbers. Computationally this has the advantage to restrain the study to single localised initial disturbances, closer to computational studies such as Ref. [313]. A further comment about the choice for an initial value problem formulation can be made at this point. Under a permanent disturbance it would sound more adequate to look for another framework. Nucleation of spots in the bypass picture proceeds however as a series of discrete localised events (see figure 4.4). It thus makes sense to reverse the arrow of time and to assign to an incipient spot at time T a predecessor, i.e. a velocity field corresponding to an "initial" time $t = 0$. The relevance of the initial value concept would be less credible if the generation of new turbulence was continuous in time. The problem becomes again the identification of the most unstable modes of a relevant streaky base flow. This problem was addressed experimentally by Asai and co-workers who generated a straight low-speed streak in a boundary layer flow in order to study its instability and breakdown [312]. Two different symmetries characterise the instability of straight streaks : either spanwise-symmetric (varicose) or anti-symmetric (sinuous). Both types are illustrated in figure 4.6. In Ref. [314], the modal instability of a spatially periodic array of straight streaks has been considered instead, except that the base flow consists of synthetic streaks whose spatial structure was determined from a numerical fit. The same qualitative conclusions as the localised case arise : both symmetric and anti-symmetric streamwise modulations of the streaks stand out as least stable. The threshold amplitude levels required for this instability to occur might still depend on the localisation features [315]. Later, non-modal instability was also predicted [316] to lead to very similar structures without the need for a proper exponential streak instability. Some confusion is still present, entertained by the choice of a synthetic base flow which is not solution to the governing equations. The suggested alternative here is to generate a new relevant base flow using an edge tracking method, as it ensures that the resulting velocity field will belong to an invariant set of the governing equations.

4.1.3 Difficulties associated with state space picture

A pedagogically clear state portrait of the state space of the Blasius system would be a formidable achievement, both from a fundamental and applicative point of view. There are however fundamental obstacles to such a task. The main theoretical difficulty compared to, say, the pipe flow problem, might be due to the spatial development of the boundary layer. Let us list the possible invariant sets of interest for such a challenge.

The laminar base flow is steady and should hence be represented as a fixed point of the state space. The issue of its stability is more subtle. The definition of (linear) stability indicates that a fixed point is unstable as soon as one unstable direction exists. This is here clearly the case since TS waves, although analytically predicted for frozen base flows only, have been found experimentally. The troubling detail is that the critical Reynolds number of 519 suggested has no relevance to the stability problem since Re is not an external control parameters any longer. As a consequence, the linear instability of the Blasius base flow is of an *unconditional* type : the right perturbation at the right initial location leads to an exponentially growing mode at large times, and this is all that matters to declare the base flow unstable.

The notion of turbulent attractor is more problematic. Consider an initial disturbance with a spatially localised support. In the right conditions this perturbation will advect downstream while growing spatially. It will increase in size and its kinetic energy, enstrophy etc... will all diverge. The system can hence not support a bounded attractor, at least not using the usual energy-based metrics. One might argue that the situation is similar for slugs in pipe flow, which is true, however there is a difference. Slugs operate at constant Reynolds number. An extensive quantity used as observable would diverge with time during transition, but an intensive quantity would probably converge to a constant value. A genuine attractor is hence possible if the coordinate system is revised. In spatially developing flows yet, every perturbation is advected downstream, while it experiences increasingly larger boundary layer thicknesses as time evolves. The turbulent state needs locally to adapt to its new environment, characterised by the continuous apparition of new scales. This rules out the possibility for a well-defined turbulent equilibrium. Even by renormalising at every time the outer size of the turbulence patch or the boundary layer thickness, smaller and smaller scales would appear in its interior as time increases, as if the viscosity was decreasing with time.

The third possible regime is, without surprise, the edge state intermediate between laminar and turbulent... although there is no well-defined asymptotic turbulent state, the "turbulent" (resp. "laminar") fate of a given perturbation is often unambiguous when the perturbation energy or enstrophy is monitored in time, since it corresponds to a rapid growth (resp. decay) of the corresponding observable. The same argument holds as for the turbulent state, namely that there is a risk to deal with an unbounded relative attractor as an edge state. As shown in Ref. [317] bisection is still possible because of the self-similarity property of the edge state. Eventually, it is shown in Ref. [318] that the issue of long-time asymptotic states is in practice irrelevant because of the instability of TS waves.

There are further difficulties associated with the boundary layer context, all related to the issue of finite times. Most perturbations travel in the positive downstream direction no matter their wall-normal position [319]. Once perturbations have exited the computation domain it does not make sense to recycle them using periodic boundary conditions. The situation might seem analog in channels and pipes ; however in these parallel flows the equivalence between incoming and outgoing disturbances makes it reasonable to recycle outputs into inputs, computationally and even experimentally (see Ref. [320]). There is a simple, disappointing perhaps, but at least rigorous to handle this problem in spatially developing flows : one needs to i) use computational domains that are as long as possible and ii) consider all the dynamics as a *finite-time* phenomenon. The former condition is solely a matter of computational cost and duration. The latter has deep mathematical implications, since even the notion of attractor does not make any sense anymore. In particular, although the term "edge state" (formally an asymptotic regime only) is still used, the right concept here is only that of "edge trajectory". Fortunately, a majority of other concepts such as stable and unstable manifolds, Lyapunov exponents etc.. are easily generalisable

to the finite-time framework [321].

Eventually, provided the edge manifold can be defined in finite time, so can the minimal seeds. Their definition does not differ from the one used in previous flow cases since it is intrisically a finite-time notion with an associated time horizon T. Nonlinear optimal perturbations in boundary layer flows have been computed first in Ref. [309, 310] (initially without energy minimisation), whereas minimal states have been computed recently in Ref. [322].

4.2 Competition between two transition scenarios

The application of the classical edge tracking requires, as always, the definition of a global observable which vanishes for the laminar flow and reaches high values in the turbulent regime. The quantity chosen in this study is the enstrophy associated with the streamwise vorticity only :

$$a = \left(\frac{1}{vol(V)} \int_V |\omega_x|^2 \mathrm{d}v \right)^{\frac{1}{2}}, \tag{4.3}$$

(note that the denominator $vol(V)$ is not crucial in the definition). Reporting on the results of bisection best supposes a "short" and a "long" time horizon.

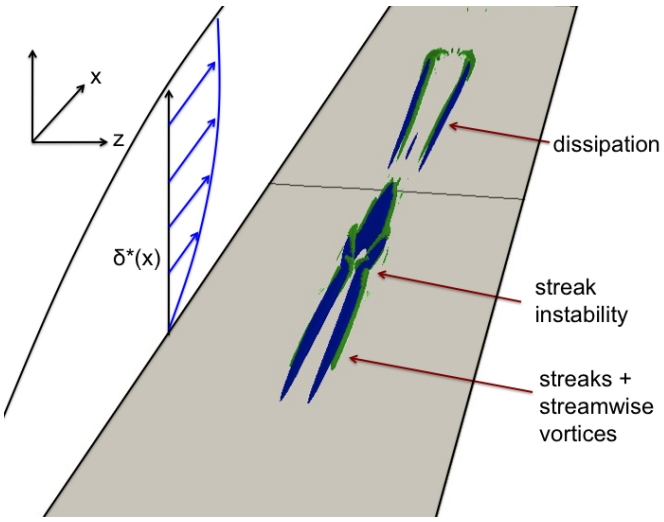

FIGURE 4.7 – Three-dimensional rendition of streamwise velocity perturbation along the edge trajectory at $t = 1050$ (symmetric case). From Ref. [317].

4.2.1 Impact on edge tracking

The "short" time horizon corresponds to a computational domain of length $L_x = 2000\delta_0^*$, where δ_0^* is chosen such that $Re_{\delta_0^*} = \frac{U_\infty \delta_0^*}{\nu} = 300$. This allows to carry out converged edge tracking over a time horizon of $T \approx 2000$ [317]. The "long" time horizon corresponds to a computational domain of length $L_x = 3000\delta_0^*$, still with $Re_{\delta_0^*} = 300$. This is not much longer except that a new trick was used, as detailed in the appendix of Ref. [318] : perturbations to the base flow are considered in frame moving with prescribed velocity $0.8U_\infty$. This numerical technique allows for much longer edge tracking with $T \approx 15,000$. The technique might be useful in many instances where localised disturbances travel through spatially varying environments.

For the *short time* bisection there is essentially no strong difference from the planar cases, except that the bisection time is limited. A localised initial condition similar to Ref. [270, 313] was first imposed with spanwise symmetry. The reason for this choice was initially a scientific interest in hairpin vortices suggested to impose their symmetry, coupled to the initial hope to find a simpler edge state in the presence of discrete symmetries as in Refs [106, 128]. Two bounds a_L and a_T have been chosen by trial and error. The dynamics of $a(t)$ and other observables shows no sign of convergence and is characterised by a few large-amplitude bursts. A snapshot of the velocity field along the edge trajectory after roughly 10^3 time units is shown in figure 4.7. The striking features of this perturbation include its spatial localisation in three directions, the robust presence of long low-speed streaks (in blue). The length of the state fluctuates in time as the main structure upstream sheds short-lived perturbations further downstream, in a manner comparable to puffs in pipe flow. Despite these fluctuations, it was found that a simple rescaling of most spatial quantities by the "local" displacement thickness δ simplifies much the dynamics.

$$\Omega_x = (\delta_0^*/\delta)^{\frac{1}{2}} \left(\frac{1}{vol(V)} \int_V |\omega_x|^2 \mathrm{d}v \right)^{\frac{1}{2}}, \tag{4.4}$$

$$\Omega_y = (\delta_0^*/\delta)^{\frac{1}{2}} \left(\frac{1}{vol(V)} \int_V |\omega_y|^2 \mathrm{d}v \right)^{\frac{1}{2}}, \tag{4.5}$$

$$W = (\delta_0^*/\delta)^{\frac{3}{2}} \left(\frac{1}{vol(V)} \int_V |u_z|^2 \mathrm{d}v \right)^{\frac{1}{2}}. \tag{4.6}$$

δ can be evaluated in several ways. In Ref. [317] the location of the edge state was monitored at every time by the maximum local wall shear stress, and δ was simply the value of δ^* at this location. In Ref. [318] a velocity barycenter was determined at every time, and the value of δ^* was determined at this location. The rescaling follows Eq. 4.6, and the dynamics expressed in these variables is included in figure 4.8. This state portrait suggests an approximate time periodicity. Note that the original time coordinate also needs to be rescaled by δ^*. This suggests that, even if the edge state was time-periodic in the rescaled variables, the time between two sucessive bursts would diverge in the original units. Besides, since the wall-normal and spanwise extents of the edge state both increases as fast as $\delta^*(t)$, larger domains are required for longer time horizons. This sets a severe limit to the number of bursts that can be captured in a single bisection. As for non-symmetric initial conditions, on short timescales the situation is not very different. No convergence towards a simple state is found, instead bursts seems unavoidable.

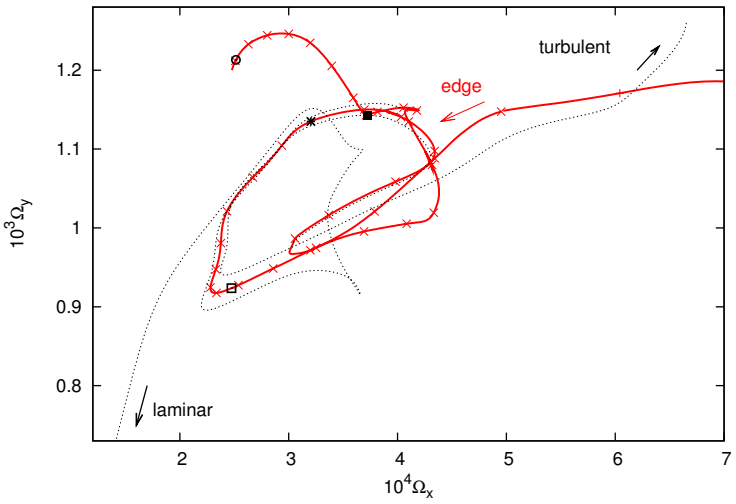

FIGURE 4.8 – Left : Phase portraits using recaled variables (symmetric case).

Despite the relative shortness of the edge tracking, figure 4.8 suggests that a relative attractor with a

self-similarity property can exist. We note that, in analogy with the reduction of continuous symmetries that has emerged recently [40], there is also a possibility to reduce continuous symmetries together together with self-similarity [323], but it has never been used in fluids. The present self-similarity property is surprisingly straightforward to justify : the factor (δ/δ_0^*) prefactor rules how the boundary layer thickness evolves with time, as well as the effective width of the localised state. Quantities such as enstrophies, edge state dimensions etc... simply adapt to the ever-thickening boundary layer. It is surprising that the size of this coherent structure manages to adapt to its changing environment on such a fast timescale, rather than adiabatically given that the edge state travels at speed $O(U_\infty)$. Nevertheless it is simple enough to warrant that *a priori* the concept of relative attractor makes sense in the Blasius boundary layer. As we shall see yet, longer time horizons blur this simple picture.

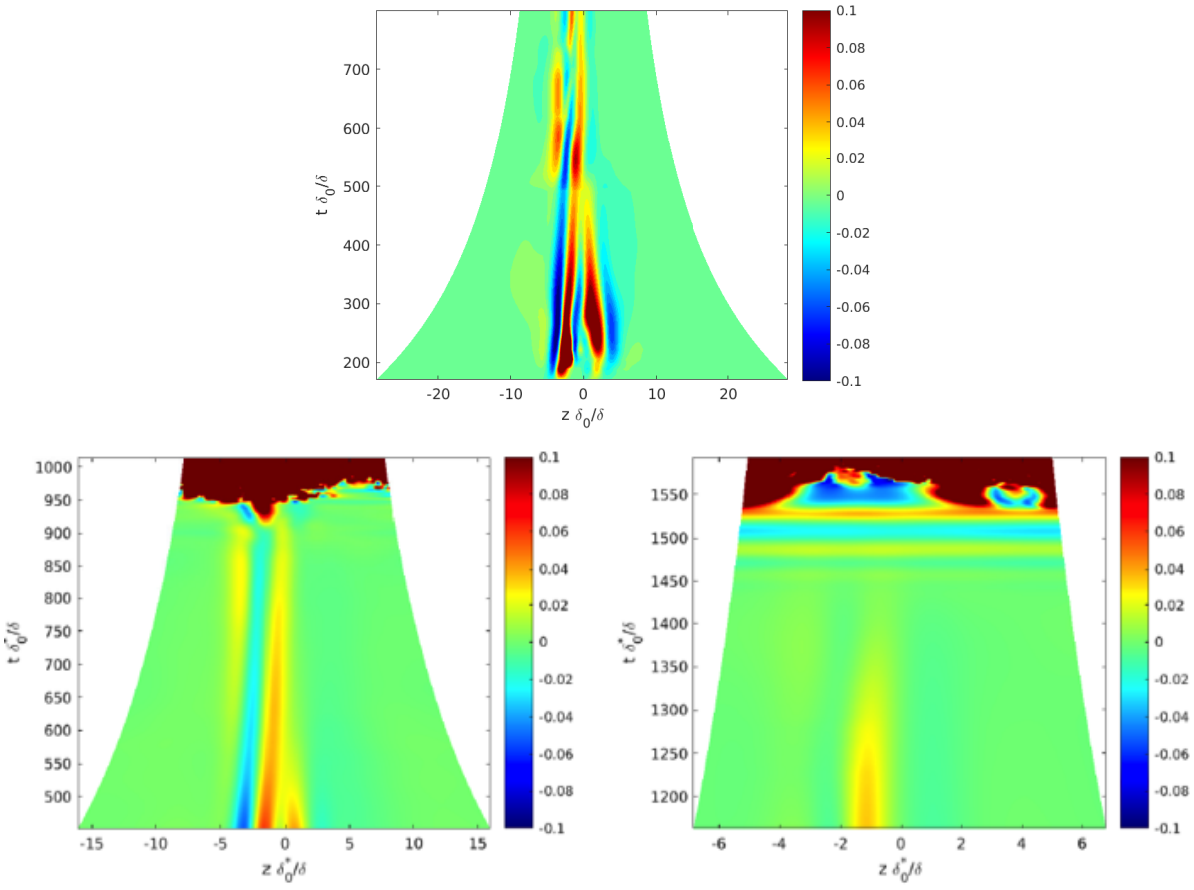

FIGURE 4.9 – Phase portraits using rescaled variables in the non-symmetric case for subliminal (left) and supraliminal (right) perturbations.

The *long-time* case has been analysed only in the presence of non-symmetric initial condition. Three space-time diagrams (using only rescaled variables) illustrate the situation : figure 4.8 documents the liminal perturbation, while figure 4.9 illustrates the late-time dynamics of supra- and sub-liminimal perturbations, respectively. These diagrams have been constructed by monitoring at every time the streamwise position x_G and speed $\dot{x}_G$ of the velocity barycenter, then using $\dot{x}_G$ as a moving frame. Figure 4.8 illustrated the dynamics non-symmetric edge trajectory. Again it features a small number of bursts that correspond in space to streak switching events. Although no conclusion related to the long-time dynamics can be made at this point, the dynamics of the fully localised Blasius edge state on such time scales is comparable to that of the fully localised edge state in ASBL : long localised streaky flow where low-

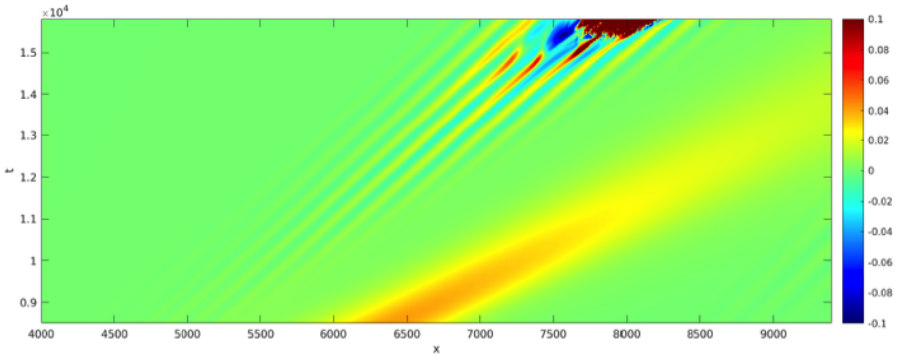

FIGURE 4.10 – Space-time diagram of $u_x(x, y, z, t)$ for $z = -10$ and $y = y_p$ for the trajectory away from the edge manifold. Streaks decay while the Tollmien-Schlichting wavepacket grows in amplitude and form a turbulent spot.

and high-speed streaks switch spanwise position quasi-periodically. For the supra-liminal perturbation, the differences with other localised edge states are not striking : the central low-speed streak undergoes an instability which very rapidly (less than 50 rescaled time units) induces a turbulent flow. It takes approximately the same timescale of 50 reduced time units for the ensuing turbulent spot to spread in the spanwise direction and fill the computational domain downstream. The difference concerns the sub-liminal case. From $t^* = (\delta_0^*/\delta^*)t$=1200 to 1400, the edge state appears to decay in amplitude like in a standard relaminarisation event where the largest scales decay last. For 1400<t^*<1500, spanwise-independent waves start to propagate downstream while increasing in amplitude. At $t^* \approx 1400$ these waves undergo several destabilisations at various z-positions. Each destabilisation invariably leads to a turbulent spot, and the flow appears fully turbulent for t^*>1600. There is no doubt that these waves are Tollmien-Schlichting waves. This is confirmed by their phase speed, range of wavelengths and by the space-time diagram (x, t) displayed in figure 4.10. An interesting feature in this diagram is how TS waves grow upstream of the streaky edge state, not at the same location (the mechanism pointed out in Ref. [324] actually prevents TS waves to grow on streaks). Since streaks and TS waves travel at unambiguously different velocities, the TS waves are quickly left behind. It is thus not strictly impossible to observe, out of one single localised initial condition, two patches transitioning through different mechanisms.

The above results unfortunately has nasty consequences for the classical bisection process. On short times it is still possible to monitor without ambiguity, out of a single observable $a(t)$, on which "side" of the edge manifold the perturbation lies : the laminar side is characterised by trajectories where $a(t)$ decrease monotonically to zero. Over longer times one observable is no longer enough for such a task : an initial decay has little meaning given that ultimately, all trajectories will experience transition (be is via TS waves or streaks) and display increasing $a(t)$. It is hence no longer possible to know on which side of the edge manifold a given state lies. This has nothing to do with the choice of the observable $a(t)$. It is not even known whether the edge manifold is still orientable and whether its sides have a particular meaning. The situation in practice is illustrated in figure 4.11 using precisely the observable $a(t)$ used in Ref. [318]. For a given choice of the bound a_L, some trajectories might be interpreted on short times as going laminar, whereas in fact they turn turbulent at later times. Bracketing a given trajectory becomes thus impossible as long as one cannot monitor whether the ensuing transition is due to the destabilisation of TS waves or not. Long-time bisection leads hence to an 'uncertain area'.

Although this is the initial definition adopted in other contexts, one can no longer claim that the stable manifold of the edge state divides the state space into two distinct basins of attraction. All perturbations end up at later time turbulent, except perhaps the ones lying directly on that manifold to be found. There is however an edge which, to the accuracy permitted in the "uncertain area', marks the boundary between two different types of trajectories : those experiencing transition through streak breakdown and

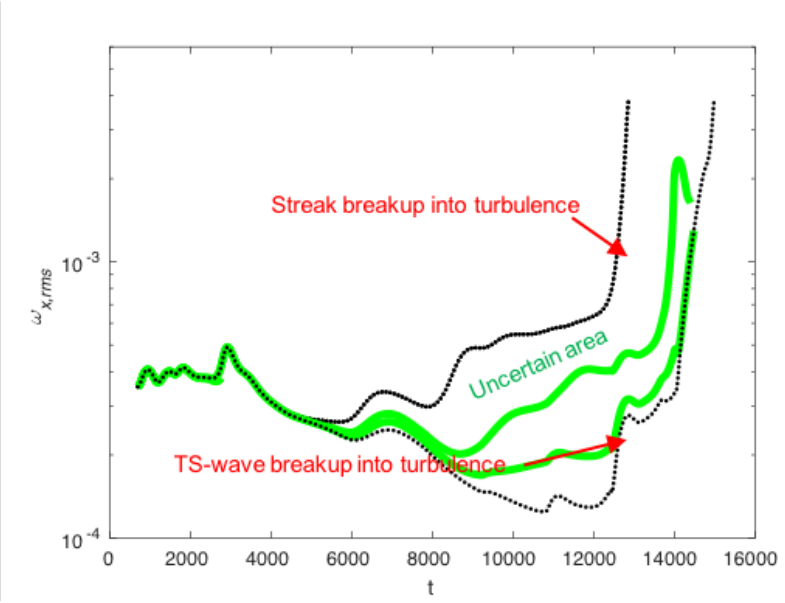

FIGURE 4.11 – Observable $a(t)$ vs. t during application of the bisection algorithm. The green vertical line marks the maximum time for the edge tracking algorithm using that observable, and the two dotted lines stand for the observable bounds $a = a_L$ and a_T (see text).

those undergoing destabilisation of TS waves. In other words, the edge marks the boundary between bypass and classical transition. The latter involves trajectories with, in principle, an *early and transient relaminarisation stage* as in figure 4.9 (right). The existence of an uncertain area suggests that some perturbations might transition twice at two different locations, in a mixed-type transition.

4.2.2 Application to wind tunnel experiments

The conclusion from the previous results is difficult to handle : bisection in spatially developing flows can only be trusted over finite time horizons, however the edge state is defined as an asymptotic state only. This contradiction is not necessarily important for the original purpose of explaining the main mechanisms occuring during bypass transition. Indeed, as long as the excitation parameters do not favour the rapid growth of TS waves over streaks breakdown, bypass remains the only important phenomenon. It is hence important to delimitate the parameter range of applicability of the edge-bypass picture. Figure 4.12 contains parts of the experimental database by S. Shahinfar and J. Fransson [325, 326] for wind tunnels excited by incoming grid turbulence, namely the transition values of $Re_x = xU_\infty/\nu$ depending on the turbulence level Tu (in %). These x-locations are compared with the locations where transition occurs latest in the present initial value problem. Such locations are close to $Re_x \approx 10^6$, to be compared also to the theoretical onset for TS waves at $Re_x = 9.1 \times 10^4$. This gives a lower bound for the Tu levels required in practice to observe transition earlier than suggested by edge tracking. The minimal corresponding Tu levels are around 1.5%. This corresponds to the "weak bypass regime" reported originally by Narasimha [327]. As a reminder, classical transition dominates for $Tu < 1\%$ whereas bypass is classically observed even up to 6%. The above limitations still offer a comfortable zone in which to investigate streak breakdown with the help of the edge state as a base flow.

4.2.3 Low-order modelling

The results from Ref. [318] make it clear that the bistable picture in the introduction of Chapter 3 does not apply to the Blasius flow, because the laminar fixed point is itself unstable. This property is not

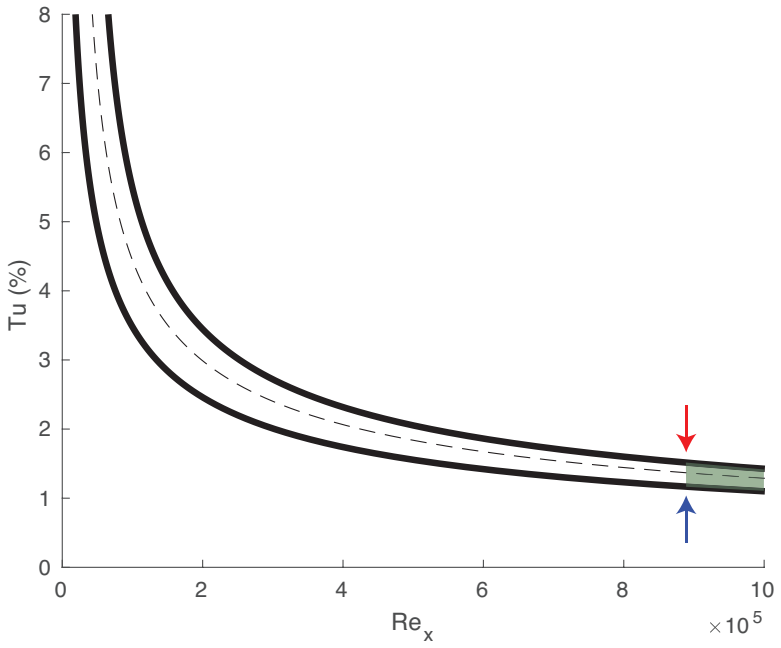

FIGURE 4.12 – $Tu(\%)$ versus Re_x for experimental bypass transition data [325], showing intermittency of 10% and 90% (thick lines) and 50% (dashed line). The arrows mark the Re_x-limitation of the bisection algorithm. For larger times and Re_x, mixed transition is expected (grey area).

a consequence of the spatial development of the boundary layer, and it can *a posteriori* manifest itself in other flows including planar ones. The instability of the laminar base flow to Tollmien-Schlichting waves has been also reported in plane Poiseuille flow [20], in ASBL [328], annular pipe flow and many others (it is shorter to insist instead on the fact that such unstable waves are *not* found only in pipe and pCf). However in these flow parametrised by a meaningful Reynolds number Re, this instability occurs only above a given value $Re = Re_c$ which in general exceeds by several orders of magnitude the onset of bypass transition. For all these flow cases one expects, in analogy with the results in the Blasius flow, that the notion of edge manifold changes or loses its relevance beyond Re_c. Two such cases have been documented recently. The simplest is bent pipe flow [329] for which the turbulent regime can be in competition with a Hopf bifurcation of the laminar flow. From a dynamical point of view, this case is hardly more complex than the standard case without Hopf bifurcation. Indeed, the Hopf bifurcation is supercriticial : the possible attractors are, on one hand, either the fixed point or the limit cycle and, on the other hand, the turbulent state. Bisection and edge tracking are expected to proceed well and to identify the edge state. A second example is plane Poiseuille flow in a small periodic box [330]. This case is more difficult : the edge state exists before Re_c as a TW state, which can be continued beyond Re_c. The instability to TS waves is known to be subcritical [331] and to include many bifurcations. As a consequence, does the TW state remain an edge state beyond Re_c ? The amount of open questions regarding the edge manifold in the presence of an additional instability of the base flow suggests the use of a low-dimensional model. The reduced cost of the simulations would leave ample room for parametric studies or exploration, as opposed to the very costly Blasius simulations.

Autonomous model

The two-dimensional DM2D model by Dauchot and Manneville [17] was used in Chapter 3 to introduce the concept of edge in the bistable context. In the same way we wish to introduce a new low-order model that would cope with the above constraints, yet with maximal simplicity. It was decided to generalise the

DM2D model into a three-dimensional "DM3D" model, with the same variables x_1, x_2 and an additional variable x_3. The model should satisfy the following properties :

— when restricted to the two first dimensions x_1 and x_2 (i.e. when $x_3 = 0$), the model coincides with DM2D
— the laminar fixed point L is linearly unstable above some parameter
— the nonlinear terms conserve the new total energy $E = x_1^2 + x_2^2 + x_3^2$.

These constraints lead to the three-dimensional below :

$$\frac{dx_1}{dt} = s_1 x_1 + x_2 + x_1 x_2 \tag{4.7}$$
$$\frac{dx_2}{dt} = s_2 x_2 - x_1^2 + \sigma x_3^2 \tag{4.8}$$
$$\frac{dx_3}{dt} = s_3 x_3 - \sigma x_2 x_3. \tag{4.9}$$

Eqs. 4.7, 4.8, 4.9 are characterised by the two same constants $s_1 < 0$, $s_2 < 0$ as the original DM2D model ($s_1 = -0.1875$, $s_2 = -1$) [17] . It involves also the additional parameter s_3, interpreted as the exponential growth rate of the new instability of L. Furthermore, s_3 is the control parameter for this new study. The instability is only present if $s_3 > 0$. The constant $\sigma = -1$ allows the instability to saturate, it occurs in the third as well as the second equation by virtue of the conservation of energy by the nonlinear terms.

The bifurcation diagram of the DM3D model, as s_3 increases, is reported in figure 4.13. The hyperplane $\mathcal{P} : \{x_3 = 0\}$ is an invariant set of the dynamics for all s_3. For $s_3 < 0$, the invariant sets of the system are only those of the DM2D model, embedded in $\mathbb{R}^3$. The three fixed points L, E, $T \in \mathbb{R}^3$ are respectively the stable "laminar" attractor L, the hyperbolic saddle point E, which acts as the "edge state", and the stable "turbulent" fixed point T. They remain the same for all s_3 but their stability will depend on s_3. Figure 4.13 can be read as follows :

— For $s_3 < 0$, $\mathcal{P}$ is locally stable and the dynamics transverse to $\mathcal{P}$ is contracting. The edge manifold Σ is a two-dimensional surface invariant along x_3.
— At $s_3 = 0$, L loses its stability in a supercritical pitchfork bifurcation. A new stable attractor S emerges for $0 < s_3 < s_{3H} \approx 0.0296$. This is the start of zone I in figure 4.13.
— At $s_3 = s_{3H}$, via a supercritical Hopf bifurcation S becomes unstable in favour of a stable limit cycle $\mathcal{C}$. For $s_{3H} < s_3 < s_{3c} \approx 0.03125$, the limit cycle $\mathcal{C}$ increases in size.
— At $s_3 = s_{3c}$, the attracting limit cycle $\mathcal{C}$ collides with $\mathcal{P}$ simultaneously at the points E and L.
— For $s_{3c} < s_3 < s_{3d} \approx 0.063$, E still has one unstable direction but all trajectories outside $\mathcal{P}$ converge now to the turbulent attractor T. This is zone II in figure 4.13.
— At $s_3 = s_{3d}$, S merges with the saddle point E in a pitchfork bifurcation.
— Beyond $s_3 = s3d$, E still exists but it has now two unstable directions, include now one unstable direction transverse to $\mathcal{P}$. This is zone III.

The edge manifold appears robust for all $s_3 \leq s_{3c}$, in the sense that it separates two separate basins of attraction. Note that the attractor in the "laminar basin" is not necessarily the fixed point L, but can also be instead S or $\mathcal{C}$. The collapse of the edge manifold begins at the boundary crisis at $s_3 = s_{3c}$. According to the typology defined by N. Lebovitz [332], the edge turns from *strong* to *weak* : it separates the state space locally but not globally. All orbits outside Σ are attracted by T and they may "only be distinguished by features such as orbital complexity and time to reach the attractor" [332]. However for $s_{3c} < s_3 < s_{3d}$, E remains a saddle point with one unstable direction. Classical bisection would output E as an edge state. The "edge manifold" exists, yet it no longer separates the state space into two basins of attraction, rather it delimitates the *fast routes* from the *slow* ones. The slow routes comprise all trajectories that transiently visit the neighbourhood of L before converging towards T. The last bifurcation at $s_3 = s_{3d}$ corresponds to the loss of *accessibility* of E. Beyond $s_3 = s_{3d}$ no trajectory outside $\mathcal{P}$ leads to E. Classical bisection would fail in that case as it would output T. There is neither any edge state nor

edge manifold any longer [333].

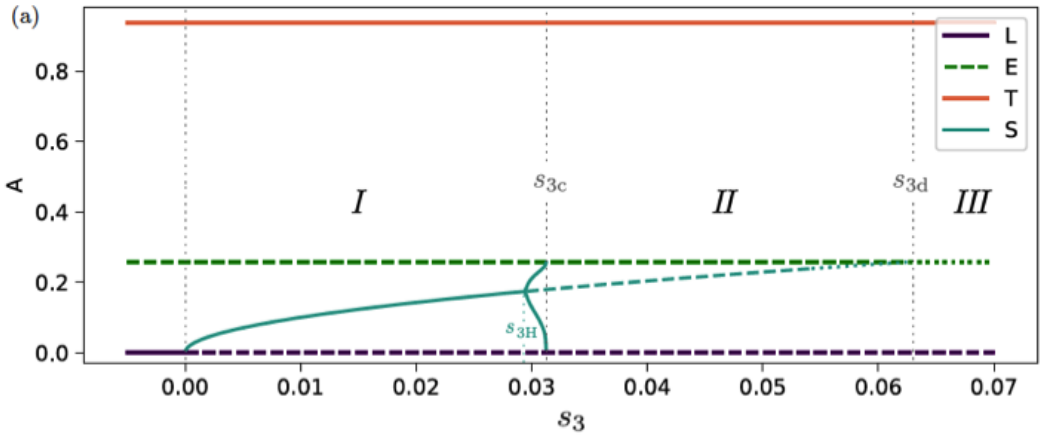

FIGURE 4.13 – Bifurcation diagram for the DM3D model as s_3 is increased. L : laminar fixed point, E : saddle point (edge state), T : turbulent fixed point, S : secondary laminar fixed point.

A surprisingly simple correspondence between the model and the hydrodynamic cases mentioned earlier can be claimed. The case of bent pipe flow corresponds to zone I in figure 4.13. It is essentially the bistable picture with the classical edge notion. The main difference is that the attractor in the laminar basin is not the laminar solution but another state bifurcating from it. Zone II corresponds to the dynamics discussed in Ref. [330] : the edge state solution still exists and can be identified using bisection. However its stable manifold does not separate the state space into two basins anymore, but into zones with different transition properties. State portraits corresponding to Zones I and II are displayed in figure 4.14. Eventually zone III displays the dynamics closest to the Blasius case, where bisection reveals unable to identify any edge state. The edge state existing for lower s_3 is still a solution of the system but it has changed stability and dynamical role.

Non-autonomous model

Eq. 4.9 is still relatively ill-adapted to the description of the edge dynamics in the Blasius boundary layer because it depends explicitely on an external parameter s_3. By contrast, for the Blasius flow (or any spatial developing flow) one would expect the control parameter to evolve with time, in analogy with the Reynolds number which evolves with the position of the localised state as time progresses. Assuming for simplicity a single propagation velocity, Eq. 4.9 can be turned easily into an *non-autonomous* O.D.E. system by decreeing $s_3 = k_1 t + k_2$ (with $k_1 > 0$). The resulting system reads

$$\frac{dx_1}{dt} = s_1 x_1 + x_2 + x_1 x_2 \tag{4.10}$$

$$\frac{dx_2}{dt} = s_2 x_2 - x_1^2 + \sigma x_3^2 \tag{4.11}$$

$$\frac{dx_3}{dt} = (k_1 t + k_2) x_3 - \sigma x_2 x_3, \tag{4.12}$$

The time interval is restrained to $t \in [t_0, t_0 + T_F]$, with $k_1 = 0.73/T_F$ and $k_2 = -0.1$. Two trajectories are represented in a three-dimensional state portrait displayed in Figure 4.15. The two corresponding initial conditions lie at $t = 0$ on either side of the original edge manifold (i.e. the manifold existing for $s_3 < 0$) with a small non-zero value of x_3. The non-autonomous dynamics is easier to describe than its autonomous counterpart : either the trajectory reaches T directly, or it does so by first approaching transiently the neighbourhood of L, leaving $\mathcal{P}$ locally near L and approaching it again near T.

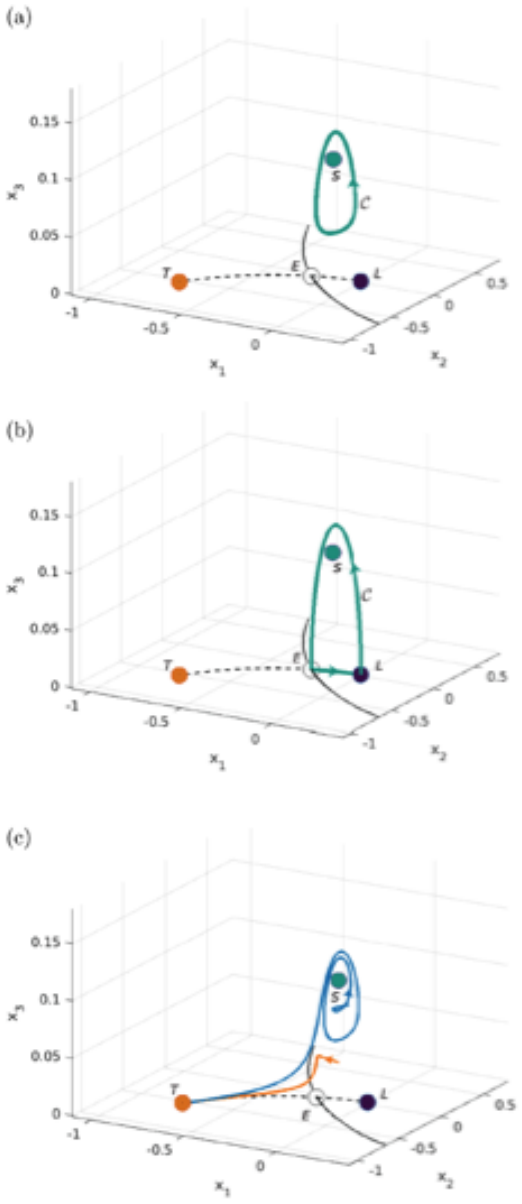

FIGURE 4.14 – Autonomous DM3D. Comparison between region I and II. Phase portraits for different values of s_3 close to the global bifurcation : (a) $s_3 = 0.031$. The system presents a hard edge between $\mathcal{C}$ and T, region I (b) $s_3 = 0.03125$. Heteroclinic cycle close to s_{3c} (c) $s_3 = 0.032$, beyond s_{3c} the heteroclinic connection collapses and the edge $\mathcal{W}^s(E)$ becomes of the weak kind, region II. The blue and orange trajectories illustrate the two newly born different routes to transition.

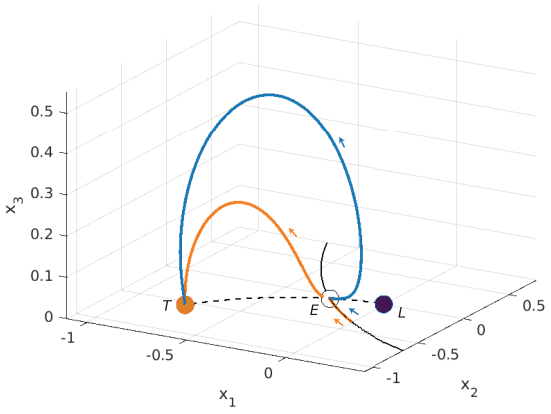

FIGURE 4.15 – DM3D nonautonomous model. state portrait for two trajectories starting close to the edge of DM2D and to the invariant plane $\mathcal{P}$.

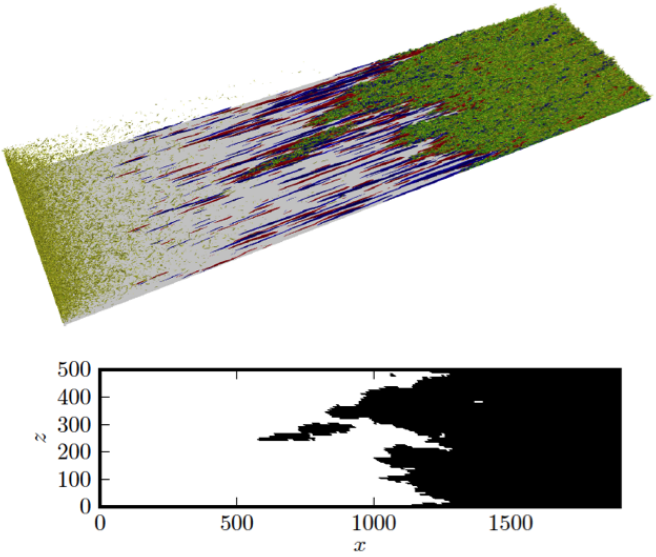

FIGURE 4.16 –

4.3 Low-order modelling using cellular automata

We would eventually like to test the validity, in the Blasius boundary layer, of the nucleation scenario involving a localised edge state. The nucleation scenario is based on the simple idea that the nucleation and the spreading phenomena are two decoupled phenomena. The main idea is to analyse quantitatively a real simulation of the bypass transition process in the Blasius boundary layer, in order to *learn* the basic rules of turbulence spreading. Then in a second phase, the nucleation scenario, in the form of a space-dependent nucleation probability, can be tested inside a simple automaton model featuring the same probabilistic spreading rules. The transition statistics obtained that way can be compared with the original statistics from the large-scale simulation or even from experiments. The nucleation scenario is later labelled 'valid' in case the turbulence statistics match well.

For simplicity, this study is restricted to short-time edge state dynamics explained earlier, so that no Tollmien-Schichting wave is expected to interfere with the transition proces. This implies that the equivalent turbulence level at the entrance (located at $Re_{\delta_0^*} = 300$) must lie strictly above 2%. The chosen range of values of Tu is therefore 3–4%, while the integral lengthscale of the incoming turbulence is set to $L = 10$.

The whole transition process was reproduced using costly Large-Eddy numerical simulation (LES) of the incompressible Navier-Stokes equations with suitable boundary conditions, in a computational domain of width $L_z = 500\delta_0^*$. The same code and methodology as Brandt *et al.* [303] were used, as illustrated in Fig. 4.16(top). The massive amount of space/time data collected in such simulations was post-processed and reduced to binarised data on a plane, with a focus on laminar-turbulent coexistence. A given location at the wall is either laminar or turbulent with a given probability $p(R)$, where R is the Reynolds number coordinate, e.g. Re_{δ^*}. In practice, because of the finite correlation lengths within the flow, probabilities need not be defined pointwise but rather *cell*-wise, where the dimensions of a typical cell will be defined later. This reduced dynamics becomes akin to a two-dimensional probabilistic cellular automaton (PCA), consisting of two phases : laminar or turbulent, as illustrated in Fig. 4.16(bottom). Within this approach, turbulent is identified using a Boolean variable. In a given cell at a given time the laminar/turbulent nature of the flow depends, *in a probabilistic way*, on the neighbouring variables at previous times.

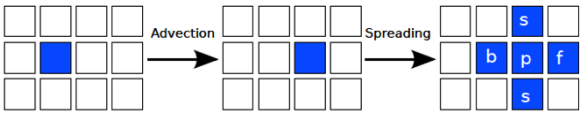

FIGURE 4.17 – Update rules determined directly from the LES simulations.

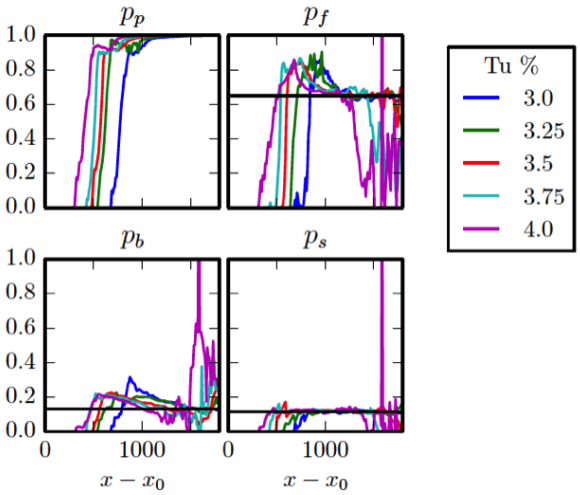

FIGURE 4.18 – Probabilities p_p p_f, p_b and p_s for turbulence to respectively persist, move forward, backwards or sideways among the cells defined in figure 4.17. These probabilities are deduced from the LES data and plotted versus the streamwise position $x - x_0$ for different values of the free-stream turbulence level Tu from 3 to 4 (expressed in %).

As an indicator for turbulent motion the local spanwise shear stress at the wall $Q = \partial w/\partial y|_{y=0}$ is used with a threshold value of 0.3. The size of a cell, as well as the timestep in the automaton, are deduced from the autocorrelation functions of Q in space and time. The data is finally regularised using Gaussian filtering in order to remove spurious events. This yields a two-dimensional array with discretisation on $N_x \times N_z = 204 \times 76$ gridpoints.

The probability rules of the PCA are schematically shown in 4.17. Each temporal update follows two steps. The first step is deterministic and models the advection, translating all cells by one unit in the downstream direction. In the second step, a turbulent cell can persist with probability p_p and infect neighbouring cells, spreading turbulence forward, backward or sideways (left and right) with probabilities p_f, p_b and p_s, respectively. In addition, spontaneous nucleation of turbulence is allowed for with probability p_c as in Ref. [259]. The four probabilities p_p, p_f, p_b and p_s are directly identified as functions of R from the simulation data. Their small variations in the transitional region suggest to model these functions as constants, represented as solid lines in figure 4.18.

The exact choice for the nucleation rate $p_c(R)$ is however more delicate and has a crucial influence on the dynamics of the automaton. It is clear that $p_c = cst$ is not a physically relevant hypothesis. The experimental literature often assumes, instead, p_c to be a Dirac function, consistently with the old "concentrated breakdown hypothesis" [334, 335]. Determining the exact function form for p_c from data turned out to be too demanding in terms of simulations to be deduced and was given up. The nucleation rate has instead been modelled using a minimal one-dimensional approach to the edge state concept. This requires the knowledge of a scalar quantity $A(x(t))$ to be defined. Let A_E be the amplitude of the edge state, assumed constant at leading order. For turbulence to develop downstream from a nucleation event, it is required that the amplitude $A = A_0$ at the entrance of the domain satisfies $A_0 \geq A_E$. The

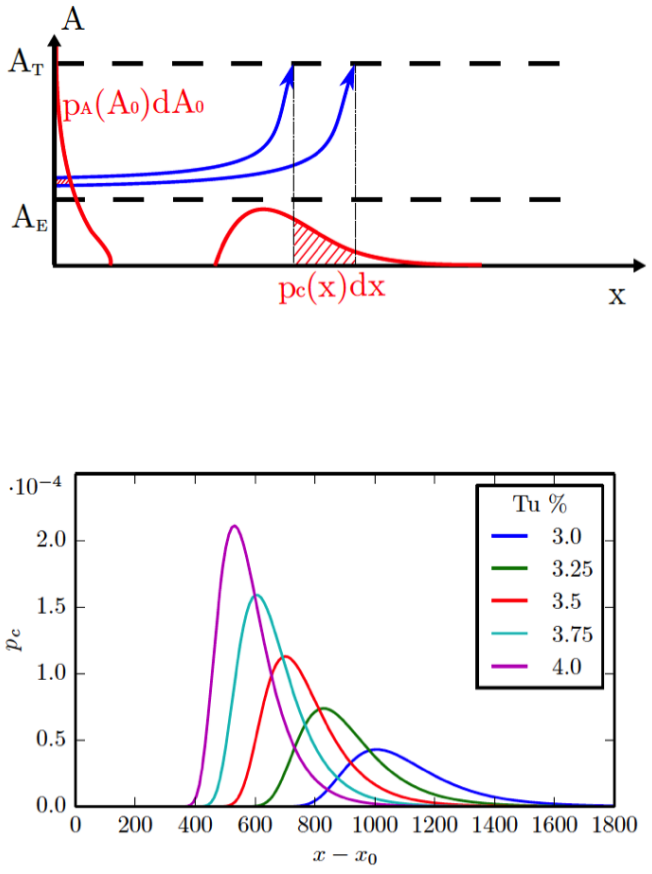

FIGURE 4.19 – Top : Sketch to explain the nucleation model based on the edge state concept and yielding the nucleation rate $p_c(x)$. Bottom : Nucleation rate $p_c(x)$ estimated for various values of the free-stream turbulence level Tu from 3 to 4 (expressed in %).

instability of the edge state implies that, after some time corresponding to a distance x, the amplitude A grows exponentially from A_0, until it reaches the threshold value A_T. The way how A_0 is distributed statistically at the entrance of the domain $x = 0$ determines indirectly the nucleation probability, using the differential relation $p_c(x)dx = p(A_0(x))dA_0$ illustrated in figure 4.19(top). A standard Gaussian distribution has been assumed here, which leads to an analytical expression for $p_c(R)$ documented in Ref. [336] and shown in Figure 4.19(bottom) for different values of Tu. The higher the value of Tu, the earlier the nucleation of a spot, and the narrower the distribution of $p_c(x)$. Direct measurements of $u_{r.m.s.}$, considered as a relevant choice for A, have yielded different distributions closer to *Gamma* distributions, yet the philosophy behind this modelling does not change. Note that no variant of the model ever predicts concentrated breakdown.

Eventually, by seeding the flow statistically using the nucleation rate p_c displayed in figure 4.19 and using the constant fits from figure 4.18, the automaton reaches a steady regime with fluctuations. The main quantity of interest is the intermittency factor $\gamma(R)$, identical to the turbulent fraction introduced in the previous chapter. The qualitative as well as quantitative match with the experimental measurements, as well as with the computational results from the simulation, are very convincing. This suggests

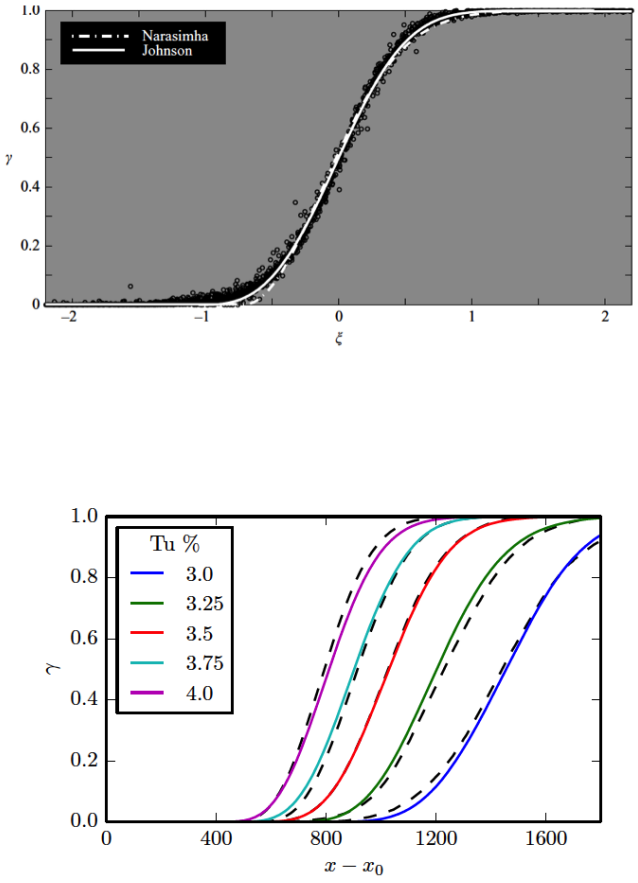

FIGURE 4.20 – Intermittency factor γ versus streamwise position. Top : experimental measurements from Ref. [304] (using a rescaled streamwise variable). Bottom : model versus LES measurements.

that the decoupled dynamics "nucleation + spreading" is a relevant picture for modelling. The match is equally good when it comes to other statistical quantities [336]. Besides, we note that independently of the details of the model, the distribution for γ is invariably sigmoid–shaped. This distribution differs from the distribution suggested by the Directed Percolation hypothesis, which exhibits a non-derivable singularity at $\gamma = 0$. Leaving aside the issue of spatial development, which probably has no influence on such local issues, the sigmoid-shaped scenario seems particularly adapted to the development of turbulence downstream of a grid, in the presence of a non-homogeneous nucleation rate. A similarly-looking curve was also found in recent experiments of channel flow [228, 337], although it was not necessarily recognised as such by the authors. By contrast, the nucleation rates in models compatible with the DP scaling are implicitely homogeneous. This important example suggests that, depending on the way turbulence can be nucleated spatially, different universal scenarios can be envisioned.

4.4 Conclusion

Establishing a state space picture for turbulent spots in the Blasius boundary layer is not a trivial generalisation of the approach followed for parallel shear flows. However, although the concept of turbulent attractor is not relevant due to the spatial development, the concept of edge manifold is tractable and can be investigated using the classical bisection algorithm. Unsteady edge trajectories become hence the new object of study. Their internal dynamics reveals localised streaks with bursts and streak switching, which is comparable to parallel flows such as channel flow or the boundary layer with suction [115]. An additional complication blurs the picture : the edge trajectory is well defined only over moderate times [317]. Over long timescales the linear instability of the laminar base flow to Tollmien-Schlichting waves can not be ignored. These waves form localised wavepackets that lead invariably to turbulent spots later downstream. Their very existence makes the usual concept of edge irrelevant as such, however trajectories on the edge manifold remain interpretable as mediators between two types of transition : the bypass and classical scenarios [318]. This distinction appears relevant in wind tunnel experiments for levels of incoming turbulence Tu above 2%. The structure of state space close to the edge manifold has been understood and reproduced using a three-dimensional O.D.E. model system, obtained as a generalisation of the two-dimensional Dauchot–Manneville [333]. Eventually, realistic LES simulations of the bypass process have been analysed directly. The short-time edge model can be used to relate theoretically the nucleation rate of turbulent spots to the distribution of incoming turbulence. The relevance of this model has been tested within the context of a data-driven celullar automaton, where the spreading probabilities have been directly inferred from the large-scale simulations [336]. The model reproduces without any difficulty the mean intermittency curve, a sigmoid-shaped curve different from the critical scalings from directed percolation, explained by the non-homogeneous nucleation rate. This project in its entirety suggests that the realistic bypass transition process in spatially boundary layers can be regarded, on moderate timescales, as an *activation process* where the edge state plays the role of the unstable saddle.

5

Conclusions and outlooks

5.1 Conclusions

5.1.1 State space organisation

A large part of the research illustrated in this thesis deals with a temptative sketch of the state space of a fluid system where transition to turbulence is possible from some (but not all) initial conditions. In most cases a robust picture needs to include an *edge* hypersurface that separates the state space in two different basins of attraction [81, 97, 100]. That picture gets challenged in a few cases : when the turbulent state is not a formal attractor, or when the laminar state itself is unstable. The edge manifold has been shown to persist in such cases although its nature as a separatrix is no longer guaranteed in the latter case [333]. Two locations on this edge manifold are worth deeper investigations : the local attractors within the edge, namely *edge states* [177], and the lowest-energy perturbations namely *minimal seed* [178]. The former forms an invariant set often displaying chaotic dynamics, while the latter is a well-defined optimal way of triggering transition in the frame of initial value problems (IVPs). Generalising such a picture to a framework different from IVPs is a welcome challenge. Resolvent analysis has been an increasingly popular tool in this regard [16, 25] although the problem of initial conditions is not fully absent of that formulation either. Another case where the edge picture needs an update is that of subcritical boundary layer flow. While parallel boundary layer flows (e.g. ASBL) do not introduce any additional difficulty with respect to the other planar flows [338], an additional complication arises in spatially developing boundary layers due to the absence of governing parameter. Achieving a description of transitioning boundary layers in terms of dynamical systems was not a trivial generalisation of the concepts developed by former authors : the mathematical notion of turbulent attractor itself is formerly fragile, and the notion of bounded edge trajectories does not emerge unless a rescaling by the boundary layer thickness is considered [318]. For spatially developing boundary layer flows, it turns out that the notion of edge trajectory is more useful that the (asymptotic) notion of edge state. Consequently a finite-time description and formalism are better suited to the description of the bypass transition process, as adopted in the recent PhD manuscript of Miguel Beneitez [339].

5.1.2 Phenomenology depending on the scale of observation

The increase in computing power in the last decades has accompanied the recent progress in understanding transition to turbulence. In particular, locally well-resolved simulations of the governing equations are now routinely achieved. However the spatial extent of the flows under consideration is in computations always finite. This has lead to difficulties related to the interpretation of the computation results. Some confusion has inevitably taken place when considering minimal flow units (MFUs), in other words spatially periodic domains of smallest size able to accommodate non-trivial flow dynamics. Designed historically [28] as a numerical means to simulating the flow at a cheaper price and in isolation from the largest turbulent scales, the MFU concept has evolved into an autonomous paradigm of computational turbulence, independently of the experimental reality. In such small domains, the velocity field is fully cor-

related with itself at least in the spatial sense. This artificial constraint turns turbulence into mainstream temporal chaos, and the clean application of dynamical systems concepts proceeds *as expected*, despite the technical difficulties associated with continuous symmetries and high dimension. Although the limitations of this deterministic view have been frequently mentioned in the last decade, notably by Paul Manneville, a few concepts developed in that framework have proved robust to generalisation. This is the case in particular for edge states and minimal seeds : as the computation domain size is increased, these structures become progressively spatially localised. In the limit of infinitely large domains the localisation property becomes robust. Edge states and minimal seeds remain hence relevant to spatially unbounded experimental contexts, although their natural instability makes their experimental investigation arduous. Since edge states are equilibrium regimes, they are governed by a nonlinear process usually referred to as *self-sustaining process* (SSP). The first SSP was originally suggested by F. Waleffe and co-authors in the context of a periodic cell of plane Couette flow [9]. The present contribution demonstrates the multiplicity of SSPs, and the crucial differences between different SSPs, notably in the presence of localisation [130, 153, 193].

The possibility to change from one scale of observation to another one, simply by considering different spatial extents among the computational parameters, completes this description. For a given periodic domain (with a size fixed in outer units), reducing the driving Reynolds number makes the turbulent state feel increasingly the boundary conditions. Whatever the domain size, below a size-dependent value of Re the flow dynamics will manifest self-correlation effects due to the spatial periodicity. The consequence is usually a boundary crisis turning a sustained (although possibly intermittent) turbulent state into a chaotic regime with finite lifetimes, i.e. a chaotic saddle. This phenomenon, rather than a computational nuisance, should be seen as a handwavy explanation for the occurrence of local relaminarisation in shear flows. Similarly, increasing the domain size makes the apparition/disappearance of the turbulent state qualitatively closer to the concept of absorbing phase transitions. Important efforts have been devoted to the question of whether or not subcritical transition to turbulence obeys the universal class of directed percolation independently of finite-size effects. Although the emerging answer is predominantly positive for parallel flows, again this thesis has highlighted different scenarios specific to boundary layer cases. For parallel boundary layer flow cases a discontinuous transition seems to be the rule [1], because wall-localised structures happen to be ruled out by kinematic effects. For spatially developing boundary layer flows, the situation is more subtle. The non-homogeneity of the base flow in the streamwise direction implies a non-homogeneous spot nucleation in space (but homogenous in time). By contrast in parallel flows, usually described as IVPs, spots have to be nucleated at early times but with equal probability through the spatial domain. Although parallel flows seem to fall, in the thermodynamic limit, into the class of directed percolation, for spatially boundary layer flows this description of the nucleation rate leads to a dramatically different dynamics : the turbulent fraction increases like a sigmoid with the distance downstream, not like a power law. This new distinction allows one to shed light on formerly ambiguous results. In recent experiments of channel flow [228] for instance, turbulence was generated upstream using a honeycomb and left to decay by itself, and the departure from power-law in intermittency statistics was rapidly attributed to finite-size effects. The present point of view (based on an analysis of the nucleation rate both as a function of space and time) suggests a situation closer to the bypass case as in developing boundary layer flows, with intermittency statistics fully consistent with a sigmoid curve.

5.2 Outlooks

5.2.1 Patterning mechanism

Although a number of new elements has contributed to a better understanding of the transitional regime of wall-bounded shear flows, much remains to be understood. In particular the missing piece in the puzzle seems to concern the origin of the streamwise localisation of turbulent patches, from which much follows. Suggesting self-sustaining processes compatible with streamwise localisation is a necessary first step. However it does not necessarily indicate why streamwise localisation is the only stable option

for the turbulent flow below some value of the Reynolds number. Another related aspect is the mechanism present at the onset of laminar-turbulent patterning, before defects start to appear inside the patterms themselves. Recent simulations suggest that the laminar-turbulent structures are the most pronouced instances of a simpler amplitude modulation [244]. Does this modulation arise as an instability of the homogeneous turbulent flow ? Can it even be compared qualitatively to a Turing instability mechanism as found in standard reaction-diffusion systems [296] ? Or is a fully different picture needed, like the crystallisation picture recently suggested in Ref. [297]. Beyond the onset, the finite-amplitude patterns themselves keep some of their best secret unanswered. The data in chapter 3 has shown that the angle as well as the wavelength selection, and their dependence on the Reynolds number, are not trivial. The values determined from numerics correspond to a given numerical or experimental protocol, which suggests multistability, a feature already noted in Ref. [66]. It is yet not understood whether the range of possible wavelengths and angles obeys well-defined rules, and whether such rules can be deduced from first principles, either the Navier–Stokes equations or even model equations. The thesis of Pavan Kashyap, currently PhD student at LISN, will aim at answering some of these open questions.

5.2.2 Rough walls

One of the reference engineering plots in hydrodynamics is the Moody diagram, which features the energy loss in the flow due to mostly viscous effects. It is a well-known fact that at sufficiently high Reynolds numbers the "smooth" part of the C_f curves is a poor description of the reality, and that the mean roughness of the walls needs to be taken into account. This observation naturally suggests that no study of transition to turbulence is complete without the eventual inclusion of wall roughness. The high-Reynolds number range where such effects manifest themselves calls for a modelling strategy. It is not fully understood how much roughness plays a role in the intermittent range of values of Re where spatio-temporal intermittency is the dominant dynamics. To start with, there has not been any convincing dynamical systems approach to the rough case so far. Although the linear stability of the corresponding laminar flow can be envisioned, the recurrent issue of selecting the right computation domain size emerges again. Although recently a minimal flow unit framework was suggested for rough flows [340], the intrinsically disordered nature of the roughness landscape appears rather incompatible with the notion of 'minimal' domain.

A preliminary study of the patterning regime of plane Couette flow under the hypothesis of rough walls has appeared recently [341, 342]. It is based on a simple statistical model where the influence of the roughness elements amounts in average to a damping force, applied in the streamwise direction and dependent only on the distance from the wall. This study suggests that the transition phenomenon is hardly affected by weak roughness amplitudes of less than 10%, consistently with the fate of the high-Re picture when considered at sufficient low Re_τ [343]. For larger amplitudes exotic structures such as non-oblique stripes were predicted. These results call for a wider range of values of Re of investigation, and possibly other flows, and compared with experimental and model-free numerical investigations. Another point of view on turbulence can be adopted by considering, rather than developed turbulent regimes, transients such as the growth of turbulent spots. This would be closer to the modelling approach adopted by Y. Pomeau [179] and later D. Barkley [180] based on front motion. Finally, "rough" wall geometries do not reduce to rigid solid walls that are not flat. A number of natural situations exists where knowledge of the fluid-structure interaction is crucial. They include non exhaustively vegetated canopies [344, 345], soft and even hairy surfaces [346].

5.2.3 Control of subcritical transition

In some circumstances (most trivially for drag reduction) one wishes the flow to remain laminar at all times. Since the laminar state is usually already linearly stable, the aim of control in such a case would be, rather than stabilising the laminar state even more, to either destabilise the turbulent state, or to reduce the size of its attraction basin. The robust presence of a saddle state at the root of the

laminar-turbulent distinction makes it ideal for nonlinear control strategies. The goal becomes simply to play on the parameters of the system such that a given initial condition finds itself on the other side of the boundary. This simple idea has been surprisingly under-exploited. A notable exception is the study by G. Kawahara [347] who managed to stabilise numerically a minimal flow unit of turbulent plane Couette flow by adding suitably quantified spanwise rotation. It is my personal opinion that simple instances of subcritical flow transition can open a new avenue of control strategies with an emphasis on nonlinear rather than linear properties. However, as often size matters : a successful algorithm in a minimal flow unit can fail in an arbitrary large domain. As seen in Chapter 3 the dynamical systems perspective becomes of a questionable interest when dealing with extended flow systems or experimental condition. Therefore an effective control strategy should be developed by taking this limitation into account. Recently, a simple methodology was suggested by Hof and co-workers [348] based on a mean flow perspective. A blunted mean flow profile is less efficient at supporting Waleffe's self-sustaining process [30], therefore any way to sufficiently blunt that mean flow should make relaminarisation effective. This method is heavily reminiscent of Large Eddy Break-up devices developed much earlier in (higher-Re) wind tunnels investigations (see e.g. Refs [349, 350]).

5.2.4 Non-Newtonian rheologies

The results presented in this thesis are limited to the context of Newtonian fluids. Basic evidence suggests that one of the simplest yet effective passive control strategies to reduce the drag is to change the fluid. This can be achieved efficiently by, in the case of liquids, adding polymers [351] whose concentration is a new parameter of the problem. There are well-known analytical closures in the literature for such rheologies such as the Fene-P model. The addition of an additional parameter (usually in the form of a Weissenberg number Wi) opens up a fully different zoology of states including the celebrated Maximum Drag Reduction state (see e.g. [352]) and the recently discovered regime of elasto-inertial turbulence [353]. Interestingly for the present purpose, the classification between edge and turbulent regimes put forward in Newtonian fluids also has its relevance in the presence of polymers at least for moderate values of Wi, mainly because the structure of the edge states make them poorly sensible to the polymers [354]. The situation for other rheologies remains almost entirely open as of now. The inclusion of surfactants (e.g. washing-up product into water), either added directly into the bullk of the fluid or inside gas bubbles fed into the flow, is also potentially interesting as another way of reducing drag (see e.g. Ref. [355]).

5.2.5 Towards more turbulent shear flows

Ultimately, like in the conclusions of most hydrodynamical studies I am expected to discuss the extension of the present theories to higher Reynolds number. Two questions arise for the present thesis. Firstly, how does the transition process evolve for higher values of Re ? Secondly, now that we can pretend to understand the transient transition process, does it teach us anything new about the nature of the turbulent flow itself ?

As for the first question, it was partially treated here in Chapter 2, where the dynamical systems picture can naturally be pushed to higher values of Re. Surprisingly, the transition process becomes simpler for larger Re at least when the computational domain scales in outer units : finite lifetimes of the turbulent flow are too large to differ from the infinite lifetime phenomenology, edge states feature critical layers and their eigenspectrum simplifies too [107]. However it is not obvious that continuation in outer units is the most relevant option from a physical point of view [136]. It was also discussed how this picture evolves in arbitrarily long computational domains. For localised states only continuation in outer units makes full sense because inner units are not appropriate for localised flows. For outer unit continuation it was confirmed that the usual saddle point picture holds, however without any critical layer in physical space. The phenomenology of a rapid spot nucleation for high enough initial disturbance amplitude, based on the existence of a high-Re localised edge state, is hence expected to be a robust picture.

As for the second question, the answer is less clear. The general trend in shear flows is that the edge regime is increasingly intermingled with the turbulent state as Re is lowered. Conversely, as Re increases, several features are worth remarking. The edge and the turbulent regime are increasingly separated both in state space and in energy levels. Although, loosely speaking they were born together in a saddle-node bifurcation, the edge and turbulent regimes are also increasingly different from the point of view of the temporal and spatial scales involved. As often speculated, a full dynamical systems description of the turbulent state at high Re, in terms of invariant sets and periodic solutions, seems vain : the state space gets increasingly complicated and high-dimensional. Besides the multi-scale and multi-frequency nature of the flow lends itself poorly to the identification of one-frequency solutions. If such solutions exist they will be both hard to find, and difficult to justify as templates for the turbulent dynamics [356]. The high-Re fate of edge states is, again, different. Edge states remain essentially large-scale structures (at odds with the initial framework of the 'near-wall turbulence' for which they were originally introduced). The only small scales supported by such solutions are found within critical layers, should they exist. However the self-sustaning process at the core of the edge state's existence stays the same as put forward in Ref. [108]. On the other hand, the self-sustained process associated with the turbulent flow, currently re-visited by several teams at higher Re [357–359], becomes increasingly complicated. That leads to an auxiliary question of, perhaps, an even deeper interest : are critical layers an important concept or a mathematical oddity ? Can they be related succesfullly to the occurrence of uniform momentum zones in developed turbulent flows [360] ? Or, more philosophically, to the occurrence of blow-up singularities and of a finite dissipation in infinite-Re turbulent flows [361] ? It is not excluded that the state space concepts developed in simple shear flows, all revolving around the notion of unstable states, sheds some light on this mysterious and singular infinite-Re limit.

6

Acknowledgements

I would like to warmly thank all the members of the committee for accepting to take the time to read this thesis. More generally I would like to thank warmly all people who have at some point believed in my ability to contribute to science. If you recognise yourself in this description you are automatically thanked !

There are a few people who deserve personal acknowledgements because they played a special role in my evolution since the last thesis defended. Rich Kerswell supported my application for a post-doc with him in Bristol, and allowed me into the small circle of experts working on subcritical transition. It was a pleasure to work with Rich together with Ashley Willis and Chris Pringle. Once in the business I have to acknowledge the rare opportunity I had to spend time with recognised scientists and get personal tutoring from them. Looking back in retrospect I feel very lucky that I could spend so much time with Bruno Eckhardt, Predrag Cvitanović, Laurette Tuckerman, Dwight Barkley, Paul Manneville, Genta Kawahara and Olivier Dauchot, and learn so much formally and informally from them even without working on a common project. The story continued at KTH Mechanics in Stockholm for a second post-doctoral position. I owe truly a lot to Dan Henningson, Philipp Schlatter for the collaboration that started there and is still active and fruitful today. In general I would like all the nice people that I met at KTH Mechanics who (without knowing it) taught me to how to take pleasure in accomplishing productive work in team, among them Luca, Geert, Shervin, Espen, Antonios and many more.

Time came to apply for further positions and this is perhaps the time when you realise most who helped you for real. Thanks again to Alvaró Meseguer, to Bruno Eckhardt and to Lennaert van Veen, and to all anonymous committee members who have supported my various applications. Sorry for the positions that I did not take. In the end I chose to go back to my hometown Paris by joining CNRS, and I am still thankful to Patrick Le Quéré for having supported my CNRS application at LIMSI in 2009. I thank those at LIMSI who have shown some interest in my work and personality, and among them Claudine Delcarte, Caroline Nore, Olivier Le Maître, Luc Pastur, François Lusseyran, Laurent Martin Witkowski, Michel Pons, Lionel Mathelin, Onofrio Semeraro and Alessandro Bucci.

Other scientists deserve genuine acknowledgements. That includes in no particular order former colleagues from my office at LMFA in Ecully, Wouter Bos, Denis Martinand and Hatem Touil, Franciliens such as Eduardo Wesfreid, with whom I took pleasure in organising workshops, Romain Monchaux, Marie Couliou, Bérengère Dubrulle, François Daviaud, Olivier Dauchot, most people at ENSAM/Dynfluid, Joran Rolland, foreign colleagues such as Björn Hof, Marc Avila, Burak Budanur, Stefan Zammert, Divakar Viswanath, Peter Schmid, Grégoire Lemoult, Michael Schatz, Roman Grigoriev, Nigel Goldenfeld, Colmcille Caulfied, Carlo Cossu, Cédric Beaume, Yongyun Hwang, Florence Marcotte, Thomas Boeck, all the French and Japanese participants to the France-Japan workshops that we organised (Genta Kawahara, Takahiro Tsukahara, Masaki Shimizu, Koji Fukudome, and their many students). I thank the whole community of applied mathematicians working on chimera states, notably Yuri Maistrenko, Oleh and Iryna Omel'chenko, Matthias Wolfrum, Eckehard Schöll, Arkady Pikovsky, Anna Zakharova, Laurent Larger and Bogdan Penkovskyi. Thank you for the invitations. I liked the people I met in this community and I

learned so much from this excursion outside the usual territories. And thank you to all the attendants to all colloquia that I organised, in particular those who spread the word that Euromech 565 held in Cargèse in 2014 was a success.

Funding was more than necessary to achieve all these projects. In almost chronological order I would like to thank the European Commission for funding my first post-doc, Dan Henningson for funding not only my second post-doc but also almost all subsequent projects done at KTH, Bruno Eckhardt and the DFG for funding my stays in Marburg, Genta Kawahara, The French Ministry of Foreign affairs as well as CNRS for funding in total 6 visits to Japan, The Airbus Group (formerly Fondation EADS) for funding my first project at LIMSI, Euromech for funding the colloquium EC565 held in Cargèse, the Agence National de la Recherche for funding the ETAE project led by Laurent Martin Witkowski, and the French Ministry of Research and Higher Education for funding three theses under my supervision as well as conferences and a few laptops.

Numerical simulations relies on numerical codes, and a large part of my research after the PhD was based on original DNS codes developed by more skilled colleagues rather than by me. So this is another opportunity to thank Ashley Willis, Philipp Schlatter, Shihe Xin, John F. Gibson, the developers of Channelflow and Dedalus, as well as Yann Fraigneau for allowing me to use the codes developed by them. Consistently with the need to provide more open-source codes to scientists, I did not try to claim that these works are mine since I simply used them.

When it comes to the writing of this thesis, all the people who gave me constructive advices are thanked. Those who tried to scare me or to tell me that I was too late are not thanked. Special thanks go to Frédéric Alizard for giving me his LaTeX template.

Eventually, I have to thank individually all the students that contribute to this thesis since some of the work contained here is in priority their work. Chronologically, these thanks go to Robin Larsson, Ludomir Oteski, Taras Khapko, Takahiro Ishida, Shrayas Acharya Neelavara, Wang Zhe, Chaitanya Paranjape, Antoine Faugaret, Miguel Beneitez, Pavan Kashyap, as well as Kento Higashitsutsumi, Kohei Kunii, Kazuki Takeda, Elyes Sleimi. Thank you and good luck for what follows. The other students that I have supervised are also implicitly acknowledged.

Last but not least, I would like to dedicate these writings to my dear wife Elena, to my son Ilya and to my grandfather Viorel Sergiescu, who inspired me as a theoretical physicist and is just about to celebrate his 100th birthday. Merci encore une fois.

Bibliographie

[1] T. Khapko, P. Schlatter, Y. Duguet et D. Henningson, "Turbulence collapse in a suction boundary layer", *J. Fluid Mech.*, t. 795, p. 356–379, 2016.

[2] Y. Hasegawa, M. Quadrio et B. Frohnapfel, "Numerical simulation of turbulent duct flows with constant power input", *J. Fluid Mech.*, t. 750, p. 191–209, 2014.

[3] A. Faugaret, Y. Duguet, Y. Fraigneau et L. M. Witkowski, "Influence of interface pollution on the linear stability of a rotating flow", *J. Fluid Mech.*, t. 900, A42–1, 2020.

[4] A. Lozano-Durán et J. Jiménez, "Effect of the computational domain on direct simulations of turbulent channels up to re_τ=4200", *Physics of Fluids*, t. 26, n° 1, p. 011 702, 2014.

[5] Y. Hwang, "Statistical structure of self-sustaining attached eddies in turbulent channel flow", *Journal of Fluid Mechanics*, t. 767, p. 254–289, 2015.

[6] A. Townsend, *The structure of turbulent shear flow*. Cambridge university press, 1980.

[7] Y. Hwang et Y. Bengana, "Self-sustaining process of minimal attached eddies in turbulent channel flow", *J. Fluid Mech.*, t. 795, p. 708–738, 2016.

[8] A. J. Smits, B. J. McKeon et I. Marusic, "High–Reynolds number wall turbulence", *Annual Review of Fluid Mechanics*, t. 43, 2011.

[9] J. Hamilton, J. Kim et F. Waleffe, "Regeneration mechanisms of near-wall turbulence structures", *J. Fluid Mech.*, t. 287, p. 317–348, 1995.

[10] P Alfredsson et M. Matsubara, "Free-stream turbulence, streaky structures and transition in boundary layer flows", in *Fluids 2000 Conference and Exhibit*, 2000, p. 2534.

[11] N. Nikitin et V. Pimanov, "Numerical study of localized turbulent structures in a pipe", *Fluid Dynamics*, t. 50, n° 5, p. 655–664, 2015.

[12] D. Moxey et D. Barkley, "Distinct large-scale turbulent-laminar states in transitional pipe flow", *Proceedings of the National Academy of Sciences*, t. 107, n° 18, p. 8091–8096, 2010.

[13] K. Avila, D. Moxey, A. de Lozar, M. Avila, D. Barkley et B. Hof, "The onset of turbulence in pipe flow", *Science*, t. 333, n° 6039, p. 192–196, 2011.

[14] P. V. Kashyap, Y. Duguet et O. Dauchot, "Flow statistics in the transitional regime of plane channel flow", *Entropy*, t. 22, n° 9, p. 1001, 2020.

[15] W. S. Saric, H. L. Reed et E. J. Kerschen, "Boundary-layer receptivity to freestream disturbances", *Annual Review of Fluid Mechanics*, t. 34, n° 1, p. 291–319, 2002.

[16] A. Towne, O. T. Schmidt et T. Colonius, "Spectral proper orthogonal decomposition and its relationship to dynamic mode decomposition and resolvent analysis", *J. Fluid Mech.*, t. 847, p. 821–867, 2018.

[17] O. Dauchot et P. Manneville, "Local versus global concepts in hydrodynamic stability theory", *J. Phys. II*, t. 7, n° 2, p. 371–389, 1997.

[18] P. Schmid et D. Henningson, *Stability and Transition in Shear Flows*. New York : Springer-Verlag, 2001.

[19] S. C. Reddy, P. J. Schmid et D. S. Henningson, "Pseudospectra of the Orr–Sommerfeld operator", *SIAM Journal on Applied Mathematics*, t. 53, n° 1, p. 15–47, 1993.

[20] S. A. Orszag, "Accurate solution of the Orr–Sommerfeld stability equation", *J. Fluid Mech.*, t. 50, n° 4, p. 689–703, 1971.

[21] L. N. Trefethen et M. Embree, *Spectra and pseudospectra : the behavior of nonnormal matrices and operators*. Princeton University Press, 2005.

[22] F. Charru, *Instabilités hydrodynamiques*. EDP Sciences, 2012.

[23] J. Moehlis, H. Faisst et B. Eckhardt, "A low-dimensional model for turbulent shear flows", *New J. Phys.*, n° 56, p. 56, 2004.

[24] J. F. Gibson, J. Halcrow et P. Cvitanović, "Visualizing the geometry of state space in plane Couette flow", *J. Fluid Mech.*, t. 611, p. 107–130, 2008.

[25] P. J. Schmid, "Nonmodal stability theory", *Annu. Rev. Fluid Mech.*, t. 39, p. 129–162, 2007.

[26] D. Henningson, "Comment on 'Transition in shear flows. Nonlinear normality versus non-normal linearity' [Phys. Fluids 7, 3060 (1995)]", *Physics of Fluids*, t. 8, n° 8, p. 2257–2258, 1996.

[27] F. Waleffe, *Physics of Fluids*, n° 9, p. 883, 1997.

[28] J Jiménez et P Moin, "The minimal flow unit in near-wall turbulence", *J. Fluid Mech.*, t. 225, p. 213–240, 1991.

[29] W Schoppa et F. Hussain, "Coherent structure generation in near-wall turbulence", *J. Fluid Mech.*, t. 453, p. 57–108, 2002.

[30] F. Waleffe, "On a self-sustaining process in shear flows", *Phys. Fluids*, t. 9, n° 4, p. 883–900, 1997.

[31] F. Waleffe, *private communication*, 2008.

[32] G. Kawahara et S. Kida, *J. Fluid Mech.*, n° 449, p. 291, 2001.

[33] W. Waleffe, *J. Fluid Mech*, n° 435, p. 93, 2001.

[34] H. Faisst et B. Eckhardt, *Phys. Rev. Letters*, n° 91, p. 224 502, 2003.

[35] H. Wedin et R. Kerswell, *J. Fluid Mech.*, n° 508, p. 333, 2004.

[36] M. Nagata, *J. Fluid Mech.*, n° 217, p. 517, 1990.

[37] J. Gibson, J. Halcrow et P. Cvitanović, "Visualizing the geometry of state space in plane Couette flow", *J. Fluid Mech.*, t. 611, p. 107, 2008.

[38] J. Halcrow, J. Gibson, P. Cvitanović et D. Viswanath, "Heteroclinic connections in plane Couette flow", *J. Fluid Mech.*, t. 621, p. 365, 2009.

[39] P Cvitanović et J. Gibson, "Geometry of the turbulence in wall-bounded shear flows : periodic orbits", *Physica Scripta*, t. 2010, n° T142, p. 014 007, 2010.

[40] N. B. Budanur, P. Cvitanović, R. L. Davidchack et E. Siminos, "Reduction of SO(2) symmetry for spatially extended dynamical systems", *Phys. Rev. Lett.*, t. 114, n° 8, p. 084 102, 2015.

[41] A. P. Willis, P Cvitanović et M. Avila, "Revealing the state space of turbulent pipe flow by symmetry reduction", *J. Fluid Mech.*, t. 721, p. 514–540, 2013.

[42] B. Budanur, K. Short, M. Farazmand, A. Willis et P. Cvitanović, "Relative periodic orbits form the backbone of turbulent pipe flow", *J. Fluid Mech.*, t. 833, n° 1, p. 274–301, 2017.

[43] S. Bottin, "Streamwise vortices as finite-amplitude solutions of the Navier–Stokes equations", *Physics of Fluids*, p. 143–155, 1998.

[44] B. Hof, C. W. Van Doorne, J. Westerweel, F. T. Nieuwstadt, H. Faisst, B. Eckhardt, H. Wedin, R. R. Kerswell et F. Waleffe, "Experimental observation of nonlinear traveling waves in turbulent pipe flow", *Science*, t. 305, n° 5690, p. 1594–1598, 2004.

[45] C. C. Pringle et R. R. Kerswell, "Asymmetric, helical, and mirror-symmetric traveling waves in pipe flow", *Phys. Rev. Lett.*, t. 99, n° 7, p. 074 502, 2007.

[46] A. De Lozar, F. Mellibovsky, M. Avila et B. Hof, "Edge state in pipe flow experiments", *Phys. Rev. Lett.*, t. 108, n° 21, p. 214 502, 2012.

[47] T. Duriez, J.-L. Aider et J. E. Wesfreid, "Self-sustaining process through streak generation in a flat-plate boundary layer", *Phys. Rev. Lett.*, t. 103, n° 14, p. 144 502, 2009.

[48] B. Suri, J. Tithof, R. O. Grigoriev et M. F. Schatz, "Forecasting fluid flows using the geometry of turbulence", *Phys. Rev. Lett.*, t. 118, n° 11, p. 114 501, 2017.

[49] B. Suri, L. Kageorge, R. O. Grigoriev et M. F. Schatz, "Capturing turbulent dynamics and statistics in experiments with unstable periodic orbits", *Phys. Rev. Lett.*, t. 125, n° 6, p. 064 501, 2020.

[50] S. K. Robinson, "Coherent motions in the turbulent boundary layer", *Annual Review of Fluid Mechanics*, t. 23, n° 1, p. 601–639, 1991.

[51] P. Cvitanović, "Recurrent flows : the clockwork behind turbulence", *J. Fluid Mech.*, t. 726, p. 1–4, 2013.

[52] T. Kreilos, "Turbulence transition in shear flows and dynamical systems theory", thèse de doct., Univ. Philipps Marburg, 2014.

[53] P. Cvitanovic, R. Artuso, R. Mainieri, G. Tanner, G. Vattay, N. Whelan et A. Wirzba, "Chaos : classical and quantum", *ChaosBook. org (Niels Bohr Institute, Copenhagen 2005)*, t. 69, 2005.

[54] P. Gaspard, *Chaos, scattering and statistical mechanics*. Cambridge University Press, 2005, t. 9.

[55] P. Cvitanović, "Dynamical averaging in terms of periodic orbits", *Physica D : Nonlinear Phenomena*, t. 83, n° 1-3, p. 109–123, 1995.

[56] P. Cvitanovic et B. Eckhardt, "Periodic orbit expansions for classical smooth flows", *Journal of Physics A : Mathematical and General*, t. 24, n° 5, p. L237, 1991.

[57] B. Eckhardt et G. Ott, "Periodic orbit analysis of the Lorenz attractor", *Zeitschrift für Physik B Condensed Matter*, t. 93, n° 2, p. 259–266, 1994.

[58] E. Ott, *Chaos in dynamical systems*. Cambridge university press, 2002.

[59] R. Devaney, *An introduction to chaotic dynamical systems*. CRC Press, 2018.

[60] B. R. Hunt et E. Ott, "Defining chaos", *Chaos : An Interdisciplinary Journal of Nonlinear Science*, t. 25, n° 9, p. 097 618, 2015.

[61] G. Kawahara et S. Kida, "Periodic motion embedded in plane Couette turbulence : regeneration cycle and burst", *J. Fluid Mech.*, t. 449, p. 291–300, 2001.

[62] A. Darbyshire et T. Mullin, "Transition to turbulence in constant-mass-flux pipe flow", *J. Fluid Mech.*, t. 289, p. 83–114, 1995.

[63] B. Hof, J. Westerweel, T. M. Schneider et B. Eckhardt, "Finite lifetime of turbulence in shear flows", *Nature*, t. 443, n° 7107, p. 59, 2006.

[64] A. P. Willis et R. R. Kerswell, "Critical behavior in the relaminarization of localized turbulence in pipe flow", *Phys. Rev. Lett.*, t. 98, n° 1, p. 014 501, 2007.

[65] S. Bottin et H. Chaté, "Statistical analysis of the transition to turbulence in plane Couette flow", *European Phys. J. B*, t. 6, n° 1, p. 143–155, 1998.

[66] Y. Duguet, P. Schlatter et D. S. Henningson, "Formation of turbulent patterns near the onset of transition in plane Couette flow", *J. Fluid Mech.*, t. 650, p. 119, 2010.

[67] T. Tél et Y.-C. Lai, "Chaotic transients in spatially extended systems", *Physics Reports*, t. 460, n° 6, p. 245 –275, 2008.

[68] P. Gaspard et S. A. Rice, "Scattering from a classically chaotic repellor", *The Journal of chemical physics*, t. 90, n° 4, p. 2225–2241, 1989.

[69] C Jung, T Tél et E Ziemniak, "Application of scattering chaos to particle transport in a hydrodynamical flow", *Chaos : An Interdisciplinary Journal of Nonlinear Science*, t. 3, n° 4, p. 555–568, 1993.

[70] L Oteski, Y Duguet et L. Pastur, "Lagrangian chaos in confined two-dimensional oscillatory convection", *J. Fluid Mech.*, t. 759, p. 489, 2014.

[71] T. M. Schneider, B. Eckhardt et J. Vollmer, "Statistical analysis of coherent structures in transitional pipe flow", *Phys. Rev. E*, t. 75, n° 6, p. 066 313, 2007.

[72] G. Yalniz, B. Hof et N. B. Budanur, "Coarse graining the state space of a turbulent flow using periodic orbits", *Phys. Rev. Lett.*, t. 126, p. 244 502, 2021.

[73] J. Halcrow, J. F. Gibson, P. Cvitanović et D. Viswanath, "Heteroclinic connections in plane Couette flow", t. 621, p. 365–376, 2009.

[74] M. Farano, S. Cherubini, J.-C. Robinet, P. De Palma et T. Schneider, "Computing heteroclinic orbits using adjoint-based methods", *J. Fluid Mech.*, t. 858, 2019.

[75] N. B. Budanur et B. Hof, "Heteroclinic path to spatially localized chaos in pipe flow", *J. Fluid Mech.*, t. 827, 2017.

[76] S. Smale et al., "Differentiable dynamical systems", *Bulletin of the American mathematical Society*, t. 73, n° 6, p. 747–817, 1967.

[77] L. van Veen et G. Kawahara, "Homoclinic tangle on the edge of shear turbulence", *Phys. Rev. Lett.*, t. 107, n° 11, p. 114 501, 2011.

[78] J. R. T. Lustro, G. Kawahara, L. van Veen, M. Shimizu et H. Kokubu, "The onset of transient turbulence in minimal plane Couette flow", *J. Fluid Mech.*, t. 862, 2019.

[79] P. Doohan, A. P. Willis et Y. Hwang, "Two-scale interaction in near-wall turbulence", *Bulletin of the American Physical Society*, t. 64, 2019.

[80] L. N. Trefethen, A. E. Trefethen, S. C. Reddy et T. A. Driscoll, "Hydrodynamic stability without eigenvalues", *Science*, t. 261, n° 5121, p. 578–584, 1993.

[81] M. Beneitez, Y. Duguet, P. Schlatter et D. S. Henningson, "Edge manifold as a Lagrangian coherent structure in a high-dimensional state space", *Phys. Rev. Research*, t. 2, n° 3, p. 033 258, 2020.

[82] H.-D. Chiang et L. F. Alberto, *Stability regions of nonlinear dynamical systems : theory, estimation, and applications*. Cambridge University Press, 2015.

[83] G. Haller, "Lagrangian coherent structures", *Annu. Rev. Fluid Mech.*, t. 47, n° 1, p. 137–162, 2015.

[84] G. Haller et G. Yuan, "Lagrangianian coherent structures and mixing in two-dimensional turbulence", *Physica D*, t. 147, n° 3, p. 352 –370, 2000.

[85] T. Peacock et G. Haller, "Lagrangian coherent structures : the hidden skeleton of fluid flows", *Phys. Today*, t. 66, n° 2, p. 41–47, 2013.

[86] A. Junginger et R. Hernandez, "Lagrangian descriptors in dissipative systems", *Phys. Chem. Chem. Phys.*, t. 18, n° 44, p. 30 282–30 287, 2016.

[87] G. Haller, "Lagrangian coherent structures from approximate velocity data", *Phys. Fluids*, t. 14, n° 6, p. 1851–1861, 2002.

[88] A. Hadjighasem, M. Farazmand, D. Blazevski, G. Froyland et G. Haller, "A critical comparison of Lagrangian methods for coherent structure detection", *Chaos*, t. 27, n° 5, p. 053 104, 2017.

[89] G. Haller et T. Sapsis, "Lagrangian coherent structures and the smallest finite-time lyapunov exponent", *Chaos*, t. 21, n° 2, p. 023 115, 2011.

[90] H. Babaee et T. P. Sapsis, "A minimization principle for the description of modes associated with finite-time instabilities", *Proceedings of the Royal Society A : Mathematical, Physical and Engineering Sciences*, t. 472, n° 2186, p. 20 150 779, 2016.

[91] H. Babaee, M. Farazmand, G. Haller et T. P. Sapsis, "Reduced-order description of transient instabilities and computation of finite-time lyapunov exponents", *Chaos*, t. 27, n° 6, p. 063 103, 2017.

[92] C. Mendoza et A. M. Mancho, "Hidden geometry of ocean flows", *Phys. Rev. Lett.*, t. 105, n° 3, p. 038 501, 2010.

[93] A. M. Mancho, S. Wiggins, J. Curbelo et C. Mendoza, "Lagrangian descriptors : a method for revealing phase space structures of general time dependent dynamical systems", *Commun. Nonlinear Sci.*, t. 18, n° 12, p. 3530–3557, 2013.

[94] C. Lopesino, F. Balibrea-Iniesta, V. J. García-Garrido, S. Wiggins et A. M. Mancho, "A theoretical framework for Lagrangian descriptors", *Int. J. Bifurcat. Chaos*, t. 27, n° 01, p. 1 730 001, 2017.

[95] S. Naik et S. Wiggins, "Finding normally hyperbolic invariant manifolds in two and three degrees of freedom with hénon-heiles-type potential", *Phys. Rev. E*, t. 100, n° 2, p. 022 204, 2019.

[96] M. R. Allshouse et T. Peacock, "Lagrangian based methods for coherent structure detection", *Chaos*, t. 25, n° 9, p. 097 617, 2015.

[97] T. Itano et S. Toh, "The dynamics of bursting process in wall turbulence", *Journal of the Physical Society of Japan*, t. 70, n° 3, p. 703–716, 2001.

[98] S. Toh et T. Itano, "A periodic-like solution in channel flow", *J. Fluid Mech.*, t. 481, p. 67, 2003.

[99] S. Zammert et B. Eckhardt, "Periodically bursting edge states in plane Blasius flow", *Fluid Dynamics Research*, t. 46, n° 4, p. 041 419, 2014.

[100] B. Eckhardt, T. M. Schneider, B. Hof et J. Westerweel, "Turbulence transition in pipe flow", *Annu. Rev. Fluid Mech.*, t. 39, p. 447–468, 2007.

[101] H. E. Nusse et J. A. Yorke, "A procedure for finding numerical trajectories on chaotic saddles", *Physica D*, t. 36, n° 1-2, p. 137–156, 1989.

[102] D. Sweet, H. E. Nusse et J. A. Yorke, "Stagger-and-step method : detecting and computing chaotic saddles in higher dimensions", *Phys. Rev. Lett.*, t. 86, n° 11, p. 2261, 2001.

[103] E. M. Bollt, "The path towards a longer life : on invariant sets and the escape time landscape", *Int. J. Bifurcat. Chaos*, t. 15, n° 05, p. 1615–1624, 2005.

[104] T. M. Schneider et B. Eckhardt, "Edge of chaos in pipe flow", *Chaos*, t. 16, n° 4, p. 041 103, 2006.

[105] T. M. Schneider, B. Eckhardt et J. A. Yorke, "Turbulence transition and the edge of chaos in pipe flow", *Phys. Rev. Lett.*, t. 99, n° 3, p. 034 502, 2007.

[106] Y. Duguet, A. P. Willis et R. R. Kerswell, "Transition in pipe flow : the saddle structure on the boundary of turbulence", *J. Fluid Mech.*, t. 613, p. 255–274, 2008.

[107] J. Wang, J. Gibson et F. Waleffe, "Lower branch coherent states in shear flows : transition and control", *Phys. Rev. Lett.*, t. 98, n° 20, p. 204 501, 2007.

[108] P. Hall et S. Sherwin, "Streamwise vortices in shear flows : harbingers of transition and the skeleton of coherent structures", *J. Fluid Mech.*, t. 661, p. 178, 2010.

[109] P. Hall et F. T. Smith, "On strongly nonlinear vortex/wave interactions in boundary-layer transition", 1989.

[110] F. Smith et R. Bodonyi, "Amplitude-dependent neutral modes in the hagen-Poiseuille flow through a circular pipe", *Proceedings of the Royal Society of London. A. Mathematical and Physical Sciences*, t. 384, n° 1787, p. 463–489, 1982.

[111] M. Nagata, "Three-dimensional finite-amplitude solutions in plane Couette flow : bifurcation from infinity", *J. Fluid Mech.*, t. 217, p. 519–527, 1990.

[112] D. Olvera et R. R. Kerswell, "Optimizing energy growth as a tool for finding exact coherent structures", *Phys. Rev. Fluids*, t. 2, n° 8, p. 083 902, 2017.

[113] T. Kreilos, G. Veble, T. M. Schneider et B. Eckhardt, "Edge states for the turbulence transition in the asymptotic suction boundary layer", *J. Fluid Mech.*, t. 726, p. 100–122, 2013.

[114] K. T. Alligood, T. D. Sauer et J. A. Yorke, *Chaos.* Springer, 1996.

[115] T. Khapko, T. Kreilos, P. Schlatter, Y. Duguet, B. Eckhardt et D. S. Henningson, "Edge states as mediators of bypass transition in boundary-layer flows", *J. Fluid Mech.*, t. 801, 2016.

[116] M. Farazmand, "An adjoint-based approach for finding invariant solutions of Navier–Stokes equations", *J. Fluid Mech.*, t. 795, p. 278–312, 2016.

[117] K. Pyragas, "Continuous control of chaos by self-controlling feedback", *Physics letters A*, t. 170, n° 6, p. 421–428, 1992.

[118] E. Åkervik, L. Brandt, D. S. Henningson, J. Hœpffner, O. Marxen et P. Schlatter, "Steady solutions of the Navier-Stokes equations by selective frequency damping", *Physics of fluids*, t. 18, n° 6, p. 068 102, 2006.

[119] E. Vyazmina, "Bifurcations in a swirling flow", thèse de doct., Ecole Polytechnique, France, 2010.

[120] J. Sieber, E Omel'chenko et M. Wolfrum, "Controlling unstable chaos : stabilizing chimera states by feedback", *Phys. Rev. Lett.*, t. 112, n° 5, p. 054 102, 2014.

[121] M. Wolfrum, O. E. Omel'chenko et J. Sieber, "Regular and irregular patterns of self-localized excitation in arrays of coupled phase oscillators", *Chaos : An Interdisciplinary Journal of Nonlinear Science*, t. 25, n° 5, p. 053 113, 2015.

[122] M. Linkmann, F. Knierim, S. Zammert et B. Eckhardt, "Linear feedback control of invariant solutions in channel flow", *Journal of Fluid Mechanics*, t. 900, 2020.

[123] J.-P. Eckmann, S. O. Kamphorst, D. Ruelle et al., "Recurrence plots of dynamical systems", *World Scientific Series on Nonlinear Science Series A*, t. 16, p. 441–446, 1995.

[124] D. Viswanath, "Recurrent motions within plane Couette turbulence", *J. Fluid Mech.*, t. 580, p. 339–359, 2007.

[125] Y. Duguet, C. C. Pringle et R. R. Kerswell, "Relative periodic orbits in transitional pipe flow", *Physics of fluids*, t. 20, n° 11, p. 114 102, 2008.

[126] R. R. Kerswell et O. R. Tutty, "Recurrence of travelling waves in transitional pipe flow", *J. Fluid Mech.*, t. 584, p. 69–102, 2007.

[127] C. C. Pringle, Y. Duguet et R. R. Kerswell, "Highly symmetric travelling waves in pipe flow", *Philosophical Transactions of the Royal Society A : Mathematical, Physical and Engineering Sciences*, t. 367, n° 1888, p. 457–472, 2009.

[128] M. Avila, F. Mellibovsky, N. Roland et B. Hof, "Streamwise-localized solutions at the onset of turbulence in pipe flow", *Phys. Rev. Lett.*, t. 110, n° 22, p. 224 502, 2013.

[129] T. M. Schneider, J. F. Gibson, M. Lagha, F. De Lillo et B. Eckhardt, "Laminar-turbulent boundary in plane Couette flow", *Phys. Rev. E*, t. 78, n° 3, p. 037 301, 2008.

[130] C. S. Paranjape, Y. Duguet et B. Hof, "Oblique stripe solutions of channel flow", *J. Fluid Mech.*, t. 897, 2020.

[131] T. Khapko, T. Kreilos, P. Schlatter, Y. Duguet, B. Eckhardt et D. S. Henningson, "Localized edge states in the asymptotic suction boundary layer", *J. Fluid Mech.*, t. 717, 2013.

[132] F Mellibovsky et B. Eckhardt, "Takens-Bogdanov bifurcation of travelling wave solutions in pipe flow", *J. Fluid Mech*, t. 670, p. 96–129, 2010.

[133] N. B. Budanur et B. Hof, "Complexity of the laminar-turbulent boundary in pipe flow", *Phys. Rev. Fluids*, t. 3, n° 5, p. 054 401, 2018.

[134] O. Ozcakir, P. Hall et S. Tanveer, "Nonlinear exact coherent structures in pipe flow and their instabilities", *J. Fluid Mech*, t. 868, p. 341–368, 2019.

[135] M. D. Graham et D. Floryan, "Exact coherent states and the nonlinear dynamics of wall-bounded turbulent flows", *Annual Review of Fluid Mechanics*, t. 53, 2021.

[136] S. A. Neelavara, Y. Duguet et F. Lusseyran, "State space analysis of minimal channel flow", *Fluid Dynamics Research*, t. 49, n° 3, p. 035 511, 2017.

[137] S. A. Neelavara, "Numerical study of transition to turbulence in plane Poiseuille flow in physical space and state space", thèse de doct., Université Paris-Saclay, 2017.

[138] L. Keefe, P. Moin et J. Kim, "The dimension of attractors underlying periodic turbulent Poiseuille flow", *J. Fluid Mech.*, t. 242, p. 1–29, 1992.

[139] J. L. Kaplan et J. A. Yorke, "Chaotic behavior of multidimensional difference equations", in *Functional Differential equations and approximation of fixed points*, Springer, 1979, p. 204–227.

[140] M. F. Linkmann et A. Morozov, "Sudden relaminarization and lifetimes in forced isotropic turbulence", *Phys. Rev. Lett.*, t. 115, n° 13, p. 134 502, 2015.

[141] C. Cossu, "An optimality condition on the minimum energy threshold in subcritical instabilities", *Comptes Rendus Mécanique*, t. 333, n° 4, p. 331–336, 2005.

[142] B. Hof, A. Juel et T Mullin, "Scaling of the turbulence transition threshold in a pipe", *Phys. Rev. Lett.*, t. 91, n° 24, p. 244 502, 2003.

[143] S. J. Chapman, "Subcritical transition in channel flows", *J. Fluid Mech.*, t. 451, p. 35–97, 2002.

[144] A. Lundbladh, D. S. Henningson et S. C. Reddy, "Threshold amplitudes for transition in channel flows", in *Transition, turbulence and combustion*, Springer, 1994, p. 309–318.

[145] Y. Duguet, L. Brandt et B. R. J. Larsson, "Towards minimal perturbations in transitional plane Couette flow", *Phys. Rev. E*, t. 82, n° 2, p. 026 316, 2010.

[146] P. Schmid et D. Henningson, "A new mechanism for rapid transition involving a pair of oblique waves", *Physics of Fluids A : Fluid Dynamics*, t. 4, n° 9, p. 1986–1989, 1992.

[147] S. C. Reddy, P. J. Schmid, J. S. Baggett et D. S. Henningson, "On stability of streamwise streaks and transition thresholds in plane channel flows", *J. Fluid Mech.*, t. 365, p. 269–303, 1998.

[148] A. Monokrousos, A. Bottaro, L. Brandt, A. Di Vita et D. S. Henningson, "Non-equilibrium thermodynamics and the optimal path to turbulence in shear flows", *Phys. Rev. Lett.*, t. 106, n° 13, p. 134 502, 2011.

[149] Y. Duguet, A. Monokrousos, L. Brandt et D. S. Henningson, "Minimal transition thresholds in plane Couette flow", *Physics of Fluids*, t. 25, n° 8, p. 084 103, 2013.

[150] S. Rabin, C. Caulfield et R. Kerswell, "Triggering turbulence efficiently in plane Couette flow", *J. Fluid Mech.*, t. 712, p. 244, 2012.

[151] I. J. Wygnanski et F. Champagne, "On transition in a pipe. Part 1. The origin of puffs and slugs and the flow in a turbulent slug", *J. Fluid Mech.*, t. 59, n° 2, p. 281–335, 1973.

[152] F. Mellibovsky, A. Meseguer, T. M. Schneider et B. Eckhardt, "Transition in localized pipe flow turbulence", *Phys. Rev. Lett.*, t. 103, n° 5, p. 054 502, 2009.

[153] Y. Duguet, A. Willis et R. Kerswell, "Slug genesis in cylindrical pipe flow", *J. Fluid Mech.*, t. 663, p. 180, 2010.

[154] Y. Duguet, P. Schlatter et D. S. Henningson, "Localized edge states in plane Couette flow", *Phys. Fluids*, t. 21, n° 11, p. 111 701, 2009.

[155] T. M. Schneider, D. Marinc et B. Eckhardt, "Localization in plane Couette edge dynamics", in *Advances in turbulence XII*, Springer, 2009, p. 83–84.

[156] D. Marinc, T. M. Schneider et B. Eckhardt, "Localized edge states for the transition to turbulence in shear flows", in *Seventh IUTAM Symposium on Laminar-Turbulent Transition*, Springer, 2010, p. 253–258.

[157] T. M. Schneider, D. Marinc et B. Eckhardt, "Localised edge states nucleate turbulence in extended plane Couette cells", *J. Fluid Mech.*, t. 646, p. 441–451, 2010.

[158] T. M. Schneider, J. F. Gibson et J. Burke, "Snakes and ladders : localized solutions of plane Couette flow", *Phys. Rev. Lett.*, t. 104, n° 10, p. 104 501, 2010.

[159] D. Barkley et L. S. Tuckerman, "Computational study of turbulent laminar patterns in Couette flow", *Phys. Rev. Lett.*, t. 94, n° 1, p. 014 502, 2005.

[160] L. Shi, M. Avila et B. Hof, "Scale invariance at the onset of turbulence in Couette flow", *Phys. Rev. Lett.*, t. 110, n° 20, p. 204 502, 2013.

[161] L. S. Tuckerman, T. Kreilos, H. Schrobsdorff, T. M. Schneider et J. F. Gibson, "Turbulent-laminar patterns in plane Poiseuille flow", *Physics of Fluids*, t. 26, n° 11, p. 114 103, 2014.

[162] S. Gomé, L. S. Tuckerman et D. Barkley, "Statistical transition to turbulence in plane channel flow", *Phys. Rev. Fluids*, t. 5, n° 8, p. 083 905, 2020.

[163] J. F. Gibson, "Channelflow : a spectral Navier-Stokes simulator in C++", *New Hampshire*, t. 900, 2012.

[164] F. Reetz, T. Kreilos et T. M. Schneider, "Exact invariant solution reveals the origin of self-organized oblique turbulent-laminar stripes", *Nature communications*, t. 10, n° 1, p. 1–6, 2019.

[165] C Paranjape, "Onset of turbulence in plane Poiseuille flow", thèse de doct., Ph. D. thesis, IST Austria, 2019.

[166] N. Nikitin et V. Pimanov, "Sustainment of oscillations in localized turbulent structures in pipes", *Fluid Dynamics*, t. 53, n° 1, p. 65–73, 2018.

[167] M. Chantry, A. P. Willis et R. R. Kerswell, "Genesis of streamwise-localized solutions from globally periodic traveling waves in pipe flow", *Phys. Rev. Lett.*, t. 112, n° 16, p. 164 501, 2014.

[168] P. Ritter, F. Mellibovsky et M. Avila, "Emergence of spatio-temporal dynamics from exact coherent solutions in pipe flow", *New Journal of Physics*, t. 18, n° 8, p. 083 031, 2016.

[169] T. Kreilos et B. Eckhardt, "Periodic orbits near onset of chaos in plane Couette flow", *Chaos : An Interdisciplinary Journal of Nonlinear Science*, t. 22, n° 4, p. 047 505, 2012.

[170] S. Zammert et B. Eckhardt, "Crisis bifurcations in plane Poiseuille flow", *Phys. Rev. E*, t. 91, n° 4, p. 041 003, 2015.

[171] P. Ritter, S. Zammert, B. Song, B. Eckhardt et M. Avila, "Analysis and modeling of localized invariant solutions in pipe flow", *Phys. Rev. Fluids*, t. 3, n° 1, p. 013 901, 2018.

[172] T. Khapko, Y. Duguet, T. Kreilos, P. Schlatter, B. Eckhardt et D. S. Henningson, "Complexity of localised coherent structures in a boundary-layer flow", *Eur. Phys. J. E*, t. 37, n° 4, 2014.

[173] S. Rawat, C. Cossu et F. Rincon, "Travelling-wave solutions bifurcating from relative periodic orbits in plane Poiseuille flow", *Comptes Rendus Mécanique*, t. 344, n° 6, p. 448–455, 2016.

[174] Y. Pomeau et P. Manneville, "Intermittent transition to turbulence in dissipative dynamical systems", *Communications in Mathematical Physics*, t. 74, n° 2, p. 189–197, 1980.

[175] L. Van Veen, G. Kawahara et M. Atsushi, "On matrix-free computation of 2d unstable manifolds", *SIAM Journal on Scientific Computing*, t. 33, n° 1, p. 25–44, 2011.

[176] K. Deguchi, P. Hall et A. Walton, "The emergence of localized vortex–wave interaction states in plane Couette flow", *J. Fluid Mech.*, t. 721, p. 58–85, 2013.

[177] J. D. Skufca, J. A. Yorke et B. Eckhardt, "Edge of chaos in a parallel shear flow", *Phys. Rev. Lett.*, t. 96, n° 17, p. 174 101, 2006.

[178] R. Kerswell, "Nonlinear nonmodal stability theory", *Annual Review of Fluid Mechanics*, t. 50, p. 319–345, 2018.

[179] Y. Pomeau, "Front motion, metastability and subcritical bifurcations in hydrodynamics", *Physica D : Nonlinear Phenomena*, t. 23, n° 1-3, p. 3–11, 1986.

[180] D. Barkley, "Theoretical perspective on the route to turbulence in a pipe", *J. Fluid Mech*, t. 803, n° 1, 2016.

[181] M. Sipos et N. Goldenfeld, "Directed percolation describes lifetime and growth of turbulent puffs and slugs", *Phys. Rev. E*, t. 84, n° 3, p. 035 304, 2011.

[182] A. P. Willis et R. R. Kerswell, "Coherent structures in localized and global pipe turbulence", *Phys. Rev. Lett.*, t. 100, n° 12, p. 124 501, 2008.

[183] O. Reynolds, "An experimental investigation of the circumstances which determine whether the motion of water shall be direct or sinuous, and of the law of resistance in parallel channels", *P. R. Soc. London*, t. 35, n° 224-226, p. 84–99, 1883.

[184] E. R. Lindgren, "The transition process and other phenomena in viscous flow", *Arkiv fysik*, t. 12, 1957.

[185] K. Sreenivasan et R Ramshankar, "Transition intermittency in open flows, and intermittency routes to chaos", *Physica D : Nonlinear Phenomena*, t. 23, n° 1-3, p. 246–258, 1986.

[186] I Wygnanski, M. Sokolov et D Friedman, "On transition in a pipe. Part 2. The equilibrium puff", *J. Fluid Mech.*, t. 69, n° 2, p. 283–304, 1975.

[187] J. Peixinho et T. Mullin, "Decay of turbulence in pipe flow", *Phys. Rev. Lett.*, t. 96, n° 9, p. 094 501, 2006.

[188] B. Hof, A. De Lozar, D. J. Kuik et J. Westerweel, "Repeller or attractor ? Selecting the dynamical model for the onset of turbulence in pipe flow", *Phys. Rev. Lett.*, t. 101, n° 21, p. 214 501, 2008.

[189] M. Avila, A. P. Willis et B. Hof, "On the transient nature of localized pipe flow turbulence", *J. Fluid Mech.*, t. 646, p. 127–136, 2010.

[190] M. Nishi, B. Unsal, F. Durst et G. Biswas, "Laminar-to-turbulent transition of pipe flows through puffs and slugs", *J. Fluid Mech.*, t. 614, p. 425–446, 2008.

[191] A. Willis, J. Peixinho, R. Kerswell et T Mullin, "Experimental and theoretical progress in pipe flow transition", *Philosophical Transactions of the Royal Society A : Mathematical, Physical and Engineering Sciences*, t. 366, n° 1876, p. 2671–2684, 2008.

[192] M. Shimizu, P. Manneville, Y. Duguet et G. Kawahara, "Splitting of a turbulent puff in pipe flow", *Fluid Dynamics Research*, t. 46, n° 6, p. 061 403, 2014.

[193] M. Shimizu et S. Kida, "A driving mechanism of a turbulent puff in pipe flow", *Fluid dynamics research*, t. 41, n° 4, p. 045 501, 2009.

[194] D. Barkley, "Simplifying the complexity of pipe flow", *Phys. Rev. E*, t. 84, n° 1, p. 016 309, 2011.

[195] C. C. Pringle, A. P. Willis et R. R. Kerswell, "Fully localised nonlinear energy growth optimals in pipe flow", *Physics of Fluids*, t. 27, n° 6, p. 064 102, 2015.

[196] Y. Nishiura et D. Ueyama, "Spatio-temporal chaos for the Gray–Scott model", *Physica D : Nonlinear Phenomena*, t. 150, n° 3-4, p. 137–162, 2001.

[197] B. Song et B. Hof, "Deterministic and stochastic aspects of the transition to turbulence", *Journal of Statistical Mechanics : Theory and Experiment*, t. 2014, n° 2, P02001, 2014.

[198] V. Lucarini, D. Faranda, J. M. M. de Freitas, M. Holland, T. Kuna, M. Nicol, M. Todd, S. Vaienti et al., *Extremes and recurrence in dynamical systems*. John Wiley & Sons, 2016.

[199] N. Goldenfeld, N. Guttenberg et G. Gioia, "Extreme fluctuations and the finite lifetime of the turbulent state", *Phys. Rev. E*, t. 81, n° 3, p. 035 304, 2010.

[200] H. Chaté et P. Manneville, "Criticality in cellular automata", *Physica D : Nonlinear Phenomena*, t. 45, n° 1-3, p. 122–135, 1990.

[201] M. Avila et B. Hof, "Nature of laminar-turbulence intermittency in shear flows", *Phys. Rev. E*, t. 87, n° 6, p. 063 012, 2013.

[202] B. Song, D. Barkley, B. Hof et M. Avila, "Speed and structure of turbulent fronts in pipe flow", *J. Fluid Mech.*, t. 813, p. 1045–1059, 2017.

[203] D. Coles, "Interfaces and intermittency in turbulent shear flow", *Mécanique de la Turbulence*, t. 108, p. 229–248, 1962.

[204] D. Coles, "Transition in circular Couette flow", *J. Fluid Mech.*, t. 21, p. 385–425, 1965.

[205] R. P. Feynman, R. B. Leighton et M. Sands, "The Feynman lectures on physics ; vol. i", *American Journal of Physics*, t. 33, n° 9, p. 750–752, 1965.

[206] C. Van Atta, "Exploratory measurements in spiral turbulence", *J. Fluid Mech.*, t. 25, p. 495–512, 1966.

[207] C. D. Andereck, S. Liu et H. L. Swinney, "Flow regimes in a circular Couette system with independently rotating cylinders", *J. Fluid Mech.*, t. 164, n° 3, p. 155–183, 1986.

[208] A Goharzadeh et I Mutabazi, "Experimental characterization of intermittency regimes in the Couette-Taylor system", *The European Physical Journal B-Condensed Matter and Complex Systems*, t. 19, n° 1, p. 157–162, 2001.

[209] A. Prigent, G. Grégoire, H. Chaté, O. Dauchot et W. van Saarloos, "Large-scale finite-wavelength modulation within turbulent shear flows", *Phys. Rev. Lett.*, t. 89, n° 1, p. 014 501, 2002.

[210] A. Meseguer, F. Mellibovsky, M. Avila et F. Marques, "Instability mechanisms and transition scenarios of spiral turbulence in Taylor-Couette flow", *Phys. Rev. E*, t. 80, n° 4, p. 046 315, 2009.

[211] S Dong, "Evidence for internal structures of spiral turbulence", *Phys. Rev. E*, t. 80, n° 6, p. 067 301, 2009.

[212] N. Tillmark et P. Alfredsson, "Experiments on transition in plane Couette flow", *J. Fluid Mech.*, t. 235, p. 89–102, 1992.

[213] F. Daviaud, J. Hegseth et P. Bergé, "Subcritical transition to turbulence in plane Couette flow", *Phys. Rev. Letters*, t. 69, p. 2511–2514, 1992.

[214] J. Hegseth, "Turbulent spots in plane Couette flow", *Phys. Rev. E*, t. 5, n° 54, p. 4915, 1996.

[215] O. Dauchot et F. Daviaud, "Finite amplitude perturbation and spots growth mechanism in plane Couette flow", *Physics of Fluids*, t. 7, n° 2, p. 335–343, 1995.

[216] O. Dauchot et F Daviaud, "Streamwise vortices in plane Couette flow", *Physics of Fluids*, t. 7, n° 5, p. 901–903, 1995.

[217] S. Bottin, F. Daviaud, P. Manneville et O. Dauchot, "Discontinuous transition to spatio-temporal intermittency in plane Couette flow", *Europhys. Lett.*, t. 43, p. 171–176, 1998.

[218] A. Prigent, G. Grégoire, H. Chaté et O. Dauchot, "Long-wavelength modulation of turbulent shear flows", *Physica D : Nonlinear Phenomena*, t. 174, n° 1-4, p. 100–113, 2003.

[219] A Prigent et O. Dauchot, "Transition to versus from turbulence in subcritical Couette flows", in *IUTAM Symposium on Laminar-Turbulent Transition and Finite Amplitude Solutions*, Springer, 2005, p. 195–219.

[220] M. Couliou et R. Monchaux, "Large-scale flows in transitional plane Couette flow : a key ingredient of the spot growth mechanism", *Physics of Fluids*, t. 27, n° 3, p. 034 101, 2015.

[221] M. Couliou et R. Monchaux, "Spreading of turbulence in plane Couette flow", *Phys. Rev. E*, t. 93, n° 1, p. 013 108, 2016.

[222] M. Couliou et R Monchaux, "Childhood of turbulent spots in a shear flow", *Phys. Rev. Fluids*, t. 3, n° 12, p. 123 901, 2018.

[223] D De Souza, T Bergier et R Monchaux, "Transient states in plane Couette flow", *J. Fluid Mech.*, t. 903, 2020.

[224] A. Prigent, *PhD, La spirale turbulente : motif de grande longueur d'onde dans les écoulements cisaillés turbulents*. Université Paris Sud - Paris XI, 2003.

[225] G. Lemoult, L. Shi, K. Avila, S. V. Jalikop, M. Avila et B. Hof, "Directed percolation phase transition to sustained turbulence in Couette flow", *Nature Physics*, t. 12, n° 3, p. 254–258, 2016.

[226] S Hashimoto, A Hasobe, T. Tsukahara, Y. Kawaguchi et H. Kawamura, "An experimental study on turbulent-stripe structure in transitional channel flow", in *Turbulence Heat and Mass Transfer 6. Proceedings of the Sixth International Symposium On Turbulence Heat and Mass Transfer*, Begel House Inc., 2009.

[227] G. Lemoult, J.-L. Aider et J. E. Wesfreid, "Turbulent spots in a channel : large-scale flow and self-sustainability", *J. Fluid Mech.*, t. 731, 2013.

[228] M. Sano et K. Tamai, "A universal transition to turbulence in channel flow", *Nature Physics*, t. 12, n° 3, p. 249–253, 2016.

[229] J. Liu, Y. Xiao, M. Li, J. Tao et S. Xu, "Intermittency, moments, and friction coefficient during the subcritical transition of channel flow", *Entropy*, t. 22, n° 12, p. 1399, 2020.

[230] R. Agrawal, H. C.-H. Ng, E. A. Davis, J. S. Park, M. D. Graham, D. J. Dennis et R. J. Poole, "Low-and high-drag intermittencies in turbulent channel flows", *Entropy*, t. 22, n° 10, p. 1126, 2020.

[231] T. Tsukahara, Y. Seki, H. Kawamura et D. Tochio, "DNS of turbulent channel flow at very low Reynolds numbers", in *Fourth International Symposium on Turbulence and Shear Flow Phenomena*, Begel House Inc., 2005.

[232] T. Tsukahara, Y. Kawaguchi, H. Kawamura, N. Tillmark et P. H. Alfredsson, "Turbulence stripe in transitional channel flow with/without system rotation", in *Seventh IUTAM Symposium on Laminar-Turbulent Transition*, Springer, 2010, p. 421–426.

[233] X. Xiong, J. Tao, S. Chen et L. Brandt, "Turbulent bands in plane-Poiseuille flow at moderate Reynolds numbers", *Physics of Fluids*, t. 27, n° 4, p. 041 702, 2015.

[234] J. Tao, B. Eckhardt et X. Xiong, "Extended localized structures and the onset of turbulence in channel flow", *Phys. Rev. Fluids*, t. 3, n° 1, p. 011 902, 2018.

[235] L. Klotz, G. Lemoult, I. Frontczak, L. S. Tuckerman et J. E. Wesfreid, "Couette-Poiseuille flow experiment with zero mean advection velocity : subcritical transition to turbulence", *Phys. Rev. Fluids*, t. 2, n° 4, p. 043 904, 2017.

[236] T Liu, B Semin, L. Klotz, R Godoy-Diana, J. Wesfreid et T Mullin, "Decay of streaks and rolls in plane couette–poiseuille flow", *Journal of Fluid Mechanics*, t. 915, 2021.

[237] F Hayot et Y Pomeau, "Turbulent domain stabilization in annular flows", *Phys. Rev. E*, t. 50, n° 3, p. 2019, 1994.

[238] D. Barkley et L. Tuckerman, "Mean flow of turbulent–laminar patterns in plane Couette flow", *J. Fluid Mech.*, t. 576, p. 109–137, 2007.

[239] P. Manneville et F. Locher, "A model for transitional plane Couette flow", *Comptes Rendus de l'Académie des Sciences-Series IIB-Mechanics-Physics-Astronomy*, t. 328, n° 2, p. 159–164, 2000.

[240] M. Lagha et P. Manneville, "Modeling transitional plane Couette flow", *The European Physical Journal B*, t. 58, n° 4, p. 433–447, 2007.

[241] K Seshasayanan et P. Manneville, "Laminar-turbulent patterning in wall-bounded shear flows : a galerkin model", *Fluid Dynamics Research*, t. 47, n° 3, p. 035 512, 2015.

[242] M. Chantry, L. S. Tuckerman et D. Barkley, "Turbulent–laminar patterns in shear flows without walls", *J. Fluid Mech.*, t. 791, 2016.

[243] M. Chantry, L. S. Tuckerman et D. Barkley, "Universal continuous transition to turbulence in a planar shear flow", *J. Fluid Mech.*, t. 824, 2017.

[244] M. Shimizu et P. Manneville, "Bifurcations to turbulence in transitional channel flow", *Phys. Rev. Fluids*, t. 4, n° 11, p. 113 903, 2019.

[245] T Kanazawa, "Lifetime and growing process of localized turbulence in plane channel flow", thèse de doct., PhD thesis, Osaka University, 2018.

[246] X. Xiao et B. Song, "Kinematics and dynamics of turbulent bands at low Reynolds numbers in channel flow", *Entropy*, t. 22, n° 10, p. 1167, 2020.

[247] J. Liu, Y. Xiao, L. Zhang, M. Li, J. Tao et S. Xu, "Extension at the downstream end of turbulent band in channel flow", *Physics of Fluids*, t. 32, n° 12, p. 121 703, 2020.

[248] P. Manneville, "Modeling the direct transition to turbulence", *Laminar-Turbulent Transition and Finite Amplitude Solutions, ed. T. Mullin, R.R. Kerswell*, p. 1, 2005.

[249] L. S. Tuckerman et D. Barkley, "Patterns and dynamics in transitional plane Couette flow", *Physics of Fluids*, t. 23, n° 4, p. 041 301, 2011.

[250] S. B. Pope, *Turbulent flows*, 2001.

[251] J. Clerk-Maxwell, "On the dynamical evidence of the molecular constitution of bodies", *Nature*, 1875.

[252] K. Avila, "Shear flow experiments : characterizing the onset of turbulence as a phase transition", thèse de doct., Univ. Göttingen, 2014.

[253] P. Colovas et C. Andereck, "Turbulent bursting and spatiotemporal intermittency in the counterrotating Taylor-Couette system", *Phys. Rev. E*, t. 55, p. 2736, 1997.

[254] P. Grassberger, "On phase transitions in Schlögl's second model", *Zeitschrift für Physik B Condensed Matter*, t. 47, n° 4, p. 365–374, 1982.

[255] H.-K. Janssen, "On the non-equilibrium phase transition in reaction-diffusion systems with an absorbing stationary state", *Zeitschrift für Physik B Condensed Matter*, t. 42, n° 2, p. 151–154, 1981.

[256] T. Bohr, M. H. Jensen, G. Paladin et A. Vulpiani, *Dynamical systems approach to turbulence*. Cambridge University Press, 2005.

[257] N. Goldenfeld, *Lectures on phase transitions and the renormalization group*. CRC Press, 2018.

[258] K. A. Takeuchi, M. Kuroda, H. Chaté et M. Sano, "Directed percolation criticality in turbulent liquid crystals", *Phys. Rev. Lett.*, t. 99, n° 23, p. 234 503, 2007.

[259] F Daviaud, M Dubois et P Bergé, "Spatio-temporal intermittency in quasi one-dimensional rayleigh-bénard convection", *EPL (Europhysics Letters)*, t. 9, n° 5, p. 441, 1989.

[260] L. S. Tuckerman, M. Chantry et D. Barkley, "Patterns in wall-bounded shear flows", *Annual Review of Fluid Mechanics*, t. 52, 2020.

[261] K. Avila et B. Hof, "Second-order phase transition in counter-rotating Taylor–Couette flow experiment", *Entropy*, t. 23, n° 1, p. 58, 2021.

[262] K. Takeda, Y. Duguet et T. Tsukahara, "Intermittency and critical scaling in annular Couette flow", *Entropy*, t. 22, n° 9, p. 988, 2020.

[263] K. Kunii, T. Ishida, Y. Duguet et T. Tsukahara, "Laminar-turbulent coexistence in annular Couette flow", *J. Fluid Mech.*, t. 879, p. 579–603, 2019.

[264] M. Cho, Y. Hwang et H. Choi, "Scale interactions and spectral energy transfer in turbulent channel flow", 2018.

[265] T. Kawata et T. Tsukahara, "Scale interactions in turbulent plane Couette flows in minimal domains", *J. Fluid Mech.*, t. 911, 2021.

[266] P. Sagaut, *Large eddy simulation for incompressible flows : an introduction*. Springer Science & Business Media, 2006.

[267] Y. Duguet, O. Le Maitre et P. Schlatter, "Stochastic and deterministic motion of a laminar-turbulent front in a spanwisely extended Couette flow", *Phys. Rev. E*, t. 84, n° 6, p. 066 315, 2011.

[268] Y. Duguet et P. Schlatter, "Oblique laminar-turbulent interfaces in plane shear flows", *Phys. Rev. Lett.*, t. 110, n° 3, p. 034 502, 2013.

[269] L Klotz, A. Pavlenko et J. Wesfreid, "Experimental measurements in plane Couette–Poiseuille flow : dynamics of the large-and small-scale flow", *J. Fluid Mech.*, t. 912, 2021.

[270] A. Lundbladh et A. Johansson, "Direct simulation of turbulent spots in plane Couette flow", *J. Fluid Mech.*, t. 229, p. 499–516, 1991.

[271] M. Lagha et P. Manneville, "Modeling of plane Couette flow. i. large scale flow around turbulent spots", *Physics of Fluids*, t. 19, n° 9, p. 094 105, 2007.

[272] F. Li et S. E. Widnall, "Wave patterns in plane Poiseuille flow created by concentrated disturbances", *J. Fluid Mech.*, t. 208, p. 639–656, 1989.

[273] P. V. Kashyap, Y. Duguet et M. Chantry, "Far field of turbulent spots", *Phys. Rev. Fluids*, t. 5, n° 10, p. 103 902, 2020.

[274] E. Brand et J. F. Gibson, "A doubly-localized equilibrium solution of plane Couette flow", *J. Fluid Mech*, t. 750, 2014.

[275] Z. Wang, C. Guet, R. Monchaux, Y. Duguet et B. Eckhardt, "Quadrupolar flows around spots in internal shear flows", *J. Fluid Mech.*, t. 892, 2020.

[276] R. Jeanneret, D. O. Pushkin et M. Polin, "Confinement enhances the diversity of microbial flow fields", *Phys. Rev. Lett.*, t. 123, n° 24, p. 248 102, 2019.

[277] P. Manneville, "On the growth of laminar–turbulent patterns in plane Couette flow", *Fluid Dynamics Research*, t. 44, n° 3, p. 031 412, 2012.

[278] G. Lemoult, K. Gumowski, J.-L. Aider et J. E. Wesfreid, "Turbulent spots in channel flow : an experimental study", *The European Physical Journal E*, t. 37, n° 4, p. 25, 2014.

[279] M. Ferro, "Experimental study on turbulent boundary-layer flows with wall transpiration", thèse de doct., KTH Royal Institute of Technology, 2017.

[280] M. Ferro, B. E. Fallenius et J. H. Fransson, "Experimental study on turbulent asymptotic suction boundary layers", *J. Fluid Mech.*, t. 915, 2021.

[281] J. Jiménez et A. Pinelli, "The autonomous cycle of near-wall turbulence", *J. Fluid Mech.*, t. 389, p. 335–359, 1999.

[282] T. Tsukahara, N. Tillmark et P. Alfredsson, "Flow regimes in a plane Couette flow with system rotation", *J. Fluid Mech.*, t. 648, n° 5, 2010.

[283] J. P. Johnston, R. M. Halleent et D. K. Lezius, "Effects of spanwise rotation on the structure of two-dimensional fully developed turbulent channel flow", *J. Fluid Mech.*, t. 56, n° 3, p. 533–557, 1972.

[284] G. Brethouwer, Y. Duguet et P. Schlatter, "Turbulent-laminar coexistence in wall flows with coriolis, buoyancy or lorentz forces", *J. Fluid Mech.*, t. 704, p. 137, 2012.

[285] V. Armenio et S. Sarkar, "An investigation of stably stratified turbulent channel flow using large-eddy simulation", *J. Fluid Mech.*, t. 459, p. 1, 2002.

[286] M. Garcia-Villalba et J. C. del Alamo, "Turbulence modification by stable stratification in channel flow", *Physics of Fluids*, t. 23, n° 4, p. 045 104, 2011.

[287] C. Ansorge et J. P. Mellado, "Global intermittency and collapsing turbulence in the stratified planetary boundary layer", *Boundary-layer meteorology*, t. 153, n° 1, p. 89–116, 2014.

[288] E. Deusebio, C. Caulfield et J. R. Taylor, "The intermittency boundary in stratified plane Couette flow", *J. Fluid Mech.*, t. 781, p. 298, 2015.

[289] P. He et S. Basu, "Direct numerical simulation of intermittent turbulence under stably stratified conditions", *Nonlinear Processes in Geophysics*, t. 22, n° 4, p. 447–471, 2015.

[290] D. Lee et H. Choi, "Magnetohydrodynamic turbulent flow in a channel at low magnetic Reynolds number", *J. Fluid Mech.*, t. 439, p. 367, 2001.

[291] T. Boeck, D. Krasnov et E. Zienicke, "Numerical study of turbulent magnetohydrodynamic channel flow", *J. Fluid Mech.*, t. 572, p. 179, 2007.

[292] D. Krasnov, O. Zikanov et T. Boeck, "Numerical study of magnetohydrodynamic duct flow at high Reynolds and hartmann numbers", *J. Fluid Mech.*, t. 704, p. 421, 2012.

[293] O. Zikanov, D. Krasnov, T. Boeck, A. Thess et M. Rossi, "Laminar-turbulent transition in magnetohydrodynamic duct, pipe, and channel flows", *Applied Mechanics Reviews*, t. 66, n° 3, 2014.

[294] T. Ishida, Y. Duguet et T. Tsukahara, "Transitional structures in annular Poiseuille flow depending on radius ratio", *J. Fluid Mech*, t. 794, R2, 2016.

[295] T. Ishida, Y. Duguet et T. Tsukahara, "Turbulent bifurcations in intermittent shear flows from puffs to oblique stripes", *Phys. Rev. Fluids*, t. 2, n° 7, p. 073 902, 2017.

[296] P. Manneville, "Turbulent patterns in wall-bounded flows : a turing instability ?", *EPL (Europhysics Letters)*, t. 98, n° 6, p. 64 001, 2012.

[297] G. Linga, "Fluid flows with complex interfaces : modelling and simulation from pore to pipe", thèse de doct., University of Copenhagen, Faculty of Science, Niels Bohr Institute, 2018.

[298] H. Schlichting et K. Gersten, *Boundary-layer theory*. Springer, 2016.

[299] M. Gaster et I. Grant, "An experimental investigation of the formation and development of a wave packet in a laminar boundary layer", *Proceedings of the Royal Society of London. A. Mathematical and Physical Sciences*, t. 347, n° 1649, p. 253–269, 1975.

[300] E. Reshotko, "Boundary-layer stability and transition", *Annual Review of Fluid Mechanics*, t. 8, n° 1, p. 311–349, 1976.

[301] M. Goldstein et L. S. Hultgren, "Boundary-layer receptivity to long-wave free-stream disturbances", *Annual Review of Fluid Mechanics*, t. 21, n° 1, p. 137–166, 1989.

[302] M Matsubara et P. H. Alfredsson, "Disturbance growth in boundary layers subjected to free-stream turbulence", *J. Fluid Mech.*, t. 430, p. 149, 2001.

[303] L. Brandt, P. Schlatter et D. S. Henningson, "Transition in boundary layers subject to free-stream turbulence", *J. Fluid Mech.*, t. 517, p. 167, 2004.

[304] J. H. Fransson, M. Matsubara et P. H. Alfredsson, "Transition induced by free-stream turbulence", *J. Fluid Mech.*, t. 527, p. 1, 2005.

[305] T. A. Zaki et P. A. Durbin, "Mode interaction and the bypass route to transition", *J. Fluid Mech.*, t. 531, p. 85, 2005.

[306] J. H. Fransson, "Flow control of boundary lagers and wakes", thèse de doct., KTH, 2003.

[307] M. V. Morkovin, "On the many faces of transition", in *Viscous drag reduction*, Springer, 1969, p. 1–31.

[308] V. Ovchinnikov, M. M. Choudhari et U. Piomelli, "Numerical simulations of boundary-layer bypass transition due to high-amplitude free-stream turbulence", *J. Fluid Mech.*, t. 613, p. 135, 2008.

[309] S. Cherubini, P. De Palma, J.-C. Robinet et A. Bottaro, "Rapid path to transition via nonlinear localized optimal perturbations in a boundary-layer flow", *Phys. Rev. E*, t. 82, n° 6, p. 066 302, 2010.

[310] S. Cherubini, P. De Palma, J.-C. Robinet et A. Bottaro, "The minimal seed of turbulent transition in the boundary layer", *J. Fluid Mech.*, t. 689, p. 221–253, 2011.

[311] S. Cherubini, F. Picella et J.-C. Robinet, "Variational nonlinear optimization in fluid dynamics : the case of a channel flow with superhydrophobic walls", *Mathematics*, t. 9, n° 1, p. 53, 2021.

[312] M. Asai, M. Minagawa et M. Nishioka, "The instability and breakdown of a near-wall low-speed streak", *J. Fluid Mech.*, t. 455, p. 289–314, 2002.

[313] D. S. Henningson, A. Lundbladh et A. V. Johansson, "A mechanism for bypass transition from localized disturbances in wall-bounded shear flows", *J. Fluid Mech.*, t. 250, p. 169–207, 1993.

[314] P. Andersson, L. Brandt, A. Bottaro et D. S. Henningson, "On the breakdown of boundary layer streaks", *J. Fluid Mech.*, t. 428, p. 29, 2001.

[315] M. Ustinov, "Stability of a spanwise nonuniform boundary layer flow", *Fluid dynamics*, t. 33, n° 6, p. 856–863, 1998.

[316] J. Hœpffner, L. Brandt et D. S. Henningson, "Transient growth on boundary layer streaks", *J. Fluid Mech.*, t. 537, n° 1, p. 91–100, 2005.

[317] Y. Duguet, P. Schlatter, D. S. Henningson et B. Eckhardt, "Self-sustained localized structures in a boundary-layer flow", *Phys. Rev. Lett.*, t. 108, n° 4, 2012.

[318] M. Beneitez, Y. Duguet, P. Schlatter et D. S. Henningson, "Edge tracking in spatially developing boundary layer flows", *J. Fluid Mech.*, t. 881, p. 164–181, 2019.

[319] P. Lenaers, Q. Li, G. Brethouwer, P. Schlatter et R. Örlü, "Rare backflow and extreme wall-normal velocity fluctuations in near-wall turbulence", *Physics of fluids*, t. 24, n° 3, p. 035 110, 2012.

[320] M. Vasudevan et B. Hof, "The critical point of the transition to turbulence in pipe flow", *J. Fluid Mech.*, t. 839, 2018.

[321] M. Branicki et S. Wiggins, "Finite-time Lagrangian transport analysis : stable and unstable manifolds of hyperbolic trajectories and finite-time lyapunov exponents", *Nonlin. Proc. Geoph.*, p. 1–36, 2010.

[322] C. Vavaliaris, M. Beneitez et D. S. Henningson, "Optimal perturbations and transition energy thresholds in boundary layer shear flows", *Phys. Rev. Fluids*, t. 5, n° 6, p. 062 401, 2020.

[323] C. W. Rowley, I. G. Kevrekidis, J. E. Marsden et K. Lust, "Reduction and reconstruction for self-similar dynamical systems", *Nonlinearity*, t. 16, n° 4, p. 1257, 2003.

[324] C. Cossu et L. Brandt, "On Tollmien–Schlichting-like waves in streaky boundary layers", *European Journal of Mechanics-B/Fluids*, t. 23, n° 6, p. 815–833, 2004.

[325] S. Shahinfar et J. H. Fransson, "Effect of free-stream turbulence characteristics on boundary layer transition", in *Journal of Physics : Conference Series*, IOP Publishing, t. 318, 2011, p. 032 019.

[326] J. H. Fransson et S. Shahinfar, "On the effect of free-stream turbulence on boundary-layer transition", *J. Fluid Mech.*, t. 899, 2020.

[327] R. Narasimha, "A report on the workshop on end-stage transition", *Current Science (Bangalore)*, t. 67, n° 1, p. 6–9, 1994.

[328] L. Hocking, "Non-linear instability of the asymptotic suction velocity profile", *The Quarterly Journal of Mechanics and Applied Mathematics*, t. 28, n° 3, p. 341–353, 1975.

[329] J. Canton, E. Rinaldi, R. Örlü et P. Schlatter, "Critical point for bifurcation cascades and featureless turbulence", *Phys. Rev. Lett.*, t. 124, p. 014 501, 1 2020.

[330] S. Zammert et B. Eckhardt, "Transition to turbulence when the tollmien–schlichting and bypass routes coexist", *J. Fluid Mech.*, t. 880, 2019.

[331] J. T. Stuart, "Nonlinear stability theory", *Annual Review of Fluid Mechanics*, t. 3, p. 347–370, 1971.

[332] N. R. Lebovitz, "Boundary collapse in models of shear-flow transition", *Commun. Nonlinear Sci.*, t. 17, n° 5, p. 2095–2100, 2012.

[333] M. Beneitez, Y. Duguet et D. S. Henningson, "Modeling the collapse of the edge when two transition routes compete", *Phys. Rev. E*, t. 102, n° 5, p. 053 108, 2020.

[334] H. W. Emmons, "The laminar-turbulent transition in a boundary layer-part i", *Journal of the Aeronautical Sciences*, t. 18, n° 7, p. 490–498, 1951.

[335] N Vinod et R. Govindarajan, "Pattern of breakdown of laminar flow into turbulent spots", *Phys. Rev. Lett.*, t. 93, n° 11, p. 114 501, 2004.

[336] T. Kreilos, T. Khapko, P. Schlatter, Y. Duguet, D. S. Henningson et B. Eckhardt, "Bypass transition and spot nucleation in boundary layers", *Phys. Rev. Fluids*, t. 1, n° 4, p. 043 602, 2016.

[337] D. Seki et M. Matsubara, "Experimental investigation of relaminarizing and transitional channel flows", *Physics of Fluids*, t. 24, n° 12, p. 124 102, 2012.

[338] T. Khapko, "Edge states and transition to turbulence in boundary layers", thèse de doct., KTH Royal Institute of Technology, 2016.

[339] M. Beneitez, "Nonlinear dynamics in transitional wall-bounded flows", thèse de doct., KTH Royal Institute of Technology, 2021.

[340] M MacDonald, D Chung, N Hutchins, L Chan, A Ooi et R García-Mayoral, "The minimal-span channel for rough-wall turbulent flows", *J. Fluid Mech.*, t. 816, p. 5–42, 2017.

[341] T. Ishida, G. Brethouwer, Y. Duguet et T. Tsukahara, "Laminar–turbulent patterns with rough walls", *Phys. Rev. Fluids*, t. 2, n° 7, p. 073 901, 2017.

[342] T. Tsukahara, T. Tomioka, T. Ishida, Y. Duguet et G. Brethouwer, "Transverse turbulent bands in rough plane Couette flow", *Journal of Fluid Science and Technology*, t. 13, n° 3, 2018.

[343] J. Jiménez, "Turbulent flows over rough walls", *Annu. Rev. Fluid Mech.*, t. 36, p. 173–196, 2004.

[344] A. Sharma et R. García-Mayoral, "Turbulent flows over dense filament canopies", *J. Fluid Mech.*, t. 888, 2020.

[345] A. Monti, M. Omidyeganeh, B. Eckhardt et A. Pinelli, "On the genesis of different regimes in canopy flows : a numerical investigation", *J. Fluid Mech.*, t. 891, 2020.

[346] A. Bottaro, "Flow over natural or engineered surfaces : an adjoint homogenization perspective", *Journal of Fluid Mechanics*, t. 877, 2019.

[347] G. Kawahara, "Laminarization of minimal plane Couette flow : going beyond the basin of attraction of turbulence", *Phys. Fluids*, t. 17, n° 4, p. 041 702, 2005.

[348] J. Kühnen, B. Song, D. Scarselli, N. B. Budanur, M. Riedl, A. P. Willis, M. Avila et B. Hof, "Destabilizing turbulence in pipe flow", *Nature physics*, t. 14, n° 4, p. 386–390, 2018.

[349] P. H. Alfredsson et R. Örlü, "Large-eddy breakup devices–a 40 years perspective from a stockholm horizon", *Flow, turbulence and combustion*, t. 100, n° 4, p. 877–888, 2018.

[350] C. Chin, R. Örlü, J. Monty, N. Hutchins, A. Ooi et P. Schlatter, "Simulation of a large-eddy-break-up device (LEBU) in a moderate Reynolds number turbulent boundary layer", *Flow, Turbulence and Combustion*, t. 98, n° 2, p. 445–460, 2017.

[351] P.-G. De Gennes et J. Badoz, *Fragile objects : soft matter, hard science, and the thrill of discovery*. Springer Science et Business Media, 2012.

[352] G. H. Choueiri, J. M. Lopez et B. Hof, "Exceeding the asymptotic limit of polymer drag reduction", *Phys. Rev. Lett.*, t. 120, n° 12, p. 124 501, 2018.

[353] D. Samanta, Y. Dubief, M. Holzner, C. Schäfer, A. N. Morozov, C. Wagner et B. Hof, "Elasto-inertial turbulence", *Proceedings of the National Academy of Sciences*, t. 110, n° 26, p. 10 557–10 562, 2013.

[354] L. Xi et M. D. Graham, "Dynamics on the laminar-turbulent boundary and the origin of the maximum drag reduction asymptote", *Phys. Rev. Lett.*, t. 108, n° 2, p. 028 301, 2012.

[355] M. D. Warholic, G. M. Schmidt et T. J. Hanratty, "The influence of a drag-reducing surfactant on a turbulent velocity field", *J. Fluid Mech.*, t. 388, p. 1–20, 1999.

[356] P. Doohan, A. P. Willis et Y. Hwang, "Minimal multi-scale dynamics of near-wall turbulence", *J. of Fluid Mech.*, t. 913, 2021.

[357] Y. Hwang et C. Cossu, "Self-sustained process at large scales in turbulent channel flow", *Phys. Rev. Lett.*, t. 105, n° 4, p. 044 505, 2010.

[358] B. F. Farrell et P. J. Ioannou, "Statistical state dynamics-based analysis of the physical mechanisms sustaining and regulating turbulence in Couette flow", *Phys. Rev. Fluids*, t. 2, n° 8, p. 084 608, 2017.

[359] H. J. Bae, A. Lozano-Duran et B. J. McKeon, "Nonlinear mechanism of the self-sustaining process in the buffer and logarithmic layer of wall-bounded flows", *J. Fluid Mech.*, t. 914, 2021.

[360] C. D. Meinhart et R. J. Adrian, "On the existence of uniform momentum zones in a turbulent boundary layer", *Physics of Fluids*, t. 7, n° 4, p. 694–696, 1995.

[361] E.-W. Saw, D. Kuzzay, D. Faranda, A. Guittonneau, F. Daviaud, C. Wiertel-Gasquet, V. Padilla et B. Dubrulle, "Experimental characterization of extreme events of inertial dissipation in a turbulent swirling flow", *Nature communications*, t. 7, n° 1, p. 1–8, 2016.